ESRF
The European Synchrotron

ESRF HIGHLIGHTS 2016

ESRF
The European Synchrotron

ESRF HIGHLIGHTS 2016

EUROPEAN SYNCHROTRON RADIATION FACILITY

	Pages
Introduction	*2*
2016 at the ESRF	*4*
Status of the EBS	*6*
Scientific Highlights	*10*
Electronic structure, magnetism and dynamics	*10*
X-ray nanoprobe	*30*
Structure of materials	*48*
Structural biology	*68*
Complex systems and biomedical sciences	*92*
Matter at extremes	*112*
Industrial Research	*134*
Enabling Technologies	*138*
Accelerator and Source	*152*
Facts and Figures	*160*

Francesco Sette

DEAR READER

It is a great pleasure to present the 2016 issue of the ESRF Highlights to you. As I look back over the past year, I never cease to be impressed by the engagement of our international user community and by its impressive scientific productivity, as well as by the commitment of the ESRF staff in supporting the user programme and the facility. I invite you to enjoy a taste of our science in this report as well as the scientific and technological progress realised in 2016.

2016 has been a very productive and important year for the ESRF.

As in its previous 23 years of operation, the ESRF machine delivered another year of high quality, reliable and stable beam thanks to a continuous and dynamic research – development – refurbishment - maintenance programme. Since last April, user operation benefits from the new "top-up" storage ring injection mode, which is proving to be particularly beneficial for users who rely on the ESRF timing modes. It allows a substantially higher average intensity at low vertical emittance. The overall 2016 delivery, currently in line with best-year statistics, enabled an excellent operation of the beamlines and gave outstanding scientific results.

2016 was also an exceptional year for the user programme with an increase of around 10% in the number of submitted user proposals. In 2016, the ESRF was also able to support a record number of experimental sessions: approximately 1820 scheduled at the time of writing, corresponding to about 10% more than our previous record year in 2009. This result is even more striking if we consider that two public beamlines are closed until the end of 2022, and some of the beamlines were not fully operational in 2016. This increase is a direct consequence of our renewed beamline portfolio, which – thanks to the Upgrade Programme Phase I – allows not only new scientific investigation but also shorter and more effective experiments, thereby resulting in the observed increased number of experimental sessions.

The ESRF-Extremely Brilliant Source programme - the ESRF-EBS – is, overall, on schedule. Most importantly, the project is well off the starting blocks and substantial progress has been made on both the accelerator and experimental sides.

The accelerator project team is fulfilling its objectives in terms of procurement, pre-series activities for the new storage ring, and initiating the in-house assembly of a critical dipole magnet family based on a revolutionary design fully developed at the ESRF. The first pre-series magnet and girder components have arrived on site, and some of them can be seen in the Chartreuse Hall. The Accelerator Project Office is now focussing its efforts on procurement follow-up, component design finalisation and on the organisation of the logistics aspects required for the forthcoming assembly and installation phases.

The EBS experimental programme is also taking shape. Based on 48 Expressions of Interest received from the scientific community at large and from the ESRF users by March 2016, about eight projects have been identified by the ESRF's Science Advisory Committee (SAC) and ESRF scientists as being very promising and with the potential to evolve into new state-of-the-art beamlines and instruments. Expert teams have been identified for each of these projects, with a mandate to draft Conceptual Design Reports (CDRs). These CDRs were presented and discussed with the scientific community at a dedicated workshop which was held in December 2016. The aim of these combined efforts is to enable the ESRF SAC and Council, in 2017, to express a consolidated view of the best scientific opportunities with the new EBS storage ring at the ESRF, and to specify the priorities for future EBS beamlines

in the context of the existing ones and of the portfolio developed during the ESRF Upgrade Programme Phase I.

Similarly, during the last few months, important progress has been made in the procedure and technical aspects linked to the future ESRF and CRG beamlines on today's dipole magnet (BM) front ends. Source characteristics have been identified and settled, existing CRG beamlines have been endorsed by the SAC and Council for their continuation with the new storage ring source, and the planning for their upgrade and adaptation is going ahead.

The stakes are high but so are the rewards. The successful completion of ESRF-EBS will not only consolidate the position of the ESRF as a global leader in a new generation of synchrotron sources but will result in the writing of a new chapter in X-ray science. All this is possible, thanks to the experience and the engagement of the ESRF staff, in all of its Divisions. It is also possible, thanks to the strong engagement of the ESRF users, and of the 21 ESRF partner countries that continue to support the entire ESRF programme financially. In this respect, I wish to underline our gratitude to France for providing an exceptional financial contribution to the ESRF-EBS in the context of the ongoing CPER programme. It is also rewarding to note the interest of new and existing partner countries in accessing or strengthening their participation in the ESRF.

The work carried out at the ESRF and the quality of its results and contributions are widely recognised internationally. An illustration of this is the inclusion of the ESRF-EBS Programme as one of the eight new European Landmarks in the ESFRI Roadmap Update, published in March 2016. Similarly, I wish to mention that the new ESRF storage ring lattice has established a new standard for present and future synchrotron centres, as demonstrated by its wide adoption in the future construction of new synchrotrons and in the upgrade plans of existing ones in Europe and worldwide.

The greatest impact of the ESRF is in contributing to science and to the advancement of human knowledge by promoting the use of synchrotron radiation. In this respect, we are very pleased that the three 2016 Nobel Prizes for the advancement of science (Physics, Chemistry, and Medicine and Physiology) were granted to studies that all benefit from synchrotron work and applications, and that the Chemistry Nobel Laureate, Prof. J.L. Sauvage from the Strasbourg University "L. Pasteur", appears on key papers using the ESRF. Furthermore, the ESRF is also deeply engaged in providing services to industry and innovation, and in supporting programmes to interest and educate the younger generations in scientific and technological careers. Besides the approximately 130 positions dedicated each year to undergraduate trainees, PhD students, post-doctoral fellows, and junior scientists, the ESRF continues to support: 1) The HERCULES School for graduate students and post-doctoral fellows, 2) the ESRF-ILL summer school for undergraduate students, and 3) the programme "Synchrotron@school", in partnership with the "Académie de Grenoble", dedicated to pupils in scientific and technical secondary schools.

All in all, the ESRF is succeeding in creating a unique international hub for staff, visitors, users and young people, which makes spending time at the ESRF tremendously interesting and productive. By bringing together different cultures, points of view and working methods, we can overcome the challenges facing our modern world and prove that scientific advancement knows no frontiers, and is for the benefit of all humankind.

I wish to end by thanking the ESRF users, to whom this new issue of the ESRF Highlights is dedicated, for their support and to congratulate them for the excellent science that they carry out at the ESRF.

FRANCESCO SETTE
Director General,
ESRF

2016 at the ESRF

Full and open access to scientific data

The adoption of a data policy in February 2016 means the ESRF will be the custodian of raw data and metadata collected during research on its publicly funded beamlines. Following a three-year embargo period, the data will be released into the public domain with open access.

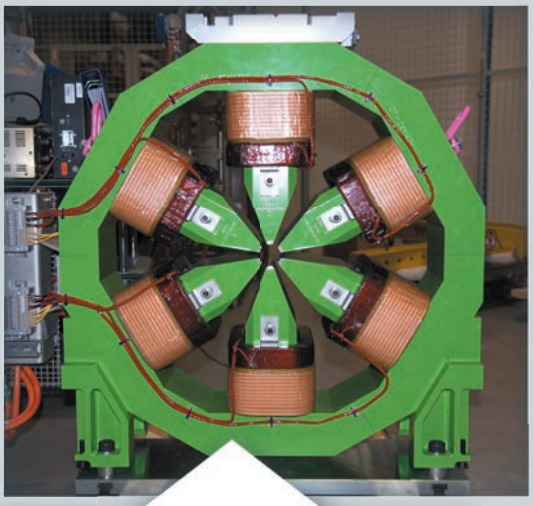

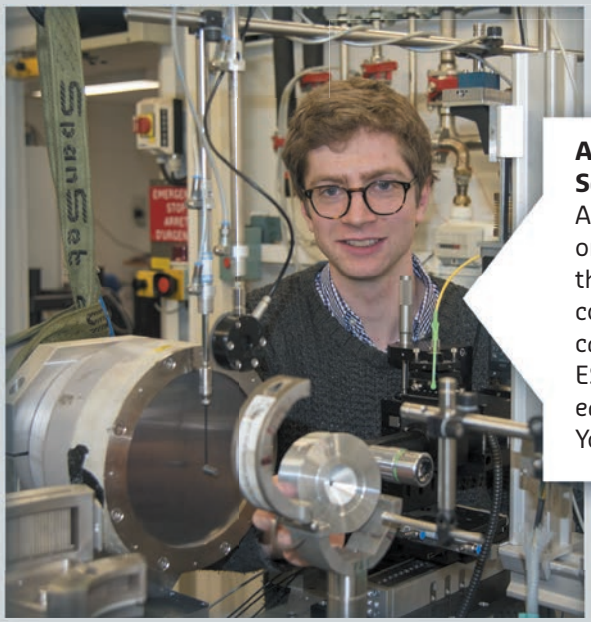

Andrew Cairns wins Young Scientist Award

Andrew's outstanding work on identifying materials with the strongest negative linear compressibility yet known caught the attention of the ESRF User Organisation and earned him the 2016 title of Young Scientist of the Year.

ESRF-EBS is landmark for ESFRI 2016

In March 2016, the European Strategy Forum on Research Infrastructures selected the ESRF-EBS as one of the 29 landmark projects identified for scientific excellence, pan-European relevance, socio-economic impact and innovation.

Italian and French ministers back signature

Italian minister for Education, Universities and Research, Stefania Giannini, and French Minister of State for Higher Education and Research, Thierry Mandon, visited the ESRF on 8 February 2016. They chaired the signature of a technical collaboration agreement between the ESRF and the INFN. The agreement will result in an exchange of expertise between ESRF and INFN for ESRF-EBS.

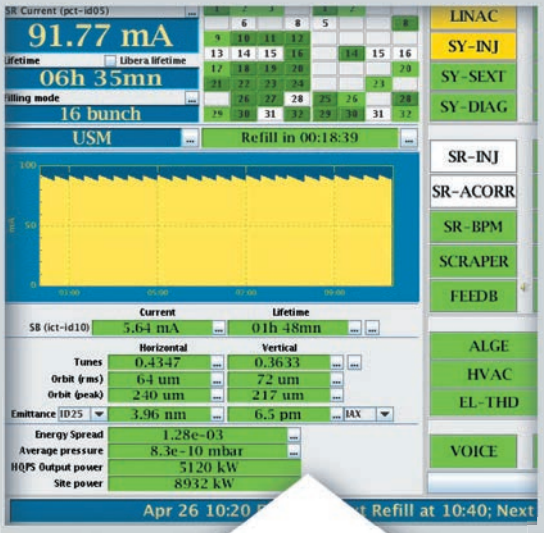

First time for top-up filling in USM
In April 2016, beam was delivered to users for the first time in top-up mode. For four consecutive weeks ESRF users could benefit from a higher integrated current over a 24-hour period, giving more photons and better beam stability due to smaller current variations.

Caroline Bissardon laureate of 2016 L'Oréal-UNESCO For Women in Science
Caroline, 25, was one of the 17 PhD students to be recognised by the l'Oréal-UNESCO For Women in Science Awards. She was rewarded for her work on the unexplored role of selenium in cartilage for which she has used the ESRF extensively, mainly beamlines ID16A and BM30B (FAME CRG). *Credit: L'Oreal.*

Inauguration of joint grant programme with Russia
On 28th June, in the presence of the Russian Minister for Education and Science, the ESRF inaugurated a joint grant programme to better promote joint scientific and technological endeavours and develop cooperation in the frame of the ESRF-EBS project. Today, the ESRF has developed more than 60 partnerships with Russian institutes and universities.

Ribbon-cutting on beamlines ID15A and ID15B
The two branches of a new beamline, ID15A and ID15B, were inaugurated during the 73rd Scientific Advisory Committee on 9 November 2016.
ID15A is a high energy X-ray beamline for materials chemistry and materials engineering while ID15B, as the successor to the old ID09A beamline, is a high pressure crystallography beamline.

STATUS OF THE EBS

The past year marked the second year of the execution phase of the ESRF's Extremely Brilliant Source (EBS) project, which will see the implementation of a new lattice for the storage ring. This lattice will reduce the natural horizontal emittance from 4 nm to about 134 pm, thus greatly increasing the brilliance and coherence of the beam, opening up new horizons for accelerator science. Much of the work of the project in 2016 concentrated on finalising the design and following up on the procurement of the components. Numerous prototypes were tested, validated and launched into production and, in the second half of the year, the first pieces of equipment were already being delivered onsite. In addition to this, great effort went into the detailed planning and organisation of the assembly, dismantling and installation phases, complex work that defines the logistical requirements, task sequences and resource needs for the next four years. Finally, by the end of the year, the first new buildings to be constructed for the project started to go up – a visual and concrete reminder that the EBS project is very much taking shape!

PROJECT MANAGEMENT

Overseen by the Accelerator Project Office (APO), the work on the ESRF–EBS project was presented for review to the Machine Advisory Committee (MAC) on two occasions during 2016. In April, the EBS team informed the panel of accelerator experts that around 90% of the design work had been completed and all of the critical prototypes and tests had been successful, with about 60% of the planned calls for tender for equipment launched. The committee was very satisfied with the progress made and, in particular, commended the team for working on the possibility of providing users with a range of different X-ray sources (the lattice dipoles or additional short bending magnets, 2-pole wigglers or 3-pole wigglers) for ESRF and CRG bending magnet beamlines. Feedback from the Committee also included a suggestion to place four fully-assembled girders in a 'mock-up' tunnel and execute all the installation tasks foreseen, such as cabling, piping, vacuum connections and alignment, which will be put into practice in 2017.

Fig. 1: The members of the Machine Advisory Committee, together with ESRF colleagues, inspect the newly-delivered dipole magnets in the Chartreuse Hall.

The MAC met again in September and was pleased to note new developments including the assembly of a prototype dipole (**Figure 1**), thermal tests on the prototype girder and ground preparations for the new EBS buildings. Chairman Richard Walker said, "The project is on track and there have not been any changes to the major project milestones. The MAC therefore sees no showstoppers at this stage for the successful and timely realisation of the project."

In addition to the MAC meetings, two EBS team events were held in July and December 2016 to discuss project strategy and focused largely on the assembly, dismantling and installation phases. Issues such as planning constraints, phase organisation and resource requirements were reviewed in detail and the most critical future actions to be taken were addressed.

Also during 2016, a series of open seminars was put in place to encourage collaboration between facilities and the sharing of experience of constructing low-emittance storage rings. Speakers including Pedro Tavares from Max IV, Michael Borland from APS, and Ferdinand Willeke from NSLS were invited to share their experience and discuss the challenges of all aspects of design, construction, installation, and commissioning of MBA-based storage rings. The seminars have been very well received by interested members of ESRF staff and are set to continue over the course of the project.

PROCUREMENT PROGRESS

Tremendous progress was made in 2016 on the procurement of the components for the new storage ring. By the end of the year, the largest calls for tenders were issued and 46 out of 47 contracts launched had been signed, while contracts were already in progress for the electromagnetic septa, RF gaskets, thermocouples and full metal isolation valves.

The girder handling system is being finalised with a specialised company in charge of the contract.

Manufacturing of prototype or 'pre-series' components began, including vacuum chambers, photon absorbers and vacuum instrumentation such as RGA analysers, gauges, bellows and pumping ports. Concerning the magnets, the pre-series manufacturing is in progress for the moderate gradient quadrupoles, dipole-quadrupoles and octupoles. The pre-series high-gradient quadrupoles, sextupoles and correctors have already been built.

Following the successful validation of prototypes or 'pre-series' equipment, production of the 'main series' of components for the new machine also started. For the magnets, this included the sextupoles, high-gradient quadrupoles and correctors. For other components, this included the girders, dipole supports, RF cavities, RF fingers, DC-DC converters, beam loss monitors and vacuum pumps. All the beam position monitor buttons for the EBS have been manufactured and delivered – these were the first serial production items completed.

Delays to the project could be caused by manufacturing set-backs and so the procurement process will continue to be closely monitored – from the first design of a component until its delivery – over the course of the project.

DELIVERY OF THE FIRST COMPONENTS

Marking a major milestone for the EBS, the first components started to arrive onsite during the second half of 2016.

The first girders for the new storage ring were delivered to the Chartreuse Hall at the end of October (**Figure 2**). These two supports, of 5 m-long and 6 tonnes, were the first of 130, the remainder to be delivered progressively in 2017. Four girders will be set up in the Chartreuse Hall and installed with real components as part of a 'mock-up cell' exercise, while the other 126 will be stored in the new building ESRF 02 until the assembly phase begins in October 2017.

As well as the girders, the first magnets also started to arrive in autumn 2016, the prototype dipole components at the end of August, and the first sextupoles at the end of November. The main series of dipole components followed soon after – with a total delivery of over 13,000 high-performance permanent magnets, 640 magnet modules and 128 dipole supports by the end of the year.

Fig. 2: The first EBS girder was delivered to the Chartreuse Hall in October 2016.

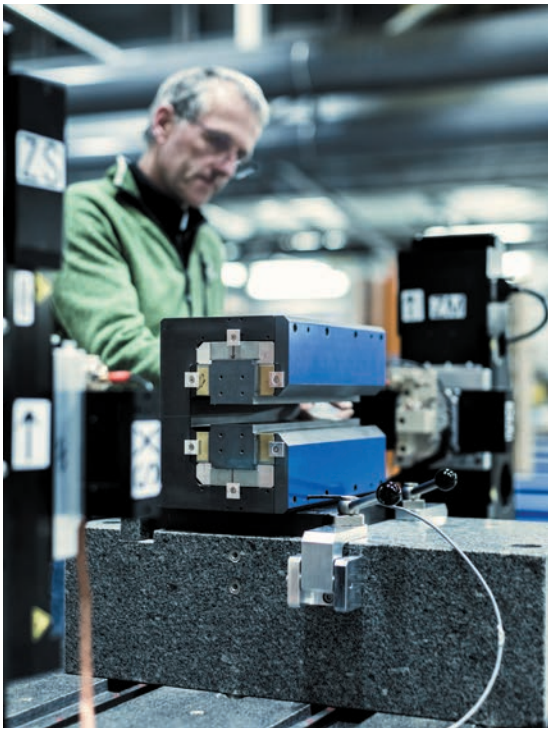

Fig. 3: Joel Chavanne takes magnetic measurements of one of the dipole magnet modules.

IN-HOUSE ASSEMBLY OF DIPOLES STARTED

Following the successful validation of a prototype and the subsequent delivery of the dipole components, the series production of the first EBS magnets began in December 2016.

The construction of a large series of dipoles needs to be carefully controlled to reach the required magnetic field quality and therefore the magnets are being assembled in-house (**Figure 3**), relying on the expertise and experience of our staff with permanent magnets. Each dipole is an assembly of around 100 samarium-cobalt permanent magnets, distributed between five magnet modules made of low-carbon steel with pure iron poles, bolted to a support.

Over the summer of 2016, a magnet assembly area was set up in the ESRF's Chartreuse Hall. A prototype dipole, consisting of support, modules and magnets, was delivered at the end of August and assembly began in September.

The modules were assembled with the magnets and measured before being mounted on the support and re-measured in order to test the strength of the magnetic fields. The exercise served to refine the assembly, measurement and calibration process, which will continue until December 2017, with over 60 tons of magnetic material to assemble over the course of the year.

RF CAVITY PRODUCTION MAKES GOOD PROGRESS

Following the validation of three prototypes, the first of the 12 new HOM-damped single-cell radio frequency cavities arrived at the ESRF in June 2016. They will replace the existing five-cell cavities in the EBS storage ring. Three more were delivered later in the year, ready to be conditioned onsite by the RF team.

Fig. 4: The dedicated RF assembly area in the ID08 zone of the experimental hall.

The cavities, which were developed in-house, are being manufactured using complicated fabrication processes involving high temperature brazing. This, along with the careful assembly under clean room conditions at the ESRF (shown in **Figure 4**) resulted in a conditioning time of just two weeks per cavity – a very comfortable match for the EBS schedule. Following delivery to the dedicated assembly area, the cavities are equipped with their ancillary equipment, baked and RF conditioned, ready to be installed on the new ring in 2019. The internal geometry of the cavities has been carefully designed to maximise beam acceleration and at the same time to efficiently damp the higher order modes (HOM) by means of their attached HOM dampers. **Figure 5** shows the first of the series of 12 cavities in fabrication.

ELECTRICAL POWER

In 2016, the power requirements for the EBS project were finalised, allowing the launch of the procurement of more than 1000 power supplies

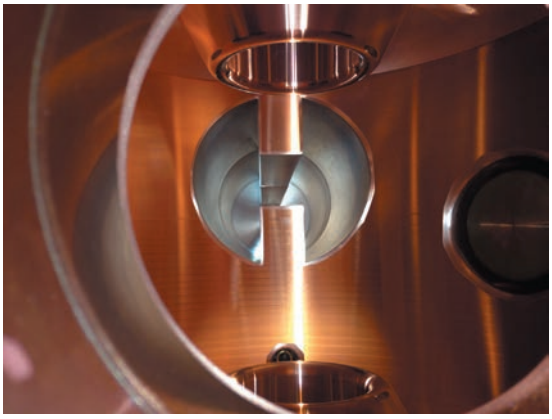

Fig. 5: Inside a HOM-damped single-cell radio frequency cavity.

to power the main magnets. Tests of the future power cabling were carried out on the prototype girder, resulting in the definition of the best cabling layout.

EBS CONSTRUCTION WORK DEVELOPS

A total of eight new buildings will be constructed in the centre of the storage ring over the course of the project to house the multitude of activities generated by the EBS.

The first of the new EBS buildings was completed in October 2016. Known as ESRF 10, the 200 m^2 temporary building will be used to store spare accelerator equipment that is currently stockpiled in the technical zones surrounding the accelerator tunnel. The technical zones will be used in the coming months to store the newly-arrived girders so space was needed quickly and the temporary building was deemed the most practical option. The foundations were laid in September and the building went up in a matter of days.

Ground preparation for the main permanent buildings, ESRF 01 (see **Figure 6**) and ESRF 02, kicked off in August and continued through the autumn. The 1100 m^2 surface of ESRF 01 will be used to assemble the girders for the new machine and then, once this is completed, it will serve as a workshop. ESRF 02A and ESRF 02B, two 500 m^2 buildings, will be used to store newly delivered components before and during the assembly phase. Ground preparation also began for three temporary buildings, ESRF 11, 12 and 13, which will be used as workshops to perform radiation activation measurements on the components removed from the tunnel. An extension to the existing accelerator technical buildings (MTBS) is also planned for November 2018 to provide a new location for the RF test stand and additional space to store RF components.

BEAMLINE UPGRADE

2016 marked the start for the preparation of the upgrade of the beamlines in the ESRF's portfolio. The upgrade includes the construction of four new beamlines as well as the preparation of the existing beamlines for the EBS.

Following a call for expressions of interest from the user community, launched in October 2015 and concluded in March 2016, the ESRF received 48 proposals. The proposals have been assessed by ESRF experts and grouped by scientific theme. The outcome of this analysis was discussed at the meeting of the Science Advisory Committee (SAC) in May 2016. This resulted in the selection of eight scientific themes to be served by upgraded beamlines and a shortlist of a number of major refurbishment projects to existing beamlines.

During the last three months of 2016, the ESRF started the preparation of Conceptual Design Reports (CDRs) for the potential new beamlines to be constructed within the EBS project. For each of the eight selected scientific themes, a working group (external experts, SAC observer, beamline scientists) has been mandated to develop a draft CDR condensing the scientific case into a potential beamline project, with the results as follows:

CDR1 – Beamline for coherence applications
CDR2 – Beamline for hard X-ray diffraction microscopy
CDR3 – High throughput large field phase-contrast tomography beamline
CDR4 – Surface science beamline
CDR5 – Advanced high-flux nano-X-ray diffraction beamline for science under extreme conditions
CDR6 – Facility for dynamic compression studies
CDR7 – High brilliance XAS beamline
CDR8 – Serial crystallography beamline

The draft CDRs were presented to the public in a two-day event called the EBS Science Workshop, held on 8-9 December 2016 at the ESRF, to solicit input from the user community at large for further refinement of the CDRs. The CDRs are now available in final form and will be further analysed by the SAC before they make a recommendation on the future beamline portfolio of the ESRF.

INSTRUMENTATION AND DATA MANAGEMENT

The EBS programme comprises an ambitious instrumentation and technology programme, which is required to gain the greatest benefit from the new source properties. This programme is centred on the following five themes:

1. New advanced metrology tools and methods for X-ray optics to cope with the challenging characteristics of the new optical components required to preserve the new source properties
2. The development of a double-crystal monochromator for spectroscopy with unprecedented characteristics
3. Generic end station design, using mechatronic concepts and on-line metrology for performance enhancement in terms of stability, accuracy, speed, automation and user-friendliness
4. A robust detector development plan, mandatory for optimum exploitation of the new source properties
5. An ambitious modernisation programme on beamline control and new data analysis platforms including innovative solutions to manage and process large volumes of data

While there was progress on all five themes, emphasis was put on the online data reduction and analysis. First versions of the library of common software routines for analysing data from synchrotron sources (code name SILX) have been released in the past months (https://github.com/silx-kit). Furthermore, the implementation of the ESRF Data Policy has started. The systematic recording of metadata is under test at ID01, ID11, ID31, and the MX beamlines, progressing at a rate of ten beamlines per year, as part of the plans to complete the implementation of the ESRF data policy by 2020. Hand in hand with the work on the beamlines, the IT infrastructure is being upgraded to increase the bandwidth and capacity of the storage and to allow for the long-term archival of the data from the beamlines. Additional compute nodes have been procured and made available to process the rapidly increasing data volume produced by the beamlines.

R. DIMPER, M. KRISCH, P. RAIMONDI, H. REICHERT, J. SUSINI *and* **A.J. JOLY**

Fig. 6: The frame structure of the new assembly building ESRF 01 was put into place in December 2016.

Electronic structure, magnetism and dynamics

The beamlines of the Electronic Structure, Magnetism and Dynamics (EMD) Group were fully dedicated to user operation in 2016. We are grateful to the many users who agreed to give presentations at the spectroscopy meetings during their visits to the ESRF. The scientist in the EMD group working on theoretical spectroscopy, M. Retegan, released (via GitHub) his program Crispy that provides a graphical user interface (written in Python) for the code Quanty written by M. Haverkort (University of Heidelberg) to perform calculations of core-level spectra. Crispy is a user-friendly tool to model X-ray spectra that is particularly powerful when intra-atomic electron-electron interactions strongly influence the spectral shape. Future developments will include interfaces to density functional calculations thus broadening the range of applications. Crispy has a modular design open to contributions from the user community; it runs on Windows, macOS and Linux. This important software development, made in collaboration with a growing number of external groups, will help the ESRF users applying spectroscopy to extract more information from their experimental data.

This highlight chapter presents some of the outstanding research that was performed on the beamlines of the EMD group (ID12, ID20, ID26, ID28, ID32) as well as the CRG beamlines BM01 and BM08.

ID12 is a unique instrument worldwide devoted to X-ray spectroscopy with extreme sensitivity using polarised synchrotron radiation in the energy range from 2 to 15 keV. Its outstanding performance is illustrated with the detection of the influence of an external electric field on X-ray absorption spectra (Ney *et al.*). It became possible to detect the spectral changes thanks to remarkable reproducibility of the energy scale at the level of 10^{-7}. The magnetism community benefits from an experimental station dedicated to X-ray magnetic circular dichroism spectroscopy at low temperatures (down to 2 K) and high magnetic field (up to 17 Tesla). This technique is becoming increasingly popular amongst chemists, which is illustrated by the results obtained on iridium based molecular complexes (Pedersen *et al.*). Moreover, an end station at ID12 dedicated to XMCD studies under high pressure was upgraded in autumn 2016. Users can now perform measurements in a magnetic field of 8 Tesla and temperatures below 3 K.

ID20 provides multiple X-ray spectroscopic techniques for the investigation of the electronic structure of materials, including resonant and non-resonant inelastic X-ray scattering. The research activity at ID20 in 2016 was largely focused on hard condensed matter, chemistry, material science and environmental science. One highlight (Donner *et al.*) describes the study of magnetic excitations in a prototypical pyrochlore iridate. A very interesting application of X-ray Raman spectroscopy is shown by Sahle *et al.* who followed the evolution of the hydrogen storage material $Mg(BH_4)_2$ under *in situ* conditions. Recent technical developments concerned the installation of a chamber that hosts a pair of phase plates and of an additional end station in the first experimental hutch. This new end station facilitates studies that require a reduced beam divergence (~10 µrad) and can host experiments with unconventional setups that do not require the instruments for inelastic X-ray scattering located in the other experimental hutches.

ID26 is a user-friendly beamline for X-ray absorption and emission spectroscopy that many researchers visit for *in situ* studies and dilute and radiation sensitive samples. The power of combining X-ray spectroscopy with diffraction is demonstrated in the highlight by Lezcan-González *et al.* where the authors studied Mo species during the catalytic conversion of methane. In the highlight by Butorin *et al.*, the authors exploit resonant inelastic X-ray scattering (RIXS) at the M-edges of actinides to directly probe the crystal field splitting. This work anticipates the advent of a new spectrometer for X-ray emission spectroscopy in the energy range 1.5 – 5 keV thus extending the existing capacities on ID26 to lower energies. The instrument that is being realised in collaboration with the Université Grenoble Alpes (ANR - EcoX Equipex) will be installed starting in spring 2017 and commissioned after the summer. Besides the M emission lines of actinides, the energy range covers the L emission lines of 4d transition metals and the K emission lines of Al, Si, P, S, Cl and K.

ID28 pursued its traditional activity in the study of lattice dynamics in strongly correlated systems and ferroelectrics and observed an increased interest in thermoelectrics and a revival of activity in biological systems. The detectors in the inelastic X-ray scattering spectrometer now employ a new, sustainable

sensor material based on CdTe. It has been in operation for nearly one year with very good performance. The main milestone that was achieved in 2016 was the end of the construction and commissioning of a new side station that operates in parallel with the main branch spectrometer and is devoted to diffuse scattering studies. The use of roadmaps obtained by diffuse scattering for the inelastic scattering experiments is expected to significantly increase the efficiency of the beamline. First users will benefit from its tandem operation starting in March 2017. The side station has been commissioned for wavelengths ranging from 0.52 Å to 0.98 Å, providing flux in the order of 10^{12} photons/second with a focal spot size below 50 µm. Temperatures between 85 and 1000 K are available as well as diamond anvil cells for high pressure studies. Test experiments on a variety of systems, including ferroelectrics, high-temperature superconductors, oxygen conductors, zeolites, quasicrystals, disordered alloys, show very good performance owing in part to the use of a photon counting pixel array detector and stable, versatile goniometry.

The emphasis of the soft X-ray beamline, **ID32**, in 2016 has been on developing the user programme for the very high energy resolution RIXS branch. The branch is running full time and many experiments have been carried out that will certainly contribute to the Highlights in the coming years. The soft X-ray dichroism branch (XMCD) has continued its successful operation, examples of which are given by Donati *et al*. and Candini *et al*. The surface science complex for preparing samples *in situ* **[1]** is proving to be very effective and allows unique samples to be fabricated and measured at the beamline. Consequently, the prospects for many interesting results in 2017 look very promising.

P. GLATZEL

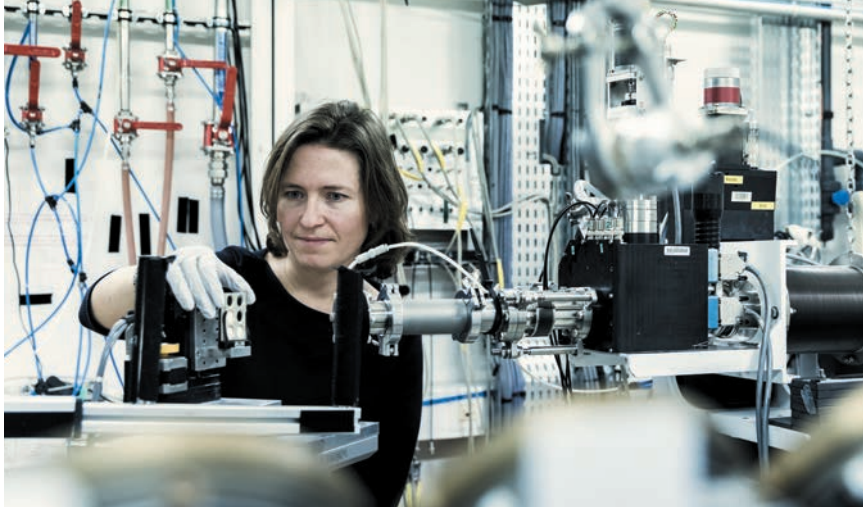

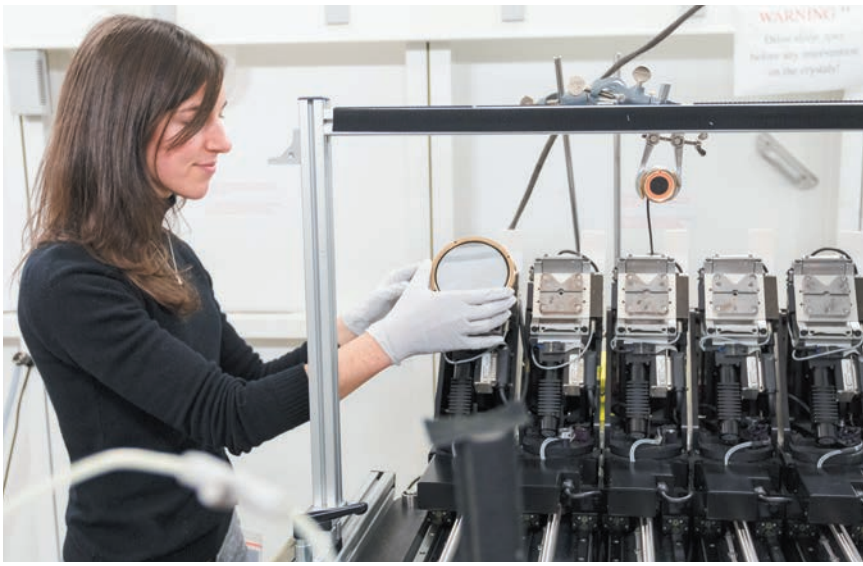

REFERENCES

[1] K. Kummer *et al.*, *J. Synchrotron Rad.* **23**, 464-473 (2016).

EXPERIMENTAL REALISATION OF SINGLE-ATOM MAGNETS

The existence of single-atom magnets has been proven by X-ray magnetic circular dichroism. Monodisperse holmium atoms adsorbed on a nonmagnetic MgO thin film display magnetic hysteresis up to a temperature of 30 K and with a magnetic relaxation time of the order of 1500 s. This stability is exceptional for such tiny structures. This study unveils key factors to improve the stability of atom-sized magnets in a solid state environment.

Magnets possess both strength and memory. These two properties make them useful for a broad variety of applications, which involve action at a distance or retention of magnetic information. Yet, as a magnet is reduced in size, thermal fluctuations overcome the anisotropy barrier that keeps the magnetic axis stable, leading to the loss of permanent magnetisation.

Scientists have been working for a long time to define and reduce the size of permanent magnets down to the smallest possible limit. A recent study that we have carried out at the ESRF and SLS may have brought us to the end of this quest. Exceptional magnetic stability can be achieved by combining the properties of rare earth atoms, such as holmium, with that of a weakly-interacting but mechanically-stiff supporting thin film, such as a 1 nm thick MgO layer. **Figure 7** shows the adsorption geometry of individual Ho atoms on the O sites of the MgO(001) lattice calculated by density functional theory (DFT) and probed by scanning tunnelling microscopy (STM).

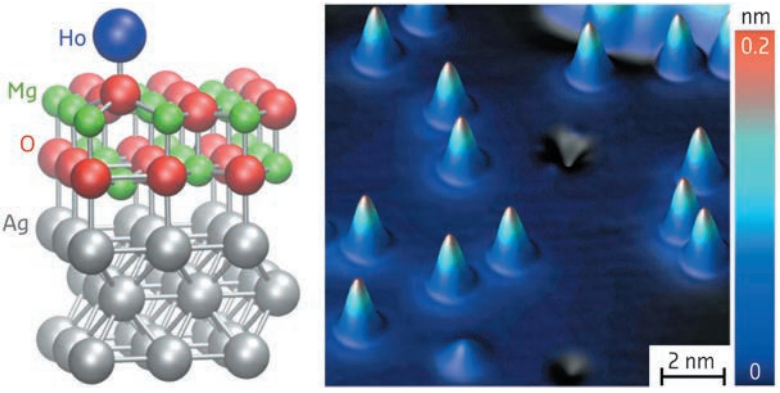

Fig. 7: Adsorption geometry of Ho atoms on a two-monolayer-thick MgO film deposited on Ag(100) as calculated by density functional theory (left) and measured by scanning tunnelling microscopy (right).

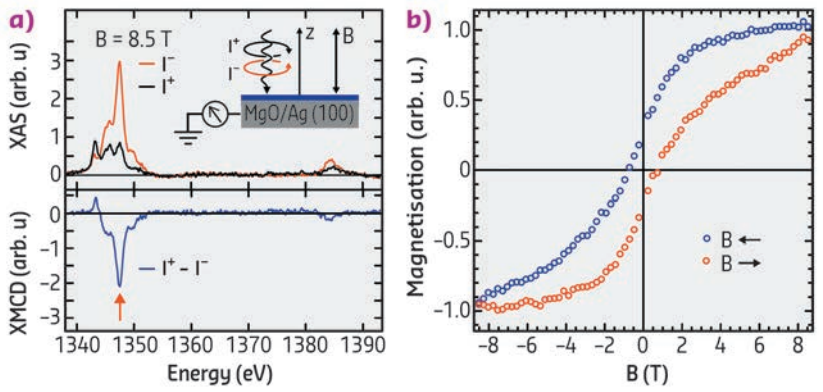

Fig. 8: a) X-ray absorption spectra and circular magnetic dichroism of an ensemble of individual Ho atoms adsorbed on MgO measured at the $M_{4,5}$ Ho edges at 6 K in a magnetic field of 8.5 T. b) Magnetic hysteresis curve measured at 6 K. The dots represent the maximum of the XMCD signal indicated by the arrow in (a) recorded as a function of magnetic field.

X-ray magnetic circular dichroism measurements at the $M_{4,5}$ absorption edges of Ho (**Figure 8a**), carried out at beamline **ID32**, indicate that the Ho atoms possess a high magnetic moment in a magnetic field of 8.5 T and at 6 K. Surprisingly, hysteretic behaviour appears as the magnetisation is measured as a function of applied field (**Figure 8b**), revealing that the Ho atoms display magnetic remanence, just like a permanent magnet. Additional measurements, carried out at the SLS, show that magnetic hysteresis persists up to 30 K and correlates with the thickness of the MgO film. The magnetic relaxation time was found to be of the order of 1500 s or possibly larger, being limited by the X-ray photon flux used to probe the atoms. For comparison, the magnetic relaxation time in the most stable single molecule magnets reported to date is of the order of 1 ms at such temperatures.

Ligand field multiplet calculations and density functional theory show that, due to the symmetry of the ligand field, the electronic ground state of the Ho atoms is a superposition of angular momentum states that is immune to quantum tunnelling and first order spin reversal processes. Furthermore, MgO is a stiff insulating material that provides insulation from both electrons and thermal vibrations, which are responsible for inducing spin-flips and destroying magnetic remanence in small structures. The combination of these features enables the realisation of long-lived magnetic states in atomic scale structures.

This work is the culmination of a long-standing project that begun 15 years ago at the ESRF, where the upgrade of beamline ID12 to ID08 and then to ID32 has led to the first experiments able to probe the magnetic ground state of monodispersed single atom arrays on surfaces **[1-3]**. Identifying the conditions that allow

the stabilisation of the magnetic moment of an atom coupled to a solid state environment permits the manipulation of atomic spins using microwave fields and even dc electric currents, which is paramount for the development of model classical and quantum memory devices.

PRINCIPAL PUBLICATION AND AUTHORS

Magnetic remanence in single atoms, F. Donati (a), S. Rusponi (a), S. Stepanow (b), C. Wäckerlin (a), A. Singha (a), L. Persichetti (b), R. Baltic (a), K. Diller (a), F. Patthey (a), E. Fernandes (a), J. Dreiser (a,c), Ž. Šljivančanin (d,e), K. Kummer (f), C. Nistor (a), P. Gambardella (a) and H. Brune (a),

Science **352**, 318 (2016);
doi: 10.1126/science.aad9898.

(a) Institute of Physics, Ecole Polytechnique Fédérale de Lausanne (EPFL) (Switzerland)
(b) Department of Materials, ETH Zürich (Switzerland)
(c) Swiss Light Source, Paul Scherrer Institute, Villigen (Switzerland)
(d) Vinča Institute of Nuclear Sciences, Belgrade (Serbia)
(e) Texas A&M University at Qatar, Doha (Qatar)
(f) ESRF

REFERENCES

[1] P. Gambardella *et al.*, *Phys. Rev. Lett.* **88**, 047202 (2002).
[2] P. Gambardella *et al.*, *Science* **300**, 1130 (2003).
[3] P. Gambardella *et al.*, *Nature Mater.* **8**, 189 (2009).

UNDERSTANDING MAGNETIC COUPLING IN LANTHANIDE-BASED MOLECULES BY XMCD AND *ab initio* MODELLING

A comprehension of the mechanisms linking a molecular spin centre with its environment is crucial for the development of spintronics functionalities at the molecular scale. Here we combine X-ray magnetic circular dichroism (XMCD) with *ab initio* calculations to investigate the microscopic spin path in bis(phthalocyaninato)-lanthanide(III) single molecule magnets coupled to a Ni substrate.

Magnetic molecules of the family of bis(phthalocyaninato)-lanthanide(III) ($LnPc_2$, so called "double decker") are made by a single lanthanide ion as the magnetic centre, sandwiched between two phthalocyanines (**Figure 9**, inset). This specific structure, where the localised lanthanide f-orbitals are coupled with the delocalised π-type electrons of the organic ligands, allows the existence of a sizeable magnetic interaction with the environment, while at the same time the magnetic core is efficiently protected. The intramolecular spin communication channels are highlighted here by studying how the coupling between the molecules and a Ni substrate is varied upon the substitution of the central Ln-ion.

Our experiments were carried out at beamline **ID08** (now **ID32**). The molecular units were sublimated *in situ* on a freshly prepared Ni(111) surface with sub-monolayer coverage. Our results show that they are isolated and lying flat, with the Pc plane parallel to the surface. The low-temperature (T = 8 K) XMCD-derived magnetisation curves of the three compounds ($LnPc_2$, where Ln = Tb, Dy and Er) and of the Ni substrate are shown in **Figure 9**. The Ln-curves display a characteristic "N-shape" behaviour, in particular for small magnetic fields where the magnetisation is generally opposed to the field. These features reveal an antiferromagnetic coupling of the Ln-magnetic moment with the Ni substrate. The quantitative estimation of the coupling strength can be obtained by fitting the experimental data with a model spin-Hamiltonian, where the only fitting parameter is the Ln-Ni coupling and all the microscopic molecular details are estimated by *ab initio* methods. The results are the continuous lines

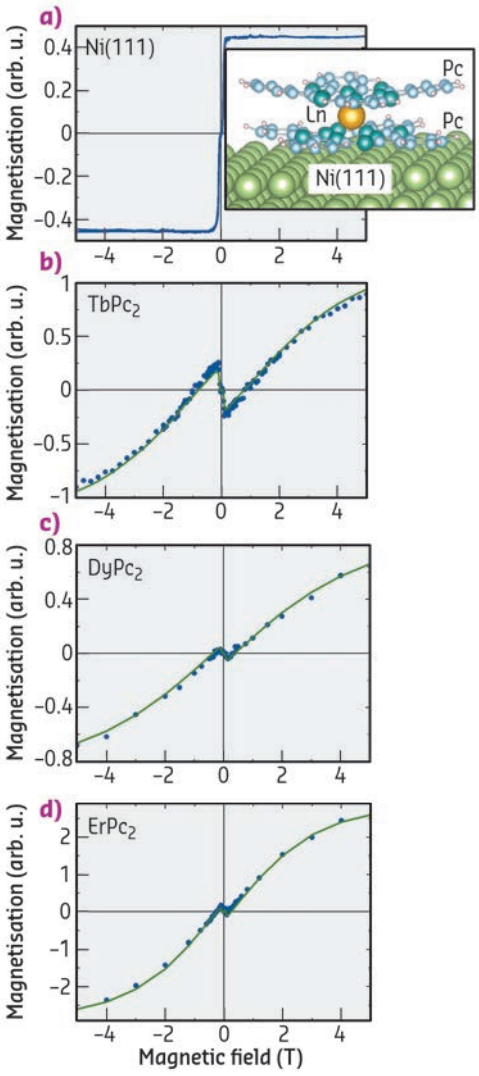

Fig. 9: Element resolved XMCD magnetisation measurements of Ni (a), Tb (b), Dy (c), Er (d) for the $LnPc_2$/Ni(111) systems, taken at the incidence angle Θ = 70° between the X-ray beam and the surface. Experimental data are shown as dots, while the theoretical fit are the continuous lines.

in **Figure 9**, while the values for the coupling strength are plotted in **Figure 10b**, showing a clear dependence of the interaction with the Ln ion, and indicating the key role of the Ln orbital wave function in determining the magnetic couplings.

Deeper insights into the intramolecular interaction are obtained by the DFT calculations of the molecular compounds. Our analysis reveals a partial occupation, together with a finite spin polarisation, of the lanthanide 5d orbitals induced by the localised 4f electrons that carry the magnetic character of the Ln ion. The values of the induced spin polarisation depend on the specific Ln atom and are shown in **Figure 10b**, displaying the same trend in going from Tb to Er as observed experimentally for the magnetic coupling strengths. The Ln 5d electrons, in turn, overlap and hybridise with the p-states of the C and N atoms in the phthalocyanines (**Figure 10a**). We can therefore conclude that such d-mediated interaction is the mechanism through which the spin information in the f-orbitals propagates to the delocalised states of the two phthalocyanines that finally communicate with the external world by direct contact (with the Ni magnetic surface in this case).

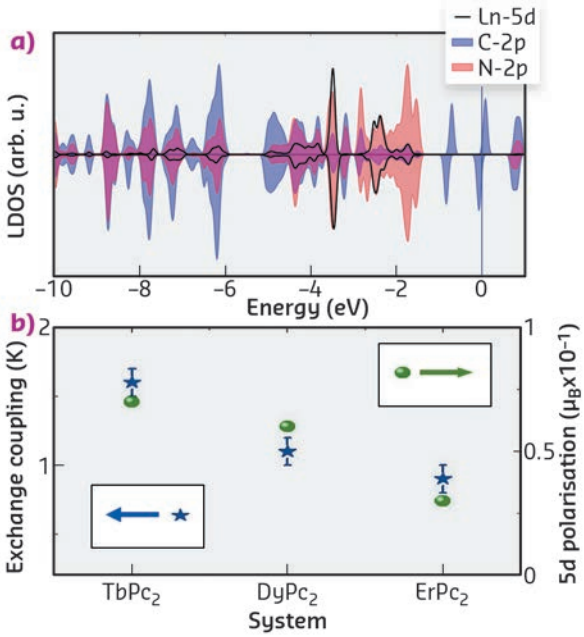

Fig. 10: a) Spin-resolved LDOS projected on the 5d orbital of Ln (very similar in all three cases) and on the 2p orbitals of the nearest-neighbours (to the Ln ions) N and C atoms in the phthalocyanines. b) Magnetic coupling strength, as determined from the fit (left axis), and magnitude of the magnetic polarisation (right axis) induced on the 5d orbitals for each Ln compound calculated from DFT.

By a combined experimental and theoretical approach, the microscopic spin communication channels are identified in the prototypical case of $LnPc_2$ magnetic molecules coupled to magnetic substrates. The most important feature is that there is not a direct overlap between the magnetic, localised 4f states and the Pc unit, but rather the interaction occurs through the auxiliary 5d orbitals of the Ln ion. This three-step spin communication channel [(4f) Ln ↔ (5d) Ln ↔ (Pc) ↔ surface] is responsible for the experimentally observed coupling between the Ln ions and their environment, yet preserving unaffected the pristine magnetic properties of the molecules.

PRINCIPAL PUBLICATION AND AUTHORS

Spin-communication channels between Ln(III) bis-phthalocyanines molecular nanomagnets and a magnetic substrate, A. Candini (a), D. Klar (b), S. Marocchi (a), V. Corradini (a), R. Biagi (a,c), V. De Renzi (a,c), U. del Pennino (a,c), F. Troiani (a), V. Bellini (a), S. Klyatskaya (d), M. Ruben (d,e), K. Kummer (f), N.B. Brookes (f), H. Huang (g), A. Soncini (g), H. Wende (b) and M. Affronte (a,c), *Scientific Reports* **6,** 21740 (2016); doi: 10.1038/srep21740.
(a) Centro S3, Istituto Nanoscienze - CNR, Modena (Italy).
(b) Faculty of Physics and Center for Nanointegration Duisburg-Essen (CENIDE), University of Duisburg-Essen, Duisburg (Germany)
(c) Dipartimento di Scienze Fisiche, Informatiche e Matematiche, Università di Modena e Reggio Emilia, Modena (Italy)
(d) Institute of Nanotechnology, Karlsruhe Institute of Technology (KIT), Eggenstein-Leopoldshafen (Germany)
(e) Institut de Physique et Chimie des Matériaux de Strasbourg (France)
(f) ESRF
(g) School of Chemistry, The University of Melbourne (Australia)

WHEN MAGNETISM MEETS TOPOLOGY

$Sm_2Ir_2O_7$ is a prototypical pyrochlore iridate with a finite temperature metal-insulator transition. The nature of its magnetic ground state and low-energy effective Hamiltonian has been revealed using resonant magnetic X-ray scattering. Also, through a combination of elastic and inelastic measurements, the magnetic ground state was established as an all-in all-out (AIAO) antiferromagnet, as required for the realisation of a correlated Weyl semimetal in this class of material.

The search for exotic particles is one of the most fascinating pursuits of modern physics. While this area of research is traditionally associated with elementary particles created in high-energy physics, simple 'quasi-particles', with sometimes highly unconventional properties, can also emerge in the complex, many-body world of materials. One such particle is the Weyl fermion. First postulated by Hermann Weyl in 1929 **[1]**, the Weyl fermion is a solution to the Dirac equation of fermion fields that describes a massless fermion with definite handedness. However, no elementary particles that behave as Weyl fermions have yet been observed.

Inside materials, the occurrence of Weyl fermions as quasi-particles hinges on stringent symmetry constraints. Mathematically, the Weyl fermion is described by a two-component spinor, compared to the four-component spinor of Dirac fermions (describing *e.g.* conventional electrons). Due to the two-component spinor, only two states must meet at the Fermi level of the material. This requires that either time-reversal or inversion symmetry must be broken, to ensure that the touching conduction and valence bands are non-degenerate. Materials hosting Weyl fermions are known as Weyl semimetals. The non-trivial topology of the Weyl points manifests in striking properties, such as Fermi arc surface states, which provide a 'smoking gun' experimental signature. In a series of breakthrough experiments in 2015 **[2]**, Weyl semimetals were discovered in a class of materials with broken inversion symmetry.

So far, all Weyl fermions have been found in 'uncorrelated' materials, where the electrons only interact weakly with each other. In general, electronic interactions can enrich topological phases. For Weyl semimetals, electronic correlations can stabilise magnetic order, which offers the possibility of a time-reversal symmetry-breaking Weyl semimetal. This correlated Weyl semimetal state is predicted to exhibited yet undiscovered exotic properties, such as the anomalous Hall effect. The most promising candidate materials for this state are iridium-based pyrochlore oxides, known as pyrochlore iridates. While the frustrated pyrochlore lattice hosts many intriguing magnetic states, such as the spin liquids, spin glasses and spin ices, the presence of iridium atoms with strong spin-orbit coupling can induce non-trivial band topology. In pyrochlore iridates, to stabilise a correlated Weyl semimetal state, the microscopic magnetic order has to preserve inversion symmetry. Theoretical studies have identified that the 'all-in all-out' magnetic order would fulfil the required symmetries. In this all-in all-out magnetic structure, all the magnetic moments point either towards or away from the centre of the tetrahedra formed by the iridium ions.

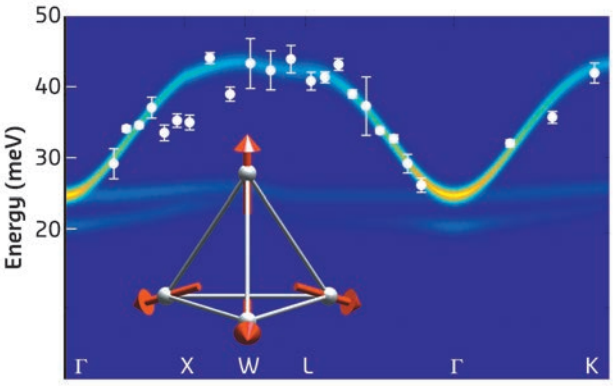

Fig. 11: Fitted energy dispersion RIXS scan as a function of momentum transfer and a potential magnetic structure proposed by theoretical calculations. Energy dispersion of magnetic excitations of the all-in all-out magnetic structure (shown in the inset) of $Sm_2Ir_2O_7$ as a function of momentum transfer, measured by resonant X-ray scattering.

We have now discovered that the magnetic moments in pyrochlore iridates do indeed order in the all-in all-out structure. This confirms theoretical predictions and allows the elusive correlated Weyl semimetal state to be realised in these materials. Using resonant X-ray scattering techniques, both the magnetic order and excitations were characterised comprehensively in the prototypical pyrochlore iridate $Sm_2Ir_2O_7$. By analysing the excitation spectrum, it was possible to deduce the effective Hamiltonian describing this class of material for the first time (**Figure 11**).

The experiments were performed at ESRF beamline **ID20** (Grenoble, France) and PETRA III (Hamburg, Germany) where the use of state-of-the-art instrumentation was critical; enabling magnetic excitations with a dispersion bandwidth of only 15 meV to be discerned. This presents a remarkable achievement for resonant X-ray scattering.

While our discovery confirms that pyrochlore iridates adopt the required type of magnetic order to host Weyl fermions, the magnetic excitations point towards strong electronic correlations, which may preclude a Weyl semimetal state. In order to achieve a correlated Weyl semimetal state in pyrochlore iridates, the application of internal or external perturbations may therefore be necessary.

PRINCIPAL PUBLICATION AND AUTHORS

All-in–all-out magnetic order and propagating spin waves in $Sm_2Ir_2O_7$, C. Donnerer (a), M.C. Rahn (b), M. Moretti Sala (c), J.G. Vale (a,d), D. Pincini (a,e), J. Strempfer (f), M. Krisch (c), D. Prabhakaran (b), A.T. Boothroyd (b) and D.F. McMorrow (a), *Phys. Rev. Lett.* **117**, 037201 (2016); doi: 10.1103/PhysRevLett.117.037201.

(a) London Centre for Nanotechnology and Department of Physics and Astronomy, University College London (UK)
(b) Department of Physics, University of Oxford (UK)
(c) ESRF
(d) Laboratory for Quantum Magnetism, Ecole Polytechnique Federale de Lausanne (EPFL) (Switzerland)
(e) Diamond Light Source Ltd, Didcot (UK)
(f) DESY, Hamburg (Germany)

REFERENCES

[1] H. Weyl, *Elektron und gravitation*, *I. Z. Phys.* **56**, 330–352 (1929).
[2] Su-Yang Xu *et al.*, *Science* **349**, 613 (2015).

DECOMPOSITION OF THE HYDROGEN STORAGE MATERIAL $Mg(BH_4)_2$ FOLLOWED BY *in situ* X-RAY RAMAN SCATTERING SPECTROSCOPY

X-ray Raman scattering spectroscopy (XRS) combines the benefits of soft-X-ray spectroscopy and the properties of hard X-rays making it especially valuable for the *in situ* study of (amorphous) lightweight/low-Z materials. This technique was used to unveil the hydrogen release reactions of the hydrogen storage material $Mg(BH_4)_2$ for temperatures up to 500°C and pressures up to 4 bar.

$Mg(BH_4)_2$ is one of the most promising candidates for next generation hydrogen storage materials based on metal borohydrides owing to its large hydrogen content and moderate hydrogen release conditions. However, the decomposition of $Mg(BH_4)_2$ is not yet fully understood and various hydrogen release pathways have been suggested. Reversibility of the hydrogen release process is a prerequisite for application as energy storage materials. The occurrence of highly stable decomposition products such as amorphous boron or $MgB_{12}H_{12}$ hinder this reversibility and their identification is difficult.

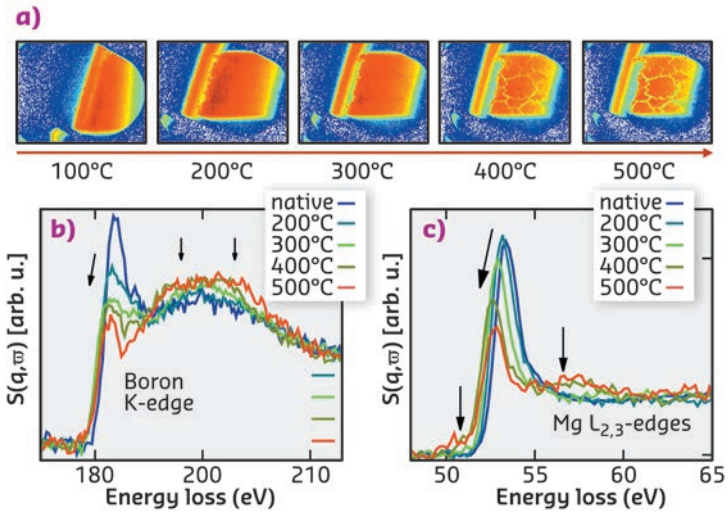

Fig. 12: a) Tomographic images of the $Mg(BH_4)_2$ sample enclosed in the reaction chamber for different annealing stages. b) XRS spectra of the boron K-edge and c) the magnesium $L_{2,3}$-edge of $Mg(BH_4)_2$ measured during the thermally induced decomposition reaction.

To clarify the possible pathways and decomposition reactions, we used XRS spectroscopy, at beamline **ID20**, at the boron K-edge and the magnesium $L_{2,3}$-edges. In comparison with spectra of reference samples such as $MgB_{12}H_{12}$, MgB_2, MgH_2, MgO, Mg, H_3BO_3, and boron, a fingerprint analysis of both edges yields detailed quantitative information about the reaction products during decomposition. Moreover, tomographic images of the samples enclosed in the reaction chamber were recorded to probe the structural changes of the sample on the macroscopic scale.

The structural integrity of the sample changed for temperatures just above 400°C as can be seen from macroscopic cracks which are due to significant volume changes during the formation of MgH, Mg, and MgO (see tomographic images in **Figure 12a**). The corresponding XRS spectra for temperatures as indicated are presented in **Figure 12b** and **c** for the boron K and the magnesium $L_{2,3}$-edges, respectively. We observe clear spectral changes with increasing temperature accompanied by hydrogen release. Employing the fingerprint analysis utilising the reference spectra, we reveal the formation of decomposition intermediate(s) at 300°C. The results of this analysis are summarised in **Figure 13**. The intermediate(s) form with significant hydrogen release (grey shaded area in **Figure 13**). The unwanted phases $MgB_{12}H_{12}$ and (amorphous) boron are not observed in this reaction step. After annealing at 400°C, crystalline MgH_2 and higher boranes (*e.g.* $MgB_{12}H_{12}$-like phases) are formed. These boranes decompose into the constituting elements magnesium and boron at higher temperatures up to 500°C. In a next step, detailed characterisation of the reaction intermediate(s) is foreseen via synthesis of possible intermediates to measure references and/or modelling of the intermediate's XRS spectra.

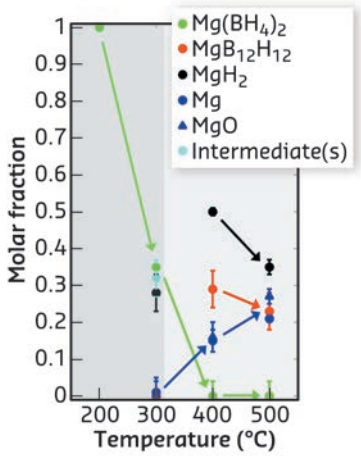

Fig. 13: Quantitative analysis of the observed phases during the decomposition reaction of $Mg(BH_4)_2$.

In this study, we were able to determine the major reaction products in the temperature

driven decomposition of $Mg(BH_4)_2$. At 300°C a significant hydrogen release without formation of stable boron phases was observed which confirms the role of $Mg(BH_4)_2$ as a promising material for reversible energy storage, *e.g.* for mobile applications. XRS has proven to be a valuable tool to obtain quantitative information even on amorphous products during the hydrogen decomposition reaction and opens new perspectives for investigations, *e.g.* of nanoconfined samples, eutectic mixtures, and layer-protected hydrides.

PRINCIPAL PUBLICATION AND AUTHORS

In situ characterization of the decomposition behavior of $Mg(BH_4)_2$ by X-ray Raman scattering spectroscopy, C.J. Sahle (a), S. Kujawski (b), A. Remhof (c), Y. Yan (d), N.P. Stadie (c), A. Al-Zein (a), M. Tolan (b), S. Huotari (d), M. Krisch (a) and C. Sternemann (b), *Physical Chemistry Chemical Physics* **18**, 5397-5403 (2016); doi: 10.1039/C5CP06571B.

(a) ESRF
(b) Fakultät Physik / DELTA, Technische Universität Dortmund (Germany)
(c) Materials for Energy Conversion, Empa, Dübendorf (Switzerland)
(d) Department of Physics, University of Helsinki (Finland)

IRIDIUM FLUORIDE COMPLEXES AS A PROXY FOR IRIDATES

Molecular fluoride complexes based on iridium ions are isolated single-metal entities that imitate the iridium sites found in inorganic iridium oxides. XMCD experiments provide evidence of the virtually identical electronic structure of these two iridium systems. These results open a novel bottom-up synthetic approach towards new materials based on heavier transition elements with exotic physical properties.

The chemistry and physics of the heavier transition element compounds have been largely overlooked when compared to the lighter first-row transition metals. Several recent key discoveries in the physics of metal oxides based on fourth (4d) and fifth (5d) row transition metals have sparked interest and opened new perspectives for the chemistry and physics of these often overlooked elements **[1,2,3]**. From recent reports, iridium in particular stands out from the rest. Oxide materials based on Ir^{4+} ions, commonly referred to as 'iridates', have shown great promise for diverse materials such as high-temperature superconductors, topological insulators and quantum spin-liquids. Their outstanding properties originate from the combined effects of the crystal field, magnetic interactions and strong spin-orbit coupling, characteristic of 5d metal ions. From a fundamental point of view and to understand in detail the origin of these unique properties, the elucidation of the intrinsic electronic structure of the constituent Ir^{4+} centres is essential. However, this task is far from trivial as the strong magnetic interactions between the iridium ions in iridates eclipse the information of the local electronic structure. To overcome this limitation, the iridate structures (**Figure 14a**) should be fragmented into its most basic structural unit. Discouragingly, the fundamental structural unit of all iridates, $\{IrO_6\}^{8-}$ (**Figure 14b**), carries a substantial charge that prevents its spatial isolation in a material with only remotely placed charge-compensating ions. Instead, our attention was recently turned towards a related molecular species, the $[IrF_6]^{2-}$ complex (**Figure 14c**). From a chemical point of view, fluoride and oxide share many characteristics, and, importantly, the reduced charge of the fluoride ion (F^-) over oxide (O^{2-}) renders the isolation of a single 'iridate centre' chemically possible. The structure of the $[IrF_6]^{2-}$ complex is virtually identical to that of the $\{IrO_6\}^{8-}$ moiety in iridates and there are no indications of disturbing magnetic interactions between adjacent $[IrF_6]^{2-}$ complexes, when isolated in the solid state with organic counter-ions. These $[IrF_6]^{2-}$-based materials therefore constitute the most realistic molecular model systems for oxide-based iridates.

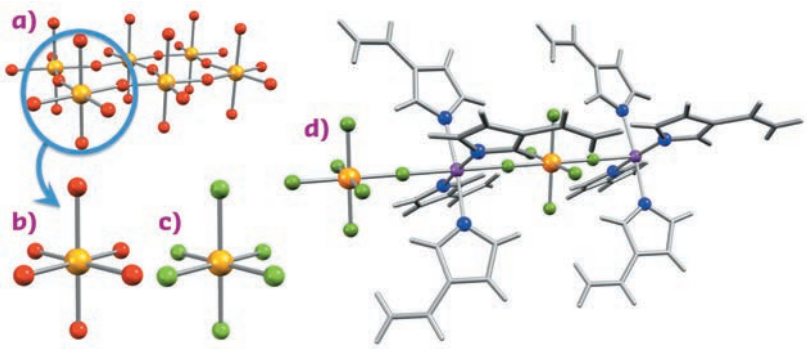

Fig. 14: a) The IrO_4-layer in the well-known Sr_2IrO_4 structure together with b) the basic structural motif $\{IrO_6\}^{8-}$ and c) its molecular fluoride-based analogue $[IrF_6]^{2-}$. d) View of the linear chain structure of $Zn(viz)_4[IrF_6]$ (viz = 1-vinylimidazole) incorporating $[IrF_6]^{2-}$ as a building block. Colour code: Ir, orange; F, pale green; O, red; N, blue; Zn, purple; C and H, grey sticks.

The evidence that the $[IrF_6]^{2-}$ complex possesses an electronic structure virtually identical to the $\{IrO_6\}^{8-}$ moiety, came from X-ray magnetic circular dichroism (XMCD) experiments conducted at beamline **ID12**. Representative spectra collected for different molecular iridate-analogues are shown in **Figure 15**. Although XMCD experiments are becoming increasingly popular amongst chemists, this technique has not, previously, been applied to molecular 5d metal ion complexes. Remarkably, the modelling of the XMCD data illuminated a large orbital magnetic moment that exceeds the magnetic moment of the electronic spin. The comparison of these results with previous experimental and theoretical studies on iridates demonstrates an almost identical electronic structure of the metal centres in these different types of materials. The $[IrF_6]^{2-}$ complex is thus an ideal model system to test hypotheses developed on the single-ion properties of the $\{IrO_6\}^{8-}$ unit in iridates. Moreover, the incorporation of this new $[IrF_6]^{2-}$ complex into various chemical environments using the tools of coordination chemistry would allow the influence of different structural modifications on its electronic structure to be probed. In this context, the robust nature of the $[IrF_6]^{2-}$ complex is an asset as it facilitates the bottom-up construction of molecule-based materials. This approach is well exemplified by the one-dimensional coordination polymer, $Zn(viz)_4[IrF_6]$ (**Figure 14d**), demonstrating the feasibility of designing materials using $[IrF_6]^{2-}$ as an 'iridate'-building block. These soft-chemistry methods contrast with the traditional inorganic solid-state chemistry used to synthesise iridates and could be used to obtain new materials with designed topologies and exotic physical properties constructed from $[IrF_6]^{2-}$ modules.

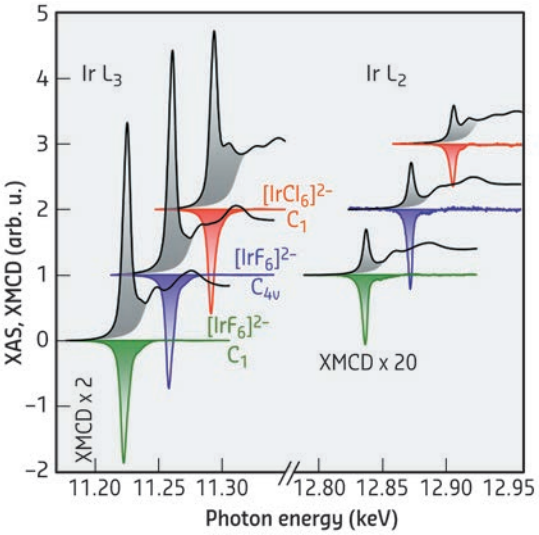

Fig. 15: Isotropic X-ray absorption (XAS) and XMCD spectra collected at 2 K for different molecular iridate analogues in a large magnetic field of 17 T.

PRINCIPAL PUBLICATION AND AUTHORS

Iridates from the molecular side, K.S. Pedersen (a,b,c,d), J. Bendix (e), A. Tressaud (c,d), E. Durand (c,d), H. Weihe (e), Z. Salman (f), T.J. Morsing (e), D.N. Woodruff (g), Y. Lan (h), W. Wernsdorfer (h), C. Mathonière (c,d), S. Piligkos (e), S.I. Klokishner (i), S. Ostrovsky (i), K. Ollefs (j), F. Wilhelm (j), A. Rogalev (j) and R. Clérac (a,d), *Nat. Commun.* **7**, 12195 (2016); doi: 10.1038/ncomms12195.

(a) CNRS, CRPP, UPR 8641, Pessac (France)
(b) Univ. Bordeaux, CRPP, UPR 8641, Pessac (France)
(c) CNRS, ICMCB, UPR 9048, Pessac (France)
(d) Univ. Bordeaux, ICMCB, UPR 9048, Pessac (France)
(e) Department of Chemistry, University of Copenhagen (Denmark)
(f) Laboratory for Muon Spin Spectroscopy, Paul Scherrer Institut, Villigen PSI (Switzerland)
(g) Department of Chemistry, University of Oxford (UK)
(h) CNRS, Inst NEEL, Grenoble (France)
(i) Institute of Applied Physics, Academy of Sciences of Moldova, Kishinev (Moldova)
(j) ESRF

REFERENCES

[1] B.J. Kim *et al.*, *Science* **323**, 1329–1332 (2009).
[2] Y.K. Kim *et al.*, *Science* **345**, 187–190 (2014).
[3] S. Nishimoto *et al.*, *Nat. Commun.* **7**, 10273 (2016).

ELEMENT-SELECTIVE MEASURE OF ATOMIC POLARISATION BY XANES IN EXTERNAL ELECTRIC FIELDS

The electrical properties of functional electric materials can be studied using a new technique involving X-ray absorption spectroscopy. External electric fields were found to produce shifts of XANES spectra providing an element-selective measure of atomic polarisation originating from the permanent electric dipoles present in polar samples.

Electrical functionality of matter plays an important role in today's technology. Functional electric materials have a variety of applications such as piezoelectric actuators used as injectors in car engines and ferroelectric materials within FRAM computer memory. Most functional electric materials exhibit permanent electric polarisation which can be manipulated by electric fields. To improve these materials, electric polarisation needs to be tailored at the atomic scale, and a measurement technique is essential to gauge results.

Absorption spectroscopy in electric fields has a longstanding history. Classical examples are the Stark-effect [1], where atomic energy levels in (non-)polarised materials shift linearly (quadratic) with the applied electric field. These classical optical experiments have now been brought to the synchrotron and the first X-ray absorption spectroscopy measurements in an electric field have been performed at beamline **ID12**. These experiments have revealed the potential of the technique to become a versatile approach to study atomic electrical properties with element selectivity.

A range of prototypical samples was selected for this study, including the functional oxides cobalt-doped zincoxide (Co:ZnO) and gadolinium gallium garnet ($Gd_3Ga_5O_{12}$; GGG) which are polar multi-constituent materials, *i.e.* the atoms in these oxides possess a permanent electric polarisation due to the low crystalline symmetry of the material. X-ray absorption near edge spectra (XANES) were recorded while applying an external voltage of up to 600 V along the polar direction of the material in a plate capacitor geometry that generates a strong electric field across the material (see **Figure 16c** for the setup). The experiment shown in **Figure 16a** reveals that there is a small difference of less than 0.1% between the XANES recorded at +600 V and –600 V at the Co K-edge of a 20% Co:ZnO sample as well as the control experiment at 0 V. The difference signal was compared with the numerical derivative of the XANES and found to be a perfect match (**Figure 16b**). It can be concluded, therefore, that the effect of the applied voltage is a shift in energy of the (unoccupied) electronic states that are probed in the XANES experiment. For a quantitative analysis, the difference signal can be made to disappear by artificially shifting the XANES (-600 V) in photon energy with respect to the XANES (+600 V). This analysis yields a shift of 2.8 meV (not shown). To demonstrate the element selectivity, the same experiment was repeated at the Zn K-edge of the same Co:ZnO sample. For these samples, it is known that Co substitutes for Zn without changing the crystalline structure of the ZnO host [2]. **Figure 17a** shows that the resulting difference signal decreases with decreasing applied voltage. **Figure 17b** demonstrates that, at a fixed photon energy, the resulting difference in X-ray absorption depends linearly on the applied voltage; a first indication that the observed effect is the X-ray variant of the linear Stark effect. **Figure 17c** is a compilation of the findings for all studied samples which reveal that the energy shift does not depend on the relative orientation of the synchrotron light and the applied voltage. Furthermore, the energy shift is the same at the Zn K-edge, no matter whether a Co:ZnO thin film or a zincselenide (ZnSe) single crystal is studied. In contrast, the shift is different for Co and Zn although both are contained in the identical Co:ZnO sample, which highlights the element specificity of the effect. Finally, it appears that the energetic shift depends linearly on the binding energy if all results for Co:ZnO, GGG(111) and ZnSe(111) are collected including the Gd L_3-edge which, however, probes electronic states of a different symmetry.

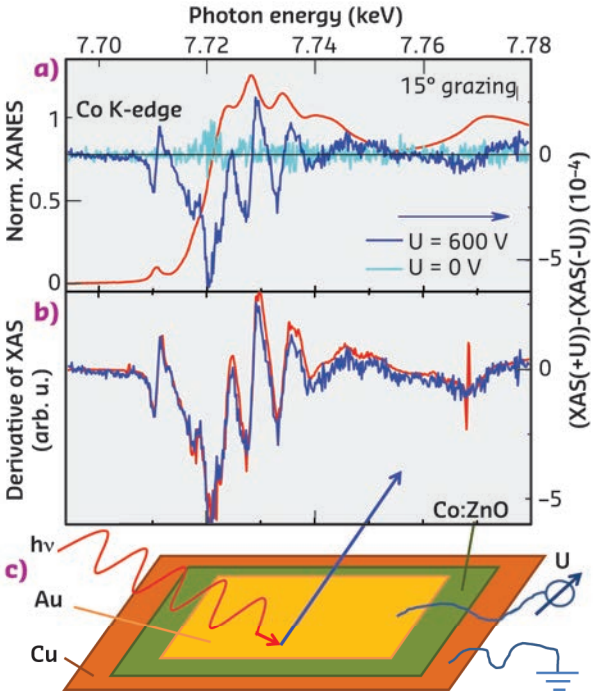

Fig. 16: a) Co K-edge XANES of 20% Co:ZnO recorded with and without electrical field and the respective difference signal. b) Difference signal in comparison with the derivative of the XANES. c) Schematic setup of the plate capacitor geometry.

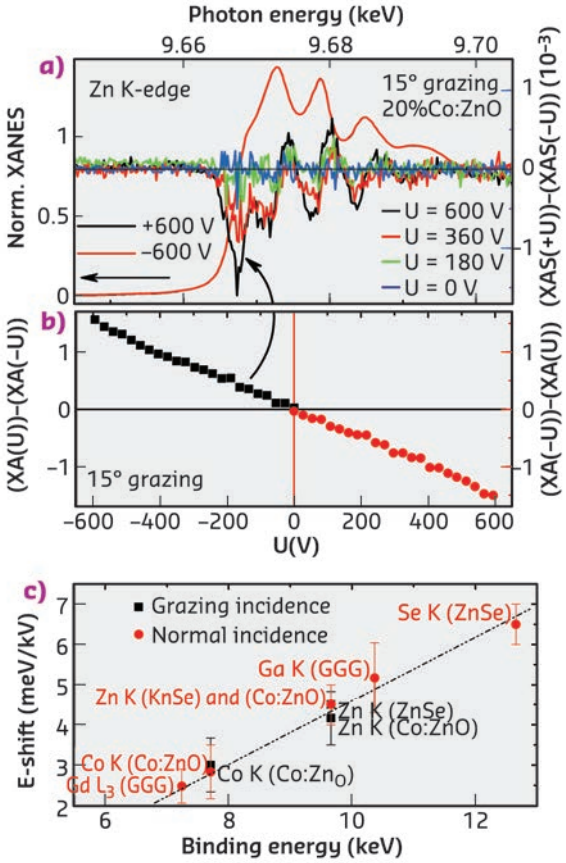

Fig. 17: a) Zn K-edge XANES of 20% Co:ZnO recorded with and without electrical field and the respective difference signal for different voltages. b) Dependence of the difference in X-ray absorption on the applied voltage at fixed photon energy. c) Dependence of the resulting voltage-induced energy shift on the binding energy of the absorption edge.

These experiments involved samples where the voltage generated an electric field parallel to the polar direction of the specimen. Further control experiments on non-polar strontium titanate ($SrTiO_3$) and on highly conducting aluminium-doped ZnO (a known transparent conducting oxide) confirm that no difference signal can be recorded in cases where the material is non-polar or when mobile carriers screen the electric field. This finally confirms that the X-ray variant of the linear Stark effect has indeed been observed, permitting electrical polarisation to be studied with element selectivity.

PRINCIPAL PUBLICATION AND AUTHORS

X-ray absorption spectroscopy in electrical fields: an element-selective probe of atomic polarization, V. Ney (a), F. Wilhelm (b), K. Ollefs (b), A. Rogalev (b) and A. Ney (a) *Phys. Rev. B* **93**, 035136 (2016);
doi: 10.1103/PhysRevB.93.035136.
(a) Institut für Halbleiter- und Festkörperphysik, Johannes Kepler Universität, Linz (Austria)
(b) ESRF

REFERENCES

[1] J. Stark, *Annalen der Physik*, **43**, 965 (1914).
[2] A. Ney *et al.*, *J. Appl. Phys.* **115**, 172603 (2014).

PHONON-MEDIATED PASSIVE TRANSPORT OF SOLUTES IN LIPID MEMBRANES

This study of the passive molecular transport through a lipid membrane has revealed evidence for the formation of transient voids through lipid density fluctuations from analysis of the phonon branches of a DPPC membrane. The finding supports the notion that passive transport is mediated by entropic expulsion of solutes from higher to lower lipid density regions within the membrane.

A biological membrane serves as a selective barrier between the internal compartment of the cell and the cell's surroundings. Most biological molecules are unable to diffuse across the lipid bilayer. However, due to thermally induced vibrations in the membrane, a cell can passively transport molecules using these natural thermal motions. It has been shown experimentally that many factors define the permeation process including solute nature, molecule type and membrane thickness. Different theories were proposed to account for other parameters such as solute hydrophobicity, molecular size and shape, membrane fluidity and packing density. However, despite these efforts, inconsistencies still persist and the exact mechanism of passive transport still remains unknown.

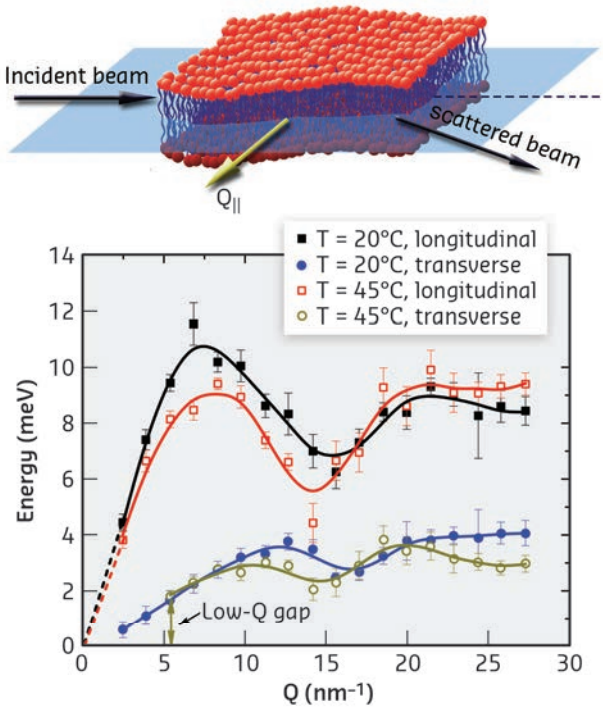

Fig. 18: (top) Geometry of the IXS experiment at beamline ID28: the incident and scattered beams (thus, the momentum transfer vector Q|| lie within the membrane plane to ensure that only the in-plane dynamics is probed. (bottom) Longitudinal and transverse phonon dispersion curves. Transverse phononic gap at high temperature is indicated by the arrow at Q ≈ 5 nm^{-1}. The solid lines are to guide eyes only and the dashed lines extrapolate the longitudinal phonon dispersions to Q = 0.

We have used a new approach to study lipid dynamics, which pinpoints the importance of collective molecular excitations in passive transport across the lipid bilayer. Using the high resolution inelastic X-ray scattering (IXS) technique combined with a newly developed phonon theory of liquids **[1]**, two important discoveries were made. First, the IXS experiment identified propagating in-plane transverse phonon modes in a DPPC (1,2-dipalmitoyl-*sn*-glycero-3-phosphocholine) lipid membrane that have not been experimentally observed before. Second, the measurements revealed the opening of a phononic gap in the transverse excitations with increasing temperature across the main (gel to liquid) phase transition.

The measurements were performed at beamline **ID28**, below (20°C) and above (45°C) of the main

transition temperature (T_m = 41°C). **Figure 18** illustrates the scattering geometry of the IXS experiment and the experimentally obtained longitudinal and transverse phonon dispersion curves.

The observation of the phononic gap is highly significant as it reveals a possible mechanism of the transmembrane passive transport. Specifically, the results confirmed the theoretical prediction **[2]** that phononic interaction induces transverse phononic gaps in disordered materials. Such gaps are related to the diffusion and relaxation processes occurring in the lipid membrane and are a direct signature of short-lived (picosecond scale) local lipid clustering in the membrane over short-to-intermediate length scales (**Figure 19**). On long length scales, the opening of the phononic gap in the transverse phonon modes signifies the formation of short-lived voids stipulating that the transverse phonon propagation is no longer supported due to the increasing lipid chain disorder.

The results of the work support the notion that the local lipid chain disordering directly mediates solute diffusion across the membrane.

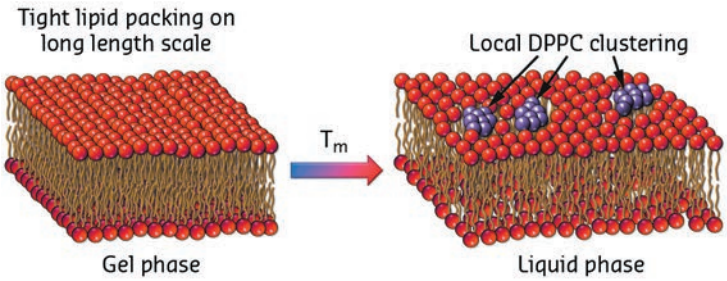

Fig. 19: The formation of the short-lived DPPC clusters upon the phase transition from the gel to the liquid phase. In the liquid phase, the lipids arrangement in the membrane is mostly disordered, however, due to the thermal fluctuations, nm-scale lipid clustering is triggered (shown by dark purple colour). Rarified regions beyond the dark purple clusters denote the formation of transient voids.

The entropic expulsion of the solute from the higher to lower lipid density regions is essentially thermally-triggered. The simultaneous lipid clustering and voids formation provide the mechanism for the solute to diffuse across the membrane via hopping between voids. Both local lipid density fluctuations on short-to-intermediate length scales and void formation on longer length scales is clear evidence for the universal phonon-triggered mechanism of passive membrane transport.

PRINCIPAL PUBLICATION AND AUTHORS

Revealing the mechanism of passive transport in lipid bilayers via phonon-mediated nanometre-scale density fluctuations, M. Zhernenkov (a), D. Bolmatov (a), D. Soloviov (b,c), K. Zhernenkov (d), B.P. Toperverg (e,f), A. Cunsolo (a), A. Bosak (g) and Y.Q. Cai (a), *Nat. Commun.* **7**, 11575 (2016); doi: 10.1038/ncomms11575.

(a) National Synchrotron Light Source II, Brookhaven National Laboratory, Upton, New York (USA)
(b) Frank Laboratory of Neutron Physics, Joint Institute for Nuclear Research, Dubna (Russia)
(c) Moscow Institute of Physics and Technology, Dolgoprudny (Russia)
(d) Institut Nanosciences et Cryogénie, Commissariat à l'Energie Atomique, Grenoble (France)
(e) Petersburg Nuclear Physics Institute, Gatchina (Russia)
(f) Institut Laue Langevin, Grenoble (France)
(g) ESRF

REFERENCES

[1] D. Bolmatov *et al.*, *Ann. Phys.* **363**, 221–242 (2015).
[2] D. Bolmatov *et al.*, *Sci. Rep.* **6**, 19469 (2016).

PROBING MAGNETOELASTIC WAVES IN QUANTUM MAGNETS

In general, lattice vibrations (phonons) in crystals interact weakly with the electronic degrees of freedom, such as charge and spin fluctuations. Here, an unexpectedly strong coupling between spin and lattice fluctuations has been discovered in a quantum magnet using inelastic X-ray scattering. In similar materials, non-resonant X-ray scattering can probe magnetism with high energy and momentum resolution.

Inelastic X-ray scattering (IXS) with meV energy resolution is an ideal tool to study lattice vibrations in crystals. IXS can also be sensitive to other degrees of freedom if strongly coupled to the phonons. One intriguing possibility is when polar phonons couple to spin waves in an ordered magnet. This creates electromagnons, quasiparticles that possess both magnetic and electric dipole moments **[1]**. Until the present discovery, direct observation of electromagnons was possible only via far-infrared light absorption. However, this technique is restricted to the measurement of spatially uniform changes (zero momentum) of the electric dipole moment due to the long wavelength of the resonant radiation. In this work, we show for the

first time that strong magnon-phonon coupling enables the study of electromagnon dynamics with arbitrary momentum using IXS and we were able to directly probe their dispersion in $LiCrO_2$.

$LiCrO_2$ is a triangular lattice antiferromagnet of spin-3/2 chromium ions. It develops a three sublattice magnetic order at low temperatures where the angle between neighbouring spins is 120° (**Figure 20a**). A previous inelastic neutron scattering study on similar systems reported an anomalous "roton-like" dip in the spin wave dispersion that linear spin wave theory failed to adequately describe **[2,3]**. Previously reported large magnetostriction on similar Cr-Cr bonds suggested a phononic origin of this anomaly **[4]**.

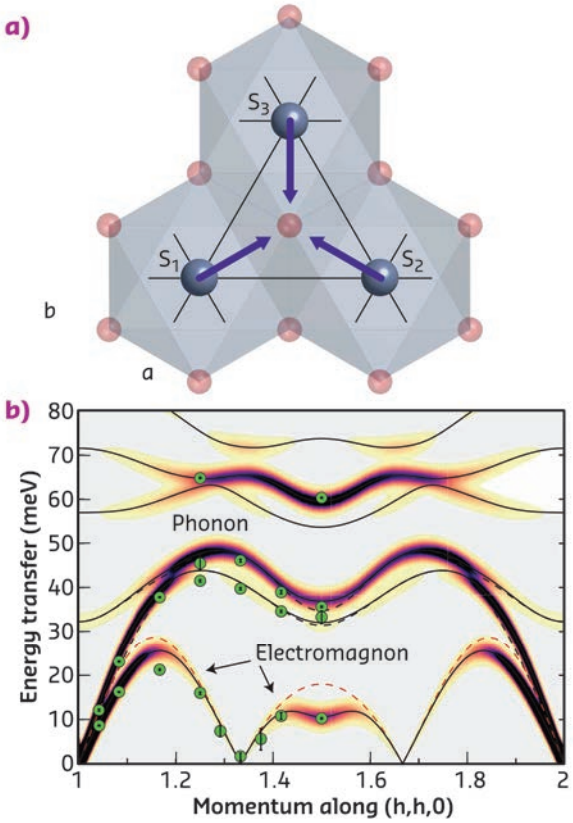

Fig. 20: a) Single triangular layer of Cr^{3+} ions (grey spheres) in $LiCrO_2$ with magnetic moments (purple arrows) showing the 120° order. b) Green circles denote the phonon and electromagnon dispersion measured by IXS. Black lines show the coupled spin lattice model and dashed lines the non-interacting model. The colour map illustrates the calculated IXS intensities.

Using the high-resolution spectrometer **ID28** designed for non-resonant inelastic X-ray scattering, we set out to look for anomalies in the phonon dispersion of $LiCrO_2$ as it is cooled below the magnetic ordering temperature. Surprisingly, we found not only a change in the phonon energies but a completely new phonon mode appearing in the magnetically ordered phase without an accompanying structural phase transition. We could successfully reproduce this excitation theoretically after including a coupling between the spins and the lattice in our *ab initio* phonon model. Our analysis showed that the new mode is a special type of a magnetoelastic wave, an electromagnon. Beside the large magnetostriction, the key ingredient of the strong magnon-phonon mixing is the non-collinear magnetic order. This enables a linear coupling between magnons and phonons that is forbidden for simple antiferromagnets with collinear magnetic order. The measured dispersion of the electromagnon is shown in **Figure 20b**, together with the prediction of the coupled model. Our model not only reproduces the dip in the spin wave dispersion at (1.5,1.5,0) but also the inelastic X-ray scattering cross section.

This experiment presents a novel opportunity to study magnetoelastic waves via IXS with meV energy resolution. These excitations carry not only phononic character but also the quantum properties of the underlying magnetism, such as finite lifetime and energy renormalisation due to many body effects **[5]**. This makes IXS an exciting alternative to inelastic neutron scattering to study selected quantum magnets with high energy and momentum resolution on µm-sized samples.

PRINCIPAL PUBLICATION AND AUTHORS

Electromagnon dispersion probed by inelastic X-ray scattering in $LiCrO_2$, S. Tóth (a,b), B. Wehinger (a,c), K. Rolfs (d), T. Birol (e,f), U. Stuhr (a), H. Takatsu (g,h), K. Kimura (i), T. Kimura (i), H.M. Rønnow (b) and Ch. Rüegg (a,c), *Nature Communications* **7**, 13547 (2016); doi: 10.1038/ncomms13547.
(a) Laboratory for Neutron Scattering and Imaging, Paul Scherrer Institute (Switzerland)
(b) Laboratory for Quantum Magnetism, EPFL (Switzerland)
(c) Department of Quantum Matter Physics, University of Geneva (Switzerland)
(d) Laboratory for Scientific Developments and Novel Materials, Paul Scherrer Institute (Switzerland)
(e) Department of Chemical Engineering and Materials Science, University of Minnesota (USA)
(f) Department of Physics and Astronomy, Rutgers University (USA)
(g) Department of Energy and Hydrocarbon Chemistry, Kyoto University (Japan)
(h) Department of Physics, Tokyo Metropolitan University (Japan)
(i) Division of Materials Physics, Osaka University (Japan)

REFERENCES

[1] A. Pimenov *et al.*, *Nat. Phys.* **2**, 97 (2006).
[2] S. Toth *et al.*, *Phys. Rev. Lett.* **109**, 127203 (2012).
[3] M. Frontzek *et al.*, *Phys. Rev. B* **84**, 94448 (2011).
[4] A.B. Sushkov *et al.*, *Phys. Rev. Lett.* **94**, 137202 (2005).
[5] M.E. Zhitomirsky and A. L. Chernyshev, *Rev. Mod. Phys.* **85**, 219 (2013).

OPERANDO X-RAY METHODS ILLUMINATE THE WAY TOWARDS CATALYST ACTIVE SITE DESIGN FOR METHANE CONVERSION

The upgrading of methane could prove a valuable alternative to oil as a source of platform chemicals. A combination of X-ray methods under real reaction conditions has provided detailed new insight into the evolution of Mo species during the catalytic conversion of methane and its influence on the reaction products.

With oil resources becoming progressively scarce, the chemical and petrochemical industry will undergo a major transformation in the coming decades. Alternative raw materials (*e.g.* coal, natural gas, biomass or CO_2) will be required, enforcing the development of step-change technologies for the large-scale production of platform chemicals. Within this context, the increasing availability of cheap natural gas has attracted growing interest towards direct routes for methane upgrading **[1]**. One of these routes, methane dehydroaromatisation (MDA), is particularly promising for the direct conversion of methane into aromatics and hydrogen using metal-exchanged zeolites such as Mo/H-ZSM-5, since it contains acid sites as well as Mo species possessing dehydrogenation and C-C coupling functionalities **[1-2]**. It is generally accepted that methane is activated on the exchanged Mo species, forming ethylene. Subsequently, ethylene reacts on the Brønsted acid sites and converts into aromatics, also leading to coke formation by consecutive reaction of aromatics with light olefins. While active species are proposed to originate from either $(MoO_2)^{2+}$ monomers or $(Mo_2O_5)^{2+}$ dimers, there is also a debate on whether the active sites are oxidic, carbidic (MoC_x) or oxycarbidic (MoC_xO_y) in nature. In addition, there is no clear understanding of the mode of catalyst deactivation, considered the main limitation for the commercialisation of the process **[1-2]**.

A rational design and tailoring of an improved catalyst can only be realised by understanding how it actually operates and deactivates under reaction conditions. Using a novel combination of techniques, coupling for the first time high energy resolution fluorescence detection X-ray absorption near-edge structure (HERFD-XANES) spectroscopy, X-ray difracction (XRD), and X-ray emission (XES) under real operando conditions at beamline **ID26** (see **Figure 21**), we have been able to correlate the evolution of the Mo species with the distinct reaction products formed during the methane dehydroaromatisation (MDA) reaction. Of particular importance has been the application of the scarcely-used X-ray emission spectroscopy (XES), which is able to distinguish

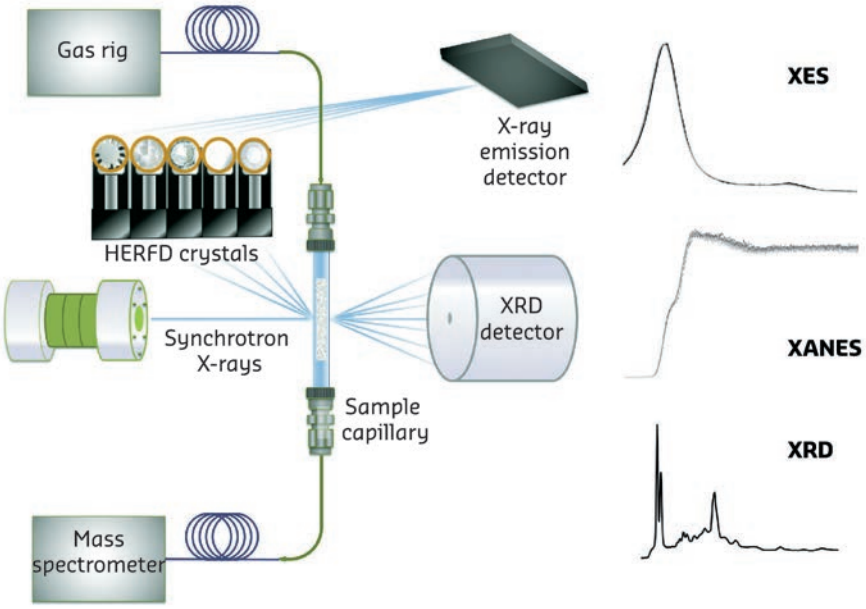

Fig. 21: Schematic representation of the setup used at ID26.

between ligands surrounding metal ions when they possess a similar Z number, *i.e.* C vs O. In this work, we used the Mo Kβ valence-to-core emission lines in conjunction with HERFD-XANES spectroscopy in order to be able to unambiguously determine the existence of both MoC_x and MoC_xO_y during the course of reaction.

Based on the operando HERFD-XANES/XES results (**Figure 22a-c**), a complete pathway for the evolution of Mo was obtained, and correlated with the distinct reaction products detected by online mass spectrometry. As illustrated in **Figure 22d**, isolated Mo-oxo centres present after calcination are seen to be converted by methane into metastable MoC_xO_y species, which are primarily responsible for the formation of light hydrocarbons. These are still attached to the zeolite framework and present varying stoichiometry depending on the extent of the carburisation. Longer reaction times eventually lead to the transition to a Mo carbide phase, involving the formation of MoC_3 sites not connected to the framework, whose

presence coincides with benzene formation. As such, these MoC_3 species are not stable and easily agglomerate. Ultimately, sintering of MoC_3 leads to the migration of the clusters to the outer zeolite surface and the formation of larger Mo_2C-like nanoparticles.

Further insight into the catalyst deactivation mode was obtained from the operando XRD data and complementary fluorescence lifetime microscopy measurements, which evidenced the formation of large hydrocarbons on the external zeolite surface, allowing us to conclude that both sintering of MoC_3 and the accumulation of carbon deposits on the outer shell of the zeolite crystals are primarily responsible for the decrease in catalytic performance.

Overall, these results demonstrate the importance of controlling, or else maintaining, Mo active species to achieve the desired product formation, which has important implications for realising the impact of methane as a source for platform chemicals. Although transient, the appeal of stabilising MoC_xO_y species is that they are highly selective to light hydrocarbons. Whilst there are issues with stabilising MoC_xO_y in the presence of the reaction mixture, this could be achieved in the presence of co-fed H_2O and/or O_2. MoC_3 species in turn are the species to target for aromatics but again either co-feeding of oxidants to mitigate carbon deposition or else enhancing the interaction with the zeolite is needed for improved stability.

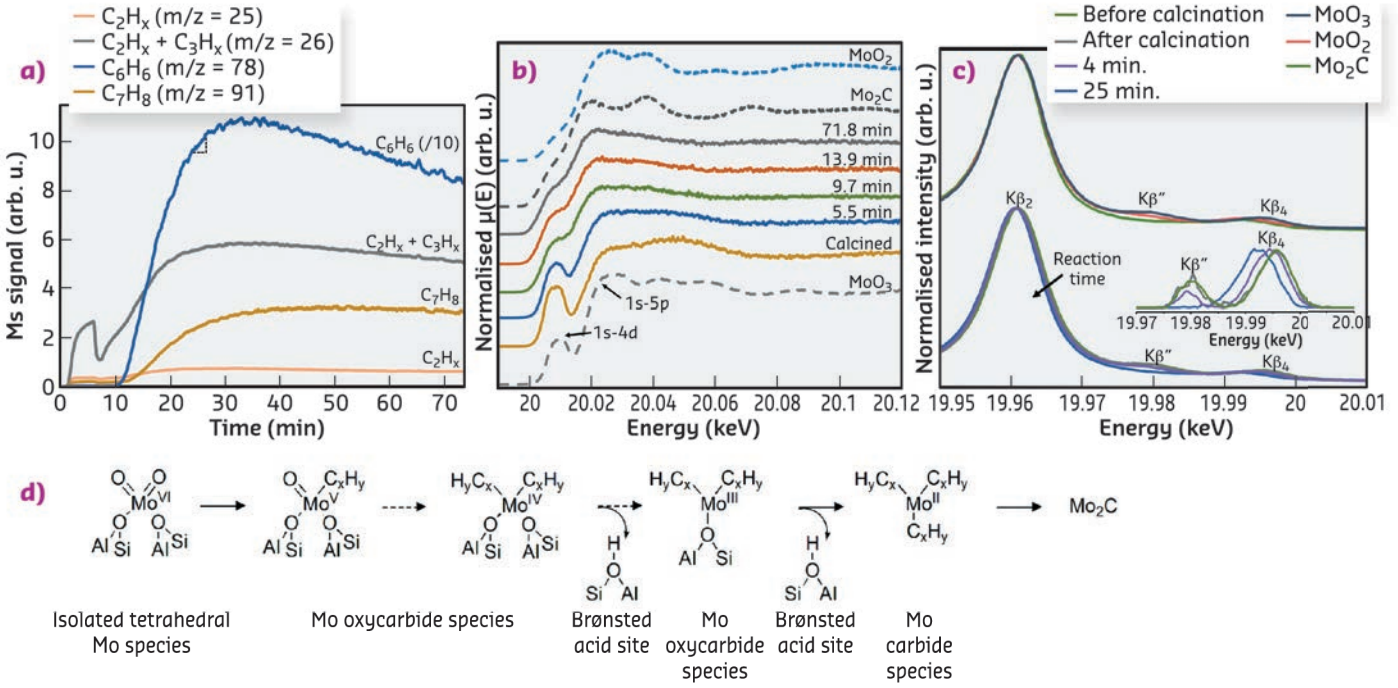

Fig. 22: a) Mass spectrometry data. b) Operando Mo K-edge HERFD-XANES spectra. c) Kβ valence-to-core emission lines. d) Evolution of Mo species.

PRINCIPAL PUBLICATION AND AUTHORS

Molybdenum speciation and its impact on catalytic activity during methane dehydroaromatization in zeolite ZSM-5 as revealed by operando X-ray methods, I. Lezcano-González (a), R. Oord (b), M. Rovezzi (c), P. Glatzel (c), S.W. Botchway (d), B.M. Weckhuysen (b) and A.M. Beale (a), *Angew. Chem. Int. Ed.* **55**, 5215 (2016); doi: 10.1002/anie.201601357.
(a) UK Catalysis Hub, Research Complex at Harwell & University College London (UK)
(b) Utrecht University (The Netherlands)
(c) ESRF
(d) Central Laser Facility (UK)

REFERENCES

[1] J.J. Spivey and G. Hutchings, *Chem. Soc. Rev.* **43**, 792 (2014).
[2] Z.R. Ismagilov *et al.*, *Energy Environ. Sci.* **1**, 526 (2008).

ADVANCED X-RAY SPECTROSCOPIC TOOL FOR ACTINIDE RESEARCH

The work is the first illustration of the ability of high-energy-resolution fluorescence-detection X-ray absorption spectroscopy (HERFD-XAS) to directly probe the crystal-field splitting in the 5f shell of actinides and to resolve the charge-transfer satellites. This is a breakthrough for actinide science, allowing for the straightforward extraction of desired information from the spectroscopic method, which is also easy to interpret and easy to calculate.

For strongly electron-correlated systems, X-ray absorption spectroscopy (XAS) is viewed as a technique capable of providing information on the ground state character despite the presence of the core-hole in the final state of the spectroscopic process. In the 3d transition metal compounds, XAS at the metal 2p edge is routinely used to probe the magnitude of the crystalline electric field (CEF) splittings in the 3d shell and the degree of the 3d hybridisation in the ground state. However, for the 5f shell of actinides, such a usage of XAS is difficult. At the U 3d and 4d edges, where the transitions to the 5f states are probed, core-hole lifetime broadenings (full width at half maximum) are about 3.2 eV and 4.2 eV, respectively, while at the 5d edge, the broadening can be as large as 6.0 eV. Therefore, the conventional XAS spectra of actinide materials at the 3d and 4d edges often appear as single lines where splittings of the 5f states (*e.g.*, due to the CEF interaction) are indistinguishable.

An advanced technique, HERFD-XAS, has been recently employed for measurements at the 3d edge of U compounds [1]. This has led to a tremendous improvement in the experimental resolution due to reduced core-hole lifetime broadening and revealed additional structures in the XAS spectra, not measurable before (see **Figure 23**). The effects of the hybridisation of the valence states of actinides with ligand states in compounds are expected to result in the appearance of charge-transfer satellites in the XAS spectra. The interpretation of such satellites can provide information on the degree of the 5f hybridisation, covalency of the compound, and the nature of the ground state.

Here, we demonstrate, using ThO_2, that the HERFD-XAS technique now allows us to directly probe the CEF splittings in the 5f shell with the results clearly shown in the spectra. An analysis of the newly-resolved charge-transfer satellites indicates significant occupancy of Th valence states which contradicts the common view of ThO_2 as an ionic system (see *e.g.* [2]).

Figure 24 shows the HERFD-XAS spectrum at the Th M_4 edge of ThO_2 (recorded at beamline **ID26**) which is compared with the results of the Anderson impurity model (AIM) calculations taking into account both Th 5f-O 2p and Th 6d-O 2p charge-transfer. In particular, the structure at around 3492.5 eV appears in the calculated spectrum only upon inclusion of the Th 6d-O 2p charge transfer. Based on agreement with experiment, the AIM calculations for the ground state indicate that the occupancy of the

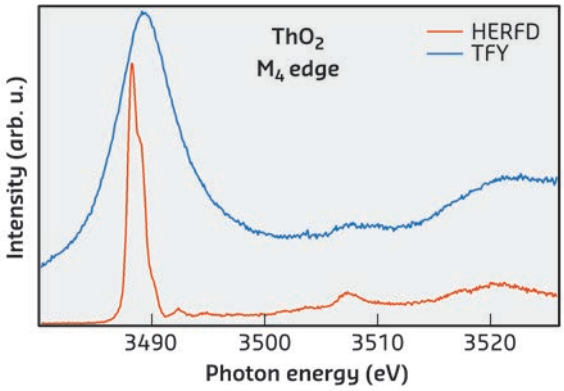

Fig. 23: Total fluorescence yield (TFY) and HERFD spectra at the Th M_4 edge of ThO_2.

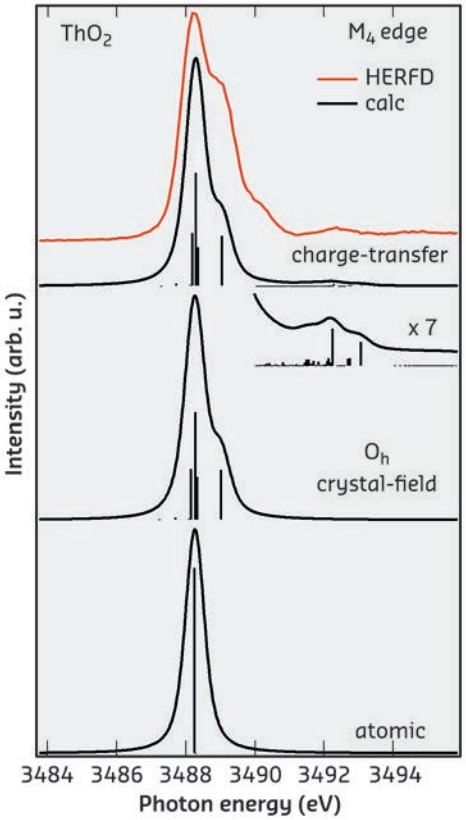

Fig. 24: Experimental and calculated XAS spectra at the Th M_4 edge of ThO_2.

Th 6d states (0.20 electrons) is larger than that of the Th 5f states (0.11 electrons). This result does not support an ionic character for ThO_2.

The improved resolution of the HERFD-XAS technique allows us to resolve the shoulder at ~0.8 eV above the main maximum of the Th M_4 edge of ThO_2. The origin of this shoulder becomes clear from a comparison of the experimental data with atomic and CEF multiplet theory for the Th(IV) ion in **Figure 24**. The atomic multiplet calculations for the transitions between the $3d^{10}5f^0$ and $3d^95f^1$ configuration in the $^1S_0$ ground state produce a single multiplet pole while putting the Th(IV) ion in the cubic (O_h) CEF environment reveals CEF split states of the $3d^95f^1$ configuration thus producing the shoulder at ~0.8 eV above the main peak in the calculated spectrum for the Wybourne's CEF parameter values of B^4=–1.30 eV and B^6=0.55 eV. The improvement in resolution offered by HERFD-XAS now allows the CEF interactions to be probed for the 5f shell and to extract the information about the CEF effects directly from the XAS data in the manner commonly used for the $L_{2,3}$-edges of 3d transition metal systems.

PRINCIPAL PUBLICATION AND AUTHORS

High-resolution X-ray absorption spectroscopy as a probe of crystal-field and covalency effects in actinide compounds, S.M. Butorin (a), K.O. Kvashnina (b,c), J.R. Vegelius (a), D. Meyer (d) and D.K. Shuh (e), *PNAS* **113**, 8093-8097 (2016); doi: 10.1073/pnas.1601741113.
(a) Uppsala University, Uppsala (Sweden)
(b) The European Synchrotron, Grenoble (France)
(c) HZDR, Institute of Resource Ecology, Dresden (Germany)
(d) CEA-ICSM, Marcoule (France)
(e) Lawrence Berkeley National Laboratory, Berkeley (USA)

REFERENCES

[1] K.O. Kvashnina, S.M. Butorin, P. Martin and P. Glatzel, *Phys. Rev. Lett.* **111**, 253002 (2013).
[2] *The chemistry of the actinide and transactinide elements*, L.R. Morss, N.M. Edelstein, J. Fuger (Eds.), Springer, Dordrecht, The Netherlands (2010).

NANOSTRUCTURED PALLADIUM-CERIA CATALYST FOR ANION EXCHANGE MEMBRANE FUEL CELLS

One of the biggest obstacles to the diffusion of fuel cells is their cost, in large part due to platinum catalysts. Here, a platinum-free fuel cell was studied that employs a mixed carbon-CeO_2 supported palladium anode catalyst and produces peak power densities of more than 500 mW cm^{-2}.

Recent analyses have shown that among fuel cell stack components around 45% of the cost comes from the platinum catalyst. Therefore, a complete removal of platinum from fuel cells and replacement with metals that are less expensive and more abundant in nature is crucial. As an alternative to traditional fuel cells that operate under corrosive acidic conditions with membranes like nafion™, the use of an alkaline membrane fuel cell (AEM-FC) may reduce costs by avoiding the use of platinum. The main obstacle to the development of this type of fuel cell is the challenge of overcoming poor hydrogen oxidation (anode) kinetics in alkaline media.

We present a nanoparticle palladium based catalyst (10 wt% Pd) with a composite support made of Vulcan XC-72 carbon and CeO_2 (C-CeO_2) which exhibits enhanced kinetics in alkaline media. Our fuel cell containing this catalyst

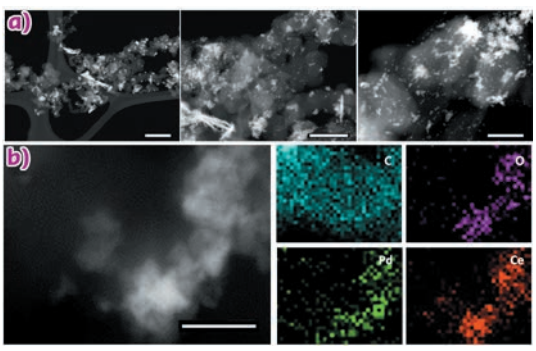

Fig. 25: a) STEM micrographs of Pd/C-CeO_2 (scale bars from left to right; 200 nm, 100 nm and 50 nm respectively) and b) STEM image of Pd/C-CeO_2 and related EDX maps for C, O, Pd and Ce respectively (scale bar is 20 nm).

performs with no platinum in the catalysts (Pd at the anode and Ag at the cathode) and produces 500 mW cm^{-2} peak power output running on dry hydrogen and air.

High angle annular dark field (HAADF) scanning transmission electron microscopy (STEM) and high-resolution transmission electron microscopy (HR-TEM) were used to study the catalyst morphology. Z-contrast STEM micrographs of Pd/C-CeO_2 are shown in **Figure 25a**. The CeO_2 structures appear brighter than carbon on the STEM images. Palladium nanoparticles are visible only on the carbon part of the sample due to poor resolution between Pd and CeO_2 (mean size of carbon supported nanoparticles 2.0 nm). Therefore, we used STEM-EDX (energy dispersive X-ray) elemental map analysis to investigate the Pd distribution over both the carbon and ceria parts of the catalyst. A representative area of the catalyst is shown in **Figure 25b**, that shows a notable accumulation of Pd on the ceria-rich regions. Our electrochemical investigations show that the Pd-CeO_2 interaction is responsible for the enhanced activity of this catalyst.

Strong Pd-CeO_2 interactions would have a significant effect on the oxidation state of the Pd due to the oxide spillover capacity of ceria that would leave most of the Pd in the oxidised form. To verify this, the Pd oxidation state in the Pd/C-CeO_2 catalyst was investigated by X-ray absorption spectroscopy (XAS) and compared to a simple Pd on carbon catalyst (Pd/C) with the same loading. XAS data were obtained at beamline **BM08** (LISA CRG). Spectra were also collected on PdO and on a foil of metallic Pd as standards. In **Figure 26a**, a comparison of the XANES (X-ray absorption near-edge structure) spectra clearly shows that Pd in Pd/C-CeO_2 is mostly oxidised, while in Pd/C the palladium is prevalently in its metallic state. EXAFS (extended X-ray absorption fine structure) analysis was carried out modelling the data with two components, *i.e.* metallic Pd and PdO. The raw EXAFS data and related Fourier transforms are shown in **Figures 26b** and **26c** respectively. The EXAFS analysis shows PdO accounts for 87 wt% of the total Pd content in Pd/C-CeO_2. This is unusual as carbon supported Pd nanoparticles (ca. 2 nm in diameter) are usually found to be at least 50% metallic. As expected, only 17 wt% of PdO was found in the Pd/C system. The XAS data therefore shows that the Pd exists primarily as oxide for the C-CeO_2 supported catalyst also confirming that Pd is largely supported on the ceria regions.

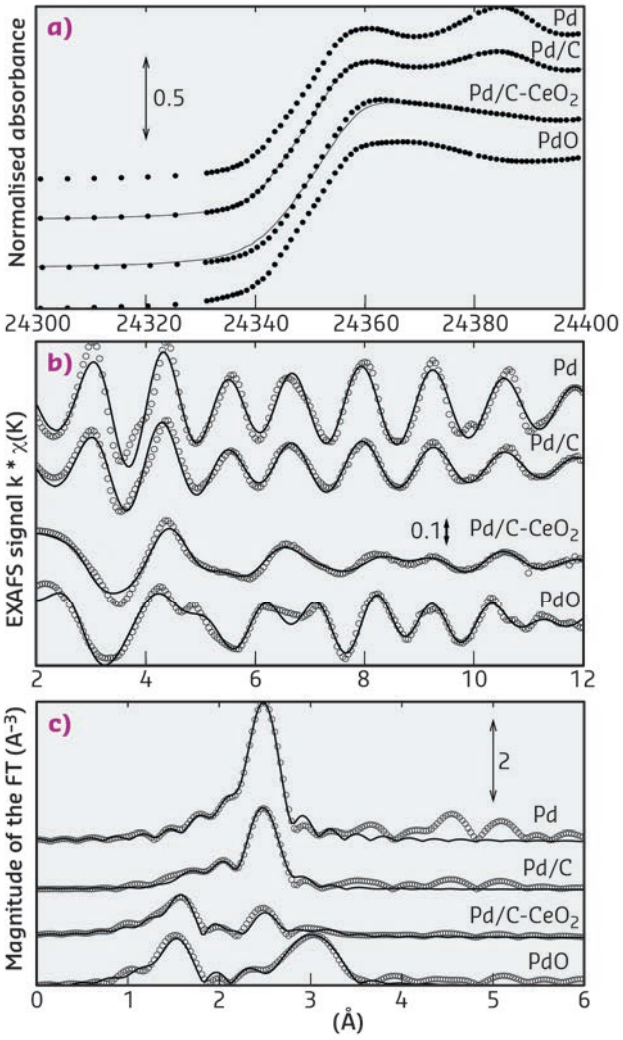

Fig. 26: a) XAS at the Pd Kα edge of Pd/C-CeO_2 and Pd/C (XANES spectra of Pd-foil and PdO standards are also shown), b) EXAFS data and the related c) Fourier transforms at the Pd Kα edge.

In summary, we studied an entirely Pt-free fuel cell that produces a peak power density of over 500 mW cm^{-2}. This performance is due to a Pd/C-CeO_2 catalyst where the Pd-CeO_2 interactions enhance hydrogen oxidation kinetics.

PRINCIPAL PUBLICATION AND AUTHORS

A Pd/C-CeO_2 anode catalyst for high-performance platinum-free anion exchange membrane fuel cells, H.A. Miller (a), A. Lavacchi (a), F. Vizza (a), M. Marelli (b), F. Di Benedetto (c), F. D'Acapito (d), Y. Paska (e), M. Page (e) and D.R. Dekel (f), *Angew Chem Int Edit* **55**, 6004-6007 (2016); doi: 10.1002/anie.201600647.

(a) CNR-ICCOM, Firenze (Italy)
(b) CNR-ISTM, Milan (Italy)
(c) Department of Earth Sciences, Università di Firenze (Italy)
(d) CNR-IOM-OGG c/o ESRF, Grenoble (France)
(e) CellEra, Caesarea (Israel)
(f) Technion – Israel Institute of Technology, Haifa (Israel)

SPIRAL SPIN-LIQUID AND THE EMERGENCE OF A VORTEX-LIKE STATE IN $MnSc_2S_4$

Spiral spin-liquid is a short-range correlated state where spins fluctuate collectively as spirals in real space. Such a correlation is highly unusual: in conventional paramagnets, spins fluctuate in a completely random fashion. We present direct experimental evidence for the existence of the spiral spin-liquid state in A-site spinels, reveal the multi-step ordering of the spiral spin liquid and discover a vortex-like triple-*q* phase on application of a magnetic field.

The A-site spinel $MnSc_2S_4$ is a promising candidate to realise the spiral spin-liquid state **[1,2]**. In $MnSc_2S_4$, Mn^{2+} (S = 5/2) ions occupy the A-sites and constitute a diamond lattice as is shown in **Figure 27a**. The bi-partite character of the diamond lattice allows the definition of the J_1-J_2 model, with the ferromagnetic J_1 and the antiferromagnetic J_2 couplings. In the weak frustration regime of J_2/J_1 < 0.125, the spin correlations are similar to that of conventional paramagnets. However, in the strong frustration regime of J_2/J_1 > 0.125, the propagation vector will form a continuous surface in the reciprocal space, shown in **Figure 27b**. Since each q-vector on this surface represents a spiral state under the mean-field theory, such a continuous surface is named the 'spiral surface'. Previous experiments using a powder sample of $MnSc_2S_4$ have revealed a long-range order transition at T_N = 2.3 K and suggested the existence of the spiral surface at $T > T_N$ **[3]**. However, direct proof of the spiral surface was missing, which requires single crystal samples.

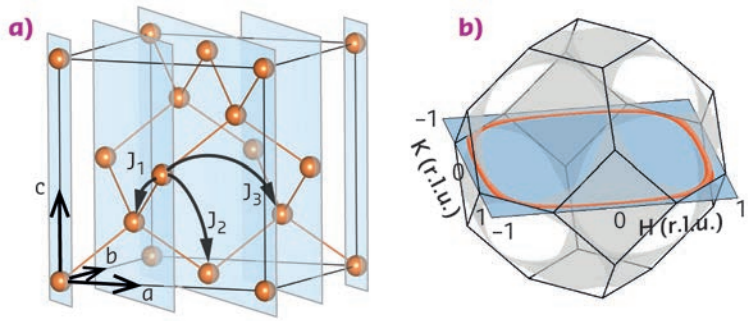

Fig. 27: a) Mn^{2+} ions in $MnSc_2S_4$ constitute a diamond lattice. b) The predicted spiral surface (grey) in $MnSc_2S_4$ with the frustration ratio J_2/J_1 = 0.85.

Recently we succeeded in growing single crystals of $MnSc_2S_4$ using the chemical transport technique. To check the quality, we performed single-crystal synchrotron diffraction experiments at beamline BM01 (Swiss-Norwegian CRG beamline). Altogether 2738 Bragg reflections were collected at room temperature, our refinement of the spinel structure did not detect any Mn-Sc anti-site disorder and confirmed the good quality of our single crystals.

To study the short-range correlations in $MnSc_2S_4$, we performed polarised neutron diffuse scattering experiments on DNS at MLZ. **Figure 28a** presents the results measured at T = 2.9 K. A squared ring feature near the Brillouin zone boundary can be clearly resolved, which is consistent with the existence of the spiral surface. Considering that the spiral surface extends towards the zone boundary with increasing frustration ratio J_2/J_1, it is clear that the frustration should be strong in $MnSc_2S_4$.

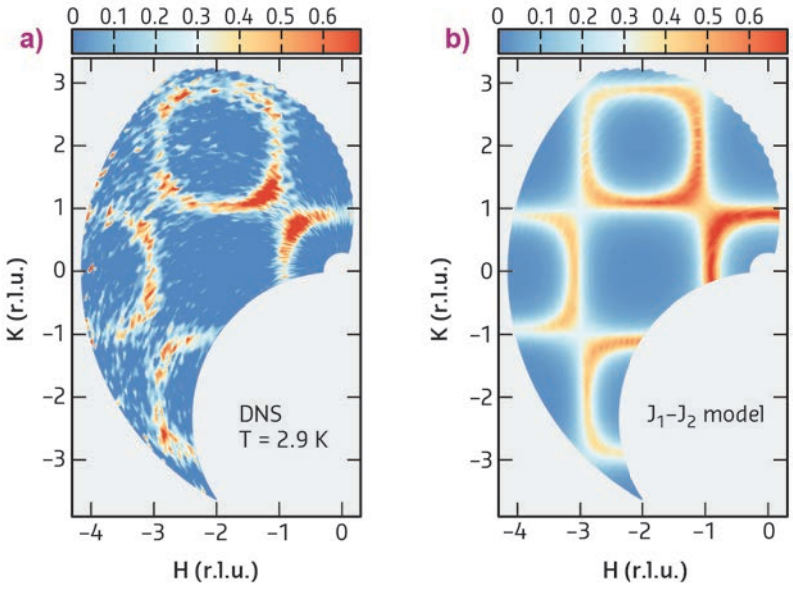

Fig. 28: a) Diffuse neutron scattering results measured on DNS at 2.9 K. The 50 K data has been subtracted as the background. b) Monte Carlo simulation results using the J_1-J_2 model with a frustration ratio of J_2/J_1 = 0.85.

To fix the frustration ratio J_2/J_1 in $MnSc_2S_4$, we performed classical Monte Carlo simulations using the ALPS package **[4]**. As shown in **Figure 28b**, the simulation results with J_2/J_1 = 0.85 can reproduce the observed squared ring feature very well. Such a high ratio of J_2/J_1 puts $MnSc_2S_4$ deep in the spiral spin-liquid phase **[1]** and thus the observed ring feature is direct evidence of the spiral surface.

Besides the spiral spin-liquid state, we also investigated the long-range ordered state at $T < T_N$ performing single crystal neutron diffraction on TriCS at SINQ of PSI and spherical neutron polarimetry on TASP with MuPAD at SINQ and IN22 with CryoPAD at ILL. Our experiments revealed multi-step transitions: at 2.2 K, the system first enters a sinusoidally modulated collinear phase with q = [0.75 0.75 0]; at 1.64 K, it then enters a transitional incommensurate phase with q = [0.75±0.02 0.75±0.02 0]; and finally, at 1.46 K, the system enters a helical phase with q back to the [0.75 0.75 0] position. Such a multi-step transition is direct evidence of the importance of perturbations from the third-neighbour coupling J_3 and the dipolar interactions **[2]**.

Under a magnetic field along the [001] direction, a triple q phase with $\Sigma_i q_i = 0$ is observed through the analysis of the domain population. Although neutron diffraction is not sensitive to the phase factor, candidate structures all exhibit a winding feature for the spin components in the [111] plane. Therefore the observed triple-q structure is in fact a vortex lattice. We note that the q-combination rule of the triple-q phase is very similar to that of the skyrmion lattice **[5]**.

PRINCIPAL PUBLICATION AND AUTHORS

Spiral spin-liquid and the emergence of a vortex-like state in $MnSc_2S_4$, S. Gao (a,b), O. Zaharko (a), V. Tsurkan (c,d), Y. Su (e), J.S. White (a), G.S. Tucker (a,f), B. Roessli (a), F. Bourdarot (g), R. Sibille (a,h), D. Chernyshov (i), T. Fennell (a), A. Loidl (c) and C. Rüegg (a,b), *Nature Physics* (2016); doi: 10.1038/nphys3914.

(a) Laboratory for Neutron Scattering and Imaging, Paul Scherrer Institut, Villigen PSI (Switzerland)
(b) Department of Quantum Matter Physics, University of Geneva (Switzerland)
(c) Experimental Physics V, University of Augsburg (Germany)
(d) Institute of Applied Physics, Academy of Sciences of Moldova, Chisinau (Republic of Moldova)
(e) Jülich Center for Neutron Science JCNS-MLZ, Forshungszentrum Jülich GmbH, Outstation at MLZ, Garching (Germany)
(f) Laboratory for Quantum Magnetism, École Polytechnique Fédérale de Lausanne (Switzerland)
(g) CEA et Université Grenoble Alpes, INAC-MEM-MDN, Grenoble (France)
(h) Laboratory for Scientific Developments and Novel Materials, Paul Scherrer Institut, Villigen PSI (Switzerland)
(i) Swiss-Norwegian Beamlines at the ESRF, Grenoble (France)

REFERENCES

[1] D. Bergman *et al.*, Nat. Phys. 3, 487 (2007)
[2] S. B. Lee *et al.*, Phys. Rev. B 78, 144417 (2008)
[3] A. Krimmel *et al.*, Phys. Rev. B 73, 014413 (2006)
[4] B. Bauer *et al.*, *J. Stats. Mech.* **2011**, P05011 (2011)
[5] S. Mühlbauer *et al.*, *Sci.* **323**, 915 (2009).

X-ray nanoprobe

After the major efforts made during 2015, swapping from start-up to routine operation of the three beamlines built within Phase I of the ESRF upgrade, all five XNP beamlines have been in full user operation in 2016. They provide a vast spectrum of techniques, imaging, diffraction and spectroscopy to our user community and offer nanobeams over an X-ray energy regime ranging from 2 to 35 keV. This flexibility in techniques is reflected in the great variety of scientific highlights ranging from hard condensed matter to biological and archaeological samples, and sample sizes ranging from individual nano-objects of 100 nm in size to samples of several centimetres.

Depending on the status of their development, the XNP beamlines have continued to polish their recently commissioned equipment or have launched ambitious refurbishment plans in accordance with the EBS project. The general trend shows a rapid increase in data recording speed and data dimensionality revealing the future challenges imposed by the treatment of huge amounts of data during experiments.

In this context, at **ID01,** we have started to implement sample environments such as high-temperature furnaces (up to 1000°C) and gas flow reactors in the Bragg coherent diffraction setup. These lightweight and compact environments can be carried by piezo scanners and scanned in the 100 nm beam in continuous motion to resolve structural changes on the sample or to monitor drift during temperature changes more easily. They reply as well to the ambitions of the full-field diffraction microscope, an endstation that became fully operational in 2016. For experiments requiring intense focused beams, the arrival of the KB mirrors in late 2016 should bring a decisive flux gain and will permit the use of the high-flux multilayer optics in nanofocusing mode. On the software side, a data analysis tool has been designed for ID01 with a graphical user interface able to handle the 5D datasets produced by the quick-mapping (K-MAP) of a sample in real (2D) and reciprocal space (3D).

At **ID13,** the integration of the EIGER 4M pixel array detector has progressed well allowing stable operation at up to 750 Hz. Based on this achievement, millimetre-scale fast continuous scanning with micrometre-scale resolution has become feasible. This enables scanning-SAXS/WAXS imaging of extended areas of square-millimetres yielding two-dimensional maps extracted from millions of diffraction patterns, *i.e.* resulting in megapixel raster images comparable in size to optical micrographs. The high frame rate of this detector is also being employed more often for time-resolved experiments close to one millisecond. Synchronisation with TTL-signal compatible user devices is possible. This offers many opportunities for fast *in situ*, *in vivo*, operando micro-/nano-beam studies on topics such as ultra-fast heating, mechanical testing, and micro-fluidics. Regarding nanobeam activities, ID13 has started operation of nanodiffraction with a sub 50 nm spot size for collaborators, with the aim of offering this option to all users by the end of 2017.

The nano-imaging beamline **ID16A** has successfully put into operation cryo-cooling of the sample stage. Analysing samples in the frozen hydrated state is a major milestone for the beamline and crucial to delay the effects of radiation damage in biological samples. A complete cryogenic workflow has been put in place, from fast sample freezing to analysis in the X-ray microscope. For room temperature analysis, the capacity of the sample changer has been increased from four to sixteen, leading to a significant improvement in the throughput of the instrument. All imaging modalities of the microscope, fluorescence analysis, magnified phase imaging, near-field and far-field ptychography, are now routinely used in two dimensions, but increasingly also in three dimensions through tomography techniques. The beamline offers a 'low' energy mode at 17 keV optimised for fluorescence analysis of biological samples and a 'high' energy mode at 34 keV more appropriate for materials science applications.

For **ID16B**, 2016 was mostly dedicated to the improvement of the *in situ* high-temperature nanotomography setup. The long-term stability has been much improved while both the spatial resolution range (from 35 to 300 nm) and the acquisition speed (< 20 s per tomographic scan) have been significantly increased. This paves the way to the nanoscale investigation of many high temperature driven heterogeneous dynamics in material science (such as nucleation, sintering, deformation, glass synthesis, growth of pores or cracks, etc.). In parallel, several operando experiments were successfully carried out, involving, for example, XBIC and/or XEOL measurements. Both *in situ* and operando experiments are being requested more often by

users to study samples in their real or native environment, and so ID16B is trying to respond to this clear trend emerging from the user community and in-house research programme.

At **ID21**, the tender X-ray and infrared microspectroscopy beamline, an important effort was dedicated to preparing the beamline review and the conceptual design report for the upgrade of the beamline. Based on the feedback received from the users and the review panel, main priorities were identified as: a strong refurbishment of the main optics to obtain a smaller (~ 100 nm), more stable (in particular over the EXAFS energy range) and more intense beam, over a wider energy range (including Zn K-edge); a refurbishment of XRF detectors and electronics to collect XRF and XANES data faster (hence at reduced dose), on highly concentrated and highly diluted elements both present in complex matrices; an easy-to-install and easy-to-use cryo stage, in particular for the analysis of biological materials, which constitute a high proportion of the samples studied at ID21, particularly from the fields of life science, medicine and plant science. The design and implementation of some of this equipment is already on-going (new double mirror system, new double crystal monochromator, new SDD detectors and electronics) or has been recently completed (new cryo-stage) and should be of benefit to the users before the EBS long shutdown and even more after the complete refurbishment of the beamline.

T. SCHÜLLI

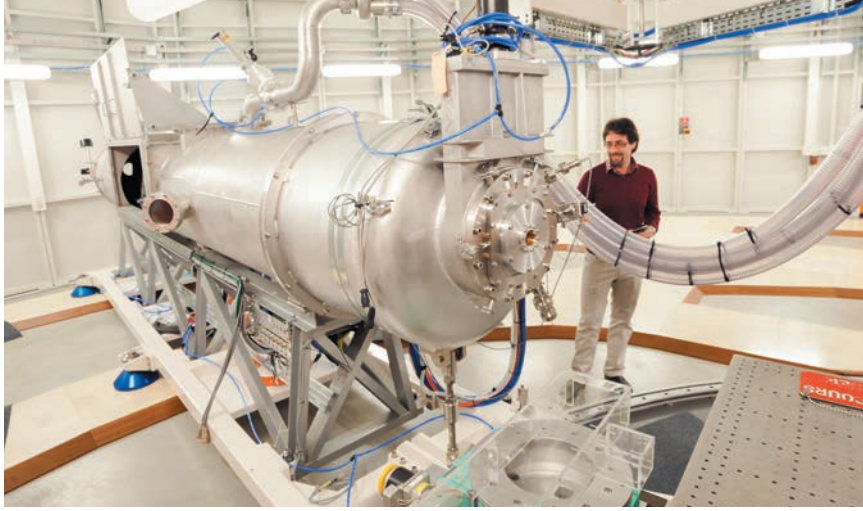

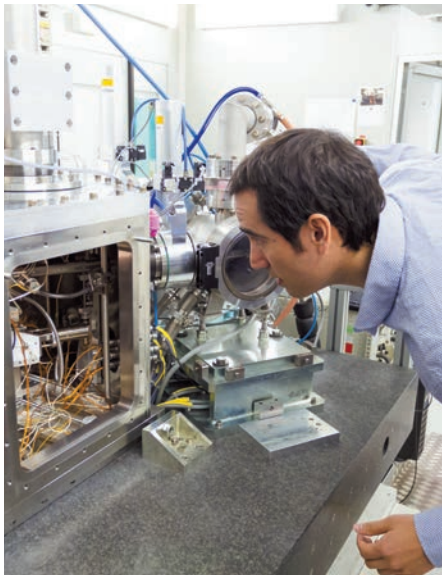

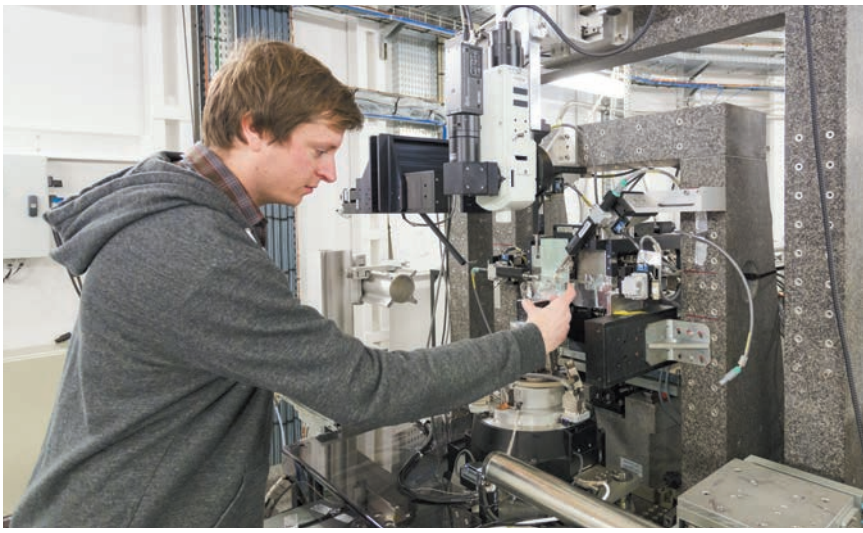

REACTIVITY AND CRYSTALLOGRAPHY OF A SINGLE ZEOLITE CRYSTAL REVEALED BY MONOCHROMATIC X-RAYS

Large-scale catalytic processes in the petrochemical industry rely heavily on the catalytic properties of zeolite ZSM-5. The structure-reactivity relationships of a single zeolite ZSM-5 crystal were investigated simultaneously using micro-X-ray diffraction (μ-XRD) and μ-X-ray excited optical fluorescence (μ-XEOF) imaging.

Establishing structure-reactivity relationships in heterogeneous catalysis is essential because structural heterogeneities can lead to significant differences in reactivity between catalyst particles. However, it is a challenge to obtain information about the interplay between structure and reactivity at the single particle level because it requires a spatial correlation of structural changes of an inorganic material with the chemical reactivity of an organic phase. One approach to achieve such correlation is to collect structure and reactivity information simultaneously within the same measurement. Here we show that it is possible to resolve the complex crystallographic structure of a single zeolite ZSM-5 crystal while simultaneously following the reactivity of organic molecules at catalytically active sites using a monochromatic X-ray beam.

Zeolite ZSM-5 crystals represent a prime example of crystallographic and compositional complexity within a single catalyst particle [1]. A 3-D porous network of Si-O and Al-O tetrahedra ultimately determines the orientation of zeolite pore channels and catalytic properties of the zeolite (*i.e.*, the arrangement of Al atoms in the zeolite framework acting as acidic sites). To study the chemistry of zeolite ZSM-5, large zeolite crystals (100×20×20 μm^3) are often used as model systems. These crystals consist of at least six subunits with so-called 90° intergrown crystalline domains. Furthermore, the crystals show pronounced Al zoning, *i.e.* significantly higher concentration of Al in the 2 μm thick outer rim [2]. As a result of this structural anisotropy, crystalline domains within one zeolite ZSM-5 crystal can be unequally affected by post-treatment methods, such as steaming at elevated temperatures, resulting in distinctly different crystallinity and reactivity.

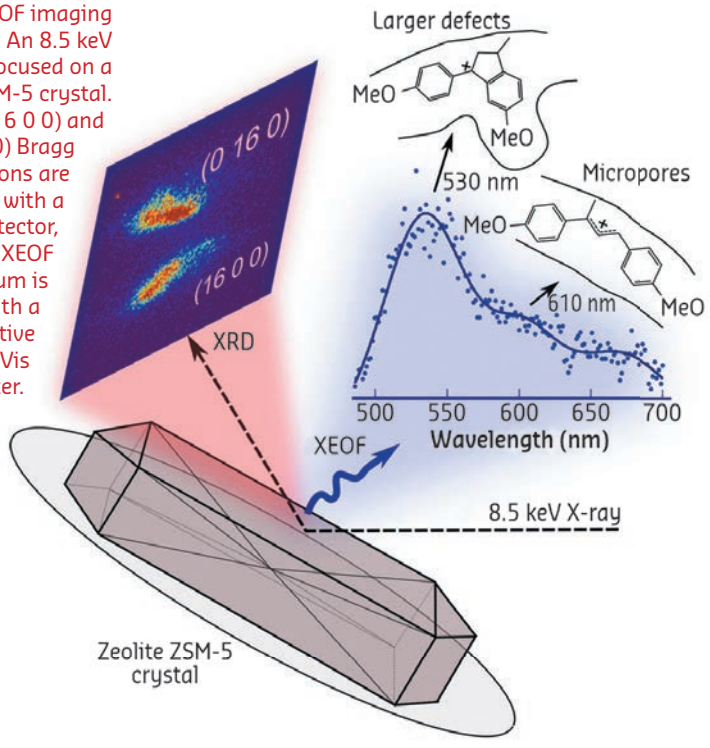

Fig. 29: Schematic of the combined μ-XRD/μ-XEOF imaging approach. An 8.5 keV X-ray is focused on a zeolite ZSM-5 crystal. The (16 0 0) and (0 16 0) Bragg reflections are detected with a 2-D X-ray detector, whereas the XEOF spectrum is collected with a highly-sensitive UV-Vis spectrometer.

To study the structure-reactivity relationship of a single zeolite ZSM-5 crystal, we employed a novel characterisation approach based on simultaneous micro-X-ray diffraction (μ-XRD) and μ-X-ray excited optical fluorescence (μ-XEOF) imaging (**Figure 29**) at beamline **ID01**. An 8.5 keV X-ray beam was used to acquire both diffraction (XRD) and spectral (XEOF) information, achieving a lateral resolution of ~ 500 nm. With this approach, the local zeolite crystallinity measured by μ-XRD, is correlated with the local Brønsted acidity measured by μ-XEOF. The latter is based on the use of X-ray excited photoemission of visible light from the fluorescent products formed upon reaction of 4-methoxystyrene probe molecules with acid sites of zeolite ZSM-5 (**Figure 29**). The linear products (detected at 610 nm in the XEOF spectrum) form selectively in the micropores of zeolite ZSM-5, whereas bulkier cyclic species (530 nm) readily form at acid sites near crystalline defects, which provide the pore space necessary to accommodate larger products (**Figure 29**).

We showcased the μ-XRD/μ-XEOF approach on an anomalously intergrown, steamed zeolite ZSM-5 crystal, which contains large structural heterogeneities. As determined by PCA (principal component analysis) and subsequent clustering, the μ-XRD data reveals five distinct intracrystalline domains with different crystallographic orientations and concentration of framework Al (**Figure 30a**). Consequently, the overlaid μ-XEOF map shows large differences in reactivity (**Figure 30b**). Several conclusions

can be drawn based on the cluster maps. Crystallographic phases within one zeolite crystal are unevenly affected by steaming and show different catalytic activity (**Figure 30 c** and **d**); this is a result of the structural anisotropy. The Al-rich outer crystalline domains appeared highly prone to dealumination. In these regions, low to moderate reactivity of the probe molecules was observed, while the inner zeolite domains that were moderately steamed showed significantly higher probe reactivity.

In summary, a single monochromatic X-ray beam can be used to acquire information in both the X-ray and the visible spectral region, which allowed us to study the impact of the crystalline structure and mesoporous defects on the reactivity of a single zeolite crystal. The method we have developed has the potential to substantiate the structure-reactivity properties of many other important functional materials, synchronously, with both spatial and time resolution.

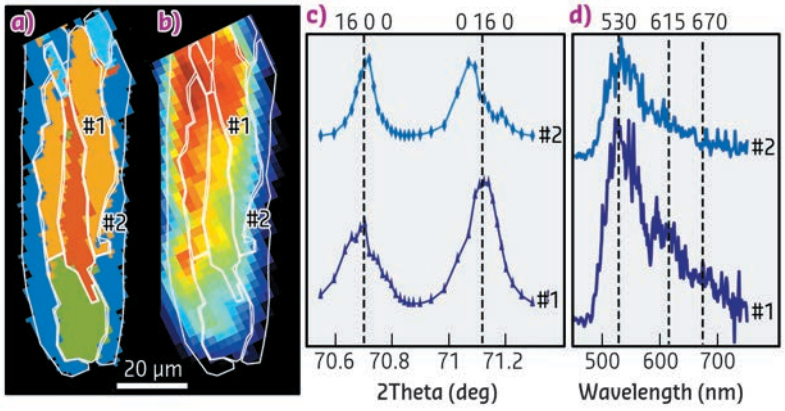

Fig. 30: a) PCA cluster map of different crystalline domains within a single zeolite ZSM-5 crystal. b) Corresponding XEOF total intensity map with the white contour plot showing clusters from (a). c,d) Comparison of c) X-ray diffractograms and d) XEOF spectra for the two regions of interest labelled in (a) and (b).

PRINCIPAL PUBLICATION AND AUTHORS

X-ray excited optical fluorescence and diffraction imaging of reactivity and crystallinity in a zeolite crystal: crystallography and molecular spectroscopy in one, Z. Ristanović (a), J.P. Hofmann (a,b), M.-I. Richard (c,d), T. Jiang (a), G.A. Chahine (c), T.U. Schülli (c), F. Meirer (a) and B.M. Weckhuysen (a), *Angew. Chem. Int. Ed.* **55**, 7496-7500 (2016); doi: 10.1002/anie.201601796.
(a) Inorganic Chemistry and Catalysis, Utrecht University (The Netherlands)
(b) Eindhoven University of Technology (The Netherlands)
(c) ESRF
(d) Aix Marseille Université, CNRS, Université de Toulon (France)

REFERENCES

[1] L. Karwacki *et al.*, *Nat. Mater.* **8**, 959 (2009).
[2] Z. Ristanovic *et al.*, *Angew. Chem. Int. Ed.* ***52***, 13382 (2013).

X-RAYS ENABLE A DIRECT VIEW INSIDE BIOLOGICAL CELLS

Structures within whole biological cells have been resolved quantitatively at the nanoscale using a combination of ptychography and scanning X-ray nanodiffraction. Employed sequentially, these techniques provided high resolution real space and reciprocal space images while exposing the cells to a comparatively small radiation dose. The structural arrangement and diameter of keratin protein bundles inside epithelial cells was revealed and filament diameters and distances could be derived.

Biological cells contain a plethora of nanometre-sized objects and structures. Much of our knowledge about cellular function has been gained from direct imaging. Traditionally, fluorescence-based techniques and electron microscopy have been used to achieve micrometre to nanometre resolution in cellular imaging. More recently, X-ray imaging methods, which take advantage of the short wavelength and high penetration power of X-rays, were developed and applied to the imaging of biological matter as well **[1-3]**. The small beams available at specialised synchrotron beamlines such as **ID13** (**Figure 31**) enable high-resolution applications. One of the greatest challenges, however, remains radiation damage by the X-rays, which becomes more pronounced as the resolution reaches smaller values.

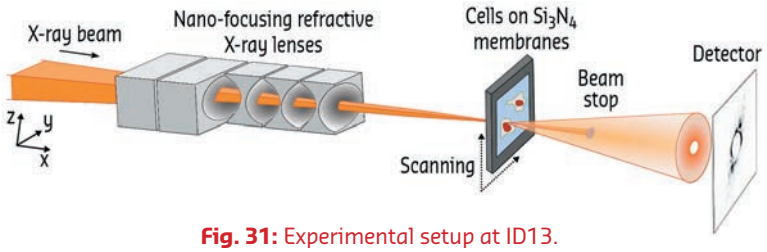

Fig. 31: Experimental setup at ID13.

By first recording ptychography overview images of whole cells at 65 nm resolution

(**Figure 32a** and **b**), cellular structures were located precisely at a comparatively low dose of 10^3 Gy. Ptychography is a coherent diffractive imaging technique whereby the electron density of the scattering material is determined from a series of two-dimensional scattering patterns via iterative reconstruction algorithms and redundant information from overlapping scanning positions. Subsequently, scanning X-ray nanodiffraction (approximate dose 10^8 Gy) was employed to record reciprocal space scattering patterns from regions of interest (ROIs). For this technique, the sample was scanned through the beam at a step size comparable to the beam size. The intensity values in the individual scattering patterns were integrated to derive dark-field-images (**Figure 32c**) at an intermediate resolution, which corresponds to the beam size in the order of 100 nm. Further analysis of each individual pattern revealed a local scattering signal (**Figure 32d**) which could be assigned to the specific position in the cell.

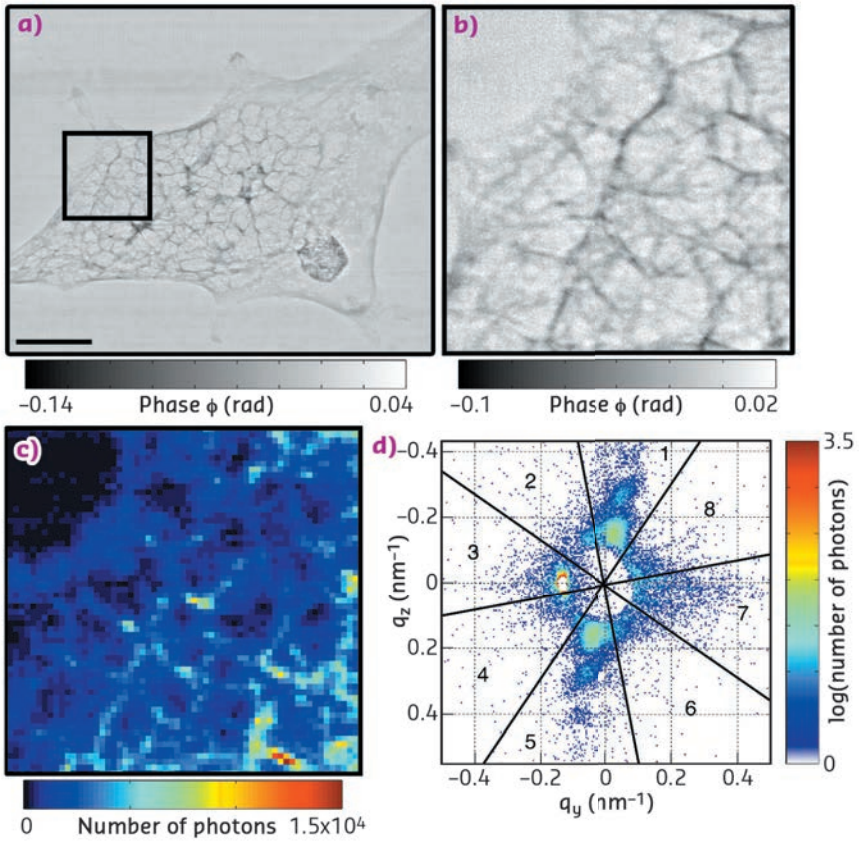

Fig. 32: a) Ptychography image, scale bar 5 µm and b) detail from the ROI shown by the black box in (a). c) Dark-field image computed from scanning X-ray nanodiffraction of the same ROI, and d) example of one pixel from (c) showing an anisotropic signal.

The mechanical properties of biological cells are to a large part governed by the so-called cytoskeleton, a composite network of fibrous proteins **[4]**. The present study focuses on keratin bundles, which in epithelial cells constitute one of the filament types. By fitting a hexagonally packed bundle model **[5]** to the data, the radius of individual filaments (r = 5.5 ± 0.7 nm), the inter-filament distance (a = 15.2 ± 1.4 nm) and the bundle diameter (D = 72.0 ± 5.5 nm) could be derived (**Figure 33**). These values are in agreement with results from electron microscopy **[6]**, but were obtained without slicing or staining the cell and are thus at a reduced risk of artifacts.

This study demonstrates the advantage of combining ptychography and scanning X-ray nanodiffraction in biological imaging since it provides nanometre resolution imaging of specific cellular structures while avoiding pronounced radiation damage of the samples.

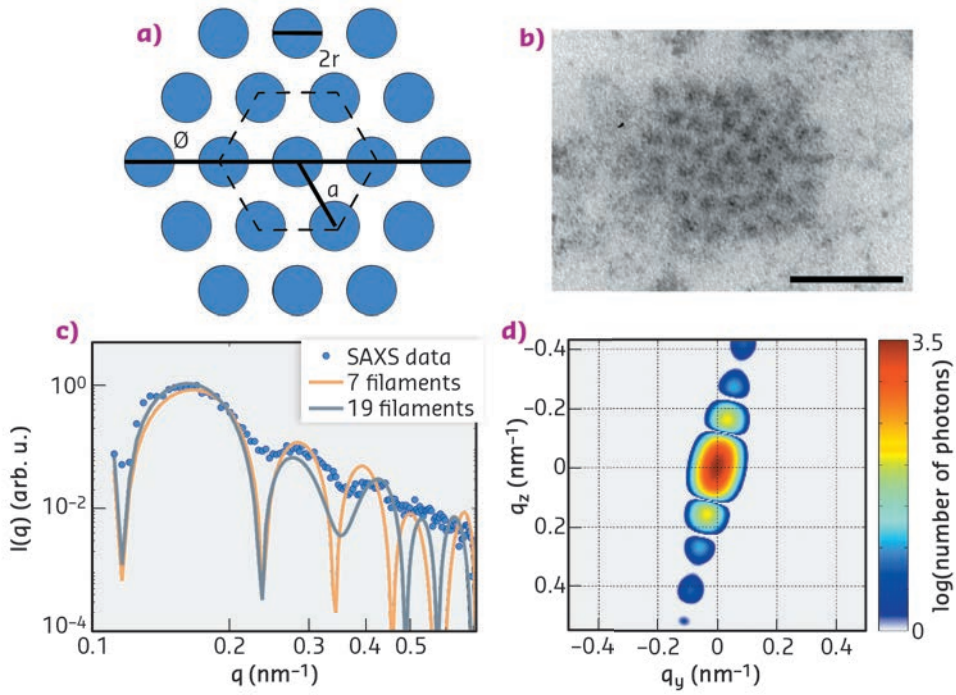

Fig. 33: a) Cross section of a model of the keratin bundles with 19 filaments per bundle. b) TEM image of the cross section of a keratin bundle in a hexagonal lattice, scale bar 50 nm. c) Radial intensity of the pattern shown in **Figure 32d** and results from the fit. d) 2D simulated pattern corresponding to the fit with 19 filaments in panel (c).

PRINCIPAL PUBLICATION AND AUTHORS

X-rays reveal the internal structure of keratin bundles in whole cells, C.Y.J. Hémonnot (a), J. Reinhardt (b), O. Saldanha (a), J. Patommel (c), R. Graceffa (a), B. Weinhausen (d), M. Burghammer (d,e), C.G. Schroer (b,f) and S. Köster (a), *ACS Nano* **10**, 3553-3561 (2016); doi: 10.1021/acsnano.5b07871.
(a) Institute for X-ray Physics, University of Göttingen (Germany)
(b) DESY, Hamburg (Germany)
(c) Institute of Structural Physics, TU Dresden (Germany)
(d) ESRF
(e) Department of Analytical Chemistry, Ghent University (Belgium)
(f) Institute for Nanostructure and Solid State Physics, University of Hamburg (Germany)

REFERENCES

[1] B. Weinhausen *et. al., New J. Phys.* **14**, 085013 (2012).
[2] B. Weinhausen *et. al., Phys. Rev. Lett.* **112**, 088102 (2014).
[3] V. Piazza *et al., ACS Nano* **8**, 12228-12237 (2014).
[4] F. Huber *et al., Curr. Opin. Cell Biol.* **32**, 39-47 (2015).
[5] M.P. Priebe *et. al., Biophys. J.* **107**, 2662-2673 (2014).
[6] J.-F. Nolting *et. al., Biophys. J.* **107**, 2693-2699 (2014).

A SUPERCONDUCTING DEVICE DRAWN BY FOCUSED X-RAYS WITHOUT ETCHING THE CRYSTAL

We describe the fabrication of a proof-of-concept Josephson device out of a single crystal of a superconducting oxide by means of X-rays nanoprobe irradiation. Our method patterns a superconducting device by selectively removing some of its atoms. This relies on a local change of electrical properties without disrupting the crystal structure and can probably be applied to oxides in general.

In the microelectronics rush towards smaller and faster circuits, the idea of establishing photolithographic processes based on X-rays to take advantage of their very small wavelength ($\lambda \lesssim 1$ nm) has already been explored, but the problems related to the fabrication of masks with the necessary contrast and small sizes have discouraged further efforts **[1]**. However, those approaches were based on the traditional scheme of light exposure and etching: a pattern is defined on some organic material, where the X-ray energy induces some difference in the chemical resistance to the developing solution, and then the pattern is transferred to the electronically active material by means of an etching process.

Nowadays, the appearance of oxide electronics is opening new possibilities. Indeed, the discovery of 2D electron liquids at some oxide/oxide interfaces or the fabrication of oxide-based memory cells are positioning oxide technology side by side with silicon technology. However, electrical properties of oxides are very sensitive to the presence of oxygen vacancies in the crystal lattice, and in principle this kind of vacancy can be directly induced by X-rays because of the small mass of oxygen atoms. It should therefore be possible to change the conducting/insulating properties of oxides locally by X-ray irradiation, with no need for mediating organic materials or etching processes. Following our recent encouraging results **[2]**, we tested this idea on the superconducting oxide $Bi_2Sr_2CaCu_2O_{8+\delta}$ (Bi-2212), whose typical critical temperature is $T_c \approx 80$-90 K.

Bi-2212 can be described as a stack of superconducting crystal planes containing Cu ions, intercalated by insulating planes containing Bi ions. There are two specific features corresponding to this crystal structure: i) the current senses much less resistance when flowing along the Cu planes compared to the normal direction, and ii) in the superconducting state, all of the Cu planes are coupled via the Josephson effect because of the thinness of the Bi insulating layers. Moreover, both the conducting and the superconducting properties depend very strongly on the content of O ions.

Therefore, we irradiated the Bi-2212 crystals with the 57 × 45 nm² probe at beamline **ID16B**, as shown in **Figure 34**, to pattern two "trench"

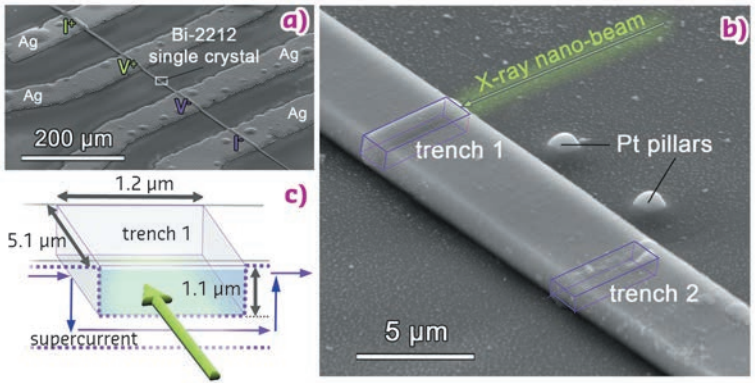

Fig. 34: a) Typical layout of the chip used for device writing. Current and voltage electrodes are labelled as I+, I–, V+ and V–. b) Irradiation geometry used at ID16B to pattern the device in the central part of the chip. Pt pillars are used for alignment purposes only. Superconducting Cu planes are parallel to the substrate. c) Sketch of trench 1, along with the supercurrent path induced by the trench. The green arrow represents the X-ray nanobeam.

regions by inducing non-superconducting properties locally. By displacing the "trenches" along the direction of the crystal thickness (trench 1: up, trench 2: down), we tried to force the current along the more difficult direction, *i.e.* normal to the Cu planes, obtaining a zig-zag path for the current. Experimental evidence of successful patterning is provided by **Figure 35a**, because the typical Josephson behaviour of these IV curves can be observed only if the current flows along the direction normal to the superconducting Cu planes. Direct SEM observation reveals that the material has not been removed from the "trench" regions (see **Figure 35b**), and that just some crystal expansion can be detected. Nano-XRD patterns measured in the "trench" regions have also shown that the Bi-2212 crystal structure is preserved, with the appearance of some Bi_2O_3 that could be compatible with oxygen loss from the crystals.

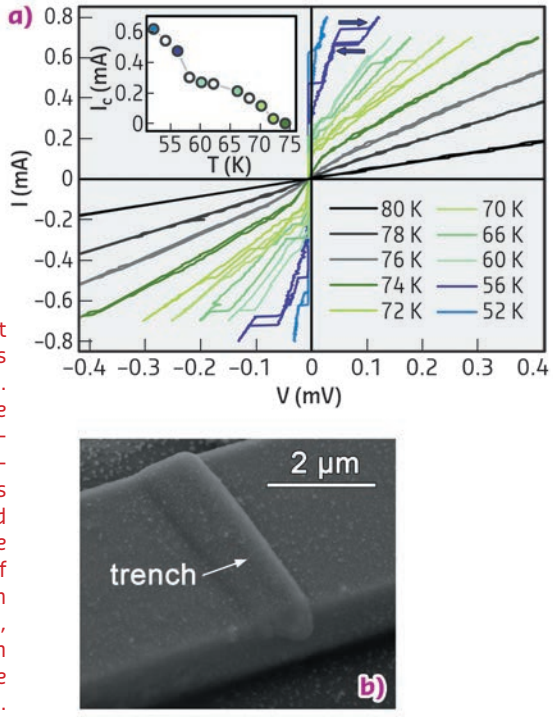

Fig. 35: a) IV curves at different temperatures for the patterned device. Violet arrows highlight the hysteresis between current-increasing and current-decreasing branches, as expected for underdamped Josephson junctions. The inset shows the increase of the critical current I_c with decreasing the temperature, typical of Josephson junctions. b) View of the sample around trench 1.

These results demonstrate a conceptually new patterning method for oxide electrical devices based on X-rays, with potential advantages in terms of heat dissipation, chemical contamination and high aspect ratio of the devices.

PRINCIPAL PUBLICATION AND AUTHORS

Direct-write X-ray nanopatterning: a proof of concept Josephson device on $Bi_2Sr_2CaCu_2O_{8+\delta}$ superconducting oxide, M. Truccato (a), A. Agostino (b), E. Borfecchia (b), L. Mino (c), E. Cara (a), A. Pagliero (a), N. Adhlakha (a), L. Pascale (b), L. Operti (b), E. Enrico, N. De Leo (c), M. Fretto (c), G. Martinez-Criado (d) and C. Lamberti (b,e), *Nano Lett.* **16**, 1669–1674 (2016); doi: 10.1021/acs.nanolett.5b04568.

(a) Department of Physics, Interdepartmental Centre NIS, University of Torino (Italy)
(b) Department of Chemistry, Interdepartmental Centre NIS and INSTM Centro di Riferimento, University of Torino (Italy)
(c) INRIM, National Institute for Metrological Research, Torino (Italy)
(d) ESRF
(e) Southern Federal University, Rostov-on-Don (Russia)

REFERENCES

[1] R.F. Pease and S.Y. Chou, *Proc. IEEE* **96**, 248 (2008).
[2] A. Pagliero *et al., Nano Lett.* **14**, 1583 (2014).

THE DISCOVERY OF METALLIC INK IN HERCULANEUM PAPYRI

Fragments of Herculaneum papyri were examined using a variety of X-ray techniques. The writing on the papyri contained a high concentration of lead, which pushes back the date of introduction of lead into inks by several centuries.

In 2015, thanks to the X-ray phase contrast technique available at the ESRF, we were able to decipher a few words and recover a complete Greek alphabet from inside a rolled-up papyrus that had been charred during the Mount Vesuvius eruption in 79 AD **[1]**.

Our study of Herculaneum papyri using synchrotron light has continued and we have focussed in particular on the materials composing the ink **[2]**. Our latest discovery changes our knowledge of writing in Antiquity and opens new prospects for the examination of these precious documents.

Pliny the Elder, naturalist and natural philosopher, who died during the Mount Vesuvius eruption, remarked that writing on some kind of support (*e.g.* papyrus) is essential to civilisation. A rigorous scientific study of writing is hence of fundamental importance for the understanding of ancient societies.

The collection of carbonised Herculaneum papyri, discovered between 1752 and 1754, represents the only complete library from Antiquity and, as such, it is a unique opportunity to understand the development of western civilisation.

In particular, it had been assumed that a carbon-based ink, described by Pliny the Elder in his Natural History, was used in Greek and Roman manuscripts and that metallic ink appears only around the fourth to fifth century AD. The ink used in Antiquity was obtained from the soot of wood burnt in furnaces without any deliberate addition of metals. Metallic ink before this period was employed only for writing secret messages in the second century BC whereas from around 420 AD a metallic iron-gall mixture was adopted as a new writing ink for parchments. Thereafter, metallic inks became the standard for parchments in late Antiquity and for most of the Middle Age.

Multi-scale X-ray fluorescence (XRF) micro-imaging at beamline **ID21** demonstrated that the ink in the fragment samples exhibits a fairly high concentration of lead. In particular, it resolved the elemental composition of both ink and papyrus (**Figure 36**). The fragments were scanned using X-ray beams of different sizes: from the sub-millimetre down to the micrometric scale. These studies were complemented by X-ray diffraction mapping at **ID11** and X-ray absorption near edge structure at **BM26**.

Figure 37 presents a fluorescence map that highlights letters in the larger sample. This means that, for Herculaneum fragments that are difficult to read, the use of spectrometric techniques sensitive to lead may render the writing more clearly. Using an iterative Monte Carlo simulation, the concentration of lead in the letters has been estimated to be as much as 84 ± 5 μg/cm^2, a quite high concentration that cannot be simply attributed to lead contamination of water from Roman aqueducts, or from an inkwell. The most plausible explanation of this high concentration is that a lead-bearing material was intentionally introduced during the ink production process.

Fig. 36: X-ray fluorescence micro-imaging technique reveals the lead contained in the ink.

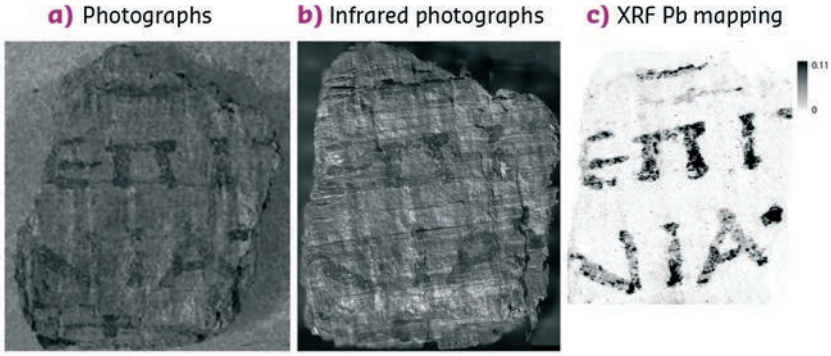

Fig. 37: Comparison of visible light photograph (a), infrared microscopy image (b) and lead distribution map obtained by X-ray fluorescence (c). The XRF map was normalised by the incident flux, in arbitrary units.

The concentrations of metal found in the ink will aid the optimisation of future tomographic experiments on undisclosed Herculaneum scrolls. More extensive research using many fragments from Herculaneum should be performed to assess the extent of lead present in the inks in Antiquity.

PRINCIPAL PUBLICATION AND AUTHORS

Revealing metallic ink in Herculaneum papyri, E. Brun (a,b), M. Cotte (c,d), J. Wright (c), M. Ruat (c), P. Tack (e), L. Vincze (e), C. Ferrero (c), D. Delattre (f) and V. Mocella (g), *PNAS* **113**, 3753 (2016); doi: 10.1073/pnas.1519958113.
(a) Inserm, U836, Grenoble (France)
(b) Université Joseph Fourier, Grenoble Institut des Neurosciences, UMR-S836 (France)
(c) ESRF
(d) LAMS (Laboratoire d'Archéologie Moléculaire et Structurale), CNRS-UPMC, UMR 8220, Paris (France)
(e) Department of Analytical Chemistry, Ghent University (Belgium)
(f) CNRS-IRHT-Institut de Recherche et d'Histoire des Textes, Paris (France)
(g) CNR-IMM-Istituto per la Microelettronica e Microsistemi-Unità di Napoli (Italy)

REFERENCES

[1] V. Mocella *et al., Nat. Commun.* **6**, 5895 (2015).
[2] P. Tack *et al., Scientific Reports* **6**, 20763 (2016).

AN INDIVIDUAL STRAINED GERMANIUM NANOWIRE PROBED USING A NANOFOCUSED X-RAY BEAM

Low dimensional systems such as nanowires attract significant attention for the development of brighter and more efficient light sources in the infra-red wavelength regime. Researchers are investigating their new opto-electronic properties and trying to control them with miniaturised functional devices.

In this work, the lattice plane spacings of individual nanometre sized objects were measured with outstanding precision using synchrotron based X-ray diffraction. Scanning X-ray diffraction (SXRD) microscopy can provide local resolution along the length of these objects, allowing minute changes in strain to be tracked within single nanowires. The wires were grown into a supporting structure between a rigid mesa and a flexible cantilever, as depicted in **Figure 38a,b**. An oxidation step during sample fabrication allowed the wire to be strained uniaxially by applying a bending force on the cantilever during wire growth, in combination with controlled relaxation afterwards **[1,2]**. While strain-induced changes of the lattice vibrations were probed using μ-Raman analysis, the underlying strain state was investigated using high-resolution XRD at beamline **ID01**.

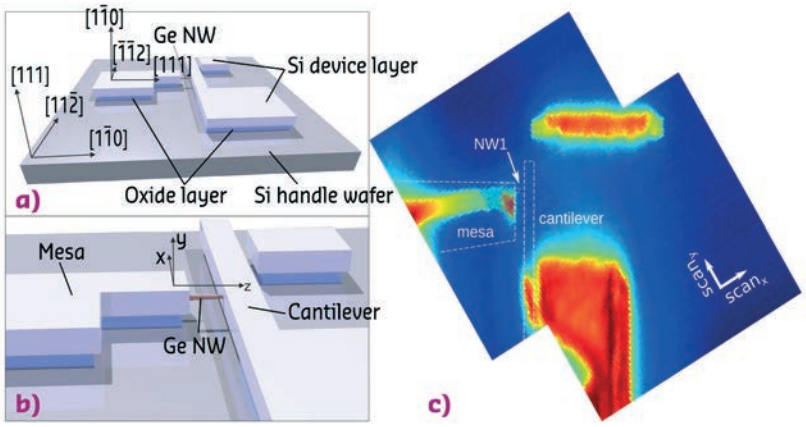

Fig. 38: Sample sketch overview (a) and close-up (b). c) Resulting real-space map of SXRD microscopy at the Si and Ge (2$\bar{2}$0) Bragg reflections. The cantilever and parts of the mesa (white dashed lines) are not visible, *i.e.* not in Bragg condition due to their torsion and bending.

To illuminate only a certain part of a single wire, a beam focused down to 250 nm was used. Due to the sample geometry, XRD data around the (2$\bar{2}$0) Bragg spot yields the strain values directly in the direction perpendicular to the wire growth axis (see **Figure 38**). Finite element method (FEM) calculations were used to estimate the strain in the axial direction. From the diffraction data, the diameter of the crystalline wire core was determined, while scanning electron microscopy data gave the total diameter including a partially-oxidised amorphous Ge shell. Both geometric parameters were used in the FEM model.

Due to the tapering of the nanowires, *i.e.*, a smaller diameter at the top compared to the bottom, the strain concentrates in the wire tip, as shown in **Figure 39a-c**. For the axial strain component, very significant values up to ε_{zz} = 1.13% have been detected, and a strain gradient was found. Laterally, the wires exhibit a small bend due to shear strains induced by the device geometry (slight twisting of the cantilever due to inhomogeneous oxidation and non-symmetrical growth of the nanowire in the gap). The amorphous shell gives rise to additional stiffening, so that overall a rather complex strain state within a single nanowire is reached.

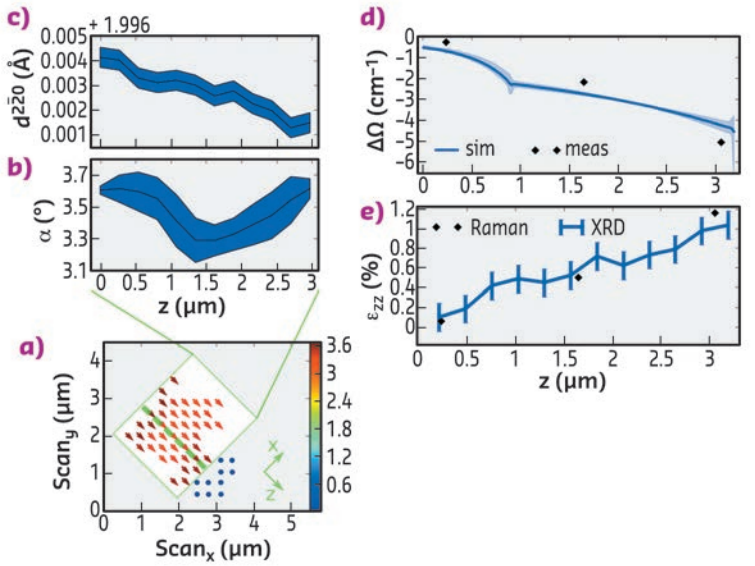

Fig. 39: a) Tilt and bending map of a nanowire, calculated from all Bragg peak positions with respect to the crystallite's Bragg peak (blue dots with 0°), at different real-space positions. The arrows indicate the direction, while the bending values are colour coded. For illustration, the green dashed line indicates the position of the nanowire. Line plots of the measured bending distribution α and the lattice plane spacing $d^{(2\bar{2}0)}$ along the nanowire growth axis are shown in (b) and (c), respectively. The blue area represents the measurement error in graph (c). However, in graph (b) the blue area reflects the lattice bending and the Bragg peak broadening due to the finite divergence of the focused beam. Comparison of the Raman simulation (blue) and the measured Raman shift (black diamonds) for the same wire (d). The blue areas show the minimum and maximum strain values from the radial strain variation within the nanowire. e) Corresponding strain ε_{zz} for the assumption of a uniaxial applied strain and a bulk Poisson ratio, calculated from Raman data (black diamonds) together with the XRD data (blue).

From the strain tensor obtained by the XRD/FEM analysis, the expected Raman peak shifts are calculated as a function of position along the nanowire, as shown in **Figure 39d,e**. They reproduce the experimentally obtained Raman shifts very well. Assuming a uniaxial strain state in the wire (which is not perfectly true but a very good approximation, considering principal and shear strain components from the XRD/FEM results), a linear strain shift coefficient of k = 434 cm between Raman response and the axial strain component, $\Delta\Omega \cong k\varepsilon_{zz}$, is found, in good agreement with bulk literature values **[3]**, indicating that the elastic response of the Ge nanowires is very much bulk-like even at such considerable levels of strain.

In summary, XRD/FEM results are corroborated by a μ-Raman analysis using a linear relationship between uniaxial strain and line shift of single Ge nanowires. Moreover, they allow additional insight to be obtained into the full strain state of the nanowires thanks to a nanofocused X-ray beam.

PRINCIPAL PUBLICATION AND AUTHORS

Strain distribution in single, suspended germanium nanowires studied using nanofocused X-rays, M. Keplinger (a), R. Grifone (a,b,c), J. Greil (d,e), D. Kriegner (a,f), J. Persson (g,h), A. Lugstein (d), T. Schülli (b) and J. Stangl (a), *Nanotechnology* **27**, 055705 (2016); doi: 10.1088/0957-4484/27/5/055705.
(a) Institut für Halbleiter- und Festkörperphysik, Johannes Kepler Universität Linz (Austria)
(b) ESRF
(c) DESY-Photon Science, Deutsches Electronen-Synchrotron, Hamburg (Germany)
(d) Institute of Solid State Electronics, Vienna University of Technology (Austria)
(e) Department of Applied Physics, Eindhoven University of Technology (Netherlands)
(f) Faculty of Mathematics and Physics, Charles University, Prague (Czech Republic)
(g) Center for Electron Nanoscopy, Technical University of Denmark, Lyngby (Denmark)
(h) Gemeinschaftslabor für Elektronenmikroskopie, RWTH Aachen (Germany)

REFERENCES

[1] A. Lugstein *et al.*, *Nano Letters* **10**, 3204–3208 (2010).
[2] J. Greil *et al.*, *Nano Letters* **12**, 6230–6234 (2012).
[3] F. Cerdeira *et al.*, *Phys. Rev. B* **5**, 580–593 (1972).

DIRECT VIEW OF SELF HEALING IN Fe-Au ALLOYS BY X-RAY NANOTOMOGRAPHY

Self healing is a promising new approach to prolong the lifetime of steels exposed to high temperatures and stress for long time periods. Under these conditions, damage accumulates by creep cavities that continuously form at grain boundaries. X-ray nanotomography demonstrates that, for Fe-Au model alloys, efficient damage healing can be achieved by autonomous gold precipitation inside the cavities.

Steels are among the most widely-used construction materials due to their excellent and tuneable mechanical properties. However, when exposed to high temperatures for long time periods, steel components can exhibit premature creep fracture, which arises from the formation, growth and coalescence of creep cavities located at grain boundaries. In the self-healing steels we have developed, the enhanced creep lifetime originates from the precipitation of solid matter at the cavity surface, which prevents further growth of the creep damage. We recently demonstrated that efficient self healing of creep damage can indeed be achieved in a model system for such steels, the binary Fe-Au (1 at.% Au) alloy **[1,2]**, as solute gold atoms show a strong tendency to form precipitates inside the creep cavities. To obtain a detailed view of the damage healing by site-specific gold precipitation inside the creep cavities (with a size of about 1 μm), the use of a 3D characterisation tool with a nanoscale resolution is essential.

We have performed synchrotron X-ray nano-imaging on creep-failed samples at beamline **ID16A**. The creep tests were carried out on homogenised samples at selected constant stress levels and at a temperature of 550°C. In the nano-imaging experiments, the X-ray beam energy of 33.6 keV made it possible to monitor the internal (nano-)structure of bar-shaped samples with a thickness of 200 μm in transmission. The high instrumental resolution with voxel sizes of 25 and 100 nm allowed us to successfully identify the open nanoscale cavities and gold precipitates within the alloy matrix. Both the open space of the cavities and the gold precipitates provided strong contrast in electron density.

Figure 40 reveals the spatial distribution of the cavities and precipitates extracted from the creep-failed sample (tested at a constant stress of 80 MPa and a temperature of 550°C). As best observed in top view, the positions of the

precipitates clearly mark the grain boundaries. With the grain-boundary positions identified, it was found that most of the cavities are indeed located on the grain boundaries. **Figure 40** also reveals that the gold particles have distinctly different shapes: particles within the matrix are mainly spherical or equiaxed, particles on the inclined grain boundaries are more elongated or flattened, while particles located on the grain junctions have a relatively complicated shape.

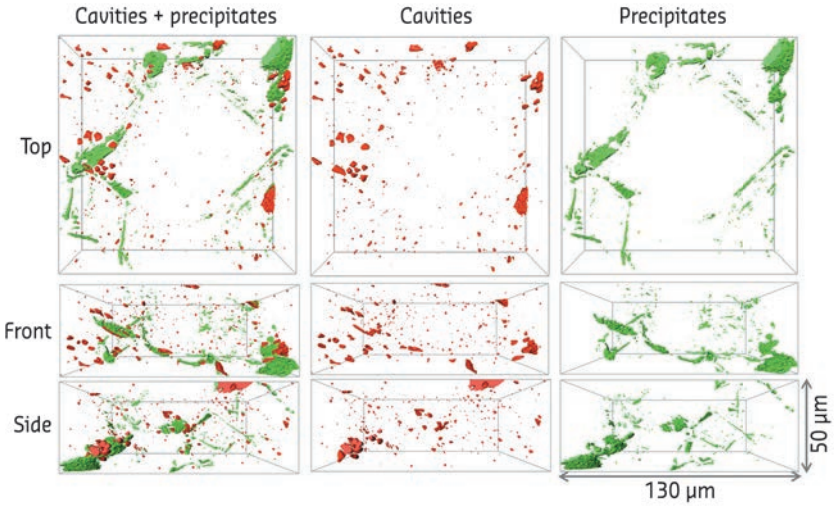

Fig. 40: Tomographic image of the microstructure in the Fe-Au alloy after creep failure (at 550°C and a stress of 80 MPa), identifying the presence of creep cavities (in red) and gold precipitates (in green). The stress is applied in the vertical direction.

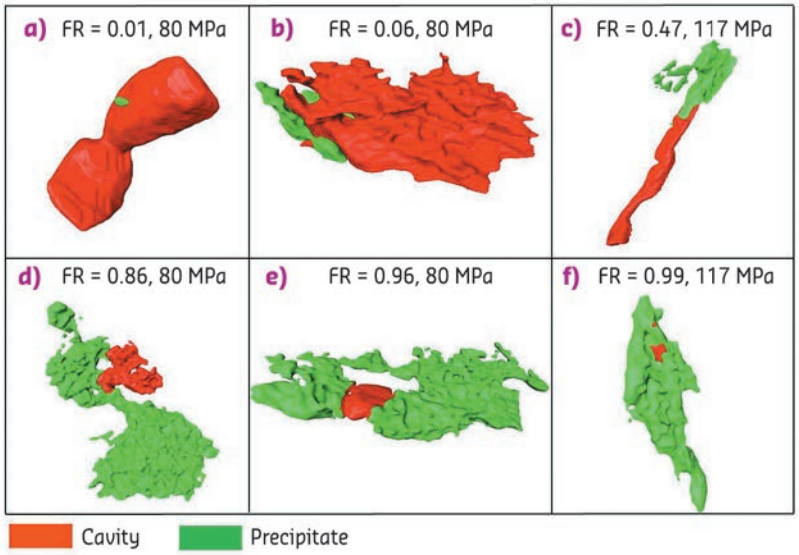

Figure 41 shows several examples of partially filled creep cavities produced at different stress levels. The observed structures indicate that the filling process generally starts from one location and develops until the cavity is completely filled. When the precipitation is induced soon after nucleation of the cavity, the rapid filling stops further cavity growth, which results in a high filling ratio (FR). Note that unfilled cavities correspond to FR = 0, completely filled cavities to FR = 1 and partially filled cavities to 0 < FR < 1. **Figure 41c** shows a rod-like cavity that is nearly half filled by the precipitate from one side. In **Figure 41f** an open cavity has nearly been fully encapsulated. This demonstrates that the precipitate is filling the cavity rather than inducing the formation of the cavity.

We have analysed the filling ratio for more than 10,000 individual creep cavities per sample, which allowed us to understand the evolution of the creep cavities. After cavity nucleation at a size of about 50 nm, the cavities start to grow. When there is a free surface available, gold precipitation starts to fill the growing cavities. The cavity growth and the faster filling by precipitation continues in most cases until the cavity is completely filled. However, when two neighbouring partly-filled cavities connect, then the combined cavities grow faster and it is found that complete filling can no longer be achieved.

X-ray nanotomography has proven to be an excellent technique to characterise the self-healing mechanism for creep damage in iron-based alloys. The unique resolution makes it possible to monitor the broad variation in volume, shape and orientation of nanoscale creep cavities and the gold precipitation within these cavities. This insight is an essential step in the transition from model alloys to real multi-component creep steels with superior life time.

Fig. 41: Experimental creep cavities (in red) with varying degrees of filling with gold precipitates (in green). Indicated is the filling ratio (FR) and the stress level during the creep tests at a temperature of 550°C.

PRINCIPAL PUBLICATION AND AUTHORS

Autonomous filling of creep cavities in Fe-Au alloys studied by synchrotron X-ray nano-tomography, H. Fang (a), C.D. Versteylen (a), S. Zhang (a), Y. Yang (b), P. Cloetens (b), D. Ngan-Tillard (a), E. Brück (a), S. van der Zwaag (a) and N.H. van Dijk (a), *Acta Materialia* **121**, 352-364 (2016); doi: 10.1016/j.actamat.2016.09.023.

(a) Delft University of Technology, Delft (The Netherlands)
(b) ESRF

REFERENCES

[1] S. Zhang *et al., Adv. Eng. Mater.* **17**, 598-603 (2015).
[2] S. Zhang *et al., Metall. Mater. Trans. A* **46**, 5656-5670 (2015).

MELANOSOMES IN PIGMENTED EPITHELIA MAINTAIN EYE LENS TRANSPARENCY DURING ZEBRAFISH EMBRYONIC DEVELOPMENT

Altered levels of trace elements are associated with increased oxidative stress eventually responsible for pathologic conditions, including cataracts. The distribution of elements in the eye of zebrafish embryos were visualised by micro X-ray fluorescence imaging. Eye melanosomes were found to protect the lens from oxidative stress by buffering trace elements.

Trace elements are essential for normal development and physiology of the organism. These elements are found at the core of functional domains of enzymes in nearly all biological pathways. The presence of metal ion transporters with diverse metal affinities and their specific subcellular localisation indicate that each metal needs to be actively transported into proper intracellular compartments. Indeed, mutations in these transporters lead to various medical conditions, including cataracts. To directly visualise sub-cellular element distributions in biological tissues, hard X-ray fluorescence microscopy (μ-XRF) provides unique information. The subcellular distribution of many different elements can be traced quantitatively with a 100-300 nm resolution and over a dynamic range of more than 10,000 fold. At beamline ID22NI (now **ID16A**), we studied zebrafish as a model organism due to its distinct advantages over other species. It develops rapidly, requiring only 24 hours after fertilisation to form the brain, the heart and the eye.

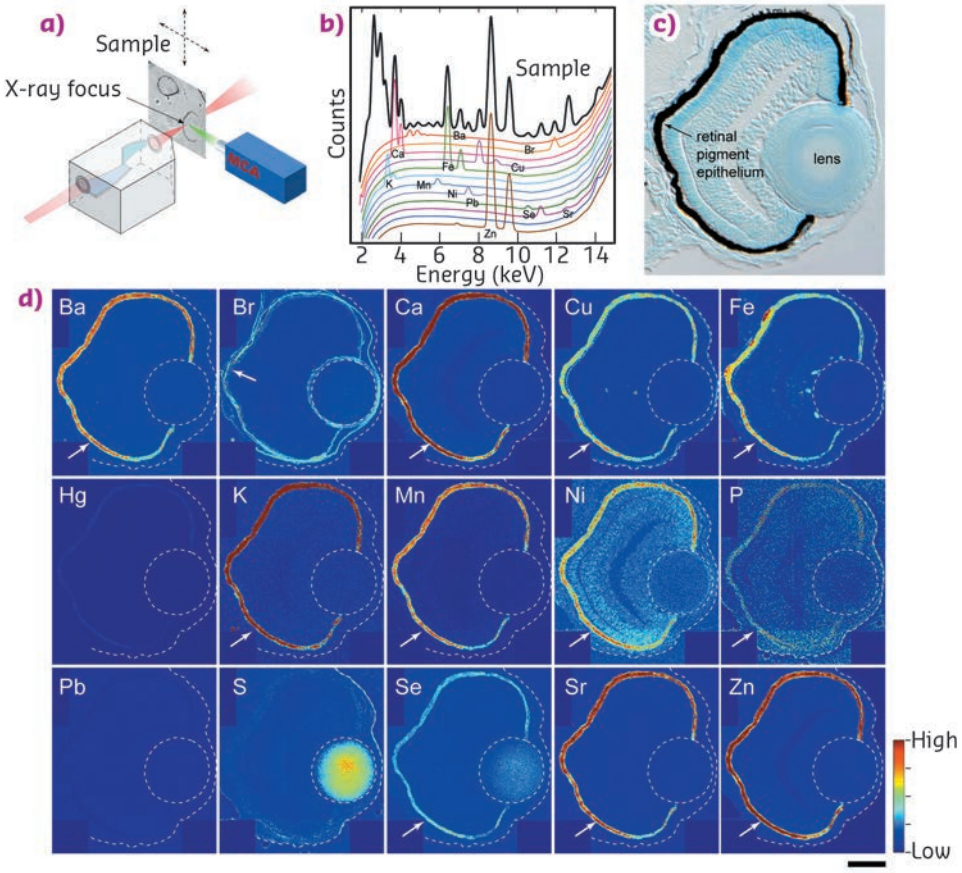

Fig. 42: a) Illustration of μ-XRF imaging setup. b) An example of a fluorescence spectrum. Elements emit X-rays at energies that are characteristic of the given element. c) Transverse 10 μm thick section of 3-day stage zebrafish eye. d) Localisation of elements in the eye. Arrows indicate pigment epithelium. Scale bar in (d): 30 μm.

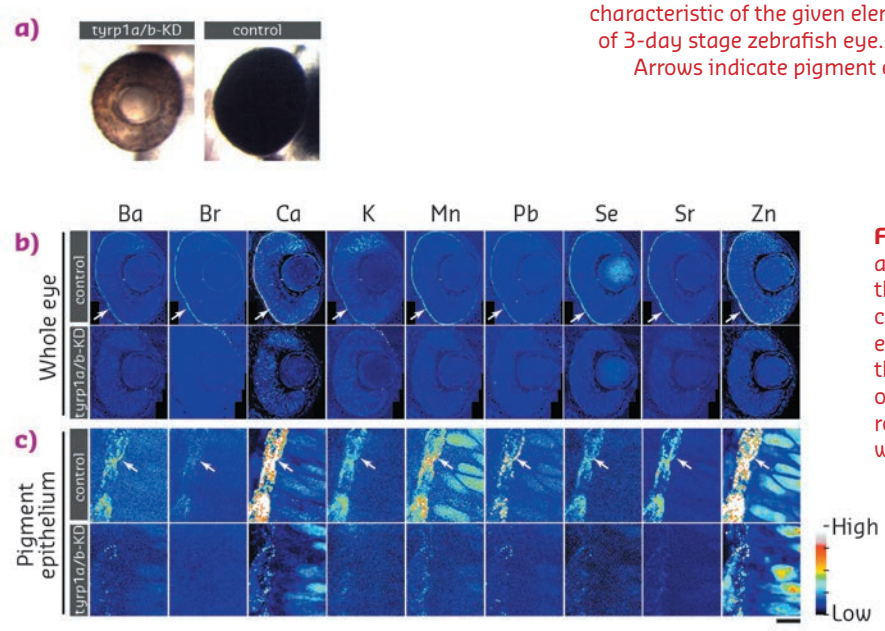

Fig. 43: a) Knockdown of *tyrp1a/b* results in the absence of mature melanosomes that produce the brown colour of the pigment epithelium, while control embryos form mature black pigment epithelium. b) Distribution of inorganic elements in the eye of embryos of control (*control*, upper row) or *tyrp1a/b*-knockdown group (*tyrp1a/b-KD*, lower row). c) Higher resolution images were scanned with a 100 nm step size.

Its small size allowed us to scan the whole eye to map trace element distribution. It also enabled us to examine the consequences of genetic mutations or gene knockdowns.

We examined the distribution of 15 elements in the eye. Many elements showed highest accumulation in the retinal pigment epithelium of the zebrafish embryo (**Figure 42**). To examine whether melanosomes are responsible for the observed enrichment of elements in the pigment epithelial layer, we analysed the distribution of these elements after knockdown of pigment genes (*tyrp1a/b*) that causes premature brown pigment formation. Knockdown of these zebrafish genes eliminated accumulation of the 15 elements in the pigment epithelium, indicating that they are bound by mature black melanosomes (**Figure 43**). Furthermore, albino (*slc45a2*) zebrafish mutants, which completely lack pigment melanosomes, developed abnormal lens reflections similar to the congenital cataract lens. An independent assay to estimate the level of oxidative stress in the tissue revealed increased oxidative stress in the lens of *albino* mutants. Based on these observations, we hypothesised that defective metal accumulation in the pigment epithelium may increase the risk of cataract formation. To test this idea, we transplanted wildtype lenses into albino mutants with no pigments. We confirmed the cataract formation of the wildtype lens inside pigment-free albino embryos. In conclusion, the results suggest that melanosomes in pigment epithelial cells protect the lens from oxidative stress during embryonic development, likely by buffering trace elements.

PRINCIPAL PUBLICATION AND AUTHORS

Melanosomes in pigmented epithelia maintain eye lens transparency during zebrafish embryonic development, M. Takamiya (a), F. Xu (b), H. Suhonen (c,e), V. Gourain (a), L. Yang (a), N. Yu Ho (a), L. Helfen (b,c) A. Schröck (a), C. Etard (a), C. Grabher (a), S. Rastegar (a), G. Schlunck (d), T. Reinhard (d), T. Baumbach (b) and U. Strähle (a), *Scientific Reports* **6**, 25046 (2016); doi: 10.1038/srep25046.
(a) Institute of Toxicology and Genetics, Karlsruhe Institute of Technology (KIT) (Germany)
(b) Institute for Photon Science and Synchrotron Radiation (IPS), Karlsruhe Institute of Technology (KIT) (Germany)
(c) ESRF
(d) Eye Center, Freiburg University Medical Center (Germany)
(e) Current address: University of Helsinki, Department of Physics (Finland)

THE INTRACELLULAR DISSOLUTION OF SILVER NANOPARTICLES REVEALS THE MECHANISM OF THEIR TOXICITY

Despite their toxicity to eukaryotic cells, silver nanoparticles are included in commercial products for their biocide activity through silver ion release. Silver nanoparticles intracellular dissolution was visualised and measured in hepatocytes, and the complexes formed by silver ions in cellulo were investigated.

Silver nanoparticles (AgNPs) are extensively used in healthcare products, fabrics, and food packaging for their antibacterial properties. Humans are therefore exposed to AgNPs, and the toxicity of AgNPs to eukaryotic cells is today a matter of concern. AgNPs can enter eukaryotic cells and the toxic effects they exert are most probably a consequence of Ag^+ release from the AgNPs surface *in cellulo*. However, quantitative information concerning AgNP intracellular dissolution is missing and the mechanisms triggered by Ag^+ poisoning are still debated. Dissolution rates in vitro depend on a variety of parameters such as particle size and coating, or pH and chemical composition of the medium.

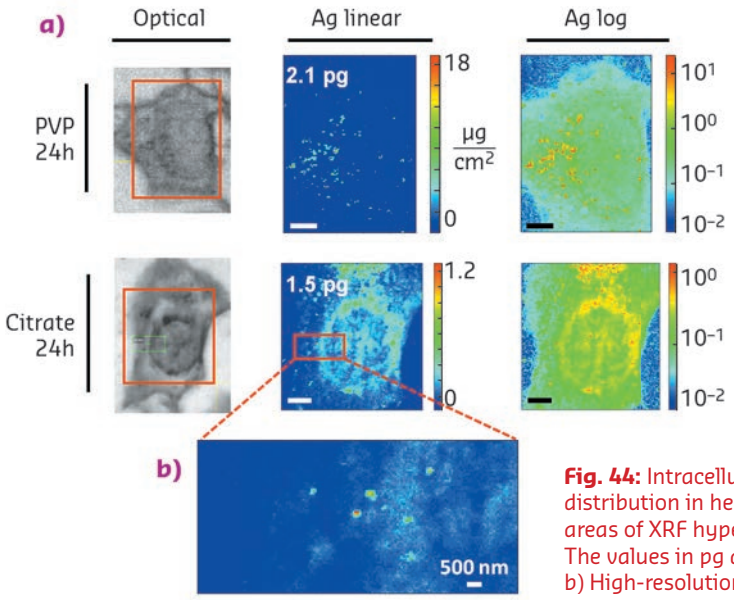

Fig. 44: Intracellular dissolution of AgNPs visualised by XRF imaging. a) Silver distribution in hepatocytes exposed to PVP- or citrate-coated AgNPs for 24 h. The areas of XRF hyperspectral images are highlighted in red over the optical micrographs. The values in pg are the total amounts of Ag in the map areas. Scale bars = 5 µm. b) High-resolution silver distribution in the area highlighted in panel (a).

Although predicting the transformations that occur in complex biological systems is extremely challenging, it is pivotal in view of the design of safer NPs.

This study made use of the high-resolution X-ray fluorescence (XRF) imaging capabilities of beamline **ID16B** to map silver distribution in individual hepatocytes (HepG2 cells) exposed to AgNPs, with the aim of measuring the metal content as a function of the exposure time and to highlight the influence of particle coating on intracellular dissolution. We studied AgNPs with coatings polyvinylpyrrolidone (PVP) and citrate, which are commonly used in industrial AgNP formulations. **Figure 44a** shows silver distribution in hepatocytes exposed for 24 hours to AgNPs. Citrate-coated AgNPs dissolve more than the PVP-coated AgNPs at equal exposure time, although the total silver uptake is similar for the two formulations; this explains the higher toxicity of the citrate-coated NPs. High-resolution (70×70 nm²) XRF maps (**Figure 44b**) allow the visualisation of Ag hotspots of a few hundreds of nm in size, which correspond to endocytic vesicles containing NPs (as confirmed by TEM observations), whereas the weaker signal diffused throughout the cell corresponds to Ag^+ species. The ionic component is not detected in TEM, but only in the nanoprobe, thanks to its attogram sensitivity.

The fate of the Ag^+ ions needs to be unravelled to obtain a deeper insight into the toxicity mechanisms. We have previously shown that Ag K-edge X-ray absorption spectroscopy (XAS) under cryogenic conditions can be used to measure the average dissolution of AgNPs in cultured cells, and to disclose the complexes formed in cellulo by the released ions **[1]**. The XANES spectra of hepatocytes exposed to AgNPs (**Figure 45a**), collected at beamline **BM30B** (FAME CRG), reveal that, after 24 h exposure, citrate-coated AgNPs released ~50% of their atomic content, while PVP-coated released only ~30%, confirming single-cell XRF observations. In both cases Ag^+ is found to form complexes with thiolate ($R\text{-}S^-$).

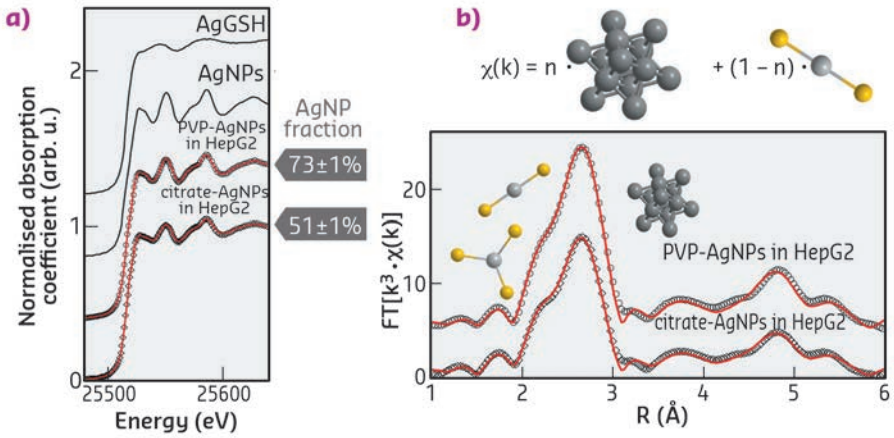

Fig. 45: Ag K-edge (a) XANES and (b) EXAFS spectra of hepatocytes exposed to AgNPs for 24 h. Open symbols represent experimental data, red traces are best fit curves. XANES data (a) are fitted as linear combinations of reference compounds (black lines), EXAFS with the *ab initio* model depicted in (b).

The binding properties of Ag^+ are similar to those of Cu^+, a physiological metal that preferentially binds to thiolates *in vivo*. Ag^+ can therefore replace Cu^+ in its native protein binding sites and induce the impairment of metal homeostasis. The *ab initio* analysis of Ag K-edge EXAFS spectra (**Figure 45b**) reveals the coordination chemistry of Ag^+ in the Ag-thiolate complexes formed upon AgNP intravesicular dissolution. A coexistence of digonal AgS_2 and trigonal AgS_3 complexes is found, with an average Ag-S distance of 2.45 Å.

According to a previous study on the complexes formed by Ag^+ with biomolecules involved in Cu homeostasis **[2]**, the AgS_2 and AgS_3 complexes found in hepatocytes are most likely silver-glutathione and silver-metallothionein, respectively. An important overexpression of the genes of the metallothionein and of the enzyme involved in glutathione synthesis was observed in cells exposed to AgNPs, confirming that these two biomolecules are the major chelators of free intracellular Ag^+.

The single-cell elemental information obtained through nano-XRF imaging combined with the averaged chemical information provided by XAS has revealed the transformations of metallic nanoparticles in a cellular model, and brought novel insight into the toxicity mechanisms.

PRINCIPAL PUBLICATION AND AUTHORS

Visualization, quantification and coordination of Ag^+ ions released from silver nanoparticles in hepatocytes, G. Veronesi (a,b), A. Deniaud (a), T. Gallon (a), P.-H. Jouneau (c), J. Villanova (b), P. Delangle (d), M. Carrière (d), I. Kieffer (e), P. Charbonnier (a) and E. Mintz (a), I. Michaud-Soret (a), *Nanoscale* **8**, 17012-17021 (2016). doi: 10.1039/c6nr04381j.
(a) CNRS/CEA/UGA LCBM, Grenoble (France)
(b) ESRF
(c) CEA/UGA INAC/MEM, Grenoble (France)
(d) CEA/UGA/CNRS, INAC/SyMMES/CIBEST, Grenoble (France)
(e) BM30B/FAME, ESRF, Grenoble (France)

REFERENCES

[1] G. Veronesi *et al., Nanoscale* **7**, 7323-7330 (2015).
[2] G. Veronesi *et al., Inorg. Chem.* **54**, 11688-11696 (2015).

PEROVSKITE SOLAR CELLS UNDER THE nXRD MICROSCOPE

A new technique based on scanning nanofocus X-ray diffraction paves the way for a better understanding of the links between crystal structure and morphology of the perovskite photo-active layer employed in third-generation solar cells.

At present, non-concentrator crystalline silicon technology dominates the photovoltaic (PV) industry with 25% record efficiency. In the past two decades, several next generation photovoltaic technologies have tried to compete with the silicon PV or attempted to occupy a position in niche PV markets. These technologies rely on photoactive materials that can be two orders of magnitude thinner than crystalline silicon, they can be printed or sprayed on flexible substrates using inexpensive methods, and some of them are as abundant as silicon. The first perovskite solar cell (PSC) was fabricated in 2009 and since then organic-inorganic hybrid PSCs have shown impressive progress, with record solar cells now achieving an astonishing certified 22.1% power conversion efficiency (PCE) [1]. This suggests that perovskites could be able to eventually replace standard crystalline silicon solar cells.

Fine control over the morphology and the crystallinity of thin film perovskites is vital to further improving the PCE. We have developed a technique based on a highly-focussed synchrotron X-ray beam to simultaneously probe the morphology and the structural properties of spin-coated mixed lead halide perovskite films for photovoltaic devices.

So far, the most widely employed techniques to investigate the crystal structure and

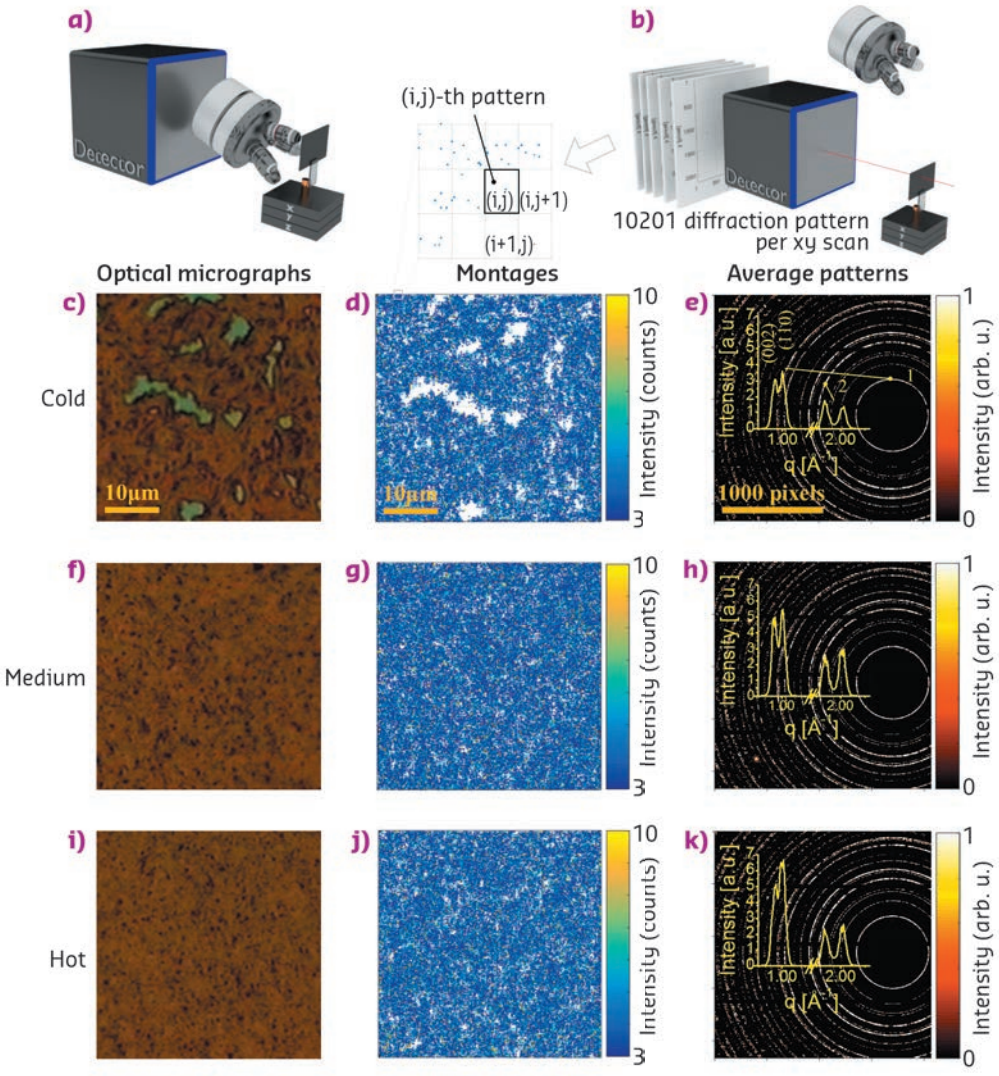

Fig. 46: Summary of measurements performed with scanning nanofocus XRD (nXRD) on perovskite films spin-coated with the substrate held at different temperatures: cold (room temperature), medium (~75°C), and hot (~90°C). a) nXRD scan area selection with the optical microscope. b) Setup during nXRD measurements. c, f, i) 40 × 40 μm² optical micrographs acquired before the scan on the scan area for the cold, medium, and hot samples. d, g, j) 40 × 40 μm² nXRD montages for the cold, medium, and hot sample. e, h, k) Average diffraction patterns recorded from the cold, medium, and hot sample (from doi: 10.1002/adfm.201603446).

morphology of perovskite films have been scanning microscopy and X-ray diffraction (XRD) techniques. With scanning microscopy methods such as scanning electron microscopy (SEM), distinguishing and isolating single perovskite crystallites in a 'messy' polycrystalline film is a difficult task. A further limitation is that these techniques are surface-sensitive, with the bulk of the material being essentially inaccessible. Synchrotron XRD methods such as grazing-incidence small- and wide-angle scattering (GI-WAXS and GI-SAXS) have been effectively employed to follow the structural evolution of perovskite films **[2]**. But in this case, typical X-ray beam sizes of hundreds of micrometres illuminate a large film area, and were therefore not small enough to examine the variation in the structural properties of the perovskite material across the sample.

We overcame these limitations by employing a highly-focussed synchrotron X-ray beam at beamline **ID13**. We were able to raster scan an X-ray 'nanobeam' across a sample, and thus combine real-space imaging with sub-nanoscale structural information from XRD (see **Figure 46**). This allowed single perovskite grains buried within a complex, polycrystalline film to be selectively isolated and structurally characterised (see **Figure 47**).

With nXRD, we were able to perform grain segmentation and extract the lateral size, strain and orientation of individual perovskite platelets. The technique was employed to determine information such as surface coverage and grain statistics from perovskite films that were spin-coated on substrates, held at different temperatures and subsequently employed in the fabrication of high performance solar cells. Films coated on substrates held at relatively high temperatures were found to have a lower density of pinholes and larger grain size.

This technique could be used to characterise a range of new perovskite materials and develop detailed models that relate their complex nano-morphology to their optical and electronic properties. We are already looking forward to future experiments at ID13 in the attempt to combine nXRD with *in situ* growth and crystallisation processes in real-time.

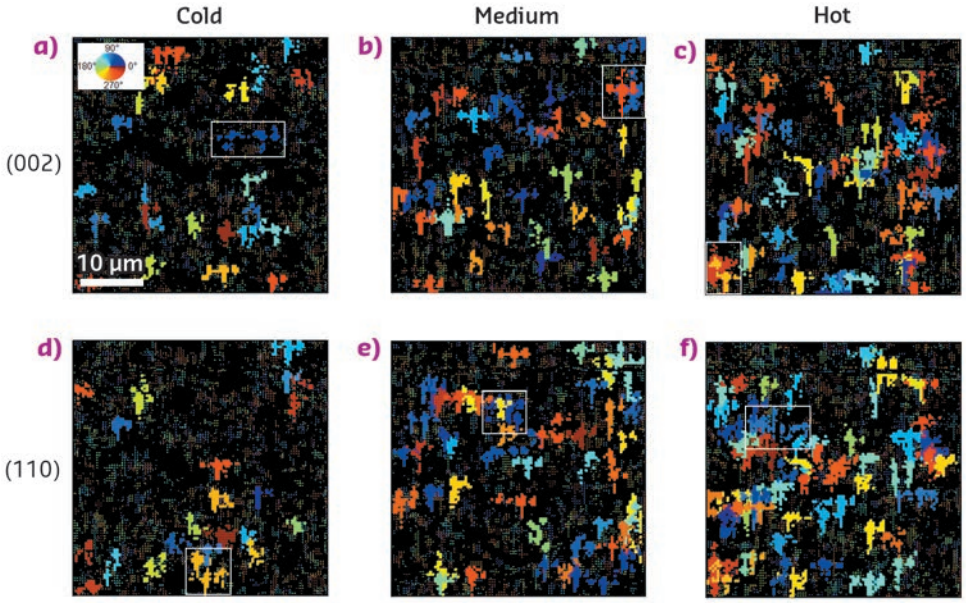

Fig. 47: 40 × 40 µm² quiver plots highlighting (002) and (110) perovskite grains larger than 4 µm². In a quiver plot, the value of one or more (002) or (110) diffraction spot peak angle (χ_p) is represented using an arrow with its centre located in the spatial position where the diffraction spot was acquired, and with an orientation and colour corresponding to χ_p. As the plots are resized for visualisation purposes, the arrows appear as single pixels. Clusters of pixels having the same colour represent single grains having the same orientation χ_p. The white boxes indicate the largest grains. Grains with different χ orientations are coloured in a different way according to the colourmap shown in inset in (a)
(from doi: 10.1002/adfm.201603446).

PRINCIPAL PUBLICATION AND AUTHORS

Mapping morphological and structural properties of lead halide perovskites by scanning nanofocus XRD, S. Lilliu (a), T.G. Dane (b), M. Alsari (c), J. Griffin (a), A.T. Barrows (a), M.S. Dahlem (d), R.H. Friend (c), D.G. Lidzey (a) and J.E. Macdonald (e), *Advanced Functional Materials* (2016); doi: 10.1002/adfm.201603446.

(a) Department of Physics and Astronomy, University of Sheffield (UK)
(b) ESRF
(c) Cavendish Laboratory, University of Cambridge (UK)
(d) Masdar Institute of Science and Technology, Abu Dhabi (UAE)
(e) Cardiff University (UK)

REFERENCES

[1] NREL. Efficiency Chart, http://www.nrel.gov/ncpv, accessed 8 Oct 2016.
[2] A.T. Barrows *et al.*, *Advanced Functional Materials* **26**, 4934-4942 (2016); doi: 10.1002/adfm.201601309.

ANGULAR ABSORPTION DEPENDENCE AT THE CALCIUM K-EDGE REVEALS BONE MINERAL ORIENTATION

A fast and straightforward method to map apatite orientation in human bone tissue is proposed that exploits the sensitivity of X-ray absorption spectroscopy at the calcium K-edge to the apatite crystal orientations.

The scanning X-ray microscope at beamline **ID21** is dedicated to micro X-ray fluorescence (μXRF) and micro X-ray absorption spectroscopy (μXANES) in the tender X-ray domain (2.0-9.2 keV). The instrument offers element sensitivity in the low ppm range and localisation of various elements with a sub-micrometric beam. X-ray absorption spectroscopy can be performed in both scanning and full-field (FF) modalities, mainly in XRF and transmission modes, respectively. FF-XANES consists of acquiring radiographic scans of thin samples, illuminating samples with an unfocussed millimetric beam, at X-ray energies around the edge of interest. In this way, up to 10^6 XANES spectra can be acquired for 2D regions with sub-micron pixel-size in a single stack of radiographs, and in a relatively short acquisition time (here 40 minutes per sample). In this study, XANES spectroscopy in both FF transmission and XRF scanning mode at the Ca K-edge was applied to the analysis of human bone tissue in different pathological states and of varying anatomical origin.

Bone is a hierarchically-structured fibre composite consisting of collagen fibres reinforced by mineral particles. The sophisticated orientation patterns and state of these mineral particles at the micron level are strongly linked to the mechanical performance of the material on the organ level.

Spectral differences, well pronounced in the XANES white line (related to 1s to 4p transitions of Ca), were observed in FF XANES (**Figure 48**). Using mathematical simulations and site-matched polarised Raman spectroscopy, which has been shown to be sensitive to the orientation of bone components, spectral differences could be associated with angular absorbance dependency of the Ca containing mineral crystals (**Figure 49**).

Our data suggested that neither the anatomical site nor the pathology affected the averaged spectral shape of the XANES spectra. Instead, we could demonstrate that the spectral variances were dominated by angular dependent absorption effects. It is indeed crucial to differentiate between structurally and chemically induced spectral alterations. The fine structure modulations observed are of high interest for structural analysis of mineral crystal orientation in highly-structured tissue matrices.

The combination of fast acquisition time, large field of view and high lateral resolution makes

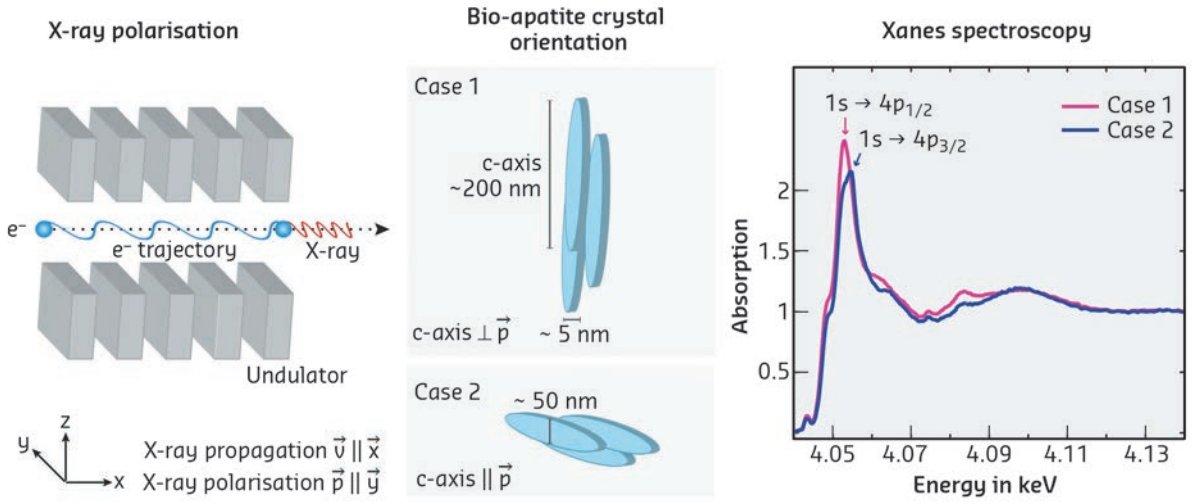

Fig. 48: Schematic view of the impact of the crystal orientation with respect to the polarisation vector on the spectral shape. The X-ray beam is generated by undulators resulting in a polarisation vector parallel to the horizontal plane. In bone apatite, crystals are arranged with the rotation axis perpendicular to the central blood vessel canals. The modulating crystal c-axis angles with respect to the polarisation vector result in a different spectral shape of the corresponding absorption spectra.

FF-XANES spectroscopy a potential alternative to standard X-ray diffraction techniques and diffraction-limited methods such as polarised Raman spectroscopy. Furthermore, collecting µXRF maps in scanning mode at only two distinct energies is already sufficient to derive information on crystal orientations. This configuration is of particular interest when XANES cannot be acquired in transmission mode. Finally, we anticipate that this approach will be valuable for the study of other highly-organised bio-materials, such as teeth, and that it could be used not only to map crystal orientation but also to evaluate alterations of apatite crystal states such as changes of the c-lattice parameters.

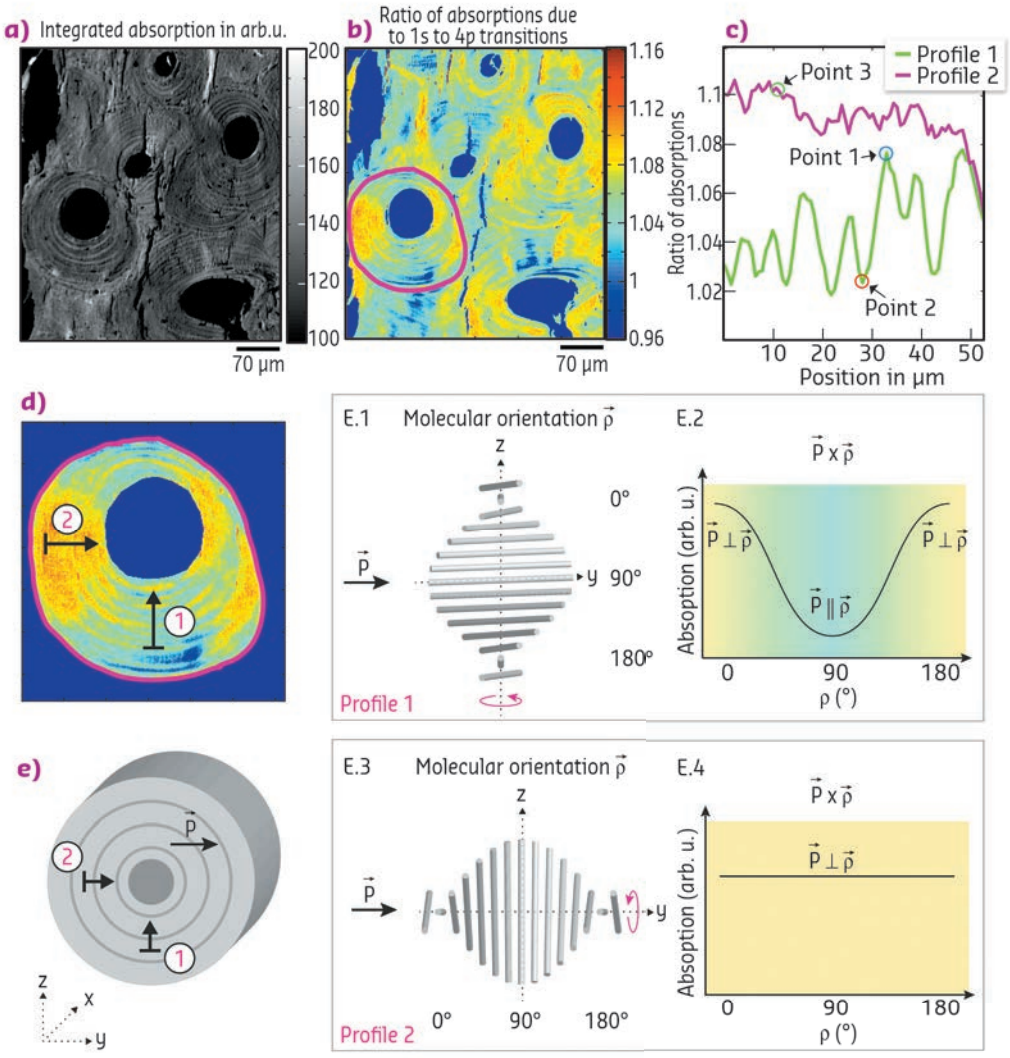

Fig. 49: FF-XANES investigation of bone structural unit section. Pixel size is 0.7×0.7 µm². a) Integrated absorption of the full XANES energy range and b) Ratios of the absorption amplitudes corresponding to the 1s to 4p transitions. c) Line plots along a vertical and horizontal direction (as indicated in (d) reveal the orientation dependence of the lamellar pattern. d) Enlargement of a sub-region as indicated in (b). The origin of the modulations is outlined in (e). Comparison of simulated model and experimental data: The X-ray beam is polarised in the x-y plane and propagating in x- direction. The cross-product between polarisation vector and mineral orientation for a twisted plywood arrangement is shown in E.2. As the cross-product is not constant, it potentially explains the variations seen in profile 1 shown in (c). In contrast, the polarisation vector is perpendicular to all molecular orientations within ROI2, therefore the cross-product is unvarying for all mineral orientations (E.4) explaining the far less pronounced contrast in profile 2 shown in (c).

PRINCIPAL PUBLICATION AND AUTHORS

Full-field calcium K-edge X-ray absorption near-edge structure spectroscopy on cortical bone at the micron-scale: polarization effects reveal mineral orientation, B. Hesse (a), M. Salome (a), H. Castillo (a), M. Cotte (a,b), B. Fayard (a), C. Sahle (a), W. De Nolf (a), J. Hradilova (c,d), A. Masic (e), B. Kanngießer (f), M. Bohner (g), P. Varga (h), K. Raum (c) and S. Schrof (c),

Analytical Chemistry **88**, 3826–3835 (2016); doi: 10.1021/acs.analchem.5b04898.

(a) ESRF
(b) Sorbonne Universités, UPMC Univ Paris 06, CNRS, UMR 8220, Laboratoire d'archéologie moléculaire et structurale (LAMS), Paris (France)
(c) Charité - Universitätsmedizin Berlin (Germany)
(d) Czech Technical University in Prague, Faculty of Nuclear Science and Physical Engineering (Czech Republic)
(e) MIT, Department of Civil and Environmental Engineering, Cambridge (USA)
(f) Technical University of Berlin, Institute for Optics and Atomic Physics (Germany)
(g) RMS Foundation, Bettlach (Switzerland)
(h) AO Research Institute Davos (Switzerland)

Structure of materials

The Structure of Materials Group (SoM) provides facilities for a range of X-ray scattering, imaging and spectroscopy experiments, relevant to the fields of energy research, catalysis, engineering, metallurgy, nanoscience and other fields of advanced technology. In addition to the traditional technological subjects, the group covers X-ray imaging studies for archaeology and palaeontology.

Commissioning of the new end-station of **ID11**, the Materials Science beamline, for nano-focussing experiments took place during 2016 and the new nanoscope is currently in routine operation. The beam can be focussed down to 100-200 nm by crossed linear Si nano-lenses and the high resolution spindle allows collection of 3D tomographic data with diffraction contrast of matching resolution. Moreover, the experiments in ID11's third experimental hutch can now also be operated with a pink beam delivered by the combined use of white-beam refractive lenses (in-vacuum X-ray transfocator located in the optics hutch) and a newly-installed, accurate slit system serving as a pinhole located in the first experiments hutch. The reduction of optical elements in this beamline configuration preserves the coherence properties of the undulator source and enables high quality phase contrast imaging experiments to be carried out, ideally complementing the portfolio of diffraction techniques provided by this beamline.

After two years of shutdown for complete renovation, **ID15A** reopened for users in autumn 2016 with radically improved performance. The new ID15A is devoted primarily to operando studies in materials chemistry and materials engineering, with two experimental hutches dedicated to those fields. The materials chemistry hutch, already fully operational, is optimised for the rapid acquisition of three-dimensional data on working chemical systems. New focusing optics based on crossed linear compound refractive lenses and either a bent double-Laue or a multilayer monochromator deliver an improved photon flux for beams ranging from several mm to micro-metres over an energy range of 25-100 keV. Coupled with a large area CdTe pixel detector, an improvement of orders of magnitude in time resolution can be achieved. From the very first two user experiments, carried out on working catalysts and batteries, data for 3D tomographic reconstructions based on diffraction data could be collected with sub-minute time resolution, unprecedented for such experiments. The complete installation of the materials chemistry station will be finalised in January 2017. The materials engineering station will receive its final instrumentation during summer 2017 and be fully functional in autumn 2017.

For **ID19**, the Microtomography Beamline, several new items of hardware were installed during 2016. Pco.edge 4.2 cameras (financed by LTP ES-295, Renard *et al.*) are now available and, owing to the increased quantum efficiency of the CMOS sensor, the image acquisition can be carried out with a substantially lower X-ray dose. To improve the image quality at high photon energies, a set of linear refractive lenses made of aluminium has been installed in the first optics hutch to condense the beam vertically. To complete the multimodal-monochromator setup, multilayer-coated mirrors are soon to be installed as a third monochromator option. The control software is already implemented for the currently-available Bragg and the Laue layouts. A new indirect detector system, the so-called TripleMIC (financed by LTP MA-1876, Salvo *et al.*) allows rapid exchange between three hard X-ray high-resolution configurations similar to the existing revolver-like design for the medium energy range. The beam enlarger system installed the year before has now been equipped with the first set of nano-lenses. As a consequence, an outstanding X-ray beam height of 6 cm at 19 keV was achieved in a proof-of-concept experiment in late 2016. In addition to the selected articles, one should note the papers by Pelliccia *et al.* **[1]** about a first demonstration of X-ray ghost imaging and by Immel *et al.* **[2]** about low-dose considerations to preserve ancient DNA in fossils.

ID22, the high-resolution powder-diffraction beamline, saw no major technical developments in 2016. The most noteworthy improvement was the implementation of automated protocols to allow the sample-changing robot (up to 75 samples) to be used with the Perkin-Elmer 2D detector that was installed in mid 2015. This has significantly improved the utility of this detector, which is used for one-shot measurements for atomic pair distribution function (PDF) analysis at high energies, and is complementary to the standard high-resolution mode of the beamline. Overall, the year was dedicated to user service, with a record number of mail-in measurements carried out for clients from the pharmaceutical industry.

The high-energy beamline for buried interface structures and materials processing, **ID31**, took first users in autumn 2015. ID31 offers a portfolio of hard X-ray characterisation techniques including reflectivity, wide-angle diffraction, both in transmission and grazing-incidence geometries, small angle X-ray scattering, imaging methods, and auxiliary techniques, coupled with a great versatility in beam sizes and detectors optimised for high-energy X-rays. In the first part of 2016, the beamline was working with a multilayer monochromator with 0.36% bandpass in the energy range 20-70 keV. The bent Laue-Laue monochromator with adjustable bandpass over the energy range 50 to 150 keV was installed during the summer shutdown in 2016 as well as the new small-gap and short-period U14 undulator. A fuel cell test station able to handle single cells and small stacks according to industrial standards was acquired. It provides control of the fuel and oxidant gases/liquids, with all the necessary safety features, and electrochemical characterisation of the fuel cell simultaneously with X-ray diffraction or spectroscopic data. It can be used with different types of fuel cells: hydrogen, solid oxide and liquid fuel cells.

The selection process of new beamlines within the EBS programme started in 2016. Of the eight candidate projects already shortlisted for further elaboration, two are within the SoM group. CDR2 proposes a beamline for hard X-ray diffraction microscopy, offering the opportunity to study bulk properties in mm-sized samples in 3D at all length scales down to 10 nm, using adapted tomographic techniques. It will allow complex, multi-scale phenomena to be characterised directly *in situ*, which is a key step towards formulating and validating multi-scale models that account for the entire heterogeneity of a material. CDR3 proposes a high-throughput large-field phase-contrast tomography beamline for materials research and engineering. It will provide a beamline for imaging large samples up to 60 cm × 200 cm on multiple length scales: from the complete sample to imaging of selected regions with sub-micrometre resolution. CDR3 would enable ID19 to be further developed for time-resolved imaging. We hope these projects will enhance the portfolio of hard X-ray characterisation techniques for our users from both academia and industry.

V. HONKIMÄKI

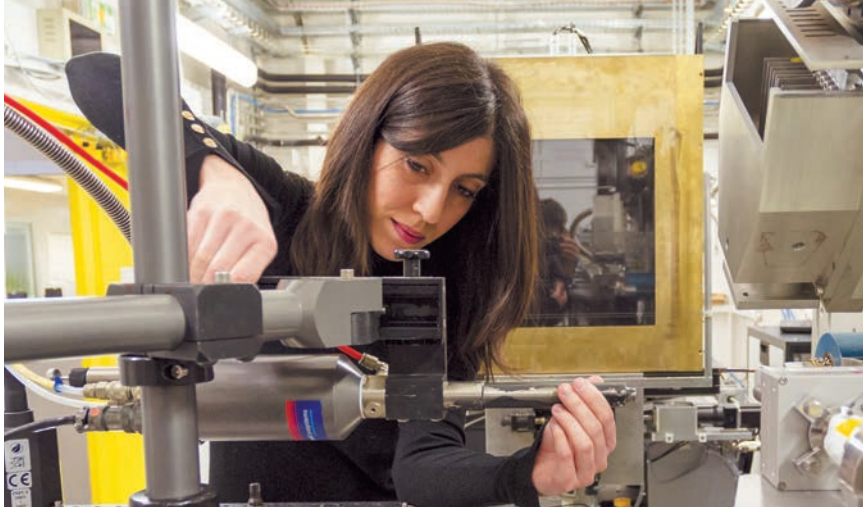

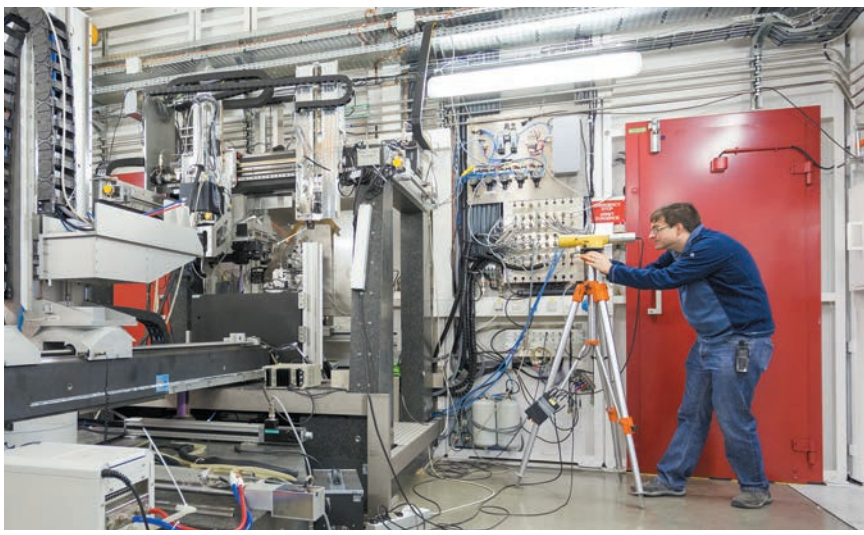

REFERENCES

[1] D. Pelliccia *et al.*, *Physical Review Letters* **117**, 113902 (2016).
[2] A. Immel *et al.*, *Scientific Reports* **6**, 32969 (2016).

THE NATURE OF ELECTROCATALYTICALLY ACTIVE SITES ELUCIDATED BY X-RAY DIFFRACTION

Catalysts based on porous hollow PtNi/C nanoparticles were prepared through a one pot synthesis followed by annealing. X-ray diffraction and electrochemical measurements revealed that the structurally disordered areas of the PtNi shell are highly active for the oxygen reduction reaction, a key reaction for proton-exchange membrane fuel cells.

In times of ongoing depletion of fossil fuel resources, it is more important than ever to find alternative energy sources. Low-temperature proton-exchange membrane fuel cells (PEMFCs) are electrochemical devices that convert the chemical energy of a reaction into electricity. They are the most promising candidates to generate electricity for both mobile and stationary applications. However, before a switch of our society to H_2-powered PEMFCs (H_2 is the fuel used at the anode) can occur there are still many fundamental limitations that need to be solved such as the sluggish oxygen reduction reaction kinetics (ORR, the cathodic reaction) and the limited durability of the cathode catalyst in real devices. The best way to improve the ORR activity and decrease the catalyst cost currently appears to be with the use of carbon supported PtM nanoalloys (PtM/C, where M is an early or late transition metal) or core-shell nanoparticles composed of a Pt-enriched shell and a metallic or alloyed core. However, these catalysts are still far from the target 8-fold mass activity (A g^{-1}Pt) improvement over state-of-the-art Pt/C required for PEMFC automotive applications.

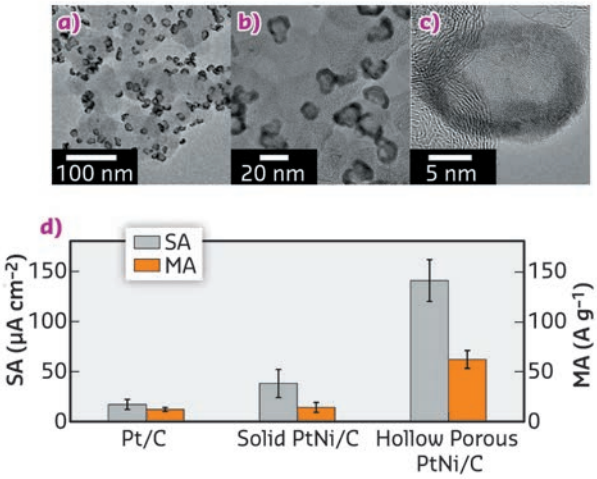

Fig. 50: a), b), c) Conventional and high-resolution TEM images of hollow PtNi/C nanoparticles and d) specific and mass activity for the ORR measured at E = 0.95 V *vs.* the reversible hydrogen electrode. The specific activity and the mass activity are normalised to a cm2 of Pt or to a g of Pt, respectively. Potential sweep rate v = 0.005 V s^{-1}, ω = 1600 revolutions per minute, T = 298 ± 1 K, 0.1 M $HClO_4$.

We have developed a simple one-pot synthesis of porous hollow PtM/C nanoparticles **[1]**. These nanoparticles are composed of a PtM shell surrounding a central void, which minimises the quantity of Pt contained in the catalyst. Moreover, their porosity allows oxygen molecules to reach the inner surface. The hollow PtNi/C nanoparticles (Pt:Ni 85:15 at.%) achieved 6-fold and 9-fold enhancement in mass and specific activity for the ORR, respectively over standard solid Pt/C crystallites of the same size. The catalytic enhancement was 4-fold and 3-fold in mass and specific activity, respectively over solid PtNi/C nanocrystallites with similar chemical composition, Pt lattice contraction and crystallite size (**Figure 50**). These results show that, beyond the classical strain and ligand effects, structural effects play a role in ORR electrocatalysis.

By combining high-resolution transmission electron microscopy (HR-TEM) and X-ray diffraction at beamline **ID31**, we have unravelled the crucial role of structural defects in the ORR activity. Conventional and high-resolution transmission electron microscopy (TEM) images of hollow PtNi/C nanoparticles displayed in **Figure 50** showed that the PtNi shell surrounding the central void contains a high concentration of point defects (vacancies), planar defects (dislocations and grain boundaries) and bulk defects (voids, pores).

This highly defective nanostructure was confirmed by the high microstrain value (deviation of the inter-planar distance from its average value) derived from Rietveld analysis of

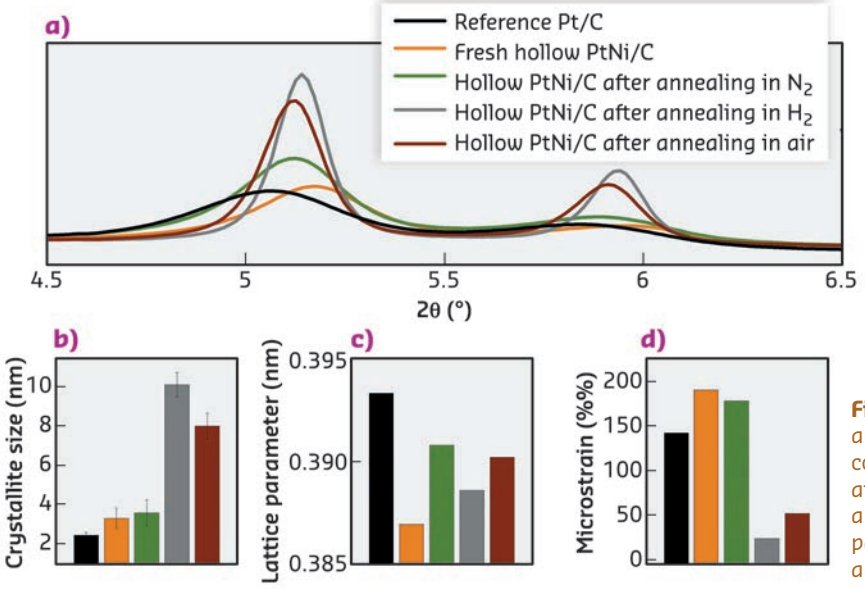

Fig. 51: Structural parameters of fresh and thermally-annealed hollow PtNi/C electrocatalysts and of a commercial reference Pt/C. a) Synchrotron XRD patterns after linear heating from room temperature to 400°C at a rate of 2°C min^{-1}, b) average crystallite size, c) lattice parameter and d) microstrain estimated by Rietveld analysis of the HR-XRD patterns.

high-energy X-ray diffraction (HR-XRD) patterns. Structural parameters of thermally-annealed hollow PtNi/C nanoparticles, which feature identical chemical composition to the mother catalyst but different morphology, crystallite size and lattice strain are displayed in **Figure 51**. Despite their relaxed lattice parameter, and their smaller crystallite size (parameters known to negatively influence the ORR activity), the materials featuring the higher microstrain values (that is the higher structural disorder) proved to be the most active for the ORR.

To gain further insight into the reactivity of these nanomaterials, *in situ* (*i.e.* under potential control) wide angle and small-angle X-ray scattering measurements during accelerated stress testing are planned. Combined with X-ray energy dispersive spectroscopy analyses these experiments should provide a detailed picture of structure-activity-stability relationships for this novel class of materials and should ultimately aid in the rational design of electrocatalysts with enhanced ORR activity.

PRINCIPAL PUBLICATION AND AUTHORS

Defects do catalysis: CO monolayer oxidation and oxygen reduction reaction on hollow PtNi/C nanoparticles, L. Dubau (a,b), J. Nelayah (c), S. Moldovan (d), O. Ersen (d), P. Bordet (e,f), J. Drnec (g), T. Asset (b,c), R. Chattot (a,b) and F. Maillard (a,b), *ACS Catal.* **6**, 4673–4684 (2016); doi: 10.1021/acscatal.6b01106.

(a) Université Grenoble Alpes, LEPMI, Grenoble (France)
(b) CNRS, LEPMI, Grenoble (France)
(c) Laboratoire Matériaux et Phénomènes Quantiques (MPQ), UMR 7162, CNRS & Université Paris-Diderot (France)
(d) Institut de Physique et Chimie des Matériaux de Strasbourg (IPCMS), UMR 7504, CNRS-Université de Strasbourg (France)
(e) Université Grenoble Alpes, Institut Néel, Grenoble (France)
(f) CNRS, Institut Néel, Grenoble (France)
(g) ESRF

REFERENCES

[1] L. Dubau *et al.*, *ACS Catal.* **5**, 5333-5341 (2015).

Na-RICH $Na_4V_2(PO_4)_2F_3$ FOR ADVANCED Na-ION BATTERIES

A scalable ball milling synthesis involving metallic sodium was used to prepare the Na-rich $Na_4V_2(PO_4)_2F_3$ cathode for Na-ion batteries. This method provides additional Na to compensate Na loss in solid electrolyte interface formation and thus brings a substantial increase in the energy density.

Na-ion batteries are the most appealing alternative to current Li-ion batteries due to the natural abundance of sodium which is expected to bring a 20% cost decrease **[1]**. Of the candidate materials for the cathode, the polyanionic compound $Na_3V_2(PO_4)_2F_3$ is of great interest since it shows high voltage plateaus near 3.6 and 4.2 V whose equal amplitudes provide a cumulative capacity of ~ 120 mAh g^{-1} **[2]**. To make practical cells, the $Na_3V_2(PO_4)_2F_3$ positive electrode is matched with hard carbon having a reversible capacity of 300 mAh g^{-1}, out of which 25% is lost to form the solid electrolyte interface (SEI) during the first cycle. Owing to the low coulombic efficiency of hard carbon in Na-ion batteries, *i.e.*, less than 80%, a strategy to compensate for Na loss to the SEI is vital.

We report herein the synthesis of Na-rich $Na_4V_2(PO_4)_2F_3$ compounds via the ball milling of Na-metal with $Na_3V_2(PO_4)_2F_3$, where the additional Na is used to build SEI on the anode side in a full cell. $Na_3V_2(PO_4)_2F_3$ powders were mixed with a metallic lump of Na and ball milled in a SPEX 8000 milling apparatus. A single phase of $Na_4V_2(PO_4)_2F_3$ was obtained after 3 hours of ball milling. X-ray diffraction patterns collected at beamline **ID22** of the pristine $Na_3V_2(PO_4)_2F_3$ and $Na_4V_2(PO_4)_2F_3$ phases are shown in **Figure 52a-b**, respectively. The diffraction peaks of the phase formed upon ball milling with Na can be indexed in the same orthorhombic cell as for the pristine $Na_3V_2(PO_4)_2F_3$, but with different lattice parameters, *i.e.* a = 9.2208(2) Å, b = 9.2641(2) Å, c = 10.6036(2) Å. This corresponds to an increase of the unit cell by 3.2% (V= 905.79(3) Å^3) relative to the pristine $Na_3V_2(PO_4)_2F_3$ phase (V = 878.05(3) Å^3), which is consistent with the uptake of extra sodium upon reduction. The Na environments in the Na-rich phase are shown in **Figure 52e-f**. The three distinct Na sites are all 7-fold coordinated with 4 oxygen and 3 fluorine atoms, which is analogous to the coordination of Na1 in $Na_3V_2(PO_4)_2F_3$ (**Figure 52c-d**). The structural analysis confirms the chemical composition ($Na_4V_2(PO_4)_2F_3$) and indicates that there is apparently no further space for Na insertion.

The benefits of preparing Na-rich $Na_4V_2(PO_4)_2F_3$ is demonstrated through assembling full cells with hard carbon anodes. **Figure 53** shows the electrochemical performances of cells C1 (blue)

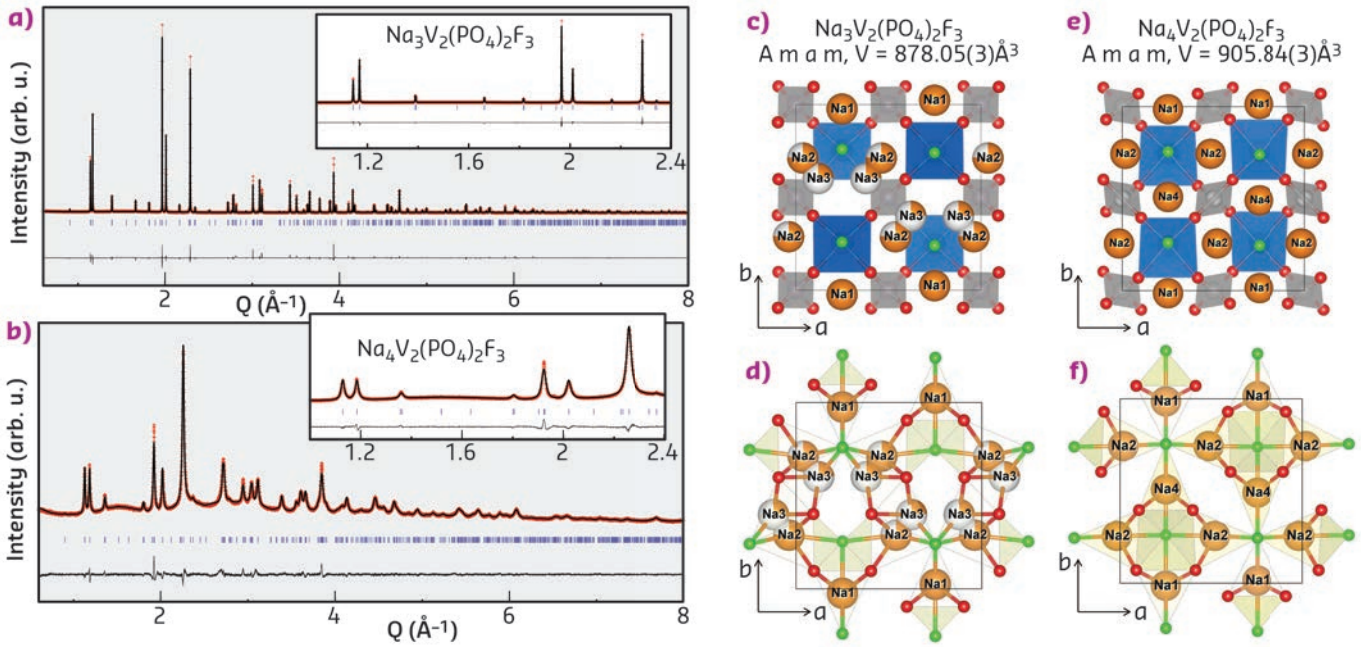

Fig. 52: Rietveld refinements of a) pristine $Na_3V_2(PO_4)_2F_3$ and b) pure $Na_4V_2(PO_4)_2F_3$. Structure of $Na_3V_2(PO_4)_2F_3$ (c,d) and of $Na_4V_2(PO_4)_2F_3$ (e,f) as deduced from the refinement of the diffraction patterns. The Na environment of $Na_3V_2(PO_4)_2F_3$ and $Na_4V_2(PO_4)_2F_3$ is respectively highlighted in (d) and (f). VO_4F_2 octahedra and PO_4 tetrahedra are coloured in blue and grey, respectively. Na and F atoms are shown as orange and green spheres, respectively. Vacancies on the Na1 and Na2 sites of $Na_3V_2(PO_4)_2F_3$ are coloured in white.

and C2 (black), having pristine $Na_3V_2(PO_4)_2F_3$ and composite "$Na_{3.5}V_2(PO_4)_2F_3$" (*i.e.*, equal amount of $Na_3V_2(PO_4)_2F_3$ and $Na_4V_2(PO_4)_2F_3$) as positive electrodes, respectively. The cells were tested electrochemically between 1.5 and 4.3 V. The voltage trace for C1 mirrors early literature reports for similar cells with a charging capacity of 129 mAh g^{-1} and a discharge capacity of 89 mAh g^{-1}, which remains stable upon cycling. Providing sacrificial Na in the form of Na-rich NVPF (C2) strongly modifies the voltage profile. Note the existence of an initial capacity near 0.5 V which corresponds to the removal of Na from "$Na_{3.5}V_2(PO_4)_2F_3$" to compensate for the SEI formation at the negative electrode. Afterwards the potential rises as expected with associated removal of Na from $Na_3V_2(PO_4)_2F_3$. Overall, the C2 cell exhibits an overall charging capacity of 167 mAh g^{-1} and a discharge capacity of 110 mAh g^{-1}, which is a 24% enhancement compared to cell C1. This corresponds to an overall 10% increase in energy density. Lastly, we have shown that the use of the Na-rich phase does not jeopardise the cycle life, since the capacity remains nearly constant over 20 cycles.

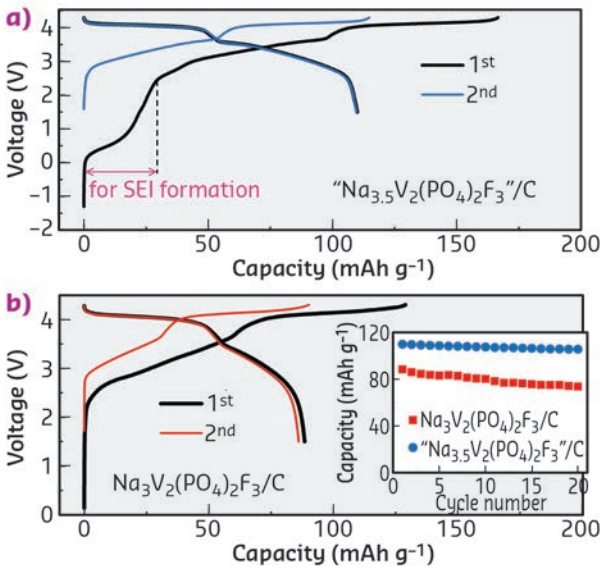

Fig. 53: Performance of C/"$Na_{3+x}V_2(PO_4)_2F_3$" Na-ion cells. Inset in (b) shows the capacity retention in the first 20 cycles.

The means to enhance the performance of Na-ion batteries discussed here should have a very positive impact on their future development for commercialisation.

PRINCIPAL PUBLICATION AND AUTHORS

Insertion compounds and composites made by ball milling for advanced sodium-ion batteries, B. Zhang (a,b,c), R. Dugas (a,b,c), G. Rousse (a,b,c,d), P. Rozier (b,c,e), A.M. Abakumov (f,g) and J.-M. Tarascon (a,b,c,d), *Nature Communications* **7**, 10308 (2016); doi: 10.1038/ncomms10308.

(a) Chimie du Solide-Energie, UMR 8260, Collège de France, Paris (France)
(b) Réseau sur le Stockage Electrochimique de l'Energie (RS2E), FR CNRS 3459, Amiens (France)
(c) ALISTORE-European Research Institute, Amiens (France)
(d) Sorbonne Universités - UPMC Univ Paris 06, Paris (France)
(e) University of Toulouse III Paul Sabatier, CIRIMAT CNRS UMR 5085, Toulouse (France)
(f) EMAT, University of Antwerp, Antwerp (Belgium)
(g) Skolkovo Institute of Science and Technology, Moscow (Russia)

REFERENCES

[1] D. Larcher *et al.*, *Nat. Chem.* **19**, 7, (2014).
[2] M. Bianchini *et al.*, *Chem. Mater.* **4238**, 26, (2014).

POLYMORPHISM ON THE NANOSCALE: UNRAVELLING STRUCTURAL DIVERSITY IN $Au_{144}(SR)_{60}$ NANOCLUSTERS

In the bulk, gold has a simple structure with atoms arrayed in a regular fashion, while on the nanoscale it can have exotic structures, with new properties and functionalities. This work used intense X-ray beams on tiny samples of nanosized gold clusters that revealed polymorphism: gold clusters can have doppelgängers.

The advancement of material science builds on understanding the intricate relations between atomic structure and properties of a material. For the last 100 years, Bragg diffraction has been the tool of choice to map this relation by providing us with the possibility to determine atomic arrangements in solids with high precision. However, the conventional crystallographic techniques fail when it comes to nanomaterials, and this 'nanostructure problem' represents one of the big challenges in nanotechnology [1]. Now, with the high-energy, high-flux X-rays available from third-generation synchrotrons, we are getting closer to a solution, as new possibilities emerge for structural characterisation. Here, we have used high energy X-ray total scattering at beamline **ID11** to solve the structure of $Au_{144}(SR)_{60}$, and show that these small gold clusters exist in two different structures; illustrating polymorphism on the nanoscale.

'Magic sized' metal nanoclusters, such as $Au_{144}(SR)_{60}$, represent a new material class between particles and molecules: unlike nanoparticles, they are atomically monodisperse meaning that the exact number of metal atoms and stabilising ligands can be controlled. While the composition of the clusters can be determined from mass spectrometry, the arrangements of the atoms remain undetermined. Atomic structure with only short-range order gives rise to diffuse scattering of X-rays, which cannot be analysed with conventional crystallographic techniques. Instead, structural information from diffuse scattering data can be extracted by collecting data to high scattering angles, and subsequently Fourier transforming the data to obtain the pair distribution function (PDF). The PDF represents a histogram of interatomic distances in the sample, allowing structural information to be extracted [2]. In this study, we used PDF to determine the atomic arrangement in the $Au_{144}(SR)_{60}$ cluster, where 'SR' represents a thiol ligand.

Figure 54a shows PDFs obtained from $Au_{144}(SR)_{60}$ clusters covered with two different thiol ligands; phenylethane thiol (PET) and *para*-mercaptobenzoic acid (pMBA). Surprisingly, we see distinct differences between the two PDFs, despite both samples containing clusters of exactly 144 gold atoms and 60 thiol ligand molecules. The data were modelled using our new software for PDF analysis, diffpy-CMI [3]. We initially tested a structure model deduced from DFT calculations [4]. This structure has a 114 atom icosahedral core, while the surface is covered by 30 –S-Au-S- 'staple' units, as illustrated in **Figure 54b**. As can be seen from **Figure 54d-e**, this structure fits well with the PET data, but does not describe the pMBA covered clusters which thus have a fundamentally different structure: the clusters exhibit polymorphism.

To determine the structure of the pMBA clusters, we first attempted fitting the bulk gold *fcc* structure to the data, as shown in **Figure 54f**. While not being a physical model for the cluster, the simple *fcc* structure model fits the data better than the icosahedral model. This result lead us to explore a series of *fcc*-derived models, including clusters in the Marks decahedron shape; built up from 5 small twinned *fcc* structures illustrated in **Figure 54b**. A decahedral 114 atom core, covered by 30 staples gave an excellent fit (**Figure 54g**) fully describing the data in a physical manner.

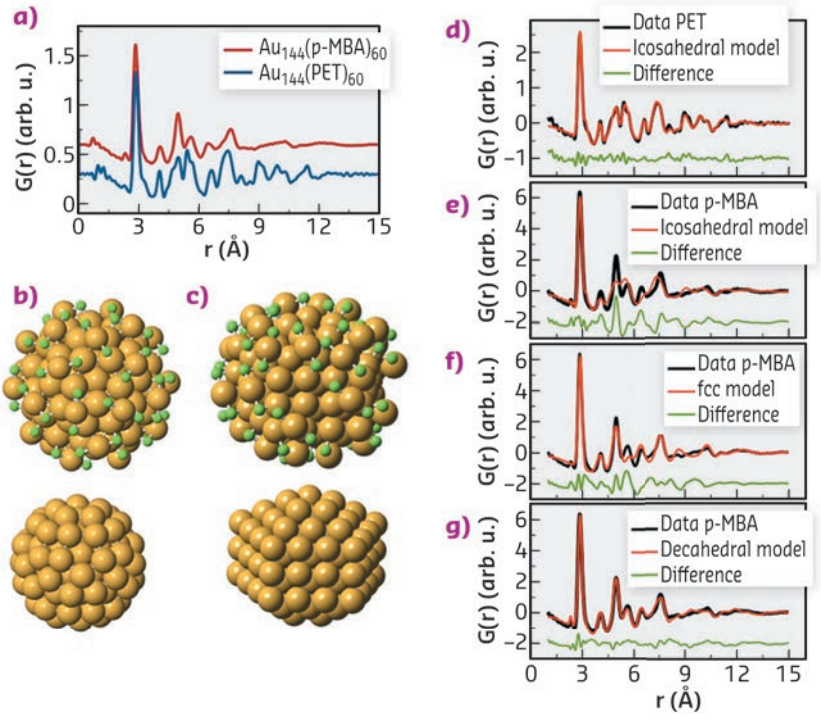

Fig. 54: a) PDFs obtained for two different $Au_{144}(SR)_{60}$ clusters. b) Full icosahedral model (top) and 114-atom core (bottom). c) Full decahedral model (top) and 114 atom core (bottom). Gold atoms are shown in orange, while green represent sulfur. d-g) PDF fits.

Two distinct structures thus exist for the Au_{144} clusters, one with an icosahedral core (form I), and a second polymorph with a decahedral core (form II). Surprisingly, we found that for certain thiol ligands, both polymorphs were present in the same sample. This result illustrates that the structural diversity is not a simple effect of *e.g.* ligand identity, but indicates that the two structures are very close in energy. The discovery of polymorphism adds a new dimension to nanoengineering, beyond control of particle size and morphology. The two structures seen in our data furthermore suggests many new studies of gold nanoclusters. Polymorphism may not be limited to the $Au_{144}(SR)_{60}$ cluster, but could exist in many different materials systems. Recently, several new metal clusters have been isolated in the size range from 50 to 300 atoms. The structures of many of these clusters remain undetermined. We believe that PDF is an excellent tool for these studies and will aid in providing full structure solutions to many new nanomaterials.

PRINCIPAL PUBLICATION AND AUTHORS

Polymorphism in magic-sized $Au_{144}(SR)_{60}$ clusters, K.M.Ø. Jensen (a), P. Juhas (b), M.A. Tofanelli (c), C.L. Heinecke (c), G. Vaughan (d), C.J. Ackerson (c) and S.J.L. Billinge (a,b), *Nature Communications* **7**, 11859 (2016); doi: 10.1038/ncomms11859.

(a) Department of Applied Physics and Applied Mathematics, Columbia University, New York (USA)
(b) Condensed Matter Physics and Materials Science Department, Brookhaven National Laboratory, Upton (USA)
(c) Department of Chemistry, Colorado State University, Fort Collins, Colorado (USA)
(d) ESRF

REFERENCES

[1] S. Billinge *et al.*, *Science* **316**, 561-565 (2007).
[2] S. Billinge *et al.*, *Chem. Commun.* 749-760 (2004).
[3] P. Juhas *et al.*, *Acta Cryst.* **A71**, 562-568 (2015).
[4] D. Bahena *et al.*, *J. Phys. Chem. Lett.* **4**, 975-981 (2013).

NANOMETRE-SCALE LIVE VIEW OF CATALYST DEGRADATION

A novel sintering mechanism was revealed through high-energy grazing-incidence X-ray diffraction studies on the composition- and shape-dependent sintering behaviour of Pt-Rh nanoparticles during catalytic CO oxidation at near-ambient pressures. This mechanism was found to be suppressed for particles grown in their equilibrium shape. The latter was achieved by increasing the Rh-content inside the Pt-Rh alloy particles.

Catalysts are materials that increase the rate of a desired chemical reaction. They are widely employed in fuel cells, automotive exhaust converters and in the chemical industry where they are essential for the production of more than 90% of the world's fine chemicals. To increase the surface area and accordingly the number of reaction sites, the catalyst materials (typically Pt, Rh, Pd and alloys thereof) are in the form of nanoparticles and are widely dispersed on highly branched oxide carriers, mainly Al_2O_3.

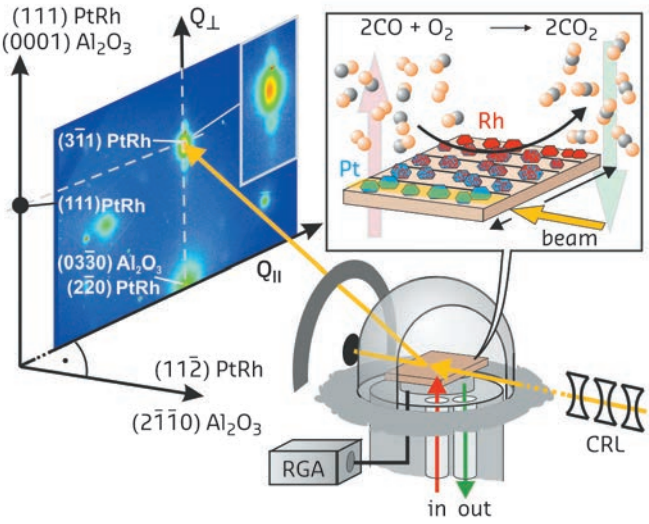

Fig. 55: Experimental strategy allowing a correlation between the sample's catalytic activity and the atomic nanoparticle structure for different Pt-Rh alloy compositions.

To improve catalyst efficiency and lifetime, an atomic-scale understanding of the processes that occur on these complex materials under reaction conditions is a prerequisite. Reaction conditions typically involve gas mixtures at elevated temperatures and ambient pressures. In recent years, much attention has been paid to the study of alloy nanoparticles, which, based on synergetic effects between the components, are promising systems for tailoring catalyst performance **[1]**. Sintering, *i.e.* the agglomeration of particles resulting in a loss of effective surface area, is viewed as a major cause of catalyst deactivation **[2]**. A better understanding of the process itself paves the way for improved sintering reduction.

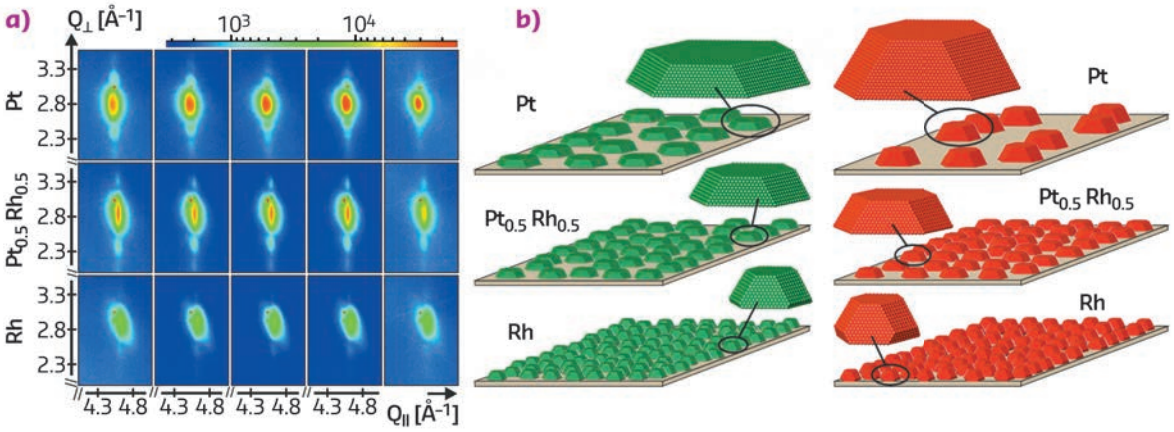

Fig. 56: a) Close-ups on the particle Bragg peaks and Laue oscillation signals measured on pure Pt, $Pt_{0.5}Rh_{0.5}$ and pure Rh particles in the transition to conditions of higher catalytic activity (from the left to the right); b) respective quantitative particle shapes before (green) and after (red) sintering.

At beamline **ID15A**, we performed a high-energy grazing-incidence X-ray diffraction study (E = 78.7 keV) which shed new light on the composition- and shape-dependent sintering behaviour of Al_2O_3(0001)-supported Pt-Rh alloy nanoparticles during CO oxidation at near-ambient pressures (p = 200 mbar; T = 550 K).

Figure 55 summarises the experimental scheme. The model catalyst consisted of stripes containing epitaxial nanoparticles of varying Pt-Rh compositions that could be probed individually by the collimated X-ray beam. It was mounted inside a beryllium dome acting as a flow reactor for catalysis. Sampling via a residual gas analyser (RGA) while detecting the scattered X-rays with a large area detector allowed the sample's catalytic activity to be correlated with the particle structure of the different Pt-Rh compositions.

The use of high photon energies allowed a large area of reciprocal space within a single image to be mapped (see **Figure 55**), which included the particle ($3\bar{1}1$) Bragg peak and its vicinity which contained finite height Laue oscillations (see inset of reciprocal space map). These intensity variations along the L-direction provided information about the particle height and the quantitative particle shape. Hence, the 2D snapshots served as a real-time probe to monitor the particle sintering.

A sequence of these 2D reciprocal space maps taken during the transition to conditions of higher catalytic activity is shown in **Figure 56a** for selected Pt-Rh compositions. In the case of pure Pt, the Laue oscillations moved progressively towards the Bragg peak, indicating a strong particle height increase. The quantitative analysis revealed that, despite this strong vertical sintering, the initially very flat Pt particles maintained their diameter and accordingly adopted a more three-dimensional shape which proved to be very stable (see **Figure 56b**). X-ray reflectivity measurements showed that the atoms involved in this growth in height were rendered from the particles' surroundings, as the particle height increase scaled with a decrease in the particle coverage on the sample surface.

With increasing Rh content, the initial particle shapes were found to be progressively more three-dimensional. Accordingly, the suppression of vertical sintering scaled with Rh content, as can be deduced from the Laue oscillations in **Figure 56a**, which almost maintained their position in the case of the Rh-rich particles.

We ascribe the particle shape change of the Pt-rich particles to a non-classical Ostwald ripening process that has not yet been described in literature. Therein, particles, kinetically trapped in an initially flat shape, use the energy released in the reaction to adopt a more compact equilibrium shape. We conclude that alloying with Rh results in the growth of stable equilibrium shapes and hence provides a possibility to reduce sintering.

PRINCIPAL PUBLICATION AND AUTHORS

U. Hejral (a,b,c), P. Mueller (a,b,c), O. Balmes (d,e), D. Pontoni (e) and A. Stierle (a,b,c), *Nature Comm.* **7**, 10964 (2016); doi: 10.1038/ncomms10964.
(a) DESY, NanoLab, Hamburg (Germany)
(b) University of Hamburg, Fachbereich Physik, Hamburg (Germany)
(c) University of Siegen, Fachbereich Physik, Siegen (Germany)
(d) MAX IV Lab, Lund (Sweden)
(e) ESRF

REFERENCES

[1] J.Y. Park *et al.*, *Nano Letters*, **8**, 673-677 (2008).
[2] C.H. Bartholomew, *Appl. Catal. A Gen.*, **212**, 17-60 (2001).

THE ELECTRONIC AND STRUCTURAL PROPERTIES OF HIGHLY LUMINESCENT OLIGOATOMIC SILVER CLUSTERS CONFINED IN ZEOLITES

Luminescent silver-zeolite composites with external quantum efficiencies close to 100% were synthesised by applying rational design rules for assembling metal clusters in zeolites. Extended X-ray absorption fine structure combined with photoelectron spectroscopies were utilised to unravel the electronic and structural properties of this novel type of functional material.

Silver clusters consisting of just a few atoms display remarkable optical properties, originating from discrete energy levels in their energy diagram **[1]**. However, current applications for such oligoatomic clusters are limited due to their tendency to aggregate into larger nanoparticle ensembles, resulting in the loss of their peculiar properties. A strategy to stabilise such clusters is to confine them within the porous framework of zeolites, resulting in stable silver clusters that retain their unique optical properties **[2]**. Zeolites are minerals that possess a high rigidity and well-defined crystal structure of small molecular-sized cavities that are either found in nature or produced synthetically on an industrial scale.

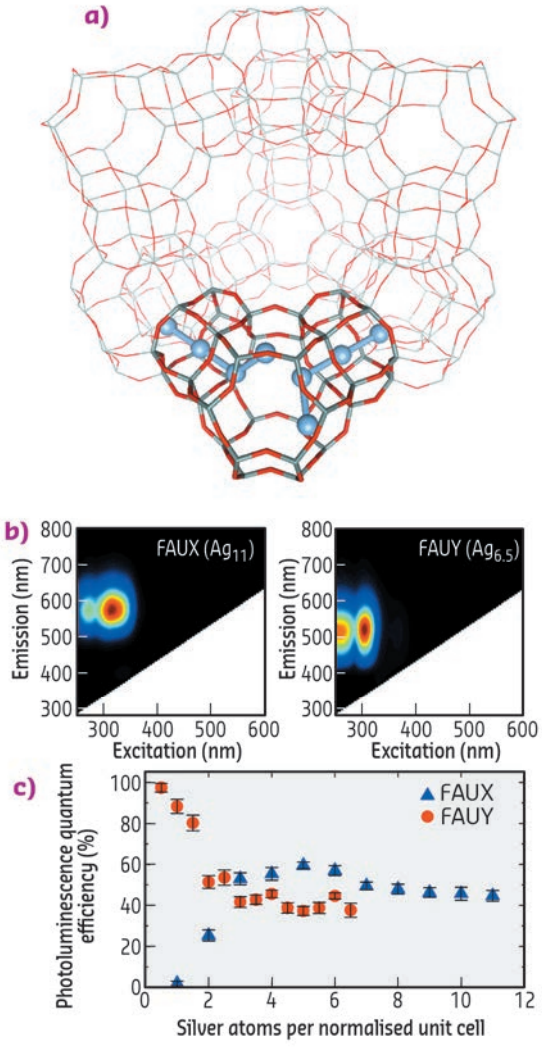

Fig. 57: a) FAU zeolite unit cell displaying a schematic representation of the Ag clusters in a sub-unit cell. b) 2D emission/excitation plot of fully Ag-exchanged FAUX and FAUY zeolites. c) PLQE values of FAUX and FAUY zeolites with different Ag exchange ratios.

In this report, the self-assembly of silver clusters in four different types of zeolites, two Linde type A (LTA) and two faujasite type (FAU) zeolites, was studied. These zeolites are all composed of sodalite cages, but differ in their secondary building units and silicon-to-aluminum (Si/Al) ratios, conferring on them different electronic features (Si/Al ratios for LTA, FAUX and FAUY are 1, 1.1, and 2.7, respectively). An in-depth characterisation of these luminescent silver-exchanged zeolites with various advanced spectroscopy techniques provided unambiguous evidence of a strong influence of the zeolite host and degree of silver uptake on the structural, electronic and optical properties of the silver clusters. The deep understanding acquired was crucial to develop rational design rules for assembling metal clusters within zeolites, leading to the synthesis of materials with luminescence efficiencies close to 100% for Ag-FAU zeolites.

The structural characterisation of these Ag-zeolites was performed by extended X-ray fine structure (EXAFS) analysis at beamlines **BM26** (DUBBLE) and **BM08** (LISA). In Ag-FAU zeolites, we found a cluster of around 4 atoms, indicative of an Ag_4 species (**Figure 57a**), whereas for clusters stabilised in LTA zeolites, nuclearities between 3 and 6 were observed, suggesting the formation of Ag_3 and Ag_6 species. Remarkably, significant differences were observed between the Ag-FAU samples possessing different Si/Al ratios (FAUX and FAUY). From the EXAFS model (**Figure 58**), it was observed that for Ag-FAUX the fraction of silver atoms forming the cluster, changed from 57% to 73% with respect to the silver loading. This observation is in line with the trend found in the photoluminescence quantum yield (PLQY) measurements (**Figure 57c**), where the PLQY of Ag-FAUX rises (reaching a plateau at around 60%) with increasing silver loading.

In contrast, Ag-FAUY samples displayed the highest PLQY, amounting to 97% for the lowest Ag loaded sample. This value decreased in samples containing higher silver loadings until reaching a similar plateau as that found in Ag-FAUX samples. However, no significant differences were detected by EXAFS for the fraction of silver atoms forming the clusters in the low-loaded Ag-FAUY sample compared to the other loadings. Detailed analysis of the local order extracted from the Debye-Waller factors showed that the cluster structure in the most efficient low loaded Ag-FAUY sample was significantly more ordered. This counter-intuitive trend in the cluster structure and PLQY values could be explained by a difference in the relative mobility of the Ag^+ and Na^+ ions inside the two faujasite structures, Ag^+ ions possess

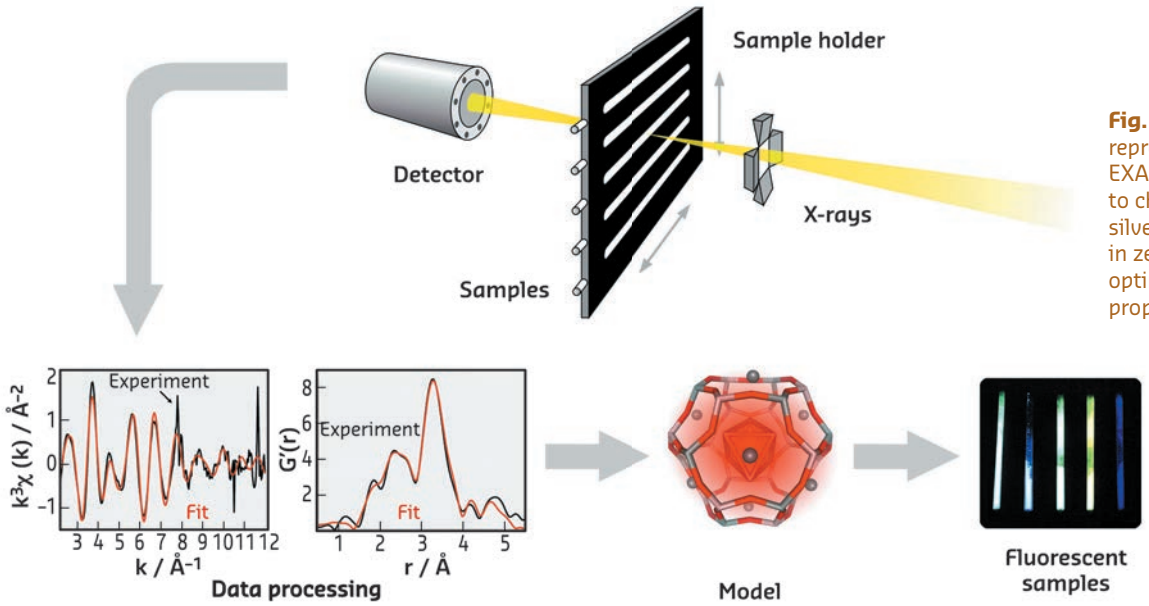

Fig. 58: Schematic representation of the EXAFS approach followed to characterise luminescent silver clusters confined in zeolites, leading to the optimisation of their optical properties.

a larger mobility than Na^+ ions in Ag-FAUY zeolites, whereas the opposite is true in Ag-FAUX samples. These findings are of paramount importance to the elucidation of the structure-to-property relationships of small metal clusters and ultimately the design principles established will be crucial for developing highly luminescent Ag-zeolite materials with potential applications in optoelectronics (luminescent tags, fluorescent lamps, LEDs).

PRINCIPAL PUBLICATION AND AUTHORS

Tuning the energetics and tailoring the optical properties of silver clusters confined in zeolites, O. Fenwick (a,b), E. Coutiño-Gonzalez (c), D. Grandjean (d), W. Baekelant (c), F. Richard (a), S. Bonacchi (a), D. De Vos (e), P. Lievens (d), M. Roeffaers (e), J. Hofkens (c) and P. Samori (a), *Nat. Mater.* **15**, 1017-1022 (2016); doi: 10.1038/NMAT4652.
(a) ISIS & icFRC, Université de Strasbourg & CNRS (France)
(b) Present address: School of Engineering and Materials Science, Queen Mary University of London (UK)
(c) Chemistry Department, KU Leuven (Belgium)
(d) Laboratory of Solid State Physics and Magnetism, KU Leuven (Belgium)
(e) Department of Microbial and Molecular Systems, KU Leuven (Belgium)

REFERENCES

[1] I. Diez and R.H.A. Ras, *Nanoscale* **3**, 1963 (2011).
[2] G. De Cremer *et al., J. Am Chem. Soc.* **131**, 3049 (2009).

RESORCINOL CRYSTAL TWISTING AND POLYMORPHISM

Resorcinol, a commodity chemical intermediate, was the first substance whose crystals showed different arrangements of molecules (polymorphs) by X-ray diffraction. Strange helicoidal resorcinol crystals form under conditions that support a third, ambient-pressure polymorph. The solution of the structure of this phase required powder diffraction data combined with computational crystal structure prediction algorithms.

Resorcinol crystals grow from the melt in the presence of tartaric acid additives as two distinct kinds of optically banded spherulites. The optical banding shown in **Figure 59** is evidence of helicoidal twisting of the composite crystallites, a common, non-classical morphology **[1]**. This very common morphology for molecular crystals was first observed in 1906 for resorcinol **[2]**, but was forgotten until much later **[3]**.

As two forms of resorcinol had been established by X-ray scattering in the 1930s, it was natural to presume that these forms had been induced to twist by the chiral additive. In fact, one was identified by powder X-ray diffraction as the long-known β form of resorcinol **[4]**. The other phase, not the expected α **[5]** form, was unknown. We called it ε. It was incumbent upon us to establish that we had indeed found a new ambient phase of resorcinol by solving its structure.

We turned to computation in order to arrive at the crystal structure whose simulated diffraction pattern matched data collected

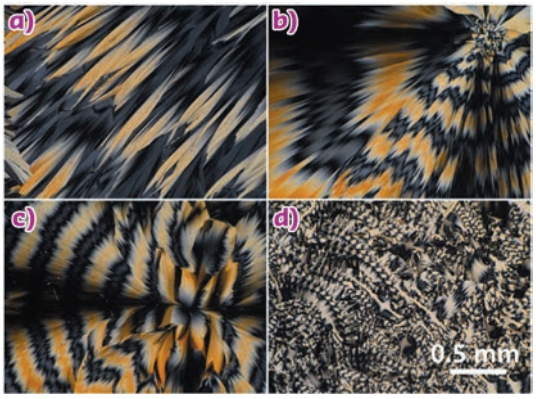

Fig. 59: A selection of polarised light optical micrographs of the new ε form of resorcinol. a) Irregular banded spherulite formed at 80°C. b) Banded spherulite formed at 75°C, showing distinct twisting periods. c) Banded spherulite formed at 51°C. Irregular pattern with small areas of banded spherulites formed at 35°C (d).

at beamline **ID22**. Several crystal structure prediction attempts have been made, one of which applied a resorcinol-specific force field for energy minimisation **[6]**. Ultimately, the structure was matched by the USPEX evolutionary algorithm **[7]**. In addition to β (**Figure 60b**) and ε (**Figure 60c**), there was one other structure that was found with 5 kJ/mol of the α (**Figure 60a**) ground state. This was a monoclinic structure as shown in **Figure 60d**, a target of future experimental efforts.

Resorcinol has been so thoroughly studied in the past 80 years that some researchers were of the opinion that no additional forms could be found under ambient conditions **[8]**, a prediction that proved to be premature.

Many polymorphs of common substances can be found under highly non-equilibrium conditions that are well suited to the unusual twisted morphologies that characterise resorcinol. New regions of phase space can be reached when the driving force for crystallisation is particularly high. Nevertheless, phases prepared in this way are typically polycrystalline, and require high-resolution powder X-ray diffraction filtered through the prism of computation. Despite claims that crystal structure prediction on the basis of molecular structure alone is a solved problem, the challenges raised by the simple case of resorcinol demonstrates that such is not the case.

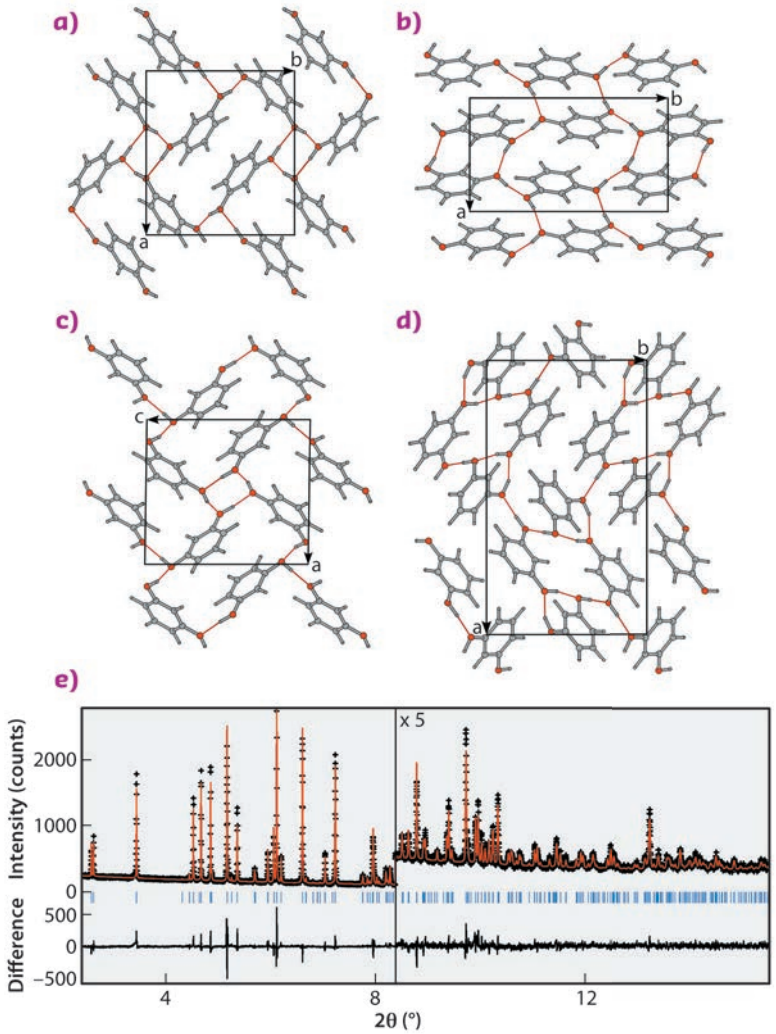

Fig. 60: Resorcinol crystal structures a) α, b) β, c) ε, and d) another low energy phase in the space group $P2_1$, not observed. The views in each case are such that the molecules in any one structure project equal areas onto the plane of the page. e) Rietveld refinement of high-resolution synchrotron powder diffraction for the ε resorcinol sample containing 5 wt.% (2*S*,3*S*)-(-)-tartaric acid crosses) and calculated (red line). R_{wp} = 7.74%, χ^2 = 0.838. Data were collected at beamline ID22 at a wavelength of 0.41064 Å and at a temperature of 200 K. The lower trace shows the difference curve.

PRINCIPAL PUBLICATION AND AUTHORS

Resorcinol crystallization from the melt: a new ambient phase and new "riddles", Q. Zhu (a), A.G. Shtukenberg (b), D.J. Carter (c), T.-Q. Yu (b), J. Yang (b), M. Chen (b), P. Raiteri (c), A.R. Oganov (a), B. Pokroy (d), I. Polishchuk (d), P.J. Bygrave (e), G.M. Day (e), A.L. Rohl (c), M.E. Tuckerman (b,f) and B. Kahr (b), *J. Am. Chem. Soc.* **138**, 4881–4889 (2016); doi: 10.1021/jacs.6b01120.

(a) Stony Brook University (USA)
(b) New York University (USA)
(c) Curtin University (Australia)
(d)Technion Israel Institute of Technology (Israel)
(e) University of Southampton (UK)
(f) New York University Shanghai (China)

REFERENCES

[1] A. Shtukenberg *et al*., *Angew. Chem., Int. Ed*. **53**, 672 (2014).
[2] F. Wallerant, *C. R. Acad. Sci. (Paris)* **143**, 555 (1906).
[3] B. Kahr *et al*. Rohl, *Cryst. Growth Des*. **11**, 2070 (2011).
[4] J.M. Robertson and A.R. Ubbelohde, *Proc. R. Soc. London, Ser. A: Math. Phys. Sci*. **167**, 136 (1938).
[5] J.M. Robertson and A.R. Ubbelohde, *Proc. R. Soc. London, Ser. A: Math. Phys. Sci*. **167**, 122 (1938).
[6] J. Chatchawalsaisin *et al*. *CrystEngComm* **10**, 437 (2008).
[7] A.R. Oganov *et al*., *Acc. Chem. Res*. **44**, 227 (2011).
[8] K. Druzbicki *et al*., J. *Phys. Chem. B* **119**, 1681 (2015).

LIVE SLOW, DIE YOUNG: LIFE HISTORY OF THE EARLY TETRAPOD *ACANTHOSTEGA* REVEALED BY X-RAY MICROTOMOGRAPHY

***Acanthostega gunnari*, which lived 360 million years ago, is one of the earliest fossil tetrapods (four-legged animals). X-ray microtomography scans of its upper arm bone reveal that all the known fossils are juveniles. *Acanthostega* had a long "childhood", spanning at least a decade, during which it lived in the water.**

The evolutionary step from water to land, when fishes evolved into the first four-legged animals or "tetrapods", was a pivotal event in the history of life. All amphibians, reptiles, birds and mammals, including the human race, can trace their ancestry back to the first tetrapods. We can obtain some clues about how the earliest tetrapods lived from their body form and the environments in which their fossils are preserved, but life history data - information about individual age, growth history, sexual maturity and so forth - have been completely absent until now.

We have used the unique capabilities of beamline **ID19** to cast light for the first time on the life history of one of the earliest tetrapods, *Acanthostega gunnari,* which lived about 360 million years ago. The results caught everyone by surprise.

Almost all fossils of *Acanthostega* come from a single locality: a sandstone layer, high up on a Greenland mountainside, which represents a dried-up river channel in a tropical inland delta similar to today's Okavango in Botswana. Dozens of *Acanthostega* skeletons lie packed together in the sandstone, suggesting that they were caught in the drying channel and perished when the water disappeared. *Acanthostega* resembles a small crocodile, about 70 cm long, but has a fish-like tail fin and feeble-looking limbs carrying eight toes each (**Figure 61**).

We used propagation phase contrast synchroton microtomography (PPC-SRμCT) with voxel sizes ranging from 20.24 to 0.638 μm to image the four known humeri (upper arm bones) of *Acanthostega*, focusing especially on the dense outer layer or cortex of the bone (c, **Figure 61**). This cortex can contain annual growth rings, which record the age of the animal. Traditionally, these have been studied by cutting physical thin sections and viewing them under the microscope. By imaging them using PPC-SRμCT, we were able to avoid damaging the unique fossils and have also revealed three-dimensional features that would not have been visible in thin section.

The humeri of *Acanthostega* have between two and six evenly spaced growth rings in the cortical bone (black arrows in **Figure 61**). They

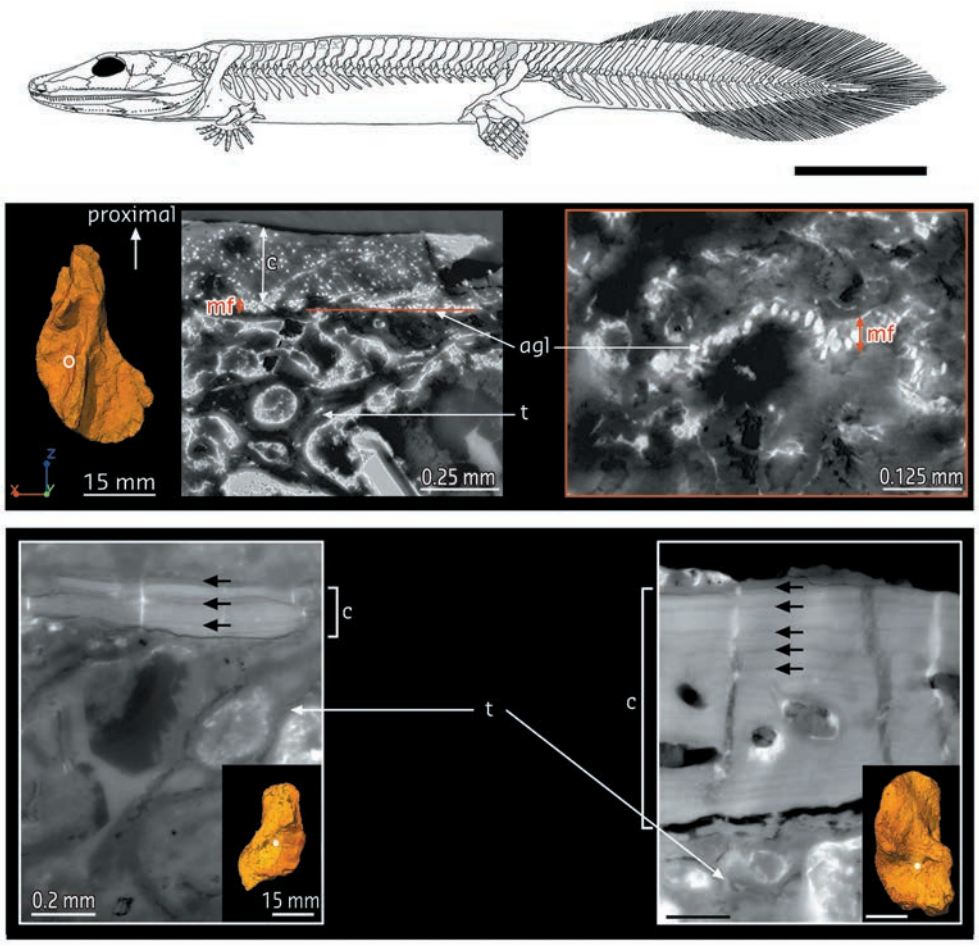

Fig. 61: Top: *Acanthostega gunnari*, from **[1]**. Scale bar, 100 mm. Middle, humerus UMZC T.1295 showing mineralisation front (mf) with remnants of calcified cartilage (agl). Bottom, humeri MGUH 29019 (left) and MGUH 29020 (right) showing cortical growth rings.

also have thin patches of calcified cartilage (agl, **Figure 61**) on the inside of the cortex, just where it joins the spongy interior bone of the humerus. To understand the importance of these features, we need to consider how a humerus grows. It starts out as cartilage, but then two things happen: cortical bone starts to be deposited on the outside of the cartilage, and the cartilage itself first calcifies and is then broken down and replaced by spongy bone (t, **Figure 61**). The removal of the calcified cartilage is not quite complete, so little patches of it remain on the inner face of the cortex (agl, **Figure 61**).

In *Acanthostega,* the cortex is very thin and the presence of calcified cartilage on the inside shows that it has not been remodelled internally. The cartilaginous humerus must thus have reached almost full size before being covered with bone. The onset of bone deposition was followed by up to six years of slow growth that only added a millimetre or so to the overall size of the humerus. *Acanthostega* must thus have had a long "childhood", perhaps spanning a decade or more, during which its limbs were entirely cartilaginous - and thus unsuited to walking on land. The even spacing of the growth rings is an even bigger surprise. In both modern and fossil vertebrates, the onset of sexual maturity is associated with a slowing of growth; this is reflected in the limb bones, where the growth rings become more tightly spaced. This is not yet happening in the *Acanthostega* humeri, so it looks like all four individuals are juveniles.

The implications are startling. It seems that *Acanthostega* had a very long aquatic juvenile phase, and that the mass-death deposit captured a shoal of such juveniles. Nobody has ever seen an adult *Acanthostega*. We don't know how big they became or where they lived. Our results provide a first precious glimpse into the lives of the earliest tetrapods, but also highlight how little we really know about their world.

PRINCIPAL PUBLICATION AND AUTHORS

Life history of the stem tetrapod *Acanthostega* revealed by synchrotron microtomography, S. Sanchez (a,b), P. Tafforeau (b), J.A. Clack (c) and P.E. Ahlberg (a), *Nature* **537**, 408-411 (2016); doi: 10.1038/nature19354.
(a) Science for Life Laboratory and Uppsala University, Evolutionary Biology Centre, Uppsala (Sweden)
(b) ESRF
(c) University Museum of Zoology, Department of Zoology, University of Cambridge (UK)

REFERENCES

[1] P.E. Ahlberg *et al., Nature* **437**, 137-140 (2005).

GETTING TO THE HEART OF FOSSILS

Most of the current knowledge on the evolution of vertebrates comes from fossilised bio-mineralised tissues such as bones and teeth. Very rarely, a fossil will present soft tissue preservation, allowing a leap in our understanding of evolution. This was the case for ca. 115 million year-old fish from Brazil, which were fossilised with their hearts.

The evolution of the chambered heart is a key point in the history of vertebrates. However, there have never been enough clues to elucidate this million-year-old process, since no proper vertebrate cardiac structures were ever described in the fossil record. This is partly because the heart is made from soft muscle tissue, which normally decays rapidly after death and is not preserved, unlike hard tissues such as bones.

The Santana Formation from the Brazilian Northeast is a geologic Konservat Lagerstätte (undisturbed sedimentary deposit), well known for its extraordinary fossils preserved in pristine conditions. From these ca. 115 million year-old sediments, the ray-finned fish *Rhacolepis buccalis* is known from hundreds of specimens, many of which are preserved in 3D in nodular concretions. Over the course of a wider study on potential heart fossilisation, a peculiar concretion was observed in one of these partially damaged fish: the location and shape of the concretion suggested it could have resulted from fossilisation of a heart.

Given the uniqueness that could represent the discovery of a fossilised heart, physical and chemical preparation techniques were excluded, favouring the non-invasive approach of X-ray tomography. To overcome the lack of contrast between this concretion and the surrounding sediment, the fossil was characterised using propagation phase contrast synchrotron X-ray microtomography (PPC-SRμCT) at beamlines **ID17** and **ID19**, along with 60 other fossils of *Rhacolepis* from the same locality, holding hopes for other similar discoveries in unbroken specimens. On both beamlines, the specimens

were characterised using high energetic beam (monochromatic on ID17, filtered white beam from a wiggler on ID19), using long propagation distances (ca. 11 m) and producing data with a resolution of 45 µm. Two of these additional fish showed structures that, when observed in reconstructed data, were undoubtedly identified as fossilised hearts. For these two, a second tomography was performed at 6 µm resolution.

The heart remains were located posterior to gills and between the bones of the pectoral girdle, as in modern ray-finned fishes (**Figure 62**). Their configuration consisting of four distinct chambers (conus arteriosus, ventricle, atrium and sinus venosus), typical ventricular and atrial muscular trabeculae and paired Cuvier duct meeting the posterior-most chamber (sinus venosus). Within this architecture, special interest was given to the conus arteriosus, a conical extension of the ventricle that helps regulate blood outflow via valves.

Modern ray-finned fishes (actinopterygians) present different types of structure responsible for the outflow tract: in basal actinopterygians, such as the freshwater bichir *Polypterus*, the outflow tract is controlled by a dozen valves contained in the conus arteriosus. These valves prevent backflow and protect the delicate gill vessels from the elevated pulsation generated by the ventricle; in derived actinopterygians (*e.g.* the teleost zebrafish *Danio rerio*), this task is rather carried out by an additional cardiac segment, the bulbus arteriosus. This valveless structure protects the gills through its prominent elastic properties. The timing and details of this evolutionary transition in the heart architecture of fishes were almost completely unknown.

The fossilised heart of *Rhacolepis* displays a large conus arteriosus enclosing five conal valves. It contrasts with *Polypterus* in having a significantly reduced number of valves, the latter exhibiting nine valvar rows, each containing three to six individual valves. *Rhacolepis* also notably contrasts with the very limited number of valves observed in modern derived actinopterygians, which vary from one to two. *Rhacolepis* clearly shows an intermediary state between the ancestral multi-valvular condition toward a significant simplification, as known in many modern ray-finned fishes and suggests an overall gradual evolution, rather than an abrupt simplification.

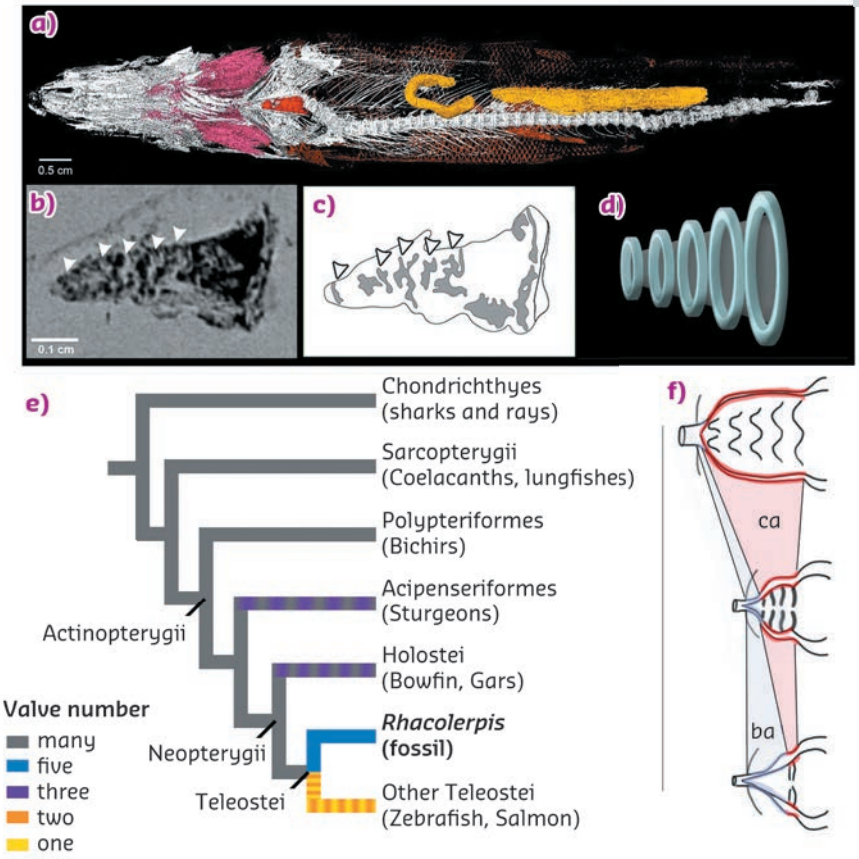

Fig. 62: Fossilised heart of *Rhacolepis*. a) 3D rendering of a complete *Rhacolepis* with various soft tissues preserved, including the heart (in red). b) tomographic slice showing the conus arteriosus in dark, partitioned by five valves (marked by white arrows). c) interpretative drawing of the tomogram. d) idealised, didactic model of the five valve system. e) simplified phylogeny of fishes showing the known number of valves observed in various lineages. f) Interpretative drawing illustrating the simplification of the heart architecture, from an outflow tract dominated by a multi-valved conus arteriosus (ca) at the top, through the only known fossil example with five valves, to the dominant, elastic, non-chambered, condition represented in the bulbus arteriosus in most modern fish (ba).

PRINCIPAL PUBLICATION AND AUTHORS

Heart fossilization is possible and informs the evolution of cardiac outflow tract in vertebrates, L. Maldanis (a,b), M. Carvalho (b,c), M.R. Almeida (d), F.I. Freitas (e), J.A.F.G. de Andrade (f), R.S. Nunes (g), C.E. Rochitte (h), R.J. Poppi (d), R.O. Freitas (g), F. Rodrigues (i), S. Siljeström (j), F. Alves Lima (g), D. Galante (g), I.S. Carvalho (k), C. Alberto Perez (g), M. Rodrigues de Carvalho (c), J. Bettini (l), V. Fernandez (m) and J. Xavier-Neto (b), *eLife* **5**, e14698 (2016); doi: 10.7554/eLife.14698.

(a) Department of Pharmacology, University of Campinas (Brazil)
(b) Brazilian Biosciences National Laboratory, Campinas (Brazil)
(c) Department of Zoology, University of São Paulo (Brazil)
(d) Institute of Chemistry, University of Campinas (Brazil)
(e) Geopark Araripe, Crato (Brazil)
(f) National Department of Mineral Production, Crato (Brazil)
(g) Brazilian Synchrotron Light Laboratory, Campinas (Brazil)
(h) Heart Institute, InCor, University of São Paulo (Brazil)
(i) Institute of Chemistry, University of São Paulo (Brazil)
(j) Department of Chemistry, Materials and Surfaces, SP Technical Research Institute of Sweden (Sweden)
(k) Departamento de Geologia, Universidade Federal do Rio de Janeiro (Brazil)
(l) Brazilian Nanotechnology National Laboratory, Campinas (Brazil)
(m) ESRF

REAL-TIME X-RAY IMAGING OF SILICON WAFER FRACTURE

Fracture and breakage of single crystal silicon wafers is a severe problem for the semiconductor industry leading to million dollar costs. It is a fast and multi-lengthscale process. Crack propagation has been observed for the first time *in situ* simultaneously by direct transmission and diffraction X-ray imaging. The movies reveal the dynamics of strain and provide visualisation of the crack tip with a time resolution of µs/frame.

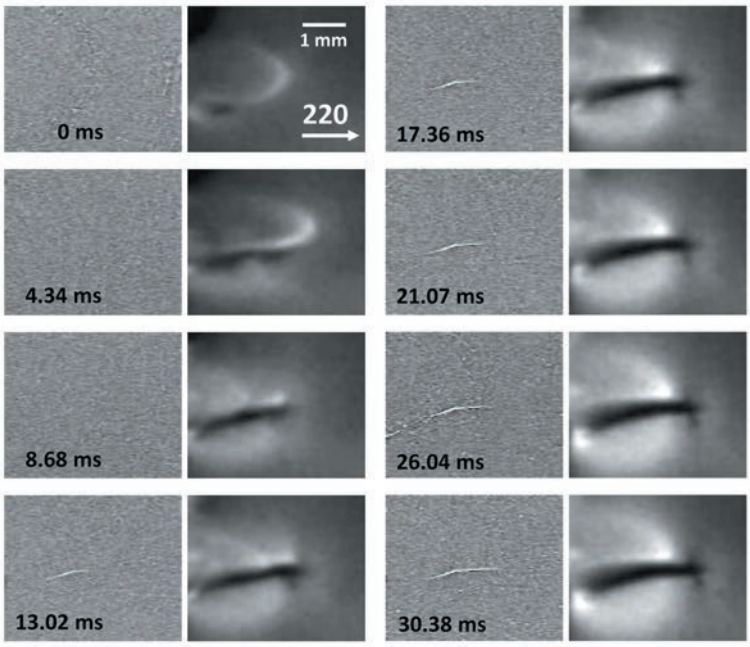

Fig. 63: Selected images from a series of 3000 showing crack propagation in a silicon wafer under thermal stress. In each pair of images, the direct transmission image is on the left and the diffraction image with the 220 reflection is on the right.

Wafer breakage during high temperature processing is a severe problem in semiconductor device manufacturing. Silicon wafers typically contain microcracks resulting from handling or shipping. Catastrophic total wafer breakage may result from such microcracks during thermal processing in semiconductor manufacturing and it is an increasingly expensive hazard for production [1]. The direct observation of cracks is a challenge because cracks can propagate in silicon with speeds of up to 1500 m/s and 3500 m/s along {110} and {111} cleavage planes respectively. Especially irregular fracturing may result in catastrophic wafer shattering, producing many small irregular pieces instead of cleaving into two pieces with smooth {110} faces.

Unprecedented temporal resolution with X-ray imaging can be reached at synchrotron light sources thanks to high-speed cameras and polychromatic illumination [2]. Recently, mechanically induced cracks in glass could be depicted by "single-bunch imaging" with exposure times short enough to exploit the pulsed time-structure of the ESRF X-ray source. We have now combined direct transmission imaging with Laue topography at beamline **ID19** to successfully track crack propagation in silicon wafers: an indirect detector acquired images in radiographic mode of the crack propagation by means of phase contrast and an intensifier-based detector coupled *via* a lens-system to a CMOS camera recorded images of the 220 reflexion from the same event (both detectors used a 1.28 µs exposure time, ca. 35,500 images/s frame rate limited only by the camera).

To create reproducible starting conditions for the cracks, standard (001) silicon wafers were damaged artificially using the nano-indentation technique. Subsequently, to induce thermal stresses

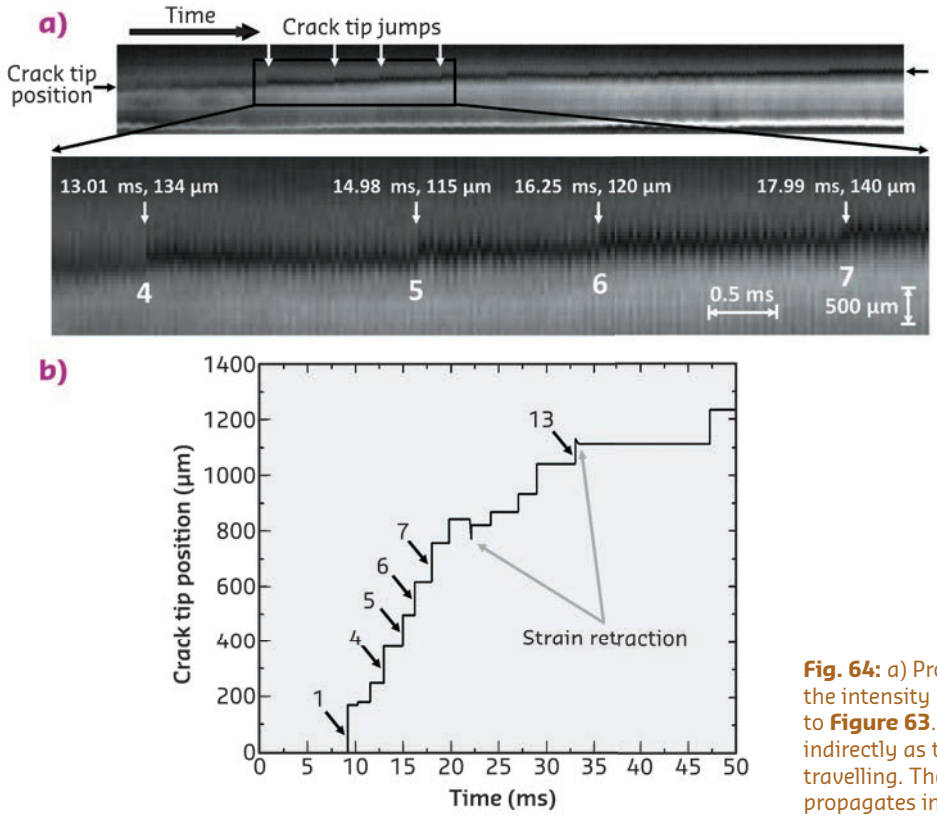

Fig. 64: a) Propagation of the crack tip as derived from the intensity profiles for all frames of the movie related to **Figure 63**. The position of the crack tip can be tracked indirectly as the tip changes the grey levels locally while travelling. The magnified region shows that the crack propagates in jumps. b) A plot of the crack tip position *vs* time.

and initiate cracking from an indent, the silicon wafer was heated up to about 1000°C by a gas burner and then quenched with a water jet while the movies were acquired. The increase of strain fields in a hot silicon wafer induced by water was resolved from the moment before new cracks nucleate until propagation stops. **Figure 63** shows selected direct transmission and diffraction images of a relatively slow-growing crack. The first segment nucleates at the indent which is outside the region of interest. The inclined part deflects into the horizontal part which runs, at the front surface of the wafer, perfectly parallel to crystal plane [1-10]. With an acquisition rate of 35,511 images/s, the temporal spacing between two frames was 28.1 µs. The first image shown was taken after the first water droplets hit the hot wafer, *i.e.* thermal stress is already present. Single water droplets as well as water wavefronts are visible in the direct transmission images.

Further details about the dynamics of the propagation of crack are revealed when looking at intensity profiles: the position of the crack tip is accessible indirectly, *i.e.* by the local change of the grey-level intensity of the strain related contrast while the tip propagates. In **Figure 64** these profiles are plotted as a function of time for the movie related to the pictures shown in **Figure 63**, starting with the frame where the first indication of a crack appears. The position of the crack tip is associated with the marked black region. Two features are visible immediately: (i) high-frequency oscillations due to vibrations of the wafer related to the impinging water and (ii) strong discontinuities (4 out of 13 are marked with white arrows). The latter clearly indicate that the crack does not propagate with constant velocity. Hence, the mean slow propagation speed observed (of about 0.055 m/s) results from pinning and reinitiating of the fast propagation of the crack tip.

Real-time imaging with two high speed detector systems is a big step towards "truly real-time" imaging and the *in situ* study of processes in the 100-picosecond range. Studying cleavage and fracture in single crystals becomes possible in a combined direct visualisation and diffraction mode and the power of such high speed imaging has been demonstrated by the example of silicon wafer fracture.

PRINCIPAL PUBLICATION AND AUTHORS

Real-time direct and diffraction X-ray imaging of irregular silicon wafer breakage, A. Rack (a), M. Scheel (b) and A.N. Danilewsky (c), *IUCrJ* **3**, 108-114 (2016); doi: 10.1107/S205225251502271X.
(a) ESRF
(b) Synchrotron Soleil, Gif sur Yvette (France)
(c) Crystallography, Albert-Ludwigs Universität Freiburg (Germany)

REFERENCES

[1] B.K. Tanner *et al., International Journal of Fracture* **195**, 79 (2015).
[2] A. Rack *et al., Journal of X-ray Science and Technology* **18**, 429 (2010).

TRACKING THE EVOLVING ARCHITECTURE OF ACTIVE MATERIALS WITHIN LITHIUM BATTERIES

High-speed *operando* X-ray computed tomography (CT) was used to capture the morphological evolution of active materials within a primary Li/MnO_2 battery during discharge. The local displacement of materials within the battery was quantified in 3D by correlating sequential tomograms using digital volume correlation (DVC), revealing degradation mechanisms and causes of performance loss.

Owing to their high energy and power density, lithium batteries are the technology of choice for applications that require compact, reliable, and high-performance energy-storage devices, such as emergency signal transmitters, and other systems in the aerospace, military and communications sectors. Understanding the causes of performance loss such as degradation mechanisms that occur during operation is a significant step towards engineering batteries with improved performance, reliability and safety. However, the degradation that stems from the dynamic changes to the internal architecture of a cell during operation remains poorly understood.

Volumetric expansion of the positive electrode occurs when lithium inserts into electrode materials (lithiation). The chemo-mechanical forces associated with lithiation can cause significant degradation, for example causing electrical isolation of the electrode from the current collector or particle cracking. Characterising the local dilation and displacement

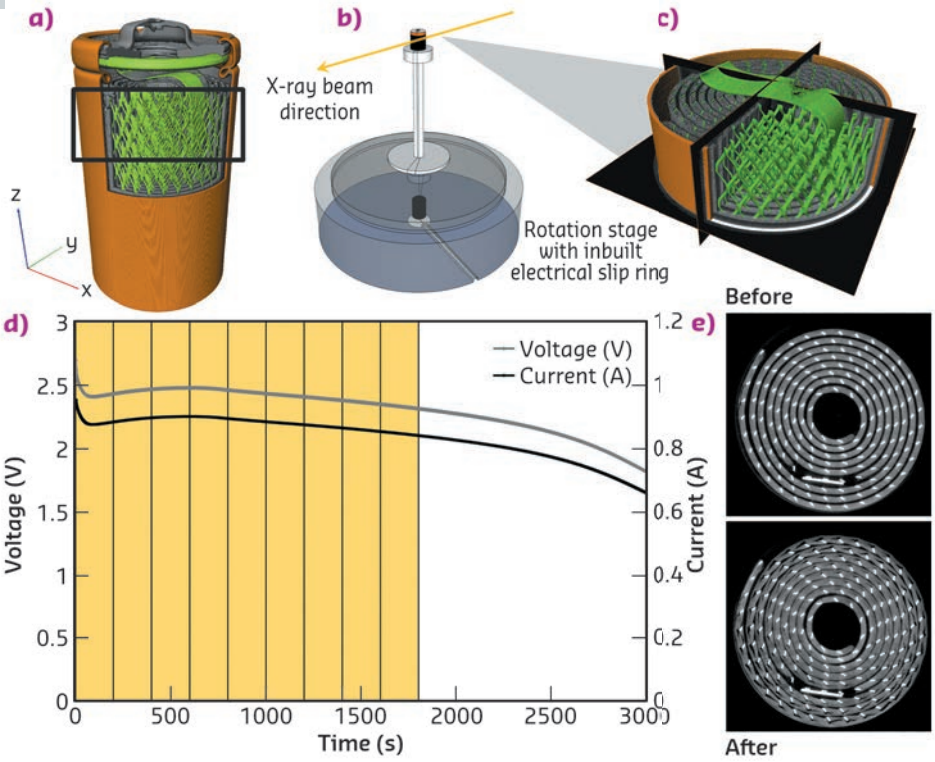

Fig. 65: a) Full Duracell CR2 battery. b) ID15A rotation stage with in-built electrical slip-ring for *operando* X-ray CT. c) Volume that was imaged during *operando* CT showing current collector (green) and MnO_2 electrode (grey). d) Discharge profile marking lapsed time between sequential tomograms used for DVC. e) *XY* slices from tomograms taken before and after discharge (excluding cell casing), showing the damaged MnO_2 electrode.

of electrode material during operation would help progress towards designing cells that cater for dynamic structural evolution, and mitigate degradation and performance loss.

The high-speed X-ray CT imaging capabilities of the ESRF present a great opportunity for non-destructive imaging of morphological evolution of active materials during cell operation. *Operando* X-ray CT has been demonstrated as a powerful diagnostic tool for battery degradation **[1]**. Image correlation techniques such as digital volume correlation (DVC), that quantify the displacement of features between consecutive tomograms, greatly complement the high acquisition rates of synchrotrons, presenting scope for performing 4D (3D with time) strain profiling of deforming materials; this has been shown to be particularly useful for identifying limitations of lithium ion batteries **[2]**. Here, we capture the morphological evolution of the spiral-wound electrode architecture of a commercial Li/MnO_2 Duracell CR2 cell during a high-rate discharge (**Figure 65**). The high photon flux of beamline **ID15A** allowed fast acquisition of tomograms (**Figure 65c**) at various stages during discharge of the cell (**Figure 65d**).

Severe delamination of the MnO_2 electrode material from the current collector started to develop at early stages of the discharge process, increasing the electrical resistance of the cell and significantly affecting its performance. To gain insight into the cause of delamination, consecutive tomograms were correlated using DVC to quantify the local displacement of electrode material over time. 3D strain maps that show the transient local displacement of the electrode during operation (**Figure 66a,b**) were generated. A significant portion of the MnO_2 electrode was shown to be inactive, particularly at the ends of the spiral wound layer (regions A and B in **Figure 66b**). Using DVC, the progression

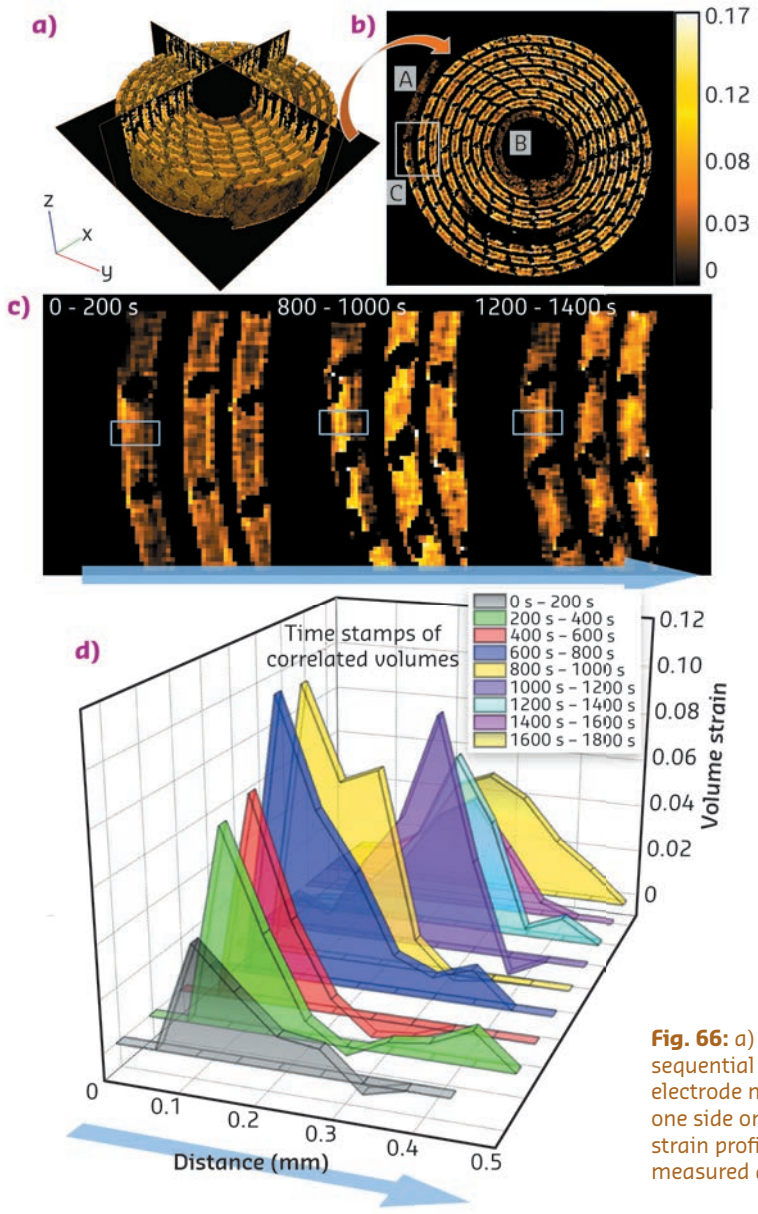

Fig. 66: a) Reconstruction of volumetric strain. b) XY slice from DVC of sequential tomograms during discharge. Regions A and B show areas where electrode material is inactive and C highlights where lithiation occurs from one side only. c) Magnified views of region C showing evolving volumetric strain profile with boxed (blue) regions of interest. d) Evolution of strain measured across the boxed regions in (c).

of lithiation through the MnO_2 layer was tracked; a displacement front that is representative of the dilation and hence lithiation of the MnO_2 is observed (**Figure 66c,d**), highlighting that the cell is limited by ion transport.

Furthermore, the chemo-mechanical effect of the dilating electrode on the mechanical environment of the cell is revealed. As well as highlighting the importance of the design of lithium batteries to accommodate changing cell architectures, this study has also demonstrated the combination of high-speed *operando* X-ray CT and image correlation techniques as an effective means to identify degradation and causes of performance loss within operating cells.

PRINCIPAL PUBLICATION AND AUTHORS

Quantifying bulk electrode strain and material displacement within lithium batteries via high-speed operando tomography and digital volume correlation, D.P. Finegan (a), E. Tudisco (b), M Scheel (c,d), J.B Robinson (a), O.O Taiwo (a), D.S. Eastwood (e,f), P.D. Lee (e,f), M. Di Michiel (c), B. Bay (g), S.A. Hall (b), G. Hinds (h), D.J.L. Brett (a) and P.R. Shearing (a), *Adv. Sci.* **3**, 1500332 (2016); doi: 10.1002/advs.201500332.

(a) Electrochemical Innovation Lab, Department of Chemical Engineering, University College London (UK)
(b) Division of Solid Mechanics, Lund University (Sweden)
(c) ESRF
(d) Synchrotron Soleil, Gif-sur-Yvette (France)
(e) Manchester X-ray Imaging Facility, School of Materials, University of Manchester (UK)
(f) Research Complex at Harwell, Didcot (UK)
(g) School of Mechanical Industrial and Manufacturing Engineering, Oregon State University (USA)
(h) National Physical Laboratory, Teddington (UK)

REFERENCES

[1] M. Ebner *et al.*, *Science* **342**, 716-720 (2013).
[2] D.S. Eastwood *et al.*, *Advanced Energy Materials* **4**, 57 (2014).

MAPPING THE FRONT OF A LOCALISED DEFORMATION BAND IN NiTi WIRE WITH 3D-XRD

The nature of localised superelastic deformation of NiTi wires in tension has been revealed with the help of the 3D-XRD method.

Although polycrystalline solids usually deform homogeneously, some materials tend to form macroscopic bands in which inelastic deformation is localised. These bands may form at the onset (Lüders bands) or at the end (shear bands) of plastic deformation. The interface between the deformed and undeformed material (band front), where the material continuity and strain compatibility has to be maintained, can be either mobile (Lüders bands) or sessile (necking). Localised deformation has always attracted the attention of mechanical engineers as well as theoreticians involved in the modelling of material deformation. Strain localisation is intrinsically a macroscopic phenomenon, governed by the rules of mechanics, though actual deformation mechanisms as well as the microstructure and texture of the material are known to play a role.

As an example, superelastic deformation of NiTi shape memory alloy under tension proceeds frequently via the propagation of martensite band fronts **[1,2]**. In flat sheet samples, the interface between the deformed and undeformed material is planar, sharp and inclined at an angle of about 55° to the loading direction. The front spreads over thousands of polycrystal grains. For wires

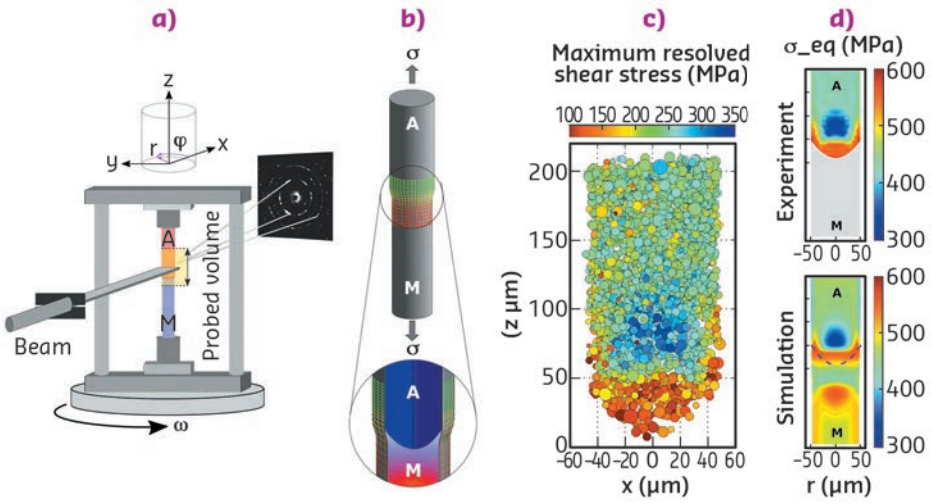

Fig. 67: The 3D-XRD method was used to evaluate grain microstructure and grain-resolved stresses within a martensite band front propagating in a polycrystalline NiTi wire exposed to external stress.

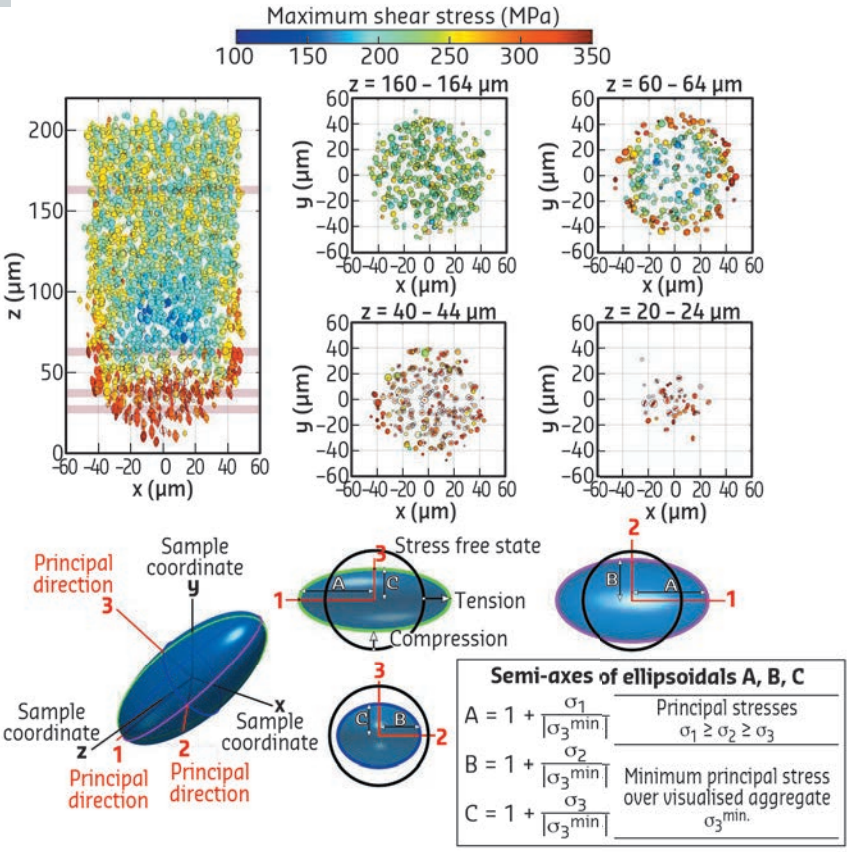

Fig. 68: Stress states in polycrystal grains of tensioned NiTi wire visualised using a tensor imaging approach (stress glyph). Ellipses visualise stress tensors in grains as 2D projections of ellipsoids with semi-axes A,B,C in the principal stress directions. The shape and inclination of an ellipse denote stress state in a single grain, colour denotes the maximum shear stresses and the black circle denotes the size of a grain at a given position.

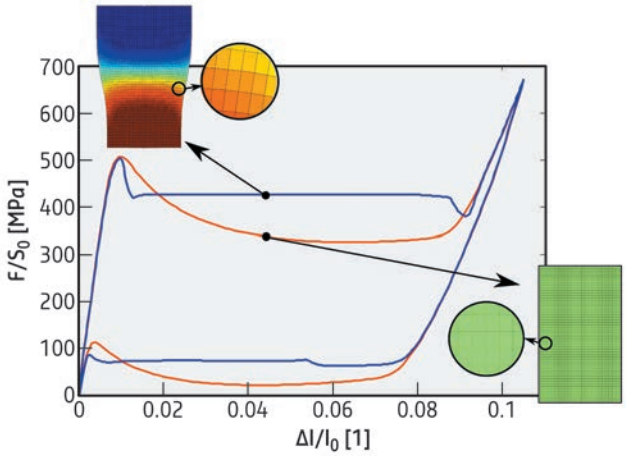

Fig. 69: Stress-strain response of superelastic NiTi wire in tension simulated by an FE implemented SMA model **[5]** - macroscopic response (blue curve) and constitutive response in each material point (red curve).

and bars, however, the interface appeared to be broad and perpendicular to the loading direction **[3]**, which was curious. Since the martensite band front in superelastic NiTi disappears on unloading, conventional microscopic methods could not be used to reveal the shape of the buried interface. Internal stresses around the moving fronts were completely unknown.

High-energy synchrotron X-rays are an ideal tool to look deep inside bulk materials during loading tests **[4]**. By applying the 3D X-ray diffraction method, 3D-XRD (**Figure 67a**), at beamline **ID11**, we managed to determine the full strain and stress tensors in ~15000 austenite grains (mean grain size 5.9 µm) within a martensite band front (**Figure 67b-d**) in a 0.1 mm diameter NiTi wire stabilised by the applied tensile stress of ~420 MPa (**Figures 67**, **68**).

The martensite band front has a shape of a buried nose cone internal interface surrounded by an internal stress field (**Figure 67b-d**). It appeared that the local stresses in grains ahead of the advancing front redistribute in such a way that the grains located at the interface experience very different stress states (**Figure 68**) compared to the grains far from the interface (~200 MPa higher effective stresses). Consequently, the grains within the front transform collectively, while very little is happening elsewhere. The widespread assumption in the literature that the martensitic transformation in NiTi wire takes place under nominal tensile stress F/S_0 was thus shown to be incorrect. Because the superelastic deformation via the martensitic transformation is limited to a few percent by the crystallography, the martensite band front moves under constant force along the wire (**Figure 69**).

Superelastic deformation of NiTi wire was also simulated by a finite element implemented constitutive shape-memory alloy model adapted for nonlocal effects **[5]**. Force - elongation response was predicted (**Figure 69**) and the moving front was reconstructed (**Figure 67d**) confirming the sharp internal stress gradients.

PRINCIPAL PUBLICATION AND AUTHORS

Grain-resolved analysis of localized deformation in nickel-titanium wire under tensile load, P. Sedmák (a,b), J. Pilch (a), L.Heller (a), J. Kopeček (a), J. Wright (c), P. Sedlák (d), M. Frost (d) and P. Šittner (a), *Science* **353**, 559-562 (2016); doi: 10.1126/science.aad6700.
(a) Institute of Physics of the CAS, Prague (Czech Republic)
(b) FNSPE CTU, Prague (Czech Republic)
(c) ESRF
(d) Institute of Thermomechanics of the CAS, Prague (Czech Republic)

REFERENCES

[1] J.A. Shaw, *Int. J. Plast.* **16**, 541–562 (2000).
[2] P. Šittner *et al.*, *J. Mech. Phys. Solids* **53**, 1719–1746 (2005).
[3] L. Dong *et al.*, *Int. J. Solids Struct.* **80**, 445–455 (2016).
[4] H.F. Poulsen, Three-dimensional X-ray Diffraction Microscopy: Mapping Polycrystals and Their Dynamics Springer, Berlin (2004).
[5] P. Sedlák *et al.*, *Int. J. Plast.* **39**, 132–151 (2012).

ORGANIC-INORGANIC X-RAY DETECTORS

Indirect flat-panel X-ray detectors provide limited resolution due to optical cross-talk. Here, a concept is presented whereby inorganic scintillating particles are embedded in an organic semiconductor matrix which effectively eliminates the optical cross-talk and increases the resolution. Experiments at the ESRF helped to gain knowledge on the device's morphology.

Radiography is an essential diagnostics branch in medicine. In projection radiography, the human body is exposed to X-rays and their transmitted intensity is captured by a detector. For decades radiologists have employed photographic paper as the detector. In spite of the introduction of solid state X-ray detectors, their full adoption has been hindered by the high cost. Researchers are now trying to develop low-cost and high-resolution flat-panel detectors for the energy range between 20 and 120 keV. Today's digital X-ray detectors mainly consist of a scintillator layer that converts X-rays into visible light and an imaging sensor that converts light into electrical signals. Apart from the high manufacturing costs, these detectors also have the disadvantage that the generated light propagates isotropically as it passes through the scintillator layer. As a consequence, the light hits a large number of adjacent pixels instead of hitting only one pixel of the image sensor. This results in a loss of spatial resolution.

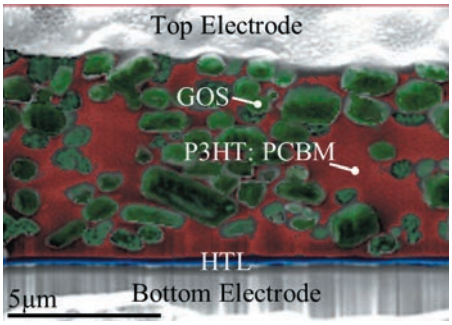

Fig. 70: Scanning electron microscopy (SEM) image of the device cross-section in false colour showing scintillating terbium-doped gadolinium oxysulfide (GOS: Tb) macroparticles (green) embedded in poly(3-hexylthiophene-2,5-diyl)) (P3HT) and phenyl-C61-butyric acid methyl ester (PCBM) bulk-heterojunction (red). HTL is the hole-transporting layer.

In our hybrid approach, this problem has been solved by embedding the scintillator directly into a blend of organic semiconductors (bulk-heterojunction), which acts as a photodiode converting light into electrical charges (**Figure 70**). This gives the emitted light no opportunity to become widely spread and a high spatial resolution is obtained. Manufacturing costs are kept low thanks to effortless and effective spray deposition.

Grazing-incidence wide-angle X-ray scattering (GI-WAXS) measurements performed at beamline **BM28** (XMaS CRG) played an important role in understanding the device physics. **Figure 71** shows diffraction images of P3HT: PCBM: GOS films at different concentrations. We observe a structural interplay between P3HT and GOS during thermal treatment. The amount of P3HT face-on lamellae increases with GOS concentration, which explains the increase in mobility measured by X-ray induced charges probed by X-ray charge carrier extraction by linearly increasing voltage (X-CELIV).

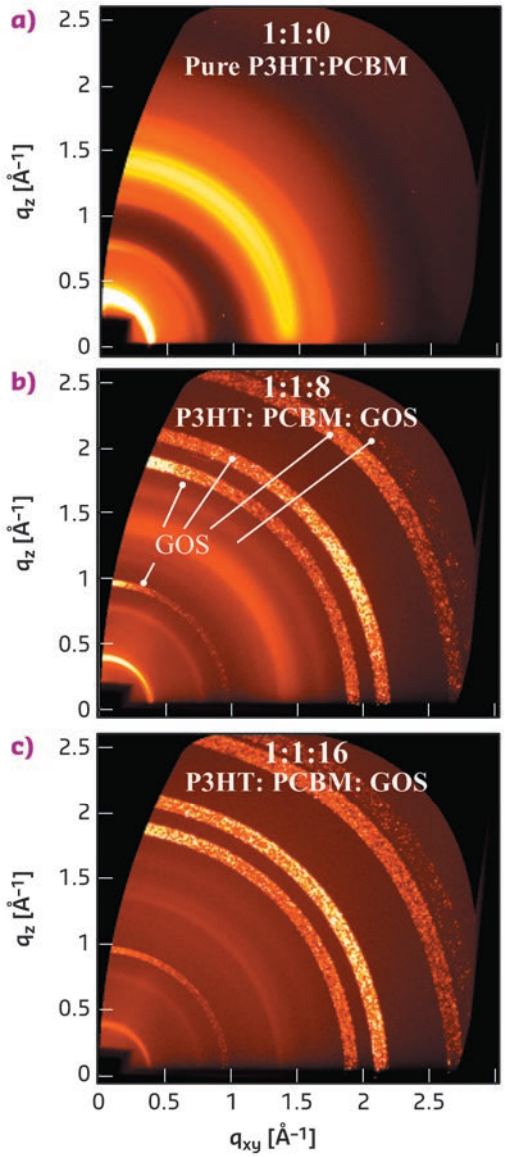

Fig. 71: GI-WAXS images of thermally annealed P3HT: PCBM: (GOS:Tb) films at different concentrations.

PRINCIPAL PUBLICATION AND AUTHORS

X-ray imaging with scintillator-sensitized hybrid organic photodetectors, P. Büchele (a,b), M. Richter (c), S.F. Tedde (a), G.J. Matt (c), G.N. Ankah (d), R. Fischer (a,c), M. Biele (a,c), W. Metzger (a), S. Lilliu (e), O. Bikondoa (f,g), J.E. Macdonald (h), C.J. Brabec (c), T. Kraus (d), U, Lemmer (b) and O. Schmidt (a), *Nature Photonics* **9**, 843–848 (2015); doi: 10.1038/nphoton.2015.216.

(a) Siemens Healthcare GmbH, Technology Center, Erlangen (Germany)
(b) Light Technology Institute and Institute of Microstructure Technology, Karlsruhe Institute of Technology (Germany)
(c) Institute of Materials for Electronics and Energy Technology (i-MEET), Friedrich-Alexander-University Erlangen-Nuremberg, Erlangen (Germany)
(d) INM – Leibniz Institute for New Materials, Saarbruecken (Germany)
(e) Masdar Institute of Science and Technology, Abu Dhabi (UAE)
(f) XMaS, The UK-CRG Beamline, ESRF, Grenoble (France)
(g) Department of Physics, University of Warwick, Coventry (UK)
(h) School of Physics and Astronomy, Cardiff University (UK)

Structural biology

As noted in the introduction to the Structural Biology Chapter in last year's ESRF Highlights, 2015 marked the end of the UPBL10 project carried out within Phase I of the ESRF Upgrade Programme. Once all four end-stations constructed during UPBL10 had entered full operation, we had hoped that 2016 would be a year of quiet consolidation and evolution of the ESRF facilities for Structural Biology. In fact, 2016 has proved to be an extremely busy year for the group, its beamlines and its user community. Indeed, the financial and human resources released by the completion of UPBL10 meant we could now turn our attention to several major projects that had been either put on hold in recent years or were required to improve the service we offer to our external user community.

The first major development of 2016 was the completion and approval of the Technical Design Report (TDR) for the ID23-2 nanobeam project, which is now underway. ID23-2 was the world's first microfocus beamline (focal spot ~5 x 7 μm^2 at the sample position) dedicated to macromolecular crystallography (MX), producing many important crystal structures, including those of G-protein coupled receptors (GPCRs). The nanobeam project, due for completion in May 2017, will see this focal spot size complemented by a much smaller spot ~1 µm in diameter, providing new opportunities in protein microcrystallography including in the relatively new technique of synchrotron serial crystallography (SSX). The second major project launched in 2016 was a campaign to replace all of the ageing SC3 sample changers with high-capacity FlexHCD devices following initial prototyping of the device on ID30B. The increased capacity and reliability of the FlexHCD – now also installed on ID23-1 and ID29 with ID23-2 and ID30A-3 waiting in the wings – will be a long-awaited benefit to our users that we hope will also result in increased remote access to our beamlines. Nevertheless, please spare a thought for the soon to be discarded SC3s. While they sometimes received a relatively bad press, particularly in recent years, they did revolutionise sample mounting at the ESRF. Indeed, in the 10 years in which they were in operation, they mounted, dismounted (and occasionally dropped!) around 500,000 samples and we probably should remember them more fondly than history might eventually record. The third major project started in 2016 marks a significant new direction for Structural Biology at the ESRF – the purchase of a start-of-the-art cryo-electron microscope. During the coming year (first external users are foreseen for the Autumn of 2017) the microscope will be installed in the Belledone experimental hall extension where it will be operated as a 'beamline' and form part of a newly-established Partnership for Structural Biology (PSB) platform for cryo-electron microscopy (cryo-EM). The creation of this PSB platform will provide two major benefits to our user community: operation of the microscope will be supported by staff from the Grenoble-based institutes, the ESRF, the IBS and the EMBL Grenoble Outstation; external ESRF users requiring cryo-EM as a vital component of their projects will eventually also have access to several other microscopes at both the IBS and the EMBL Grenoble Outstation. The conception and planning of this project has been a huge undertaking for the ESRF and its PSB partners and it may not have come to fruition if it were not for the excellent support we received from our external user community. For this, many thanks are due.

Despite the efforts and resources required to ensure the success of the projects referred to above, 2016 *did* see much of the hoped-for consolidation and evolution of our facilities. Many 'minor' improvements to our beamlines included improved omega axis rotation speed (now 720°/second) on ID29; the implementation of faster mesh scans on ID30B; the processing of the 25,000th sample on the completely automatic end-station ID30-A1 and the rolling out of the ID30A-1 workflows to ID30A-3 and ID30B; the full integration of the EIGER 4M detector on ID30A-3 (data collection at 750 Hz frame-rates is now possible); the continuing refurbishment of the ID29S Cryobench, now also equipped with an MD2M minidiffractometer and SC3 sample changer (at least one will survive!); the provision of storage areas for samples at both cryogenic and ambient (20°C) temperatures; the provision of a new data backup and processing facility.

In 2016, our beamlines have also been scientifically productive and, as in previous years, the highlights reported here cover a wide range of structural biology research, published in high-impact journals. The selection showcases the many strengths of our beamlines in facilitating high quality science that has allowed, amongst a plethora examples not included here, a fuller understanding of the molecular basis of GPCR-based signalling systems, neurotransmission, transcriptional activation in plants, the life-cycle of the influenza polymerase, natural product biosynthetic pathways, the formation of DNA

origami switch devices, the synthesis of proteins in eukaryotic cells, protein manufacture, the evolution of DNA polymerases, the synthesis of the universal nicotinamide adenosine dinucleotide cofactor, the inhibition of norovirus by human milk oligosaccharides, the inhibition of potential oncology targets and the control phosphate homeostasis in eukaryotic cells.

2016 has also been a year of looking forward, not just to 2017 but to the long-term future of Structural Biology at the ESRF. Although cryo-EM will play a large part in this future, X-rays will by no means be less relevant, particularly following the ESRF-EBS Upgrade. To ensure that future generations of scientists continue to benefit from the ESRF's world-leading expertise in providing experimental facilities for MX, we recently proposed plans, in the form of an EBS conceptual design report (CDR 8), for the evolution of ID29 that we hope will culminate in the construction of an ultra-high flux (~10^{16} photons/sec) microfocus facility for SSX and time-resolved MX. Next year, we hope to be able to report that such a beamline will be part of the long-term future of the ESRF.

Finally, 2016 has seen the closure of BM14 as an MX facility. Lately operated as an ESRF/EMBL/India collaboration, but first opened in 1996, BM14 helped popularise the use of MAD in MX and catalysed the explosion of structural biology as a scientific discipline at the ESRF. The beamline will be missed by many in our field.

G. LEONARD *and*
C. MUELLER-DIECKMANN

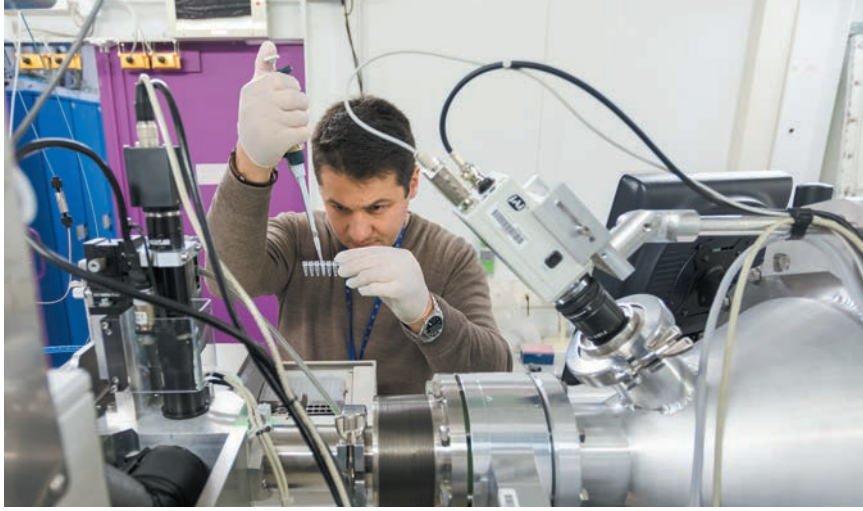

THE STRUCTURE OF AN ACTIVATED G PROTEIN-COUPLED RECEPTOR BOUND TO AN ENGINEERED G PROTEIN

Development of an engineered G protein, mini-G_s, has simplified the structure determination of a mini-G_s-bound G protein-coupled receptor (GPCR) in a fully-active state. Similar strategies can now be applied to other GPCRs, which will advance our understanding of GPCR mechanism and facilitate structure-based drug design.

G protein-coupled receptors (GPCRs) are integral membrane proteins found at the surface of every cell in the human body. They are essential constituents of the molecular signalling system that choreographs the interplay between all our internal organs so that we can function as human beings. There are about 750 different GPCRs encoded by the human genome and they are responsible for all aspects of physiology involving intercellular communication. The adenosine A_{2A} receptor ($A_{2A}R$) is activated by adenosine, a cytoprotective modulator that is released during the stress response of an organ or tissue. The receptor is inhibited by drugs such as caffeine and is a potential target for the treatment of Parkinson's disease, attention deficit hyperactivity disorder (ADHD) and in combination therapies for cancer.

Over the past 10 years there has been an explosion in our understanding of the molecular details of the structure of GPCRs. This has facilitated an in-depth understanding of how an agonist, such as adrenaline, binds to a receptor and alters its structure to facilitate the formation of an activated state that can, in turn, bind to a G protein. The G protein is then itself activated and can directly interact with other proteins that increase or decrease the concentrations of intracellular secondary messengers such as cAMP and Ca^{2+} that alter cellular function. To understand in structural terms how a receptor works we need to have at least two structures of any given GPCR: a structure of the receptor in the inactive state bound to an antagonist and a structure in the activated state bound to a G protein. Structure determination of GPCRs in the inactive state is challenging, but is possible due to the development of many protein engineering strategies that stabilise receptors during crystallisation. The inactive state of a GPCR is invariably more stable than the activated state where the intracellular surface of the receptor opens up to allow the binding of a G protein. Thus, the activated states of GPCRs are much more difficult to determine.

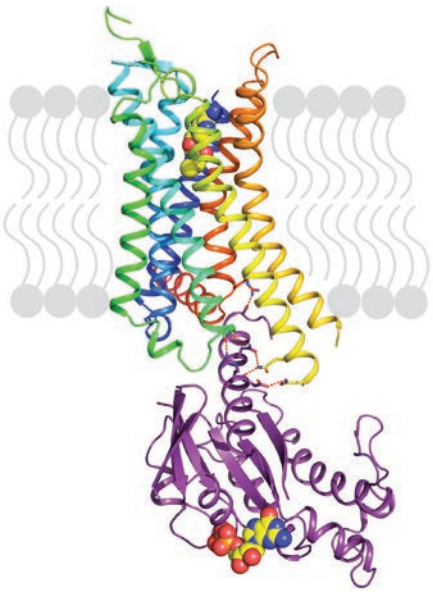

Fig. 72: Structure of agonist-bound $A_{2A}R$ coupled to mini-G_s. The receptor is shown in rainbow colouration (N-terminus blue, C-terminus red) and is bound to the agonist NECA (shown in spheres). Mini-G_s is shown in purple with specific hydrophilic contacts to $A_{2A}R$ shown as red dashed lines and the molecule of bound GDP shown in spheres.

Our previous work demonstrated that thermostabilising a GPCR can facilitate its structure determination, regardless of the affinity of the ligand bound to the receptor and whether this is an agonist or antagonist. This has also opened the door for the first time to structure-based drug design applied to GPCRs. However, in order to crystallise the active state of a receptor it must be bound to a G protein or a functional mimetic such as a nanobody. Heterotrimeric G proteins are large (90 kDa) multi-subunit proteins that are both unstable and conformationally dynamic when coupled to a GPCR. We therefore developed a novel minimal G protein, mini-G_s, in which the single G protein domain that mediates virtually all the contacts with the GPCR was isolated and thermostabilised **[1]**. Mini-G_s is only 28 kDa in size and produces all the pharmacological effects of a heterotrimeric G protein binding to a GPCR. However, because mini-G_s is small and thermostable, the complex it formed with $A_{2A}R$ was amenable to crystallisation in a short chain detergent, octylthioglucoside, by vapour diffusion. Following data collection at beamline **ID23-2**, the structure (**Figure 72**) was determined to 3.4 Å resolution and provided the molecular details of how mini-G_s binds to $A_{2A}R$. It also gave a clear view of the ligand binding pocket in the activated state. The latter was surprising as it appeared virtually identical to a previously determined structure in the absence of bound G protein, thus suggesting that the energy landscape of different receptors such as $A_{2A}R$ and the β_2-adrenergic receptor (β_2AR) are very different. The molecular details of how mini-G_s binds to $A_{2A}R$ also differ in some aspects to how G_s binds to β_2AR, despite the overall

topologies being virtually identical. This is to be expected given the different amino acid sequences between the two receptors.

The structure of $A_{2A}R$ bound to mini-G_s starts to provide a description of the molecular determinants of specificity in GPCRs that dictate which G protein it couples to. There are only 16 different Gα subunits expressed in humans compared to over 750 GPCRs, often with multiple different GPCRs and G proteins all being expressed in the same cell, and multiple different G proteins coupling to a single GPCR. A major challenge in the field is thus to understand how the complex interplay between structural determinants, kinetics and sub-cellular distribution results in the signalling characteristics of GPCRs within specific cell types.

PRINCIPAL PUBLICATION AND AUTHORS

Structure of the adenosine A2A receptor bound to an engineered G protein, B. Carpenter, R. Nehmé, T. Warne, A.G.W. Leslie and C.G. Tate, *Nature* **536**, 104-107 (2016); doi: 10.1038/nature18966.
MRC Laboratory of Molecular Biology, Cambridge (UK)

REFERENCES

[1] B. Carpenter and C.G. Tate, *Protein Eng. Des. Sel.*, 1-11 (2016) doi: 10.1093/protein/gzw049.

STRUCTURE OF THE LIGAND-BINDING DOMAIN OF THE KAINATE RECEPTOR GluK4

Ionotropic glutamate receptors play a key role for fast neurotransmission in the central nervous system and have been linked to several neurological diseases [1]. One subfamily of ionotropic glutamate receptors is the kainate receptors that are grouped into low-affinity (GluK1-3) and high-affinity (GluK4-5) receptors. Until recently, no structures were available of the ligand-binding domain of high-affinity receptor subunits. Here, the X-ray structure of the ligand-binding domain of GluK4 with kainite has been solved.

This study provides an example of the strength of combining high-throughput crystallisation and data collection when only small amounts of protein are available and crystal growth is not straightforward. A soluble construct of the ligand-binding domain of GluK4 (GluK4-LBD; Uniprot entry Q01812, residues 415-527 and 652-790 connected via a three residues (KGT) linker) was expressed in insect cells (Hi-5). The KGT linker keeps the parts together that in the full-length receptor are connected to the transmembrane region. A strepII affinity tag attached to the N-terminus of GluK4-LBD was inserted to facilitate purification. Crystallisation screening of GluK4-LBD with kainate was performed at the EMBL HTX Lab, Grenoble, in sitting-drop vapour diffusion experiments at 4°C. Only small crystal clusters could be obtained and the observed X-ray diffraction patterns obtained at beamline **ID30-A1** (Massif-1) were clearly a result of multi-lattice diffraction from the crystal cluster. However, we managed to process the data to 2.05 Å resolution using Xia2 (version 3.6.3) and XDS. GluK4-LBD crystallised as a monomer in space group $C222_1$ and the structure was solved by molecular replacement and refined to R/R_{free} values of 19.1%/26.2%.

Thermal stability of the GluK4-LBD in the presence of kainate and (*S*)-glutamate, respectively, was analysed using a differential scanning fluorimetry (DSF) assay at the HTX Lab according to a published protocol. Melting temperatures (T_m) of 39°C with (*S*)-glutamate and 53°C with kainate were seen. Compared to a model of GluK4-LBD with bound glutamate the crystal structure of kainate in complex with GluK4-LBD shows additional π-stacking and hydrophobic interactions. As hydrophobic forces are known to be strongly correlated with temperature and increase at higher temperatures, these additional

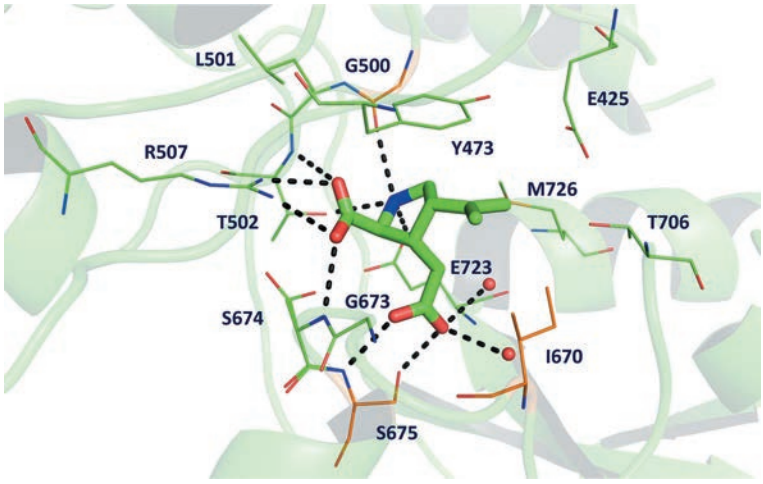

Fig. 73: The binding site of GluK4 comprises 13 residues located within 4 Å of kainate. The three residues not conserved between GluK4 and GluA2 (see main text) are coloured orange. Hydrogen bonding interactions between kainate and GluK4 residues and water molecules (red spheres) are shown as black dashed lines.

interactions explain the favourable T_m in the presence of kainate compared to glutamate. The larger thermal stability of GluK4-LBD with kainate compared to glutamate is consistent with a better binding affinity of kainate (K_d of 1.9 nM) than glutamate (K_d of 25 nM).

The amino-acid sequence of GluK4-LBD is most similar to those of the other kainate receptors. However, the binding site residues in GluK4 were found to be most similar to another subfamily of the ionotropic glutamate receptors, the AMPA receptor subfamily (**Figure 73**). Within 4 Å of kainate, only three out of 11 residues differ between GluK4 and the AMPA receptor subunit GluA2: Gly500 (Pro499 in GluA2), Ile670 (Leu671 in GluA2), and Ser675 (Thr676 in GluA2). For comparison, five binding-site residues differ between GluK4 and the low-affinity kainate receptor subunit GluK1. Characteristic features of the GluA2 binding site are conserved in GluK4. These include the presence of Met729 that has been shown to undergo major conformational changes dependent on the actual ligand bound as well as the so-called "interdomain lock" residues Glu423 in lobe D1 and Thr707 in lobe D2 **[2]**. Thus, the high-affinity kainate receptor subunit GluK4 is different from the low-affinity kainate receptor subunits GluK1-3, which contain a serine (GluK1) or threonine (GluK2-3) at the position corresponding to Met726 in GluK4 and a serine (GluK1) or asparagine (GluK2-3) at the position of Thr706 in GluK4. On the other hand, the degree of closure of the ligand-binding domain around kainate (**Figure 74**) and interlobe contacts induced by kainate were similar to those in GluK1. The high-affinity kainate receptor subunits are believed to primarily play a role in modifying functional properties of the receptor as they need to combine with one of the low-affinity kainate receptors to assemble, traffic to the membrane surface, and form a functional ion channel. The unique characteristics of the ligand-binding domain of GluK4 support such a functional role.

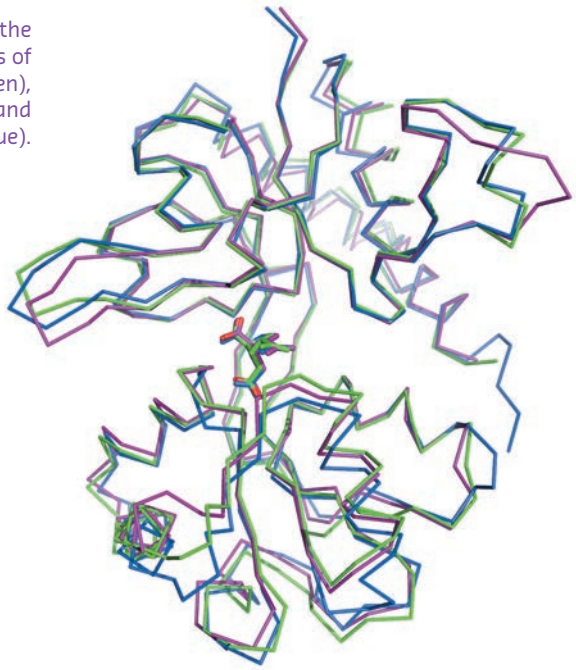

Fig. 74: Overlay of the kainate bound structures of GluK4-LBD (green), GluK1-LBD (magenta) and GluA2-LBD (blue).

PRINCIPAL PUBLICATION AND AUTHORS

The structure of a high-affinity kainate receptor: GluK4 ligand-binding domain crystallized with kainate, O. Kristensen, L.B. Kristensen, S. Møllerud, K. Frydenvang, D.S. Pickering and J.S. Kastrup, *Structure* **24**, 1582-1589 (2016); doi: 10.1016/j.str.2016.06.019.

Department of Drug Design and Pharmacology, Faculty of Health and Medical Sciences, University of Copenhagen (Denmark)

REFERENCES

[1] S.F. Traynelis *et al.*, *Pharmacol Rev*. **62**, 405-496 (2016).
[2] J. Pøhlsgaard *et al.*, *Neuropharmacology* **60**, 135-150 (2011).

UNITED LEAFY BINDS, ALONE IT FALLS

The LEAFY protein, a transcription factor responsible for flower development, is able to assemble itself into small chains made up of several proteins. This mechanism allows it to bind to and activate regions of the genome that are inaccessible to a single protein.

Flowering plants, angiosperms, represent the vast majority of plant species and are the main basis for agriculture. The flower, which contains both male and female organs in close proximity, is a very efficient structure for reproduction and in part helps to explain the impressive success of this group of plants in evolution. The protein orchestrating the development of flowers is called LEAFY **[1]**. It encodes a plant specific transcription factor that binds DNA using a unique fold based on a helix-turn-helix motif **[2]**.

LEAFY also contains a second conserved domain whose function had remained elusive. Using an integrated structural biology approach, the function of this region was shown to be an oligomerisation domain and a crystal structure was obtained following data collection at

beamline **ID23-2**, which showed it to belong to the sterile alpha motif (SAM) family **[3]**. *In vitro* experiments showed that the domain helps LEAFY to bind DNA containing multiple binding sites. This property was confirmed *in vivo* in plants expressing either the wild-type protein or an engineered variant that can no longer oligomerise. More unexpectedly, it was also found that the oligomerisation domain is required for LEAFY to bind to closed chromatin regions, which are normally poorly accessible to transcription factor binding. **Figure 75** shows a dimer of LEAFY bound to DNA.

LEAFY may therefore act as a "pioneer factor" capable of binding to the dense chromatin structure of certain genomic regions and initiating epigenetic changes that lead to gene expression. Indeed, some genes required to build floral organs such as petals or stamen are known to be under epigenetic repression and it makes sense that pioneer transcription factors would be required to initiate their expression.

Fig. 75: A dimer of LEAFY sitting on DNA. The helix-turn-helix domain is in direct contact with DNA whereas the SAM oligomerisation domain is represented above it.

Other organisms contain transcription factors with similar oligomerisation domains. Our findings suggest that they might also act as pioneer transcription factors thanks to their oligomerisation domains. This work thus opens new avenues for understanding the role of these factors in the regulation of gene expression.

PRINCIPAL PUBLICATION AND AUTHORS

A SAM oligomerization domain shapes the genomic binding landscape of the LEAFY transcription factor, C. Sayou (a), M.H. Nanao (b), M. Jamin (c), D. Posé (d,e), E. Thévenon (a), L. Grégoire (a), G. Tichtinsky (a), G. Denay (a), F. Ott (d), M. Peirats Llobet (a), M. Schmid (d,f), R. Dumas (a) and F. Parcy (a,g), *Nature Communications* **7**, 11222 (2016); doi: 10.1038/ncomms11222.

(a) Laboratoire de Physiologie Cellulaire et Végétale, Université Grenoble Alpes, CNRS UMR5168, CEA/DRF/BIG, INRA UMR 1417, Grenoble (France)
(b) European Molecular Biology Laboratory, Grenoble (France)
(c) Institut de Biologie Structurale CEA/DRF, CNRS, Universite Grenoble Alpes, Grenoble (France)
(d) Department of Molecular Biology, Max Planck Institute for Developmental Biology, Tubingen (Germany)
(e) Instituto de Hortofruticultura Subtropical y Mediterranea, Universidad de Malaga (Spain)
(f) Umeå Plant Science Centre, Department of Plant Physiology, Umeå University (Sweden)
(g) Centre for Molecular Medicine and Therapeutics, Child and Family Research Institute, University of British Columbia, Vancouver (Canada)

REFERENCES

[1] E. Moyroud *et al.*, *Trends in plant science* **15**, 346–52 (2010).
[2] C. Hamès *et al.*, *The EMBO journal* **27**, 2628–37 (2008).
[3] C. Kim and J.U. Bowie, *Trends in biochemical sciences* **28**, 625–8 (2003).

INFLUENZA POLYMERASE CAN ADOPT AN ALTERNATIVE CONFIGURATION INVOLVING A RADICAL REPACKING OF PB2 DOMAINS

Structural studies using X-ray crystallography and SAXS reveal a second configuration of influenza polymerase in which flexibly-linked domains, peripheral to the core of the polymerase, repack in a completely different way. This state is transcriptionally inactive and may correspond to an intermediate in the assembly of the newly synthesised polymerase with the viral RNA.

Influenza virus causes widespread disease each year and novel influenza strains have the potential to provoke dangerous pandemics as last happened in 2009. The key enzyme for the multiplication of the virus in infected cells is the viral RNA-dependent RNA polymerase. This is a heterotrimeric, multi-functional machine with subunits denoted PA, PB1 and PB2, which uses the viral RNA genome as template for both (a) transcription into viral mRNA coding for viral proteins and (b) replication to generate new genome copies that are eventually packaged into progeny virions. Because of its critical role in the viral life cycle, the influenza polymerase

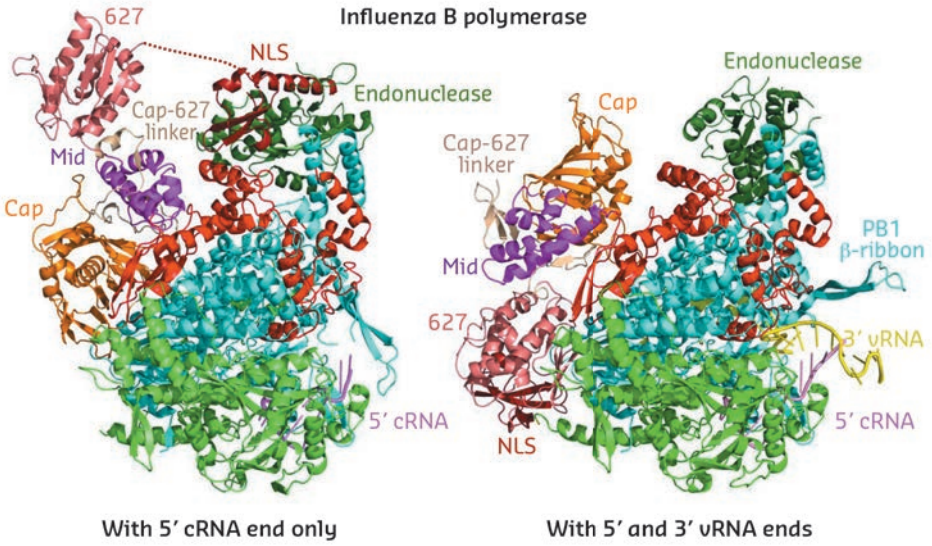

Fig. 76: Ribbon diagrams comparing the crystal structures of the new conformation of influenza B polymerase (left, 5′ cRNA bound) to the previous published conformation (right, full promoter bound). The polymerase core comprises PA-C (green), PB1 (cyan) and PB2-N (red). The flexibly linked peripheral domains are individually labelled.

is being actively pursued as a target for novel anti-viral drugs and thus detailed structural information on the various functional states of the polymerase is highly desirable.

In 2014, the crystal structure of the complete influenza A and B polymerases bound to their so-called promoter (the 3′ and 5′ extremities of the viral RNA) were determined **[1,2]**. This work led to a structure-based model that explained how the polymerase performs the first step of transcription by a unique mechanism known as 'cap-snatching' **[2]**, whereby nascent host-cell transcripts are pirated to provide short capped primers to kick-start transcription of viral mRNAs. In the follow up work described here, the influenza B polymerase was crystallised without the complete promoter in an unexpected and remarkably very different conformation.

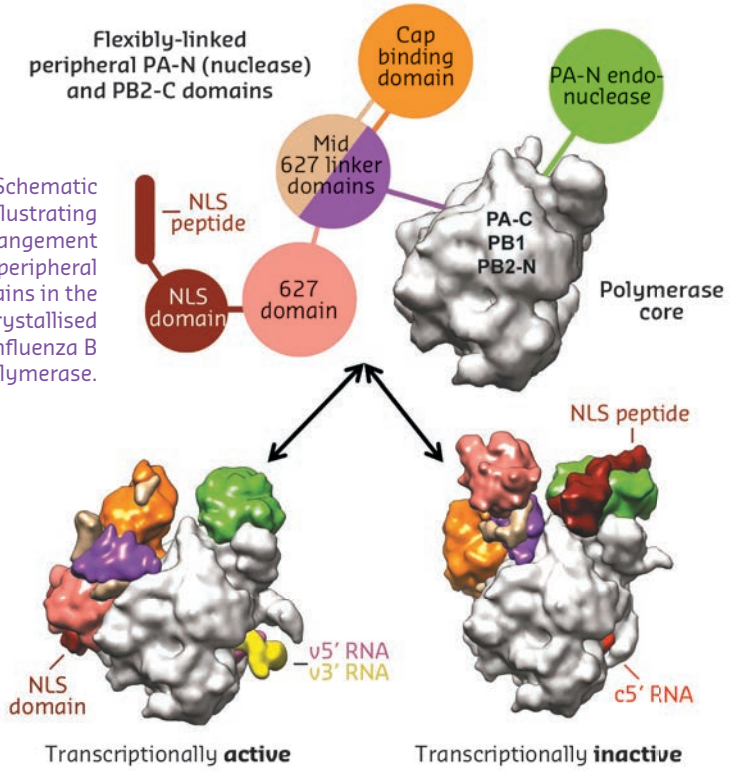

Fig. 77: Schematic diagram illustrating the rearrangement of peripheral domains in the two crystallised states of influenza B polymerase.

Whereas the core of the polymerase, comprising the C-terminal two-thirds of the PA subunit (PA-C), the PB1 subunit and the N-terminal third of the PB2 subunit (PB2-N), does not significantly change, the peripheral domains of PA-N (the cap-snatching endonuclease) and PB2-C (the cap-binding, mid-link, 627 and NLS domains), which are joined together or to the core by flexible linkers, radically change their position, orientation and packing arrangement (**Figures 76** and **77**). As an example, the small C-terminal PB2 NLS (nuclear localisation signal) domain translates a remarkable 93 Å and in the new structure makes completely novel interactions with the endonuclease domain (**Figure 76**, left). Additional high resolution crystal structures of the PB2 NLS-endonuclease interaction and of the PB2-C cap-binding, mid-link, 627 domains, which showed the same inter-domain arrangements as in the new complete polymerase structure, confirm that the observed configuration is unlikely to be a crystal packing artefact.

To complement our crystallographic studies, small-angle X-ray scattering (SAXS) and cross-link mass-spectrometry (XL-MS) studies were performed in solution. The SAXS measurements clearly showed that when no promoter is bound or just the 3′ end of the vRNA is bound, the polymerase is in a much more open conformation (*i.e.* larger radius of gyration) than when the 5′ end or the full promoter is bound. Moreover, the XL-MS results could only be explained by the polymerase interchanging between a number of configurations, probably more than the two distinct arrangements observed in crystal structures in solution. Finally, biochemical studies showed that 'cap-snatching' as assayed by endonuclease cleavage of a capped RNA, was far more efficient when the full promoter was bound than when no vRNA was bound, correlating with the difference in compaction of the corresponding structures observed by SAXS.

We do not yet know to which functional state the new influenza polymerase configuration corresponds. However, there is good structural and biochemical evidence that the previously observed conformation with the full-promoter bound corresponds to the transcriptionally active state (**Figure 77** bottom left). In contrast, the newly observed configuration, which has also been observed with Influenza C polymerase with no vRNA bound **[3]**, appears to be unsuitable for cap-snatching, due to an inappropriate alignment of the cap-binding and endonuclease domains (**Figure 77** bottom right). Instead this conformation may be an assembly intermediate in the transition from unbound to full promoter bound polymerase.

PRINCIPAL PUBLICATION AND AUTHORS

Influenza polymerase can adopt an alternative configuration involving a radical repacking of PB2 domains, E. Thierry (a), D. Guilligay (a), J. Kosinski (b), T. Bock (b), S. Gaudon (a), A. Round (a), A. Pflug (a), N. Hengrung (c,d), K. El Omari (d), F. Baudin (a,b), D.J. Hart (a), M. Beck (b) and S. Cusack (a), *Molecular Cell* **61**, 125–137 (2016); doi: 10.1016/j.molcel.2015.11.016.

(a) European Molecular Biology Laboratory Grenoble Outstation and Unit of Virus Host-Cell Interactions, University Grenoble Alpes-CNRS-EMBL Grenoble (France)
(b) Structural and Computational Biology Unit, European Molecular Biology Laboratory, Heidelberg (Germany)
(c) Sir William Dunn School of Pathology, University of Oxford (UK)
(d) Division of Structural Biology, Henry Wellcome Building for Genomic Medicine, University of Oxford (UK)

REFERENCES

[1] A. Pflug *et al.*, *Nature* **516**, 355-360 (2014).
[2] S. Reich *et al.*, *Nature* **516**, 361-366 (2014).
[3] N. Hengrung *et al.*, *Nature* **527**, 114-117 (2015).

STRUCTURAL BASIS OF AN UNUSUAL CARBOCYCLISATION IN NOGALAMYCIN BIOSYNTHESIS

The final steps in the biosynthesis of nogalamycin involve two atypical reactions, an epimerisation and a chemically challenging C–C-bond formation. These reactions are catalysed by two evolutionary-related non-heme iron α-ketoglutarate dependent enzymes. A limited set of amino acid changes in the active sites is responsible for the switch in chemistry. The two enzymes provide particularly striking examples as to how markedly different chemistry can evolve within an enzyme family.

Over the last decade, research on natural product biosynthetic pathways in microorganisms and plants has revealed novel, unexpected chemistry and enzymatic mechanisms. One such example is the biosynthesis of the aromatic polyketide nogalamycin, produced by the soil bacterium *Streptomyces nogalater*. Like all glycosylated anthracyclines, nogalamycin is a cytotoxic metabolite and has generated some interest as a potential anticancer drug. Nogalamycin contains an unusual covalent attachment of one of the carbohydrate units to the aromatic ring system via a carbon-carbon linkage (**Figure 78a**). The formation of this bond during biosynthesis requires activation of an aliphatic C-H bond and reaction with an aromatic ring system. In spite of intensive studies into the biosynthesis of nogalamycin, the mechanism of this carbocyclisation step has remained enigmatic. Previous studies also suggested that the final steps of nogalamycin biosynthesis involve an epimerisation, converting the rhodosamine sugar moiety to nogalamine **[1]**. We have used genetics, biochemistry and X-ray crystallography to identify the enzymes responsible for these biosynthetic reactions and to characterise their hitherto unknown mechanisms. We discovered two homologous Fe(II) and α-ketoglutarate dependent enzymes (**Figure 78b**), denoted SnoN and SnoK, which catalyse these two key steps in the formation

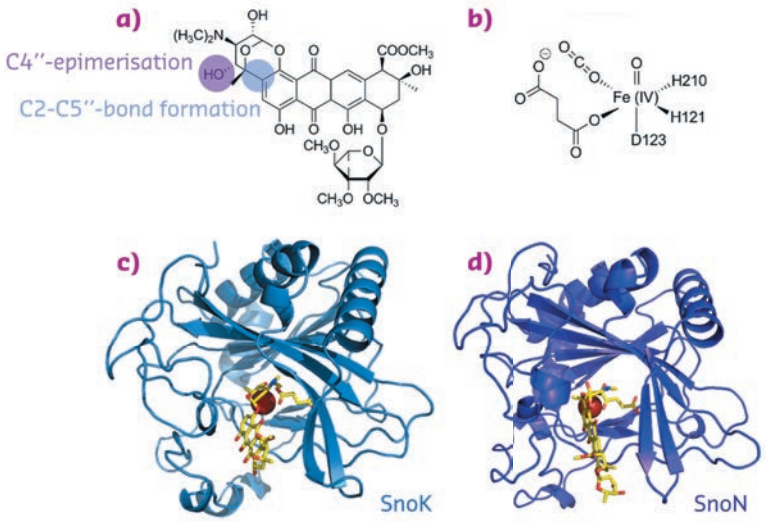

Fig. 78: Nogalamycin and the structures of SnoN and SnoK. a) the chemical structure of nogalamycin with the relevant atoms for C-C bond formation and epimerisation marked. b) the chemical structure of the activated iron centre of α-ketoglutarate dependent enzymes. The overall structures of c) SnoK and d) SnoN displaying the canonical β-sandwich fold.

of nogalamycin. SnoK is responsible for the enzymatic carbocyclisation, while SnoN is an epimerase. The crystal structures of SnoK (**Figure 78c**) and SnoN (**Figure 78d**) and several complexes with substrates were determined using diffraction data collected at beamlines **ID29, ID30A-1** and **ID30A-3**.

Both enzymes display the fold characteristic for the α-ketoglutarate-dependent oxygenase family, with the mononuclear iron ion located in the interior of the β-barrel fold. The co-substrate α-ketoglutarate is bound at the bottom of the channel and the environment of this sub-region is very similar in the two proteins (**Figure 79a** and **79b**). The polyketide substrate is bound in an open cleft, lined with predominantly hydrophobic amino acids. Our biochemical studies and the crystal structures of the enzyme-substrate complexes point towards radical mechanisms involving a high-valent Fe(IV) = O species. The structural studies further imply that the initial catalytic steps required for activation of molecular oxygen are likely to be identical in SnoN and SnoK and occur in a manner similar to other members of the protein family. The exceptional feature of SnoK is the use of the ferryl-oxo species for an oxidative carbocyclisation reaction. Such chemical transformations are challenging to accomplish selectively in organic synthesis. In SnoK, this reaction is initiated by the Fe(IV) = O species which abstracts a hydrogen atom from the primary substrate leading to the generation of a substrate radical. The intramolecular ring closure is then accomplished after attack of the aromatic C2 carbon atom on the radical centre at C5".

In spite of the different reactions catalysed by these enzymes, they display significant amino acid sequence identity (46%) and a high degree of overall structure similarity. Major differences between the enzymes appear to be restricted to parts of the active site cleft involved in the recognition and positioning of the polyketide substrates. These variations position the reactive atoms differently in front of the Fe(IV) = O centre and are likely to be critical for the differences in catalysis in the two enzymes. In SnoN (**Figure 79c**), the substrate is bound such that the site of stereoinversion is close to the iron centre. In SnoK (**Figure 79d**), the C2 carbon atom of the anthracycline aglycone and C5" of the carbohydrate are positioned adjacent to the metal centre facilitating carbocyclisation.

The characterisation of SnoN and SnoK presents an illustrative example of divergent enzyme evolution and provide a compelling case-study of how subtle differences in the positioning of substrates may lead to greatly different chemistry in homologous enzymes. Furthermore our findings expand the repertoire of reactions reported for this enzyme family.

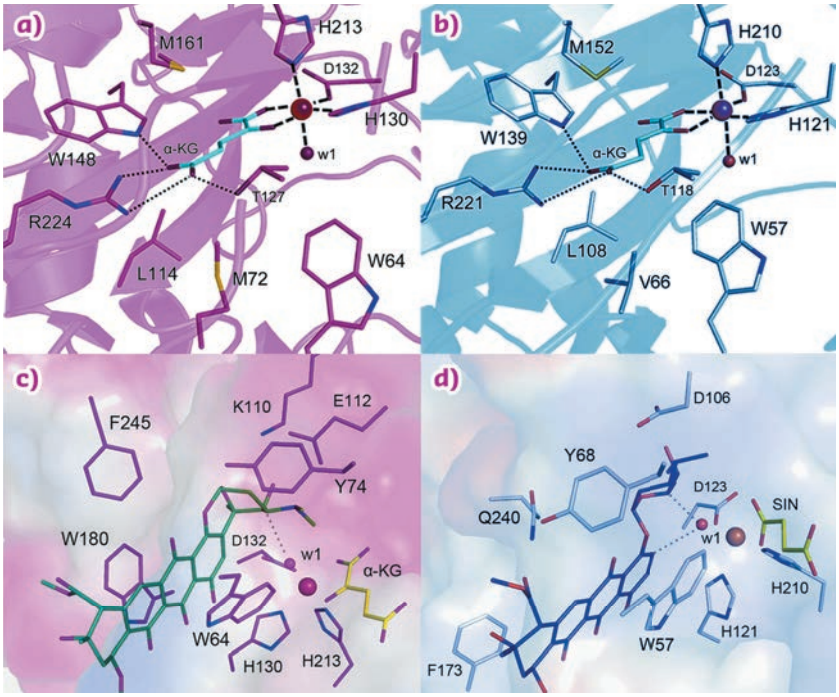

Fig. 79: Detailed views of the active sites of SnoK and SnoN. The binding sites for the α-ketoglutarate co-substrate are highly conserved in a) SnoK and b) SnoN, whereas differences in binding of primary substrates lead to distinct functions in c) SnoK and d) SnoN. The depicted ligands were derived from co-crystal structures, with the exception of the computationally-modelled primary substrate in the case of SnoK.

PRINCIPAL PUBLICATION AND AUTHORS

Divergent non-heme iron enzymes in the nogalamycin biosynthetic pathway, V. Siitonen (a), B. Selvaraj (b), L. Niiranen (a), Y. Lindqvist (b), G. Schneider (b) and M. Metsä-Ketelä (a), *PNAS* **113**, 5251-5256 (2016); doi: 10.1073/pnas.1525034113.
(a) Department of Biochemistry, University of Turku (Finland)
(b) Department of Medical Biochemistry & Biophysics, Karolinska Institutet, Stockholm (Sweden)

REFERENCES

[1] V. Siitonen *et al.*, *ChemBioChem* 13,120–128 (2012).

SAXSy DNA ORIGAMI

Small-angle X-ray scattering (SAXS) was used to quantitatively determine the conformational changes of a DNA origami switch device as a function of ionic strength in free solution.

Molecular self-assembly is a ubiquitous process in nature describing the organisation of molecules into complex structural arrangements of high spatial accuracy such as protein-based enzymes and molecular machines. To create biomimetic objects that can adopt specific conformations and carry out functions at the molecular scale ranging from nanometres to micrometres, such as in transport, signal transduction, and molecular circuitry, DNA has emerged as an ideal building block due to its chemical addressability and predictable Watson–Crick base-pairing. In this context, the development of the DNA origami technique introduced by Paul Rothemund **[1]** ten years ago is a significant landmark of structural DNA nanotechnology. Here, a several kilobase long circular single-stranded 'scaffold strand' is folded with the assistance of hundreds of short single-stranded 'staple strands' resulting in predefined, precisely controlled shapes reaching over 100 nm in size and molecular weights of several MDa **[2]**. Examples include both static structures in two- or three-dimensions and dynamic devices that can undergo controlled conformational changes. Recently, Gerling *et al.* **[3]** established a framework based on shape-complementary recognition and nucleobase stacking interactions to construct a robust and controllable DNA "switch" device (**Figure 80a**). The switch structure can change between an open and closed state upon varying solution conditions such as salt concentration and temperature.

Structural characterisation of DNA origami structures has predominantly relied on atomic force microscopy (AFM) imaging and negative-stain transmission electron microscopy (TEM), requiring immobilisation of the samples on a surface and making it challenging to detect conformational changes upon variation in solution conditions. This study demonstrates that small-angle X-ray scattering (SAXS) can quantitatively determine the conformational changes of a DNA origami switch device as a function of ionic strength in free solution. In addition, our work highlights the ability of SAXS to evaluate structural models against solution-based data, even for very large and complex DNA objects, which constitutes a promising and complementary approach to surface-based methods.

We performed solution SAXS measurements at beamline **BM29** on static switch samples, which

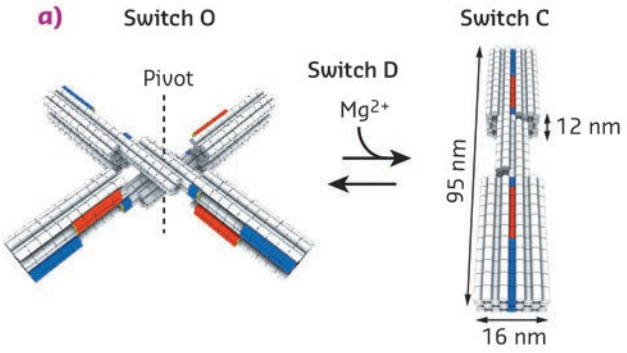

Fig. 80: Schematics of the DNA origami switch devices used in this study and scattering profiles of the static open ("O") and closed ("C") switch samples.

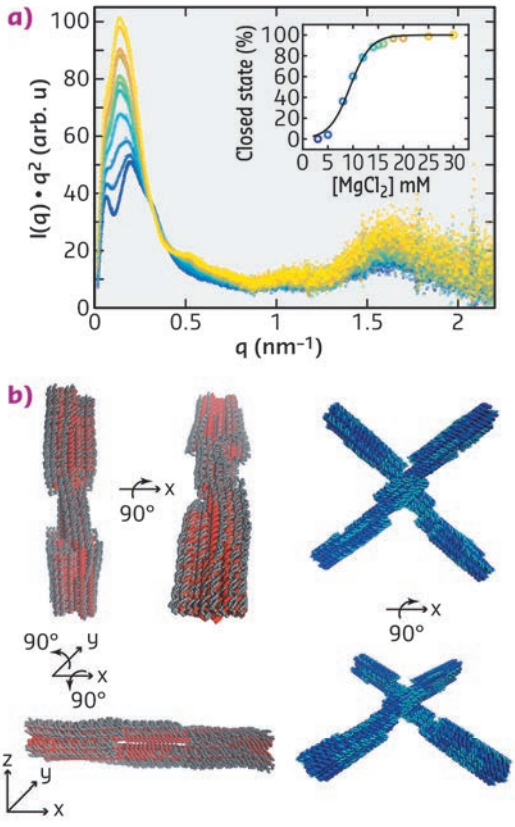

Fig. 81: a) Kratky representation of the scattering profiles of switch D samples for $MgCl_2$ concentrations ranging from 3 mM (dark blue, bottom) to 30 mM (light yellow, top). Inset: fraction of closed switch particles determined from SAXS and fit of a two-state model (black line). b) Structural models derived from the normal mode refinement. Initial models are shown in red and dark blue, refined models in grey and cyan.

are permanently locked in the open (switch O) and closed conformation (switch C), respectively, and on a dynamic switch variant (switch D), which changes its conformation from the open to the closed state upon addition of magnesium ions (**Figure 80a**). For the static samples measured at concentrations of 25 - 100 nM, we obtained scattering profiles with a dynamic range of ≥4 orders of magnitude in intensity with features identifiable up to $q \approx 3$ nm^{-1} (**Figure 80b**). To characterise the conformational transition from the open to the closed state of the dynamic switch variant upon the addition of $MgCl_2$, we performed SAXS experiments at various $MgCl_2$ concentrations, ranging from 3 to 30 mM (**Figure 81a**). The resulting scattering profiles could be described by a two-state fit, where the scattering data at each $MgCl_2$ concentration is a linear superposition of the scattering profiles of the static open and closed conformations, allowing for the determination of the populations at each salt concentration. The salt-dependence of the fraction closed could be fitted by a thermodynamic model that assumes a linear dependence of the free energy ΔG on the ion concentration *c* (**Figure 81b**).

In addition, we compared our experimental data to scattering profiles of the static open and closed switch samples predicted from computer generated, idealised three-dimensional atomistic models, revealing systematic deviations between the experimental and theoretical profiles. We employed a normal mode based elastic network model approach to refine the idealised atomistic models against the experimental SAXS data. The results of the refinement suggest that the DNA helices are deformed from the idealised geometries, consistent with electrostatic repulsion, and reveal deviations from the idealised design geometries that are otherwise difficult to resolve. Our results establish SAXS as a powerful tool to investigate conformational changes and solution structures of DNA origami and we anticipate our methodology to be broadly applicable to increasingly complex DNA and RNA devices.

PRINCIPAL PUBLICATION AND AUTHORS

Conformational changes and flexibility of DNA devices observed by small-angle X-ray scattering, L.K. Bruetzel (a), T. Gerling (b), S.M. Sedlak (a), P.U. Walker (a), W. Zheng (c), H. Dietz (b) and J. Lipfert (a), *Nano Lett.* **16**, 4871–4879 (2016); doi: 10.1021/acs.nanolett.6b01338.

(a) Department of Physics, Nanosystems Initiative Munich, and Center for Nanoscience, LMU Munich (Germany)
(b) Department of Physics, Walter Schottky Institute, TUM Munich (Germany)
(c) Physics Department, State University of New York at Buffalo (USA)

REFERENCES

[1] P.W.K. Rothemund, *Nature*, **440**, 297–302, (2006).
[2] H. Dietz *et al.*, *Science* **325**, 725–730 (2009).
[3] T. Gerling *et al.*, *Science* **347**, 1446–1452 (2015).

STRUCTURAL INSIGHTS INTO tRNA WOBBLE BASE MODIFICATION REACTION BY THE ELONGATOR COMPLEX

The Elongator complex is involved in eukaryotic cells protein manufacture. The crystal structure of Elongator complex subunit Elp3 was determined here, providing new insights into the arrangement and interplay of the two Elp3 domains within Elongator and stimulating additional biochemical, biophysical and phenotypical analyses. These allowed the tRNA binding site to be mapped and a regulatory loop was identified that seems to link tRNA binding and acetyl-CoA hydrolysis.

The synthesis of proteins is tightly controlled to assure their production in the right place and at the right time. Incorrectly-folded proteins, inappropriate expression levels or the production of a protein in the wrong cellular context leads to cellular dysfunction and can cause severe diseases and cancer in the worst case. Cells employ a multi-subunit complex, called Elongator, to attach chemical modifications to tRNAs. This guarantees that proteins are produced with the highest precision and at the correct speed.

The highly-conserved eukaryotic Elongator complex has been associated with a plethora of cellular activities, but it is now widely accepted that its main cellular function is the formation of 5-methoxycarbonylmethyl-uridine (mcm^5U) in the wobble base position of eukaryotic tRNAs **[1]**. Such uridine modifications have been shown

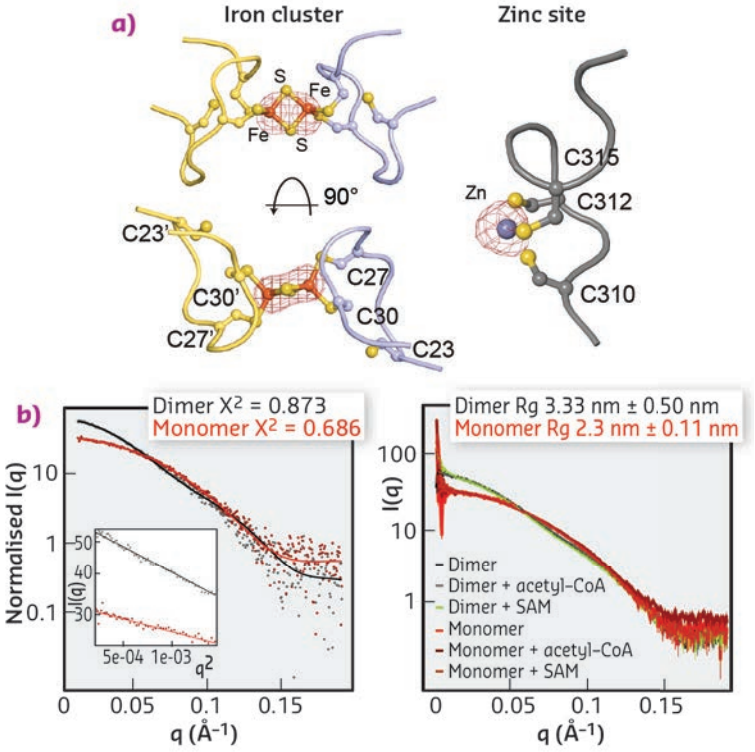

Fig. 82: a) Identification of iron (left) and zinc (right) sites using anomalous difference Fourier maps calculated from datasets recorded close to the respective absorption edges. b) Fitting of experimental SAXS data (dots) for DmcElp3 (monomer/dimer) to theoretical scattering curves calculated from the crystal structure (left). SAXS analyses of DmcElp3 in the presence and absence of acetyl-CoA and SAM (right).

to enhance tRNA binding to the aminoacyl site of the ribosome, affect the speed of translating ribosomes and secure the homeostasis of whole cellular proteomes. Among its six individual subunits, the Elongator complex Elp3 has been predicted to contain a unique combination of a KAT domain and a radical SAM binding domain. As these two well-known domains could provide the suitable radical intermediates necessary to perform the respective modification reaction, they have been suspected to constitute the active site of Elp3. We have recently determined crystal structures of other Elongator subunits **[2]** and regulatory factors **[3]**, but, as no high-resolution structural information for the enzymatically active subunit was available, the details of the uridine modification reaction remained elusive.

We expressed and purified large quantities of Elp3 from *Dehalococcoides mccartyi* (DmcElp3), an extremophilic anaerobic bacterium recently isolated from toxic waste. Subsequently, we managed to crystallise the protein and collect diffraction data at beamline **ID29** to an overall resolution of 2.15 Å, allowing us to solve the structure using the single-wavelength anomalous dispersion (SAD) phasing technique. As the purified protein and the resulting crystals showed a characteristic reddish colour, we suspected that the protein carries an iron sulfur cluster, typical of radical SAM domain proteins. We thus used X-ray fluorescence (XRF) analyses, also available at **ID29,** to confirm the presence of iron atoms in our crystals and located the cluster by collecting a complete data set close to the absorption edge of iron (λ = 1.7377 Å). Anomalous difference Fourier maps clearly indicated the type of cluster, namely [2Fe2S], as we specifically identified peaks for two coordinated iron ions. In addition, we used XRF analysis and anomalous difference Fourier maps collected at the zinc absorption edge (λ = 1.28238 Å) to locate and characterise a novel and unexpected zinc coordination motif in DmcElp3 (**Figure 82a**). Last but not least, we observed that the iron sulfur cluster is localised in the interface between two DmcElp3 monomers, something never observed before in any known radical SAM domain. We then used small-angle X-ray scattering (SAXS) at beamline **BM29** to confirm that the dimer exists in solution and that it is unchanged in the presence of specific ligands (**Figure 82b**).

Our work for the first time provides a structural framework for the previously proposed radical based modification reaction (**Figure 83**). Strikingly, the obtained structural data allowed us to locate most of the previously-published disease-related mutations. Subsequently, we tested the identified structure-guided and disease-related mutations *in vivo* and showed

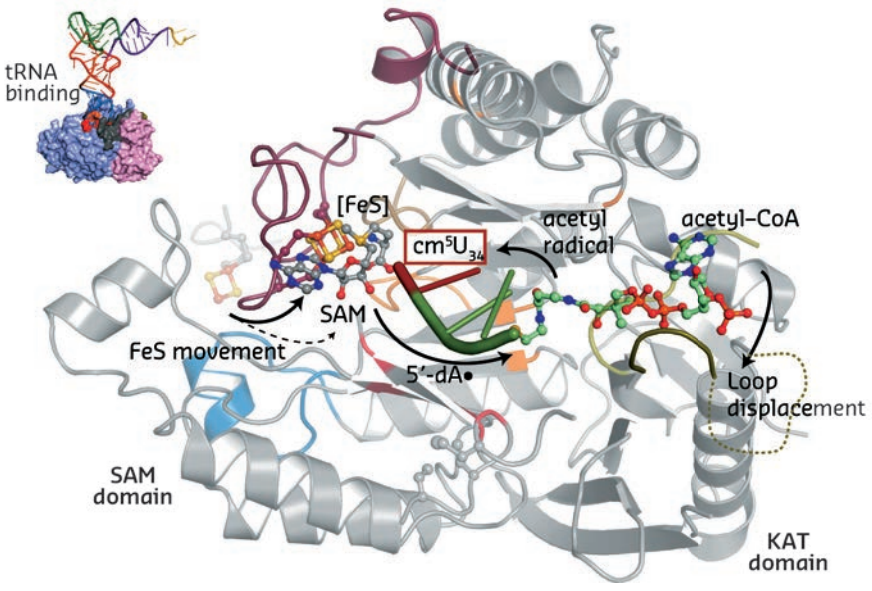

Fig. 83: Summary of the individual steps of the proposed radical based tRNA modification reaction. The two Elp3 domains, the iron sulfur cluster, SAM, acetyl-CoA and the bound tRNA anti-codon loop are highlighted.

that they indeed affect the tRNA modification activity of Elongator, thus suggesting a direct correlation between Elp3 dysfunction and disease progression.

PRINCIPAL PUBLICATION AND AUTHORS

Structural basis for tRNA modification by Elp3 from *Dehalococcoides mccartyi*, S. Glatt (a,b), R. Zabel (c), O. Kolaj-Robin (d,e,f), O.F. Onuma (c), F. Baudin (a,g), A. Graziadei (a), V. Taverniti (d,e,f), T.-Y. Lin (b), F. Baymann (h), B. Séraphin (d,e,f), K.D. Breunig (c) and C.W. Müller (a), *Nat Struct Mol Biol.* **23**, 794–802 (2016);
doi: 10.1038/nsmb.3265.
(a) European Molecular Biology Laboratory (EMBL), Heidelberg (Germany)
(b) Max Planck Research Group at the MCB/JUK (Poland)
(c) Martin-Luther-University Halle-Wittenberg (Germany)
(d) University Strasbourg, IGMBC (France)
(e) CNRS, IGMBC (France)
(f) Inserm, IGMBC (France)
(g) University Grenoble Alpes–CNRS–EMBL (France)
(h) Laboratoire de Bioénergétique et Ingénierie des Protéines (France)

REFERENCES

[1] S. Glatt and C.W. Müller, *Curr Opin Struct Biol.* **23**, 235-42 (2013).
[2] S. Glatt *et al.*, *Nat Struct Mol Biol.* **19**, 314-20 (2012).
[3] S. Glatt *et al.*, *Structure* **23**, 149-60 (2015).

CRYSTAL STRUCTURE OF PolD PROVIDES A NOVEL PARADIGM FOR THE CLASSIFICATION OF DNA POLYMERASES

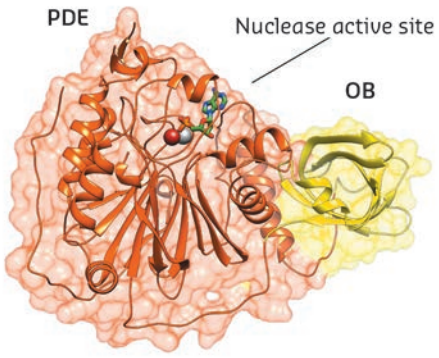

Polymerase D (PolD), an archaeal replicative DNA polymerase, is the only class of DNA-polymerases whose structure remains unknown and for which the catalytic domain has no assigned fold. The crystal structure of both catalytic subunits of PolD was determined using data collected at beamline ID23-1 and PolD was found to share an unexpected structural homology with the multisubunit transcriptases. This discovery of a common catalytic core suggests that the DNA replication and transcription apparatus may share a joint evolutionary history.

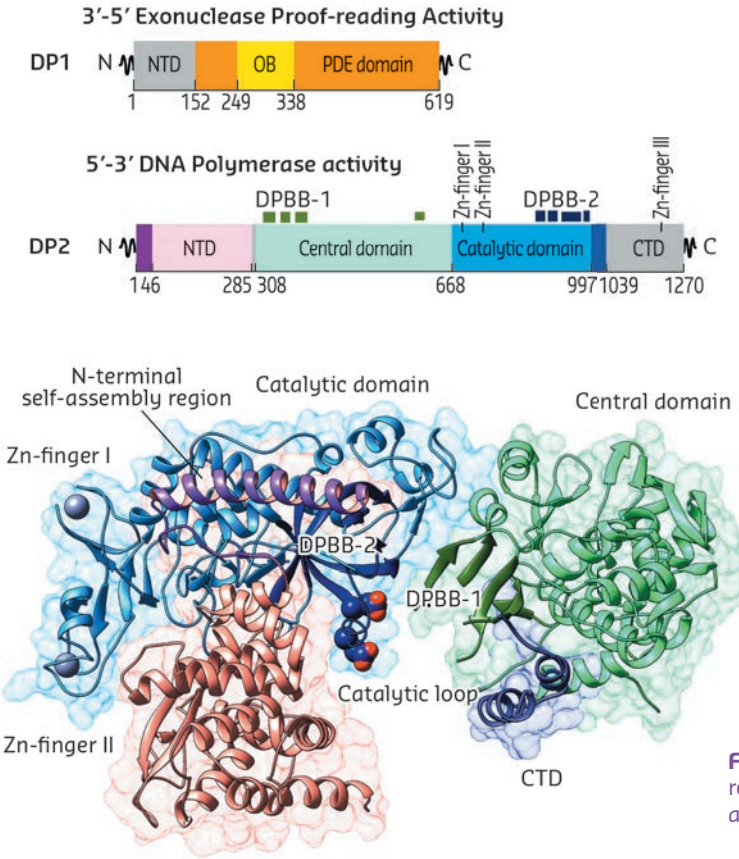

In all forms of cellular life, DNA polymerases (DNAPs) play central roles in genome replication, maintenance, and repair, and have been the subject of intensive research for decades. Over the years, all DNAPs have been grouped into various families, using sequence alignments: PolA, PolB, PolC, PolD, PolX, PolY and reverse transcriptases (RT). Strikingly, nearly all of them belong to one of two different folds, the Klenow-fold (PolA, PolB, PolY and RT), or the Polb-fold (PolC, PolX). The only class of DNA-polymerases left whose structure is unknown and for which the catalytic domain has no assigned fold is PolD.

PolD exists in all Archaea, except Crenarchaea, and is a replicative polymerase responsible for initiating DNA synthesis at both leading and lagging strands. It is composed of a large catalytic subunit (DP2) and a smaller subunit with 3'-5' proofreading exonuclease activity (DP1). Apart from the N-terminal regions of its

Fig. 84: Overview of PolD subunit structures. Cartoon representations of DP1 (top) and DP2 (bottom), structures coloured according to domain boundaries.

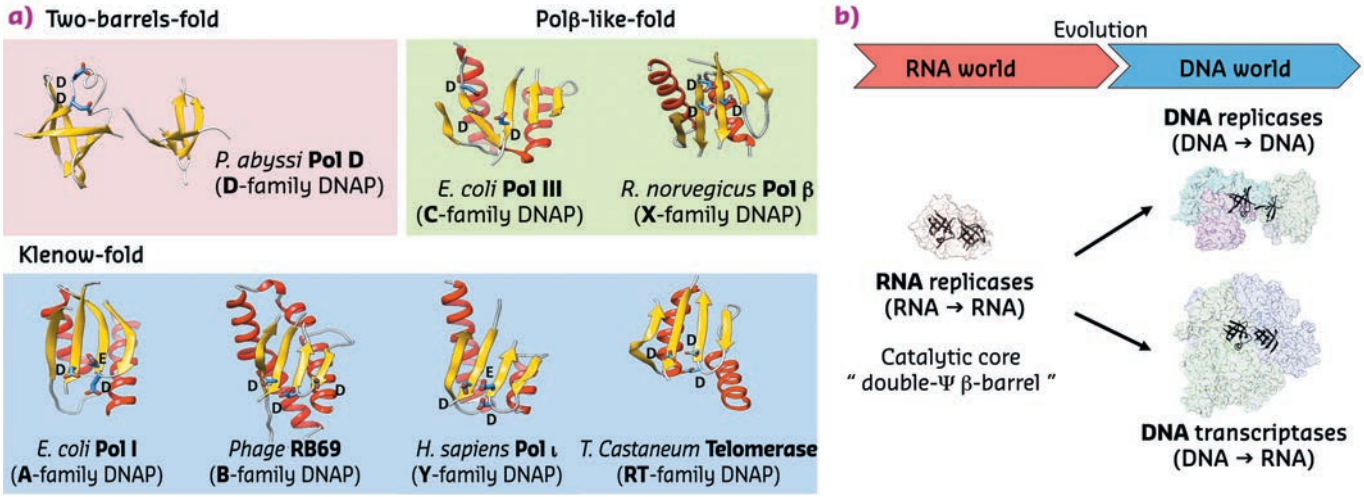

Fig. 85: a) An updated structural classification of all DNA-dependent polymerases. The following crystal structures were used: Polβ from *Ratus norvegicus* (PDBid: 1BPB), Pol III from *Escherichia coli* (PDBid: 2HNH), Polι from *Homo sapiens* (PDBid: 1T3N), PolB from *Enterobacteria phage RB69* (PDBid: 1IH7), Pol I from *Escherichia coli* (PDBid: 1KLN), PolD from *Pyrococcus abyssi* (this study). b) The "two-barrel" fold may have allowed DNA replication and transcription to jointly evolve from a common catalytic core.

DP1 (1-50) and DP2 (50-280) subunits, neither the structure of the catalytic polymerase nor that of the exonuclease domain have yet been determined. While DP1 is known to belong to the calcineurin-like phosphodiesterase superfamily, DP2 shows no sequence similarity to other proteins with the exception of a short C-terminal zinc-binding motif in eukaryotic Polε.

To help resolve the uncertainty concerning the evolutionary origins of D-family DNAP, we determined the crystal structures of two large fragments of both DP1 and DP2 subunits of the *Pyrococcus abyssi* PolD. Both DP1 and DP2 crystal structures were determined individually using data collected at beamline **ID23-1** and refined at final resolutions of 2.5 Å and 2.2 Å, respectively (**Figure 84**).

The crystal structures of both DP1 and DP2 subunits reveal that PolD is an atypical DNAP. Firstly, DP1 subunit contains a calcineurin-like phosphodiesterase fold that is responsible for the 3'-5' proof-reading exonuclease activity. However, in most other structurally-characterised DNAPs, the catalytically active proofreading domains fold into an α/β structure with a twisted five-stranded mixed β-sheet, which shares no structural homology with DP1. Secondly, the structure of DP2 catalytic subunit shows that it shares no significant structural similarity with any known DNAP. With knowledge of the structure of PolD, a third structural class of DNA polymerases has been discovered (**Figure 85a**). In fact, PolD DP2 shares an unexpected structural homology with the "two-barrel" architecture of RNA polymerases (RNAP), which includes multisubunit transcriptases from all domains of life, homodimeric RNA silencing pathway RNAPs and atypical RNAPs encoded by some viruses and phages. This defines a novel paradigm for the classification and possible evolutionary relationships between different types of both RNA and DNA polymerases, which shows, for the first time in the non-viral world, DNA transcription and DNA replication within the same protein superfamily. The finding that PolD and "two-barrel" RNAPs share a common catalytic core with similar sequence motifs suggest that the DNA replication and transcription apparatus may share a joint evolutionary history.

We hypothesise that this "two-barrel" catalytic core common ancestor was present and functional as an RNA replicase in an RNA world. The ability of this catalytic core to acquire novel nucleotide polymerisation activities, like DNA replication and DNA transcription, may have made the RNA-world/DNA-world transition easier. Indeed, the versatility of the "two-barrel" fold may have allowed DNA replication and transcription to jointly evolve from a common catalytic core, rather than being invented separately (**Figure 85b**).

PRINCIPAL PUBLICATION AND AUTHORS

Shared active site architecture between archaeal PolD and multisubunit RNA polymerases revealed by X-ray crystallography, L. Sauguet (a), P. Raia (a,b), G. Henneke (c,d,e) and M. Delarue (a), *Nature Communications* **7**, 12227 (2016), doi: 10.1038/ncomms12227

(a) Unit of Structural Dynamics of Macromolecules, Pasteur Institute & CNRS UMR 3528, Paris (France)
(b) Pierre et Marie Curie University, Paris (France)
(c) Ifremer, UMR 6197, Laboratoire de Microbiologie des Environnements Extrêmes, Plouzané (France)
(d) UBO, UMR 6197, Laboratoire de Microbiologie des Environnements Extrêmes, Plouzané (France)
(e) CNRS, UMR 6197, Laboratoire de Microbiologie des Environnements Extrêmes, Plouzané (France)

STRUCTURES OF QUINOLINATE SYNTHASE IN COMPLEX WITH A SUBSTRATE ANALOGUE, A KEY INTERMEDIATE AND PRODUCT

The enzyme NadA catalyses the synthesis of quinolinic acid (QA), the precursor of the universal nicotinamide adenosine dinucleotide cofactor. We report the crystal structures of NadA variant complexes with a substrate analog, the first reaction intermediate and the QA product, the latter two directly obtained from substrates.

The adenine dinucleotide (NAD) cofactor is involved in many fundamental biochemical reactions through hydride transfer. Most prokaryotes synthesise NAD using the *de novo* II pathway that initially involves the condensation of iminoaspartate (IA) with dihydroxyacetone phosphate (DHAP) to generate quinolinic acid (QA) **[1]**. This reaction is catalysed by the [4Fe-4S]-containing enzyme quinolinate synthase NadA. Besides possibly transforming IA into its enamine tautomer (1 in **Figure 86**), NadA catalyses the condensation of this tautomer with DHAP (2), the aldo-keto isomerisation of the condensed intermediate (3) and two dehydration steps (4 and 5).

In 2014, we determined the holo crystal structure of *Thermotoga maritima (Tm)* NadA (**Figure 87a**) and described a long tunnel connecting its active site [4Fe-4S] cluster with the molecular surface **[2]**. Now, using X-ray data collected at beamlines **BM30A**, **ID30B**, **ID23-1** and **ID30A-3** (Massif-3), we have solved the structures of complexes of the *Tm*NadA Y107F active site variant, which lacks QA synthetic activity, with (i) the DHAP analog phosphoglycolohydroxamate (PGH) at 1.45 Å resolution (**Figure 87b**) and (ii) the first condensation intermediate W at 1.9 Å resolution (**Figure 86** and **Figure 87c**). The *Tm*NadA Y107F-W complex (**Figure 87c**) was obtained by previously incubating the enzyme overnight anaerobically in a glove box with DHAP and oxaloacetic acid + ammonium ions (to generate IA non-enzymatically **[3]**.

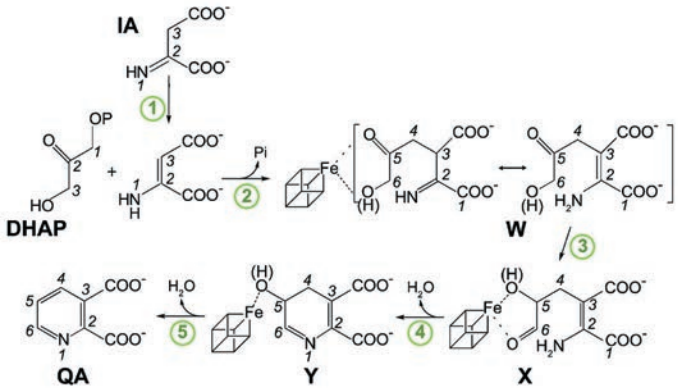

Fig. 86: Proposed pathway of quinolinic acid synthesis by NadA.

Our refined model of W has the carbonyl oxygen at C5 and a C6 terminal alkoxide group implying that the aldo-keto isomerisation does not occur in *Tm*NadA Y107F thus explaining its inability to synthesise QA. Indeed, cyclisation to yield Y from X requires a C6 terminal aldehyde **[4,5]** (**Figure 86**). W displays several of the features expected for a condensation product/reaction intermediate. First, its two carboxylic groups bind *Tm*NadA as the IA analog malate does in the *P. horikoshi* NadA structure **[6]**. Second, both the substrate analog PGH and W bind to the [4Fe-4S] cluster with their terminal –O(H) moieties and their C=O groups. Third, the structure of W also shows that, as previously suggested, the condensation of IA with DHAP involves the elimination of the phosphate

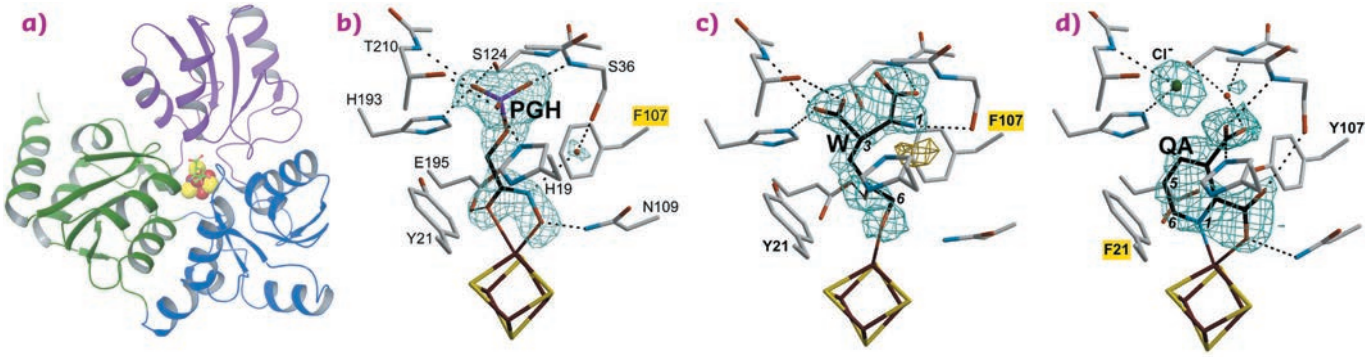

Fig. 87: a) Ribbon depiction of the quinolinate synthase NadA with bound W and colour-coded domains and omit electron density maps and atomic models corresponding to b) PGH; c) W and d) QA complexes. Mutated residues are highlighted in yellow.

group of the latter (**Figure 86** and **Figure 87c**). Fourth, W has its N atom well oriented for its nucleophilic attack on C2 and subsequent cyclisation (**Figure 86** and **Figure 87c**) **[6]**.

Using the slowly-reacting *Tm*NadA Y21F variant, we have reacted the same substrates to form a crystalline complex between this protein and the QA product and solved it at 1.9 Å resolution (**Figure 87d**).

In summary, our study shows that (i) the condensation of IA with DHAP is coupled to dephosphorylation; (ii) Tyr107 is most likely involved in the aldo-keto isomerisation of W to X and in imino-enamine tautomerisation; (iii) after the second dehydration, helped by Tyr21, the QA product rotates inside the NadA active site forming a bidentate complex with the unique Fe ion of the [4Fe-4S] cluster. Which mechanism is responsible for QA release from NadA will be the subject of future investigations.

Besides the fundamental interest of elucidating the catalytic mechanism of NadA, our structural studies constitute a solid basis for the design of novel antibiotics targeted against two human pathogens that use exclusively the *de novo* II pathway of NAD synthesis: *Helicobacter pylori,* which causes gastric ulcers and cancer and *Mycobacterium leprae*, the causal agent of leprosy.

PRINCIPAL PUBLICATION AND AUTHORS

Crystal structures of quinolinate synthase in complex with a substrate analogue, the condensation intermediate, and substrate-derived product, A. Volbeda (a), C. Darnault (a), O. Renoux (b), D. Reichmann (b), P. Amara (a), S. Ollagnier-de-Choudens (b) and J.-C. Fontecilla-Camps (a), *J Am Chem Soc* **138**, 11802 (2016); doi: 10.1021/jacs.6b05884.

(a) Metalloproteins Unit, Institut de Biologie Structurale, Grenoble (France)
(b) BIG/CBM/Biocat, CEA-Grenoble (France)

REFERENCES

[1] S.Y. Gerdes *et al.*, *J. Bacteriol.* **184**, 4555 (2002).
[2] M.V. Cherrier *et al.*, *J. Am. Chem. Soc.* **136**, 5253 (2014).
[3] S. Nasu *et al.*, *Biophys. Res. Commun.* **101**, 533 (1981).
[4] D. Reichmann *et al.*, *Biochemistry* **54**, 6443 (2015).
[5] N. Suzuki *et al.*, *Biochim. Biophys. Acta* **304**, 309 (1973).
[6] S. Nasu *et al.*, *J. Biol. Chem.* **257**, 626 (1982).

STRUCTURAL BASIS FOR NOROVIRUS INHIBITION BY HUMAN MILK OLIGOSACCHARIDES

Human noroviruses bind histo-blood group antigens (HBGAs) and human milk oligosaccharides (HMOs) at an identical pocket on the virus particles. However, HBGAs are thought to enhance norovirus infections, whereas HMOs may inhibit infections. Structurally, HBGAs and HMOs are similar, but functionally, these "sugars" may act differently.

Human noroviruses are the dominant cause of acute outbreaks of gastroenteritis. Noroviruses are known to interact with oligosaccharides, termed histo-blood group antigens (HBGAs). This interaction is thought to be important for norovirus infections. HBGAs are found in saliva and are also expressed on the mucosal epithelium of the digestive tract. In comparison, human milk oligosaccharides (HMOs), the third most abundant component of human breast milk, also contain similar building blocks to HBGAs. HMOs are thought to act as a "receptor decoy" for certain pathogens. Indeed, one study found that human milk might provide some protection to infants with a norovirus infection **[1]**.

To better understand norovirus binding interactions with these oligosaccharides from a structural perspective, we solved X-ray crystal structures of the norovirus protruding protein (P domain) in complex with HMOs, *i.e.*, 2'-fucosyllactose (2'FL) and 3-fucosyllactose (3FL). We also showed that these HMO's could block norovirus from binding to HBGA.

HBGAs bind at the top of the norovirus P domain and both 2'FL and 3FL bind at the pocket on the norovirus capsid (**Figure 88a**). The HMOs are held in place by a network of hydrophilic and hydrophobic interactions at the P domain dimeric interface (**Figures 88b** to **88e**). The fucose moiety of HMOs is held by a common set of conserved residues that also held the fucose of HBGAs. The central saccharides of HMOs are poorly held by the protein, while the terminal saccharides interact with varying residues.

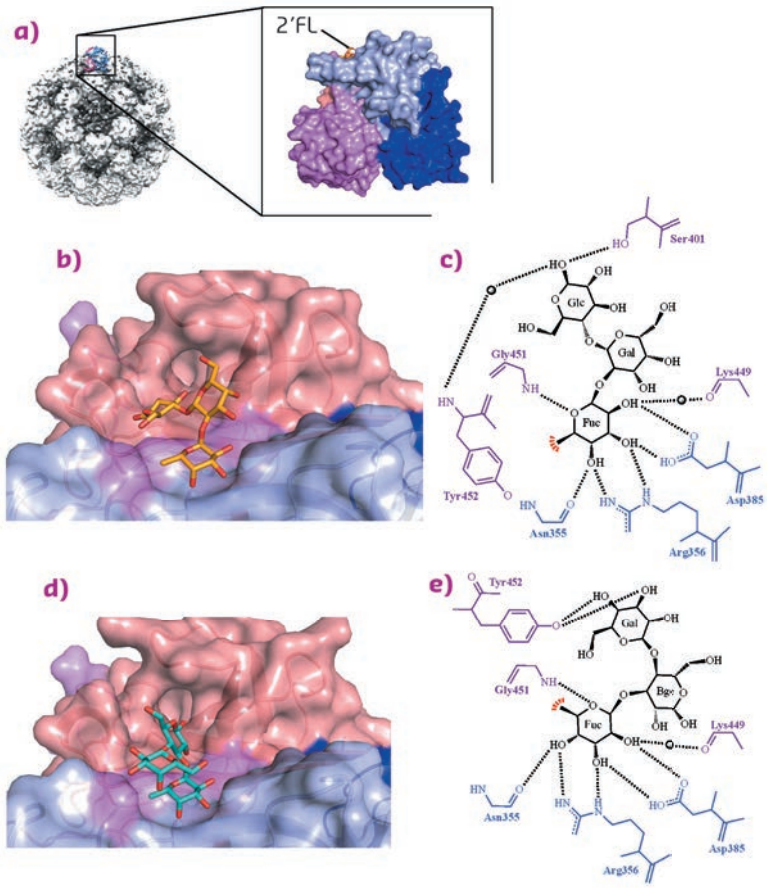

Fig. 88: HBGA and HMO interactions with norovirus. a) Cryo-EM structure of a norovirus VLP. b) The crystal structure of the norovirus P domain-2'FL complex determined to 1.55 Å resolution and coloured according to monomers (chain A and B) and P1 and P2 subdomains, *i.e.* chain A: P1 (blue), chain A: P2 (lightblue), chain B: P1 (violet), and chain B: P2 (salmon). c) P domain interactions with 2'FL, showing a-fucose (Fuc), α-galactose (Gal), and β-glucose (Glc). The black lines represent hydrogen bonds and the red fan shows the hydrophobic interaction with Tyr452. Black spheres represent water molecules. d) The crystal structure of the norovirus P domain-3FL complex determined to 1.35 Å resolution. e) P domain interactions with 3FL showing α-fucose (Fuc), β-galactose (Bgc), and β-glucose (Gal).

Overall, the HMO binding interactions were comparable to HBGA interactions **[2,3]**.

Our structural data showed that both HBGAs and HMOs bind in copious orientations. However, the fucose moiety of HBGAs and HMOs is always held in an identical position, whereas the other saccharide units are positioned differently (**Figure 89**). Terminal saccharide units are usually only held with few if any direct hydrogen bonds, suggesting a weaker interaction and likely allowing for the numerous oligosaccharide positions observed.

To describe a possible biological function for the HMOs, we performed a HMO inhibition study with norovirus particles and HBGAs. We found that the HMOs were able to block norovirus particles from binding to HBGAs in a mostly dose dependent manner. The half maximal inhibitory concentration (IC_{50}) in the HBGA assays for 2'FL and 3FL were 5.5 mM and 5.6 mM, respectively. These results showed that HMOs might block the HBGA pocket and, considering that mother's milk contains ~1-5 mM of 2'FL/3FL, might function as weak norovirus antivirals.

In summary, we showed that the norovirus HBGA/HMO binding site is a multipurpose oligosaccharide pocket. 2'FL and 3FL may act as natural decoys in an infection by mimicking the structure of the HBGAs and binding at the HBGA pocket. Currently, there is no treatment or vaccine available for human norovirus infections, which cause a massive burden of disease worldwide. Importantly, 2'FL has already been shown as a safe food supplement for infant formula **[4]**. Further clinical studies are planned with 2'FL and 3FL, as well as with more complex HMO-structures.

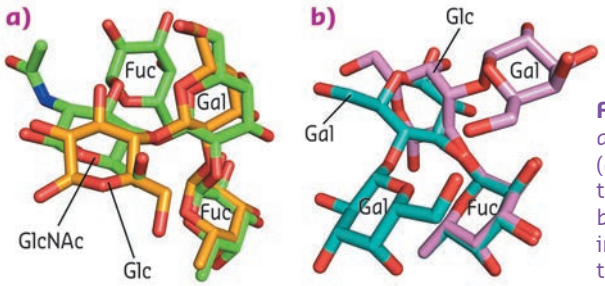

Fig. 89: HMO inhibition of the HBGA binding pocket. a) Superposition of 2'FL and Lewis-Y tetrasaccharide (green sticks) show that the 2'FL saccharide units mimick the orientations of the first three saccharides of Lewis-Y. b) Superposition of 3FL and B-trisaccharide (pink sticks) indicate that the fucose units are similarly positioned, whereas the other saccharide units are orientated differently.

PRINCIPAL PUBLICATION AND AUTHORS

Structural basis for norovirus inhibition by human milk oligosaccharides, S. Weichert (a), A. Koromyslova (b,c), B.K. Singh (b,c), S. Hansman (a,b), S. Jennewein (d), H. Schroten (a) and G.S. Hansman (b,c), *J Virol* **90**, 4843–4848 (2016); doi: 10.1128/JVI.03223-15.

(a) Pediatric Infectious Diseases Unit, University Children's Hospital Mannheim, University of Heidelberg, Mannheim (Germany)
(b) Schaller Research Group at the University of Heidelberg and the DKFZ, Heidelberg (Germany)
(c) Department of Infectious Diseases, Virology, University of Heidelberg (Germany)
(d) Jennewein Biotechnology, Rheinbreitbach (Germany)

REFERENCES

[1] A.L. Morrow *et al.*, *J Pediatr* **145,** 297-303 (2004).
[2] G.S. Hansman *et al.*, *J Virol* **85,** 6687-6701 (2011).
[3] B.K. Singh *et al.*, *J Virol* **89,** 2024-2040 (2015).
[4] M. Coulet *et al.*, *Regul Toxicol Pharmacol* **68,** 59-69 (2014).

MODE OF ACTION OF FEN1 INHIBITORS REVEALED BY X-RAY CRYSTALLOGRAPHY AND ENZYME KINETIC STUDIES

The first inhibitor-bound structure of potential oncology target Flap endonuclease-1 (FEN1), together with biophysical studies, shed light on inhibitor mode of action: the cellularly active N-hydroxyurea compounds were found to block substrate entry to the catalytic site.

FEN1 belongs to the 5'-nuclease superfamily **[1,2]** and its main role is the removal of 5' flaps generated during lagging-strand synthesis in DNA replication, thus it is essential for Okazaki fragment maturation **[3,4]**. FEN1 is overexpressed in multiple cancer types and has synthetic-lethal interactions with several genes frequently mutated in cancers. Due to its role in long-patch base excision repair, FEN1 is also a potential chemosensitising target **[5,6,7]**.

To establish the binding mode and possibly the mode of action of N-hydroxyurea inhibitors, human FEN1 was cocrystallised to form a ternary complex with Mg^{2+} and compound 1 (**Figure 90a**). The structure was solved following data collection at beamline **ID29**. Two Mg^{2+} ions, approx 4.5 Å apart, are coordinated by a number of acidic side chains that reside in the active site of the protein that forms an indentation of the kidney-bean shaped molecule (**Figure 90b** and **90c**). The inhibitor molecule completes the coordination of the Mg^{2+} ions through its N-hydroxyurea moiety.

The ligand-bound structure suggests a possible mode of action. Superposition of FEN1 in complex with product DNA and this novel liganded structure shows the ligand occupying the location of the phosphate monoester of the DNA (**Figure 90d**). Biophysical studies were applied to characterise this type of inhibitor further.

Isothermal titration calorimetry (ITC) studies showed that Mg^{2+} was necessary for inhibitor binding, and replacing these with Ca^{2+} ions resulted in loss of ligand binding.

Kinetic experiments were undertaken to characterise FEN1 inhibition by 1, 2 and 4 *vs* DNA binding. All three compounds were able to bind both the DNA-free form and the substrate DNA-bound form of the enzyme. However, only compound 1 showed binding affinity to the DNA-complex comparable to the DNA-free state.

A fluorescence resonance energy transfer (FRET) assay was used to gain insight into the conformation of the DNA upon binding the inhibitor-bound form of FEN1. Both DNA binding sites required for catalytic activity were found to be occupied with and without the inhibitor. Using a tandem 2-aminopurine exciton pair preceding

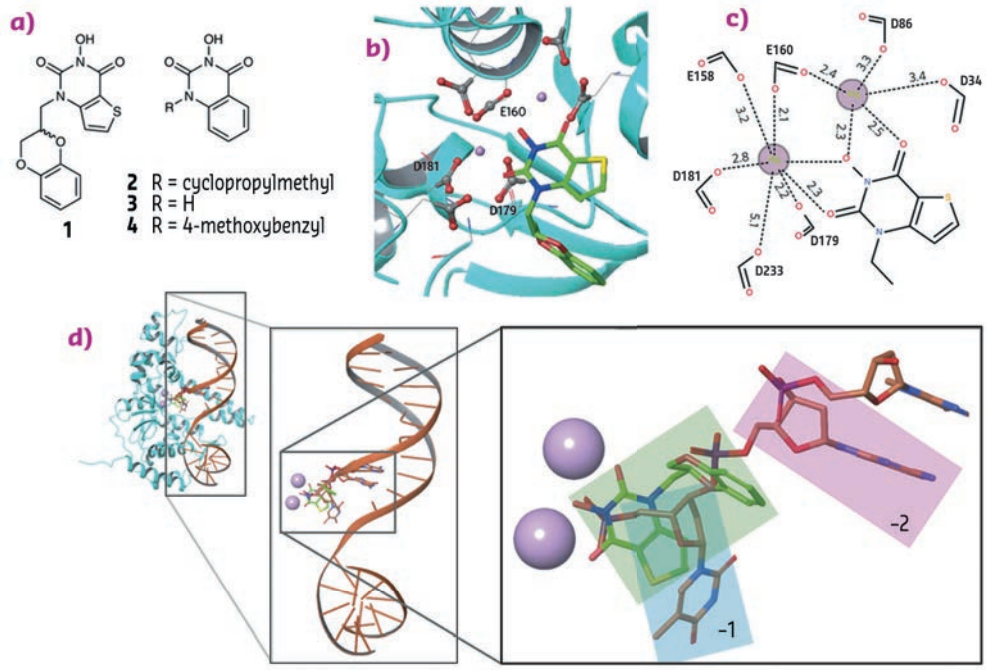

Fig. 90: a) Compounds **1-4**. b) Compound **1** bound to human FEN1 nuclease active site (PDB 5FV7). c) Schematic representation of the metal-coordination spheres. d) Structure of FEN1 in complex with product DNA (PDB 3Q8K) superimposed with FEN1 in complex with **1** (protein not shown). Metals are shown as pink spheres, the terminal 5' nucleotide (−1) is highlighted in the cyan box, the penultimate nucleotide of the product DNA (−2) is highlighted in pink, and 1 is highlighted in green.

the cleavage site of the 5'-flap strand, CD spectra confirmed that the inhibitors prevented the base unpairing required for hydrolysis.

Compounds 1 and 4 could also be shown to be cellularly active in a cellular thermal shift assay (CETSA) in SW620 colon cancer cells in spite their different inhibition modes, with similar drug activity (EC50 values). However, there was a substantial drop-off compared to biochemical assays, probably due to high local concentrations of FEN1 in the nucleus during S-phase.

PRINCIPAL PUBLICATION AND AUTHORS

Cellularly active N-hydroxyurea FEN1 inhibitors block substrate entry to the active site, J.C. Exell (a), M.J. Thompson (a), L.D. Finger (a), S.J. Shaw (a), J. Debreczeni (b), T.A. Ward (c), C. McWhirter (b), C.L. Siöberg (d), D. Martinez Molina (d), W.M. Abbott (b), C.D. Jones (e), J.W. Nissink (f), S.T. Durant (g) and J.A. Grasby (a), *Nat Chem Biol.* **12** 815-821 (2016); doi: 10.1038/nchembio.2148.

(a) Centre for Chemical Biology, Department of Chemistry, Krebs Institute, University of Sheffield (UK)
(b) Discovery Sciences, Innovative Medicines, AstraZeneca, Cambridge (UK)
(c) Bioscience, Oncology Innovative Medicines, AstraZeneca, Alderley Park, Cheshire (UK)
(d) Pelago Bioscience AB, Solna (Sweden)
(e) Chemistry, Oncology Innovative Medicines, AstraZeneca, Alderley Park, Cheshire (UK)
(f) Chemistry, Oncology Innovative Medicines, AstraZeneca, Cambridge (UK)
(g) Bioscience, Oncology Innovative Medicines, AstraZeneca, Cambridge (UK)

REFERENCES

[1] J.A. Grasby *et al.*, *Trends Biochem. Sci.* **37**, 74–84 (2012).
[2] S.E. Tsutakawa *et al.*, *Cell* **145**, 198–211 (2011).
[3] S. Waga *et al.*, *J. Biol. Chem.* **269**, 10923–10934 (1994).
[4] R.A. Bambara *et al.*, *J. Biol. Chem.* **272**, 4647–4650 (1997).
[5] D.M. van Pel *et al.*, *PLoS Genet.* **9**, e1003254 (2013).
[6] J.L. Illuzzi *et al.*, *Curr. Med. Chem.* **19**, 3922–3936 (2012).
[7] J.-C. Hwang *et al.*, *PLoS One* **10**, e0139435 (2015).

INOSITOL PYROPHOSPHATE SENSOR DOMAINS CONTROL PHOSPHATE HOMEOSTASIS IN EUKARYOTIC CELLS

SPX domains of previously unknown function are present in fungi, plants and animals. Several SPX domain crystal structures reveal a novel fold and a binding site for inositol pyrophosphates, enigmatic signalling molecules whose levels change in response to nutrient starvation.

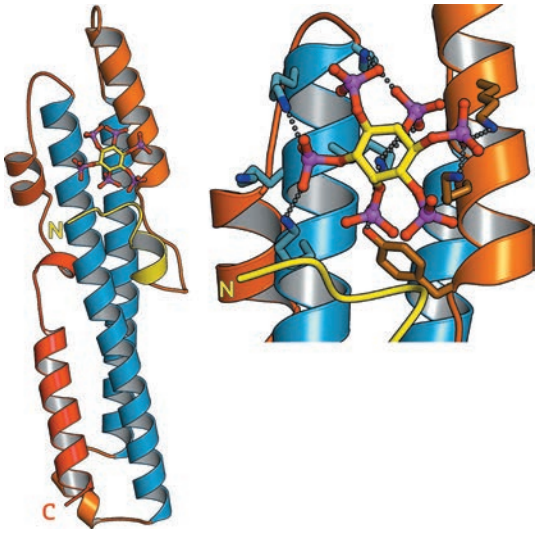

Fig. 91: Ribbon representation of the crystal structure of the SPX domain of *C. thermophilum* glycerophosphodiesterase SPX domain in complex with inositol hexakisphosphate (stick representation). Inset: close-up view of the PP-InsP binding site, with many conserved lysine residues coordinating the phosphate groups of the ligand (dotted lines).

SPX domains are small, soluble domains found in fungi, plants and animals. They can exist as stand-alone modules but are often located at the N-termini of proteins involved in phosphate uptake, transport, storage, metabolism or signalling. We determined 3.3 – 1.9 Å structures of fungal and human SPX domains from crystals obtained by carrier driven crystallisation and including data collected at beamline **ID29** [1]. The different structures revealed a new fold with two long α-helices, connected by linkers of variable size. These core helices and two smaller C-terminal helices together form a 3-helix bundle, which is preceded by a flexible N-terminal helical hairpin (**Figure 91**). Many invariant lysine residues, which represent sequence fingerprints for SPX domains, are clustered in proximity to the N-terminal hairpin structure. A combination of genetic and biochemical experiments in yeast and Arabidopsis revealed that this basic surface represents a docking platform for inositol pyrohosphosphates (PP-InsPs), signalling molecules with poorly characterised cellular functions (**Figure 91**).

The concentrations of PP-InsP are known to change in cells, depending on whether they are supplied with sufficient amounts of inorganic phosphate or whether they experience phosphate starvation. We could demonstrate that SPX domains, when bound to PP-InsPs can interact with other proteins. In plants, one such interaction partner is a transcription factor, which is switched on under phosphate starvation to induce expression of genes that allow the plant to respond to the lack of this important nutrient. Under normal growth conditions, when PP-InsP levels are high, the transcription factor is kept inactive by forming a PP-InsP-dependent complex with a plant SPX domain. Under phosphate starvation, the lack of PP-InsP leads to dissociation of the transcription factor – SPX domain complex, thereby enabling the transcription factor to transcribe its target genes.

Taken together, our work defines SPX domains as cellular receptor for PP-InsPs, which control phosphate uptake, transport, storage, metabolism and signalling in fungi, plants and animals.

PRINCIPAL PUBLICATION AND AUTHORS

Control of eukaryotic phosphate homeostasis by inositol polyphosphate sensor domains, R. Wild (a), R. Gerasimaite (b), J.Y. Jung (c), V. Truffault (d), I. Pavlovic (e), A. Schmidt (b), A. Saiardi (f), H.J. Jessen (g,h), Y. Poirier (c), M. Hothorn (a) and A. Mayer (b), *Science* **352**, 986-990 (2016); doi: 10.1126/science.aad9858.
(a) Structural Plant Biology Laboratory, Department of Botany and Plant Biology, University of Geneva (Switzerland)
(b) Department of Biochemistry, University of Lausanne (Switzerland)
(c) Department of Plant Molecular Biology, University of Lausanne (Switzerland)
(d) Department of Biochemistry, Max Planck Institute for Developmental Biology, Tübingen (Germany)
(e) Department of Chemistry and Pharmacy, University of Zürich (Switzerland)
(f) Medical Research Council Laboratory for Molecular Cell Biology, University College London (UK)
(g) Department of Chemistry and Pharmacy, University of Zürich, (Switzerland)
(h) Institute of Organic Chemistry, Albert-Ludwigs-University Freiburg (Germany)

REFERENCES

[1] R. Wild and M. Hothorn, *Protein Sci.,* (2016); doi: 10.1002/pro.3073.

MECHANISTIC INSIGHTS INTO THE DEUBIQUITINASES A20 AND CEZANNE

Ubiquitination is one of the most common posttranslational modifications of proteins. Deubiquitinating enzymes (DUBs) of the OTU family hydrolyse differently-linked polyubiquitin chains with high specificity. Crystal structures of OTU DUBs alone and trapped substrate and product complexes have revealed that the Lys11-linkage specificity of OTUD7B/Cezanne originates from large-scale conformational changes whereby ubiquitin-binding sites are formed and lost during a ubiquitin-assisted catalytic reaction.

Deubiquitinating enzymes (DUBs) are key regulators of many cellular processes. Their action can stabilise proteins from proteasomal degradation, or counteract ubiquitin-dependent signalling processes. Amongst the ~100 human DUBs are 16 OTU domain-containing enzymes with diverse cellular functions **[1]**. OTU DUBs can be further divided in subfamilies according to the size of their catalytic domain, which has been well studied for several enzymes. A20-like OTU DUBs feature the largest catalytic domain. The founding member A20 is an important negative-feedback regulator of NFκB signalling and a tumour suppressor in human cancers. Cezanne regulates NFκB as well as HIF1α signalling. A key difference between A20 and Cezanne is their ubiquitin chains specificity: while the A20 catalytic domain targets mostly Lys48-linked ubiquitin chains *in vitro*, Cezanne as well as the closely-related Cezanne2 are the only known DUBs with specificity for Lys11-linked polyubiquitin **[2]**. The molecular basis of this specificity has remained largely unclear.

To understand linkage preference in A20-like OTU DUBs, and the Lys11-specificity of Cezanne in particular, we determined crystal structures of Cezanne alone, of Cezanne bound to Lys11-linked diubiquitin (substrate complex), and of Cezanne and A20 with monoubiquitin bound (product complexes) (**Figure 92**). The key to determining the complex structures were significant advances in chemical biology. The A20–ubiquitin complex structure exploited a new Cys-attacking propargyl warhead that allowed purification and crystallisation. Moreover, a Lys11-linked diubiquitin activity-based probe (ABP) was instrumental in the generation of a Cezanne–Lys11 diubiquitin complex. This probe covalently reacts with the catalytic Cys residue

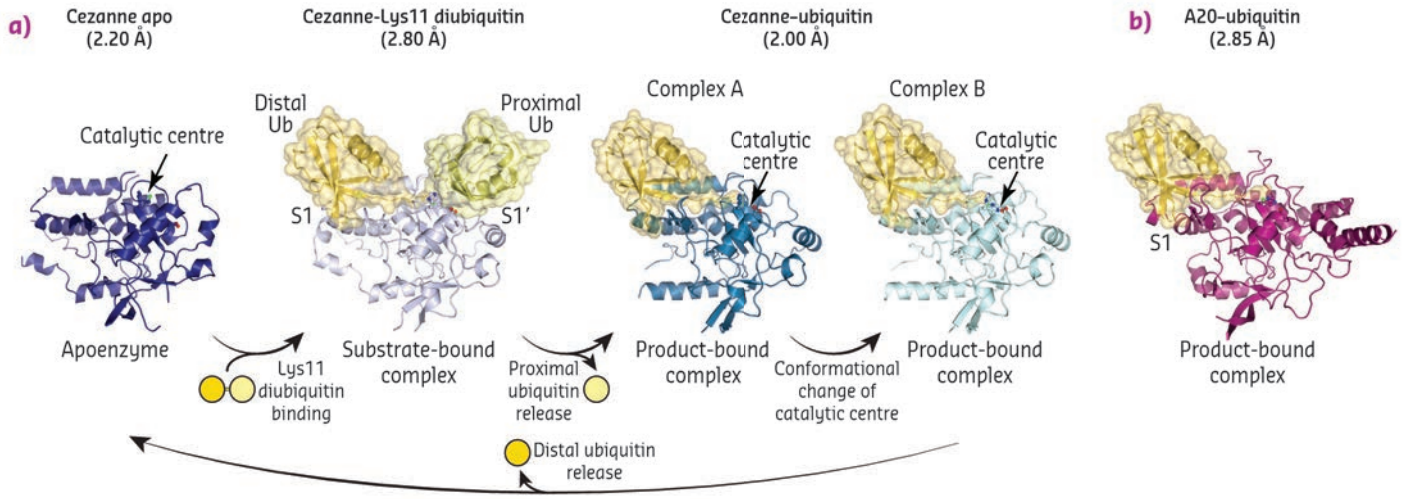

Fig. 92: a) Crystal structures of Cezanne alone, bound to its substrate Lys11-linked diubiquitin and with the cleavage product monoubiquitin. b) Structure of monoubiquitin-bound A20.

of Cezanne and enabled purification of the complex. Data for the Cezanne apo structure were collected at beamline **ID23-1** and phased using SeMet phases derived from data collected at KEK. Data for the A20–ubiquitin structure was collected at beamline **ID29**, while the remaining Cezanne structures were collected at Diamond Light Source.

Collectively, the structures for the first time followed a DUB, Cezanne, along the reaction coordinate through the various stages of its catalytic cycle (**Figure 92**). Most striking, and so far only observed in Cezanne, were large-scale conformational changes which transformed an inactive to an active enzyme, and which modulated ubiquitin binding. Two ubiquitin binding sites are required to place a diubiquitin substrate across the active site; of these, the S1 ubiquitin-binding site that is occupied in monoubiquitin complexes, was present in all structures, and was identical between A20 and Cezanne. The second, so-called S1' ubiquitin-binding site, contacts the 'proximal' ubiquitin that determines the linkage type of the preferred substrate. Surprisingly, we found that in Cezanne, this binding site only exists in the diubiquitin complex structure, and is formed *in situ* when a substrate is bound, but lost in the apoenzyme and monoubiquitin-bound complex structures (**Figure 93**).

The observed conformational changes were reconciled by hydrogen-deuterium exchange mass spectrometry (HDX-MS) experiments, and by mutagenesis and kinetic analysis. The latter further revealed a mechanism of substrate-assisted catalysis. Cleavage kinetics for differently-linked chain types showed similar K_M values, but differed in k_{cat}, with Lys11-linked

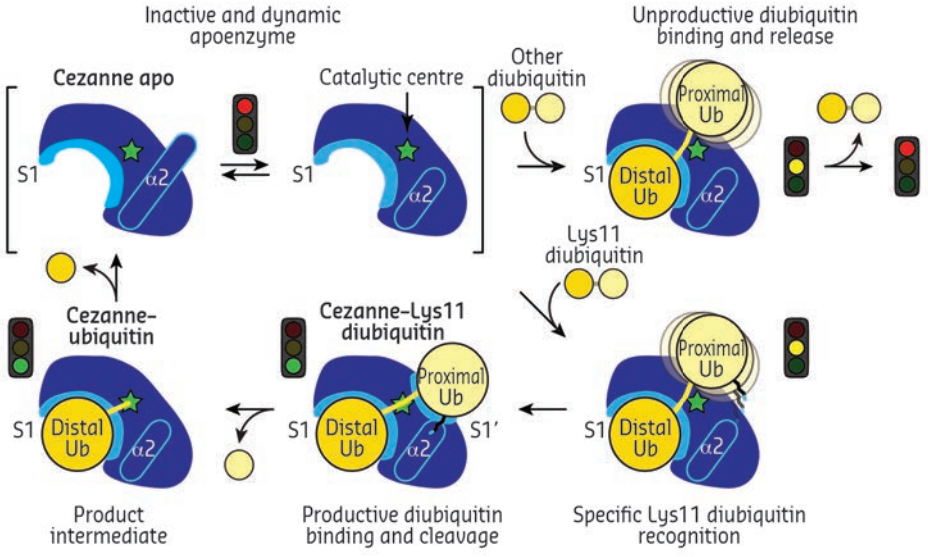

Fig. 93: Model of the catalytic mechanism for the Lys11-specific DUB Cezanne. Cezanne recruits diubiquitin via the S1 site, yet only Lys11-chains can bind productively across the catalytic centre.

diubiquitin cleavage being > 270-fold faster than other chain types. The diubiquitin complex structure revealed points of contact between the proximal ubiquitin and the enzyme that when interrupted led to a decreased k_{cat}. After the OTU enzyme OTULIN, this is the second time such mechanism of ubiquitin-assisted catalysis has been identified to determine chain linkage specificity **[3]**.

DUBs are emerging as promising drug targets in numerous human diseases, including cancer and neurodegeneration. Our work has revealed how new conformational states can occur while the enzymes perform their tasks. Knowledge of these states will be essential for rational drug design, and may enable new strategies to target DUBs with specific small molecule inhibitors.

PRINCIPAL PUBLICATION AND AUTHORS

Molecular basis of Lys11-polyubiquitin specificity in the deubiquitinase Cezanne, T.E.T. Mevissen (a), Y. Kulathu (a), M.P.C. Mulder (b), P.P. Geurink (b), S.L. Maslen (a), M. Gersch (a), P.R. Elliott (a), J.E. Burke (a), B.D.M. van Tol (b), M. Akutsu (a), F. El Oualid (b), M. Kawasaki (c), S.M.V. Freund (a), H. Ovaa (b) and D. Komander *(a), Nature 538, 402-405 (2016). doi: 10.1038/nature19836.*
(a) MRC Laboratory of Molecular Biology, Cambridge (UK)
(b) Netherlands Cancer Institute (NKI), Amsterdam (The Netherlands)
(c) High Energy Accelerator Research Organization (KEK), Tsukuba (Japan)

REFERENCES

[1] Komander *et al.*, *Nat Rev Mol Cell Biol* **10**, 550-63 (2009).
[2] Mevissen *et al.*, *Cell* **154**, 169-84 (2013).
[3] Keusekotten *et al.*, *Cell* **153**, 1312-26 (2013).

FIRST STRUCTURE AND INHIBITOR OF THE EMERGING CANCER TARGET MTHFD2

Mitochondrial MTHFD2 is highly upregulated in cancer cells to support purine and thymidylate synthesis. MTHFD2 is normally only expressed during embryonic development and not in adult cells. The structure of MTHFD2 and identification of an inhibitor now provides a promising foundation for the development of potent cancer drugs.

Rapidly dividing cells depend on one-carbon units that are supplied for the synthesis of several important compounds in the cell, most importantly the purine bases adenine and guanine, and the pyrimidine base thymidine. The one-carbon units are attached to tetrahydrofolate (THF) molecules oxidised to different states depending on the final application. One of the enzymes facilitating these oxidations is the mitochondrial methylene-THF dehydrogenase and cyclohydrolase (MTHFD2), which has previously been found to be highly expressed in several types of cancer cells. Normally expressed in embryonic cells and not in adult cells, MTHFD2 is a very interesting target for cancer treatment due to the possibility to kill cancer cells without harm to normal cells. The first structure of MTHFD2 together with the first inhibitor of the enzyme is now providing the opportunity to develop potent and selective inhibitors.

First discovered in Ehrlich ascites tumour cells in 1960 and later described as a mitochondrial NAD^+-dependent methylene-THF dehydrogenase and cyclohydrolase expressed in embryonic

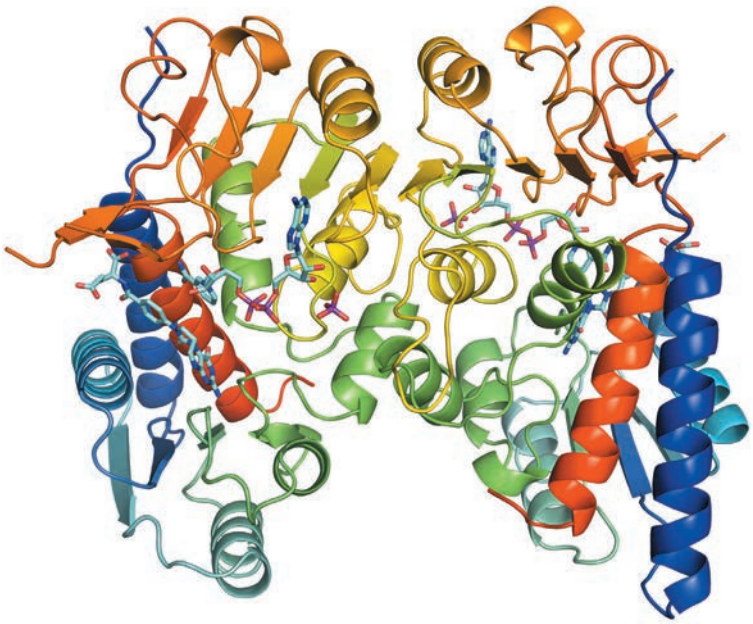

Fig. 94: Overall structure of the MTHFD2 dimer. Monomers are shown as cartoon in rainbow colouring. Ligands (NAD^+, LY345899 and inorganic phosphate) for both monomers are shown as sticks (cyan, phosphor coloured purple).

and transformed cells, MTHFD2 needs both NAD^+ and inorganic phosphate as cofactors to function. In the same protein family, the use of $NADP^+$ has also been found, for example in the cytosolic trifunctional MTHFD1, that is part of the same enzyme family as MTHFD2 and shares the dehydrogenase and cyclohydrolase functions. MTHFD1 also carries out a 10-formyl-THF-synthetase function in a second domain missing in MTHFD2.

LY345899 is a substrate-based inhibitor originally developed for MTHFD1 and very closely resembles the methylene-THF that is a substrate for both MTHFD1 and MTHFD2. To show target engagement of the inhibitor against MTHFD2, we performed several *in vitro* and *in vivo* assays. An *in vitro* dose-response curve for both MTHFD2 and MTHFD1 determined IC_{50} values for inhibition, 663 nmol/L for MTHFD2 and 96 nmol/L for MTHFD1. Binding of LY345899 to MTHFD2 was confirmed by differential scanning calorimetry (DSF), where addition of LY345899 increased the protein melting point from 44°C to 55°C. To confirm binding in a cellular context, both CETSA and DARTS assays were also performed. Cellular thermal shift assay (CETSA) show an increased stability of the protein in cell lysates with the inhibitor added. Drug affinity responsive target stability assay (DARTS) show an increased stability of MTHFD2 against protease degradation when incubated with inhibitor in cell lysates. As for CETSA, a similar effect is not seen when using intact cells. Both CETSA and DARTS measure protein stability in a cellular context upon addition of the inhibitor and in both cases MTHFD2 is stabilised by LY345899, a clear sign of target engagement.

Following data collection at beamline **ID30A-3**, the crystal structure was determined to a resolution of 1.9 Å. The structure of MTHFD2 shows clearly the binding of both cofactors as well as the inhibitor LY345899 (**Figure 94**). All substrates bind in a long, wide cleft formed between the N-terminal and C-terminal domains of MTHFD2. The protein is a dimer, as is clearly seen in **Figure 94**, and an interesting feature is that both monomers interact with inorganic phosphate (**Figure 95a**).

Detailed binding of LY345899 in the active site of MTHFD2 can be seen in **Figure 95b**, where several hydrogen bonds as well as bridging water molecules help anchor the inhibitor in place. Electron density for the inhibitor is clear and well defined. The YxxxK motif that has been proposed for the substrate binding and cyclohydrolase activity of MTHFD2 is found close to the inhibitor. The nicotinamide moiety of NAD is ideally positioned for the dehydrogenase reaction. The binding of NAD and inorganic phosphate can be seen as a NADP mimicking arrangement even though the protein prefers NAD + phosphate over NADP, **Figure 95a**.

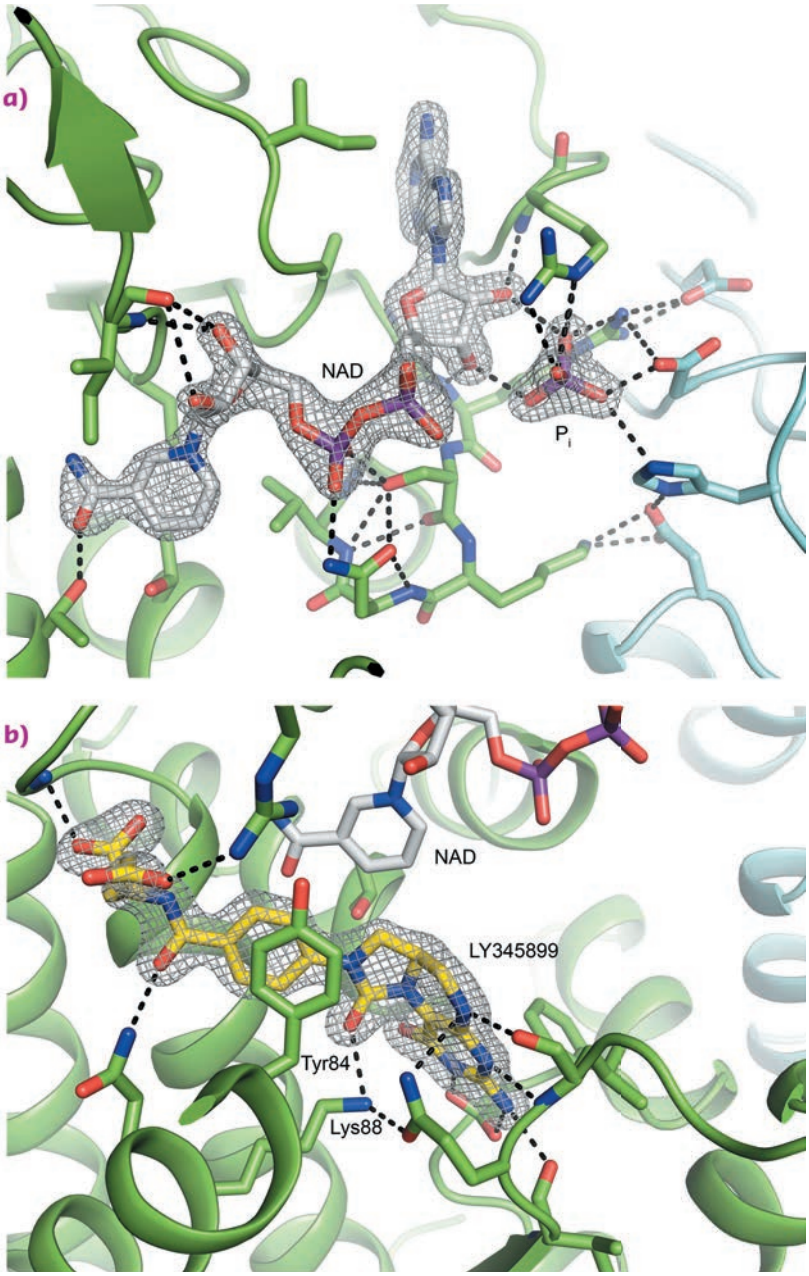

Fig. 95: Cofactor and inhibitor binding sites. Electron density: 2Fo-Fc map at 1.5 σ. Monomers shown in green and cyan. Important residues for hydrophobic interactions and hydrogen bonding are shown as sticks. Waters are omitted for clarity. Phosphorous is coloured purple. a) Binding of NAD^+ (grey) and inorganic phosphate, b) Binding of LY345899 (yellow), with NAD^+ shown in grey.

Evidence of MTHFD2 upregulation and over-expression in cancer cells is clear. The protein is expressed in embryonic cells and transformed cells independent of their tissue of origin, but importantly not in adult healthy cells. The cancer-specific expression of MTHFD2 holds the promise of fewer adverse side-effects compared to many drugs currently used in cancer therapy. Collectively, these aspects make the MTHFD2 protein highly promising as an anticancer target. The crystal structure of MTHFD2 and the identification of the first MTHFD2 inhibitor can now provide a rationale for developing highly potent and selective MTHFD2 inhibitors.

PRINCIPAL PUBLICATION AND AUTHORS

Crystal structure of the emerging cancer target MTHFD2 in complex with a substrate-based inhibitor, R. Gustafsson (a), A.-S. Jemth (b), N.M.S. Gustafsson (b), K. Färnegårdh (c), O. Loseva (b), E. Wiita (b), N. Bonagas (b), L. Dahllund (d), S. Llona-Minguez (b), M. Häggblad (e), M. Henriksson (b), Y. Andersson (d), E. Homan (b), T. Helleday (b) and P. Stenmark (a), *Cancer Research* (in press); doi: 10.1158/0008-5472.CAN-16-1476.

(a) Department of Biochemistry and Biophysics, Stockholm University, Stockholm (Sweden)
(b) Science for Life Laboratory, Division of Translational Medicine and Chemical Biology, Department of Medical Biochemistry and Biophysics, Karolinska Institutet, Stockholm (Sweden)
(c) Drug Discovery and Development Platform, Science for Life Laboratory, Department of Organic Chemistry, Stockholm University, Solna (Sweden)
(d) Drug Discovery and Development Platform, Science for Life Laboratory, School of Biotechnology, Royal Institute of Technology, Solna (Sweden)
(e) Biochemical and Cellular Screening, Science for Life Laboratory, Department of Biochemistry and Biophysics, Stockholm University, Stockholm (Sweden)

Complex systems and biomedical sciences

2016 was a very busy and productive year with the Complex Systems and Biomedical Sciences Group (CBS) beamlines providing full user service, while concurrently its staff have been planning the beamlines evolution alongside the EBS lattice. The user community is greatly involved in the science programmes and beamline designs and we received six expressions of interests from groups in surface science, coherent spectroscopy, diffraction, medical imaging and therapy. The scientific cases for upgrading ID03 and ID10 were presented at the EBS workshop held on December 8-9. Overall, the beamlines will benefit enormously from the new lattice and technology.

The main news from our beamlines and labs are discussed below.

For **ID02**, the small-angle scattering beamline, 2016 was a normal year of operation. The main event was the highly successful review in November which acknowledged the impressive output from the beamline. A new technique available to users is X-ray photon correlation spectroscopy (XPCS) in the ultra-low angle range to probe dynamics on the micrometre length scale.

ID03, the surface science beamline, welcomed new staff with the arrival of two new postdocs and a PhD student. On the technical side, significant detector improvements were made with the replacement of the sensors in the two Maxipix detectors and a refurbishment of the ADSC large-area detector. An oxygen gas cracker in the UHV diffractometer is now available for users. In the catalysis laboratory, the flow reactor for *in situ* catalysis experiments was refurbished and a new setup for *in situ*/operando electrochemical experiments with OLEMS gas detection was built in collaboration with TU Eindhoven. Finally, a new instrument combining a scanning probe microscope (SPM) and X-ray scattering at ambient-pressure was built in collaboration with Leiden University.

As for **ID09**, the time-resolved beamline, the ageing FreLoN detector was replaced with a larger Rayonix MX170. The larger field-of-view, faster readout and higher sensitivity of the new detector are increasing the efficiency of all experiments. In its high-speed mode, the detector can acquire 100 images per second. For molecules containing transition metals, X-ray emission spectroscopy is now available to monitor changes in valence and spin states during chemical reactions. The emission, which is intensified by the pink beam, can be recorded simultaneously with WAXS and thus provides complementary site-specific information. With the classical Johann spectrometer at ID09, the energy and line profiles are measured by scanning the Bragg angle of the analyser. Alternatively, the spectrum can now be recorded, without scanning, by a van Hamos spectrometer. In this spectrometer, a cylindrical crystal focuses the emission into a line on a Maxipix detector. The van Hamos covers a 100 eV wide spectrum and can record both core-to-core and valence-to-core (vct) spectra in a single measurement. The vct emission is weak, about 100 times weaker than core-to-core, but it is more sensitive to the environment and simpler to predict theoretically.

At **ID10**, there have been improvements to the instrumentation of the two stations for soft interfaces and coherent scattering. A high-resolution diffractometer with a double-crystal deflector for liquid surface and interface studies was successfully commissioned in 2016. After one year of operation, the diffractometer has proven to be excellent. A CdTe 2x2 Maxipix detector has greatly increased the efficiency of XPCS and CXDI at 21 keV, which is important for probing the dynamics and structure of objects in enclosures. Both stations are working to provide new instrumental capabilities and science to take maximum benefit from the increased coherence and brightness promised by the EBS upgrade.

ID17, the biomedical beamline, is dedicated to *in vitro* and *in vivo* medical research. For micro-CT imaging, the beamline offers a large portfolio of detectors for multiscale imaging in the energy range 25-180 keV. A Frelon and PCO.5.5 detector are used with optical lenses to define pixels from 3.1 to 47 µm and a field-of-view up to 180 mm. The most requested imaging technique is free propagation phase contrast, which is alone taking more than 40% of the beamtime. A new setup for high resolution micro-CT will be ready at the beginning of 2017. Microbeam radiation therapy (MRT), also highly requested, is aiming at studying tumouricidal properties of intense microbeams often combined with nanoparticles or other chemotherapic adjuvants. Other MRT programmes study the effect of microbeams in reducing seizures in epilepsy, etc.

The Biomedical Facility (BMF) is playing a key role in supporting experiments at ID17 and at other beamlines. In 2016, Geraldine Le Duc, scientist in charge of the BMF, took sabbatical

leave. In her absence, Alberto Bravin is acting scientist in charge. Finally, the beamline was reviewed very positively in May.

For the Partnership for Soft Condensed Matter (PSCM), the most notable new instruments are the nanodrop UV-vis spectrometer and the 3D printer for microfluidics. The former Surface Science Lab (SSL) was integrated within the PSCM and the capability of its atomic-force microscopes (AFMs) has been extended. Since September 2016, an agreement between the ESRF and ILL has allowed all ESRF users to have full access rights to the PSCM labs located in the Science Building. ESRF users can request PSCM support directly in their beamtime proposals and A-forms. Examples of science driven by PSCM partners include the nano-structure of keratin bundles in cells (C.Y.J. Hémonnot *et al.*, in the X-ray nanoprobe chapter) and the development of new texture analysis methods for composite nanomaterials (T.A. Grünewald *et al.*, in this chapter). In preparation for the EBS, we are working in collaboration with the Göttingen partner on a portable cryo-chamber for nanobeam studies of biological tissues. Finally, a partnership with Vienna-BOKU University was signed in September and it foresees the contribution of at least one visiting PhD student.

The CBS staff took part in the organisation of the International Soft Matter Conference (ISMC2016) in Grenoble in September. There were 680 participants and the participants and speakers were very happy with the quality of the presentations.

For the EBS programme, the CBS group has submitted two conceptual design reports for new beamlines: CDR1 is a proposal for a beamline for coherent beam studies of the dynamics and structure of hard and soft complex systems. The new beamline will take full advantage of the 100 times increase in coherent flux of the EBS which is expected to open up new horizons in physics, material science and biology. CDR4 is a proposal for a surface science beamline with a wide portfolio of techniques for the investigation of chemical and physical processes of nano objects on solid and liquid interfaces. The highly intense beam will create new opportunities for *in situ* and real-time studies of surfaces and interfaces for areas such as catalysis, electrochemistry, 2D materials, biomimetic membranes and polymers.

M. WULFF

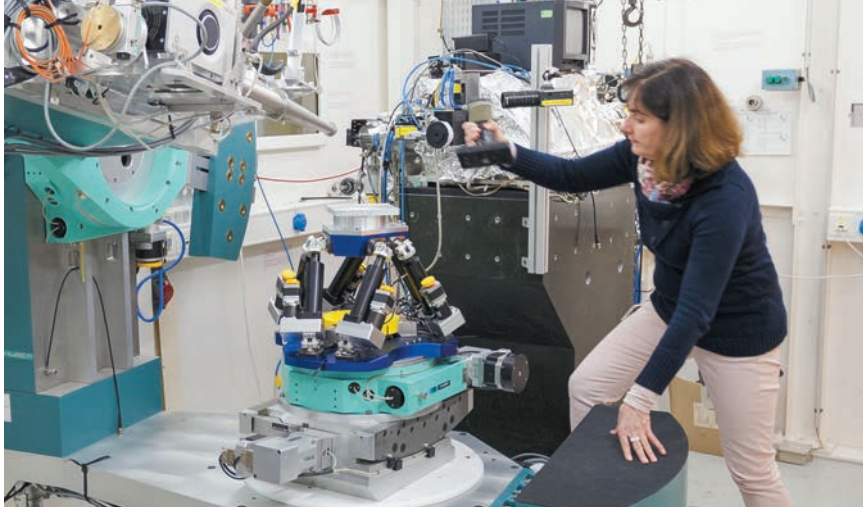

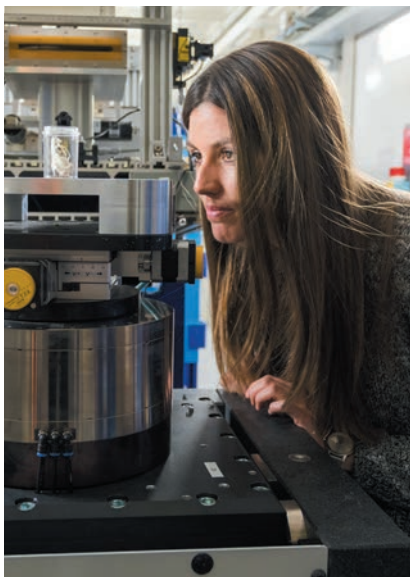

SAXS MEASUREMENTS EXPLAIN THE COLOUR NANOSTRUCTURE RELATIONSHIP IN FEATHERS

Structural colours are omnipresent in nature. Small-angle X-ray scattering has been used to understand the fine level of control that alters the size of the nanostructure in Jay feathers responsible for colour changes from blue to white. This control is made by regulating the duration of the β-keratin phase separation before vitrification.

The intensity and diversity of structural colours in nature is well-known. Only recently has the sophistication of the physics responsible for these optical effects been understood on the nanometre length scale **[1,2]**. Bird feathers have played an important role in our understanding of structural colour, as coloured feathers comprise nano-structured β-keratin materials that can be studied in great detail post mortem.

Two-dimensional Fourier analysis of electron microscopy images **[3]** showed that the blue colour in feathers is due to the constructive interference between light waves, coherently scattered by a nanostructured keratin–air matrix. Blue feathers function as Bragg reflectors. Scanning probe microscopy shows that the blue colour in the Jay's feather is caused by a foam like structure.

Fig. 96: Photograph of the Jay *Garrulus glandarius* showing the wing feathers with the periodic white blue black pattern (Open access image, credit: Luc Viatour/www.Lucnix.be).

To probe the lengthscales in the blue and white pattern in the feathers of the Jay (*Garrulus glandarius,* **Figure 96**), we used the small-angle X-ray scattering (SAXS) setup at beamline **ID02**. The spatial colour map of the feather in **Figure 97b** was obtained by the Fourier transform of the SAXS data, which probes the periodic structure, which in turn determines the optical reflectivity. The data shows the periodic modulation in the size of the domain and consequently the colour as a function of position, which has not been seen in these nanostructures before. The colour in the top panel of **Figure 97b** was extracted from the SAXS data; it faithfully matches the colour in the optical image (lower panel) showing the link between nanostructure and optical reflectivity.

Given the q-range available in the SAXS setup, we were able to follow the large dynamic range in the structure that the feather barbs span. We used one dimensional correlation analysis to extract the real space morphology and transitions in size. This approach has also been used extensively in semi-crystalline polymers, using the CORFUNC software to examine the amorphous crystalline lamellae. With the only assumption that the sample is a two-phase system with differences in electron density, the auto-correlation function allows the period and the domain width of the nanostructure to be determined.

The optical structure responsible for the colour of Jay feathers is produced by a phase-separation process that is arrested at a late stage and the colour differentiation is achieved by controlling the duration of the phase-separation. This mechanism is likely to be widely shared amongst birds, reptiles and amphibians.

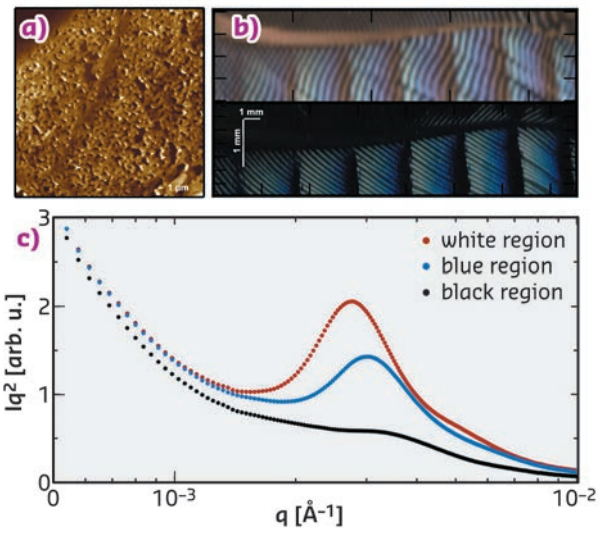

Fig. 97: a) Scanning-probe image of the dark blue region showing the sponge-like morphology responsible for the optical properties. b) The colour derived from the X-ray determined structure (top panel) and the image of the area mapped (bottom panel) using X-ray scattering, showing the correlation of the nanostructure to the reflected colour. c) Representative Lorentz-corrected SAXS data for the different structural colour regions of a Jay feather barb (measured at beamline ID02).

PRINCIPAL PUBLICATION AND AUTHORS

Spatially modulated structural colour in bird feathers, A.J. Parnell (a), A.L. Washington(a,b), O.O. Mykhaylyk (c), C.J. Hill (d), A. Bianco (b), S.L. Burg (a), A.J.C. Dennison (e,f), M. Snape (a), A.J. Cadby (a), A.J. Smith (g), S. Prevost (h), D.M. Whittaker (a), R.A.L. Jones (a), A.R. Parker (i) and J.P.A. Fairclough (b), *Nature Scientific Reports*, 18317 (2015); doi: 10.1038/srep18317.

(a) Department of Physics and Astronomy, The University of Sheffield (UK)
(b) Department of Mechanical Engineering, The University of Sheffield (UK)
(c) Department of Chemistry, The University of Sheffield (UK)
(d) Department of Molecular Biology and Biotechnology, The University of Sheffield (UK)
(e) University Grenoble-Alpes, IBS, Grenoble (France)
(f) Institut Laue-Langevin, Grenoble (France)
(g) Diamond Light Source, Didcot (UK)
(h) ESRF
(i) Department of Zoology, Natural History Museum, London (UK)

REFERENCES

[1] A.R. Parker, *J. Opt. A: Pure Appl. Opt.* **2**, R15–R28 (2000).
[2] P. Vukusic *et al.*, *Science* **315**, 348–348 (2007).
[3] R.O. Prum *et al.*, *Nature* **396,** 28–29 (1998).

HOW SEA CUCUMBERS STIFFEN AND SOFTEN THEIR TISSUES

The mutable collagenous tissue found in sea cucumbers and starfish is unique among connective tissues because it can change its mechanical state quickly. However, how it achieves this feat is not known. Using synchrotron X-rays to study collagen deformation *in situ*, the mechanical change is explained by a change in the gel-like matrix between collagen fibrils.

Collagen is a core building block of both vertebrate and invertebrate connective tissues. In mechanically critical tissues like tendons, skin and heart valves, the fibrillar composite architecture – including collagen, proteoglycans, fibrillin and other proteins and water – is adapted to the needed *in vivo* mechanical response. These mechanical properties are usually constant over short periods of time (seconds) and vary only on much longer timescales (days or months). However, one remarkable exception is the "mutable collagenous tissue" (MCT) which is found in echinoderms – such as starfish, sea cucumbers and brittle stars (**Figure 98a**). Such animals use MCT to rapidly change their mechanical properties in a few seconds, for example softening their body wall to escape predators, emit sticky tubules from their gut as a defence mechanism or engage in locomotion in an energy efficient manner (**Figure 98b**). Understanding how MCT works sheds light on the remarkable adaptation in a highly successful group of animals, the echinoderms, and it also provides insight into the development of biomaterials with changeable mechanical properties.

At the ultrastructural level, MCT consists of spindle-shaped collagen fibrils in an interfibrillar matrix of proteoglycans and noncollageneous proteins like tensilin and stiparin, which along with fibrillin-rich microfibrils comprise the extracellular matrix **[1]**. Embedded inside MCT are effector cells known as juxtaligamental cells (JLCs) that are innervated and controlled by the nervous system. Currently the proposed

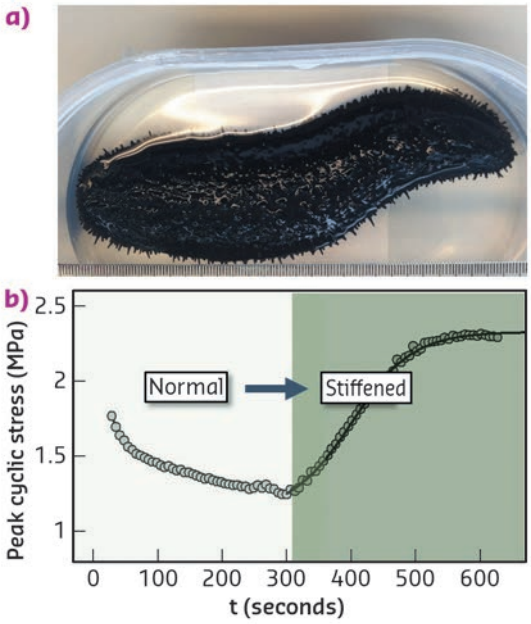

Fig. 98: a) Black sea cucumber (*Holothuria edulis*). b) Increase in peak cyclic force on MCT when changing the state of the tissue from standard to stiff (with addition of KASW) showing nearly 80% increase in stress.

mechanisms enabling MCT in echinoderm tissue suggest that the JLCs play a role by releasing proteins that crosslink the fibrils, but to date there have been no direct experimental studies of the ultrastructural mechanisms.

To resolve the fibrillar-level mechanics, we used time-resolved synchrotron small angle X-ray diffraction (SAXD) combined with *in situ* mechanical testing of MCT in different states of mechanical activation (via ionic stimulation). Collagen fibrils have a banded pattern along the fibril leading to a series of Bragg peaks in the meridional SAXD pattern. Therefore, real-time acquisition of stress-induced changes in fibrillar mechanical strain show up as shifts

in the meridional Bragg peaks [2]. We carried out *in situ* SAXD measurements at beamline **ID02** to determine fibril strain and orientation. Mechanically stimulated MCT (incubated in potassium rich artificial sea water or KASW) showed a clear increase of fibril strain with applied tissue strain (**Figure 99a**). In contrast, MCT in the soft state (incubated in calcium free sea water or CaFASW) exhibited almost no increase in fibril strain with tissue strain. Concurrently, angular SAXD intensity distributions showed that fibrils in stiffened MCT transitioned quicker (relative to softened MCT) to align along the external loading direction.

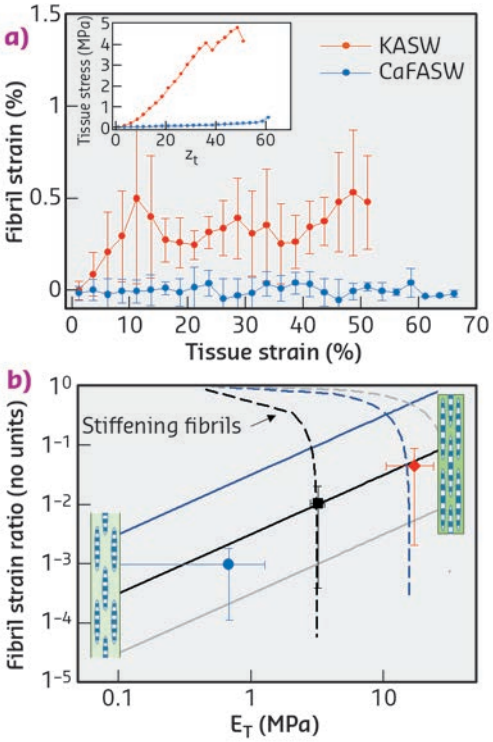

Fig. 99: a) Fibril strain increases with tissue strain for KASW-treated stiff MCT whilst showing no increase in CaFASW treated soft MCT (inset shows macroscopic stress-strain plots for the two cases). b) Using a fibril-level model of force transfer at the nanoscale in MCT, the experimental data (solid symbols) for the fibril strain fraction follow the trend for increasing interfibrillar matrix stiffness (solid lines) rather than stiffening collagen fibrils (dashed lines). Inset: schematics of interfibrillar sliding (left) and fibrillar stretching (right).

We explain these findings by considering how shear stresses in the interfibrillar matrix of proteins and glycosaminoglycans enable tensile stress and strain in the fibril. By increasing the interfibrillar matrix stiffness, both the tissue modulus and the amount of fibril strain increase (**Figure 99b**), whilst if the fibrils become more resistant to stretching, the two parameters are oppositely correlated. Our results clearly show that the mechanism for stiffening in echinoderm MCT is due to mechanical changes in the matrix between fibrils rather than changes in the fibril properties.

These results provide the first direct nanoscale evidence for the mechanism of rapid mechanical changes in echinoderm MCT. By demonstrating the importance of interfibrillar matrix proteins in this process, the work opens the way to testing the function of specific proteins (*e.g.* tensilin) in mediating the mutability mechanism. Understanding how collagenous matrices could soften or stiffen reversibly may have applications in developing treatments to combat hardening of tissues like skin in ageing.

PRINCIPAL PUBLICATION AND AUTHORS

Interfibrillar stiffening of echinoderm mutable collagenous tissue demonstrated at the nanoscale, J. Mo (a), S. Prévost (b), L.M. Blowes (c), M. Egertová (c), N.J. Terrill (d), W. Wang (a,e), M.R. Elphick (c) and H.S. Gupta (a,e), *PNAS* **113**, E6362-E6371 (2016); doi: 10.1073/pnas.1609341113.
(a) Queen Mary University of London, School of Engineering and Material Science, London (UK)
(b) ESRF
(c) Queen Mary University of London, School of Biological and Chemical Sciences (UK)
(d) Diamond Light Source, Didcot (UK)
(e) Institute of Bioengineering, Queen Mary University of London (UK)

REFERENCES

[1] I.C. Wilkie, Mutable Collagenous Tissue: Overview and Biotechnological Perspective. In: *Echinodermata* (eds), Springer Berlin Heidelberg (2005).
[2] A. Karunaratne *et al.*, *Bone* **84**, 15-24 (2016).

OPERANDO STUDY OF ELECTRODE/ELECTROLYTE INTERFACES IN SOLID OXIDE FUEL CELLS

Solid oxide fuel cells have the potential to provide green energy in the future. These cells produce electricity by burning fuel without combustion and, depending on the initial reactants, with a minimum of hazardous products. By operando interface diffraction, the buried region between the fuel cell's cathode and the electrolyte was investigated. The electrolyte surface region was found to change composition and develop atomic defects during operation. These processes form an additional oxygen diffusion barrier and play a role in the overall performance of fuel cells.

Solid oxide fuel cells (SOFCs) are very promising for the generation of sustainable and renewable power. Despite intense research, SOFC technology has not yet reached widespread commercial success. A more detailed microscopic understanding of the SOFC processes is necessary to tailor their performance and lifetime.

Typically, SOFCs consist of a solid electrolyte, usually yttria-stabilised zirconia, sandwiched

between a cathode and an anode. The overall performance depends on many different kinetic processes, of which the cathodic oxygen exchange reaction and oxygen transport through the electrode/electrolyte interface are bottlenecks for SOFC operation. A key target in SOFCs development is to obtain a high ion transport rate at relatively low temperatures. Perovskites are suitable candidate electrode materials for intermediate temperature range (800–1000 K) SOFCs. In this study, the mixed ionic-electronic conductor $La_{1-x}Sr_xCoO_{3-\delta}$ (LSC) was used due to its high oxygen conductivity and fast oxygen surface kinetics. The most widely used electrolyte material is yttria-stabilised zirconia (YSZ) due to its relatively high oxygen diffusion constant and stability. However, these properties depend strongly on the yttria doping level. Our aim was to study the surface segregation properties of YSZ under the influence of temperature, oxygen and cathode material.

By the use of anomalous surface X-ray diffraction (SXRD), it is possible to determine the interface composition and structure of YSZ(100) buried under the LSC microelectrode. At non-anomalous X-ray energies, the scattering of Y and Zr is practically indistinguishable. The experiment was performed at beamline **ID03** using a microfocused X-ray beam. This challenging experiment (**Figure 100**) allowed us to resolve the complete 3D interfacial structure and composition with subatomic resolution. To mimic the transport processes as they occur in a real fuel cell, we polarised the polycrystalline LSC microelectrode with respect to a porous Pt counter electrode below the single crystal YSZ(100) electrolyte under an oxygen atmosphere at elevated temperatures. Depending on the polarisation direction, inward or outward oxygen ion transport is controlled. The structural information was extracted from crystal truncation rods (CTRs) that originated from the polished YSZ single crystal surface buried under the electrode.

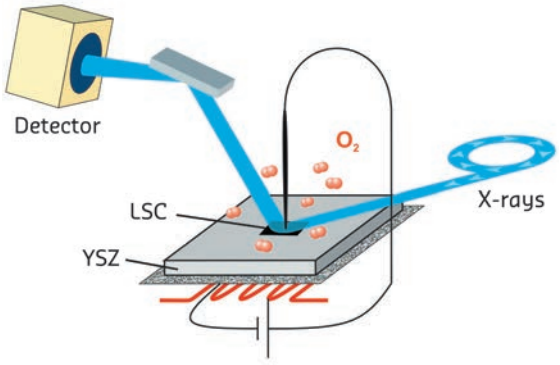

Fig. 100: Sketch of the experiment. The model SOFC is placed on a heater in an oxygen environment. The sample is polarised by a Pt backside electrode and a sharp Pt tip. An analyser crystal is used to reduce the fluorescent background reaching the detector.

The X-ray energy was precisely tuned to the Y and Zr absorption edges, thereby varying the scattering contrast between the two elements and retrieving the layer-wise composition, disclosing information about the occupancy profiles (**Figure 101**).

The results reveal that the Y cation occupancy at the electrode/electrolyte interface strongly depends on the conditions such as the applied potential. The interface was found to be Y rich after LSC film deposition; subsequent exposure to oxygen in the mbar pressure regime at 775 K strongly reduced the Y concentration at the interface, which is traced back to the complex defect chemistry and thermodynamics of LSC in contact with YSZ. Upon bias voltage application, further changes were observed, indicating enhanced Y concentration at the interface for positive bias which is expected to be detrimental for the oxygen ion transport through the interface. Further evidence for Y segregation is found by outward cation interfacial relaxation, which can be explained by considering that Y has a larger ionic radius than Zr. The LSC/YSZ(100) interface was found to stay atomically smooth under oxygen transport conditions.

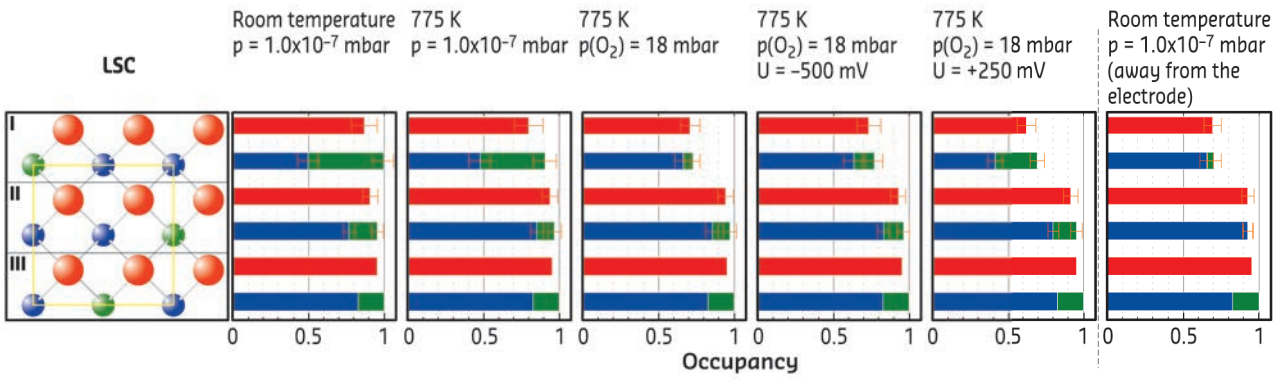

Fig. 101: Occupancy profiles of the first three atomic bilayers of the YSZ (100) electrolyte under various conditions. Shown are Y (green), Zr (blue) and O (red).

This atomic-scale information is an important input towards a microscopic understanding of the processes occurring at the cells' buried interfaces and it is instrumental in the design of next generation SOFCs.

PRINCIPAL PUBLICATION AND AUTHORS

Operando X-ray investigation of electrode/electrolyte interfaces in model solid oxide fuel cells, S. Volkov (a,b), V. Vonk (a), N. Khorshidi (c), D. Franz (a, b), M. Kubicek (d), V. Kilic (e), R. Felici (f), T.M. Huber (d), E. Navickas (d), G.M. Rupp (d), J. Fleig (d) and A. Stierle (a,b), *Chem. Mater* **28**, 3727–3733 (2016); doi: 10.1021/acs.chemmater.6b00351.
(a) Deutsches Elektronen-Synchrotron DESY, Hamburg (Germany)
(b) Fachbereich Physik, Universität Hamburg (Germany)
(c) Max-Planck-Institut für Intelligente Systeme, Stuttgart (Germany)
(d) Institute of Chemical Technologies and Analytics, Vienna University of Technology (Austria)
(e) Universität Siegen (Germany)
(f) ESRF

ROTATION AFTER RED LIGHT ABSORPTION – THE STRUCTURE OF A PHOTOACTIVATED PHYTOCHROME REVEALED

Time-resolved X-ray scattering data from red light sensitive phytochromes provide new insights into the structural changes of the protein complex upon photo activation. These findings have improved our understanding of complex sensory proteins, the manipulation of which may have future applications in agriculture and optogenetics.

Phytochromes are allosterically regulated, photoswitchable two-component signalling proteins that function in plants, fungi and bacteria. They change their conformation, and thereby their biological activity, upon the absorption of red light. In the bacterial species *Deinococcus radiodurans*, a red/far-red light absorbing phytochrome controls the production of light-protective pigments. In work carried out at beamline **ID09** at the ESRF**,** and at the SLS and APS, structural data was collected on the activation process of the full phytochrome system.

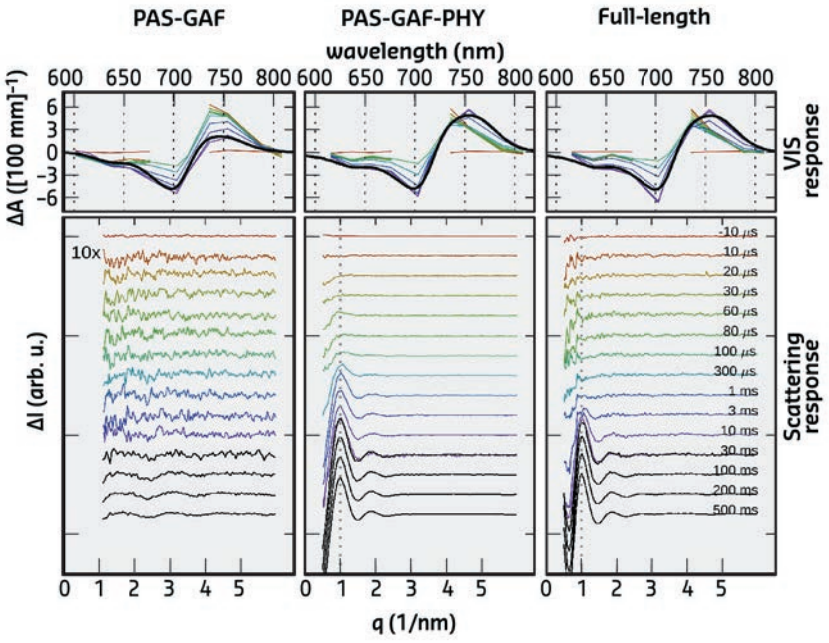

Fig. 102: Time-resolved optical absorption spectra (top) and time-resolved X-ray scattering spectra (bottom). The left panel (PAS-GAF) shows the chromophore binding domain, the middle-panel (PAS-GAF-PHY) shows the data from the photosensory unit, and the right panel (full-length) is from the full phytochrome protein complex. Colours indicate the detection time after the red-light (671 nm) laser flash.

The phytochrome protein complex contains a photo sensory module and a biological effector domain, typically a histidine kinase in bacteria. The experiments used time-resolved X-ray scattering measurements of the phytochrome constructs as they switch between the two states. To achieve this, the phytochrome solution was flashed with short bursts of red light to convert the molecules between the resting and the active state. Scattering data was collected between the flashes. The measurements were performed on both the truncated and the full-length phytochrome system. The truncated versions of the protein contained the so-called chromophore binding domain (PAS-GAF) or the photosensory unit (PAS-GAF-PHY).

The X-ray scattering data revealed major signals in the low-q range of the spectra. This reflects the large-scale structural changes in the full-length protein complex and in the photosensory unit. In contrast, the chromophore binding domain, the most compact subunit, revealed minimal structural changes in the scattering. The large-scale changes occur on the ms time scale, while the spectroscopic experiments show characteristic signals in the Vis-absorption spectra on the ns-, ms, and ms-timescale (**Figure 102**). No fast structural changes were observed by X-ray

scattering. By linking the X-ray time constants with the spectroscopic ones, it was shown that the large-scale structural changes are the end-product of the photocycle. Hence, all the early-time states contain small-amplitude structural changes and possibly chemical changes in the protein backbone, but these are too small to be detected.

Recently, it was shown that a portion of the truncated photosensory core module (PAS-GAF-PHY) undergoes refolding when it is exposed to red light and that the refolding is associated with a large-scale opening motion **[1]**. In the present study, *ab initio* structural modelling of the X-ray data revealed that the histidine kinase effector domain restricts the large-scale movements in the full-length protein. In this case the conformational push from the refolding action is used to generate a screw motion which rotates the effector domain (**Figure 103**).

To summarise, the scattering data from the photoactive protein phytochrome revealed a rotational movement of the effector domain of the protein. These large-scale structural changes are associated with the last steps of the photocycle of the phytochrome. How these large scale movements are linked to the chemical reactions in the output domain is to be shown in future studies.

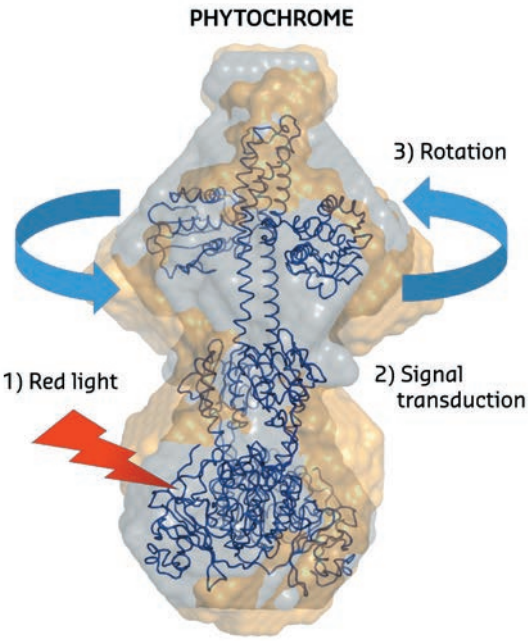

Fig. 103: The structural changes in phytochrome proteins. The phytochromes absorb red light in the biliverdin molecules located on the lower side of the protein (red arrow). After red light absorption, chemical and structural changes take place in the protein interior (signal transduction). This leads to a rotational movement on the top of the protein which generates signals to other parts of the cell. Grey spheres describe the structure of the protein in the dark state and the yellow spheres describe the structure of the illuminated state.

PRINCIPAL PUBLICATION AND AUTHORS

Structural photoactivation of a full-length bacterial phytochrome, A. Björling (a), O. Berntsson (a), H. Lehtivuori (b), H. Takala (b), A.J. Hughes (a), M. Panman (a), M. Hoernke (a), S. Niebling (a), L. Henry (a), R. Henning (c), I. Kosheleva (c), V. Chukharev (d), N.V. Tkachenko (d), A. Menzel (e), G. Newby (f), D. Khakhulin (f), M. Wulff (f), J.A. Ihalainen (b) and S. Westenhoff (a), *Science Advances* **2**, e1600920 (2016); doi: 10.1126/sciadv.1600920.
(a) University of Gothenburg (Sweden)
(b) University of Jyväskylä (Finland)
(c) The University of Chicago (USA)
(d) Technical University of Tampere (Finland)
(e) Paul Scherrer Institut (Switzerland)
(f) ESRF

REFERENCES

[1] H. Takala *et al.*, *Nature* **509**, 245 (2014).

CORRELATION BETWEEN STRUCTURAL CHANGES AND ATOMIC MOTION DURING PHYSICAL AGEING IN METALLIC GLASSES

A link between the microscopic structural mechanisms and atomic motion in metallic glasses has been discovered by a combination of dynamical and structural synchrotron techniques, providing a unique and broader view of the atomic-level complexity of these unique materials.

Metallic glasses display outstanding thermal, mechanical and chemical properties that make them forefront materials for technological applications. However, their widespread use is limited by their lack of stability over time due to physical ageing, *i.e.* the spontaneous temporal evolution of any functional physical property due to relaxation processes intrinsic to the glassy state **[1,2]**.

We have provided an overview and an atomistic understanding of the complexity of ageing in a metallic glass by connecting microscopic structural re-arrangements and atomic motion for the first time. We found that the atomic scale is dominated by the interplay between stress-releasing rearrangements leading to density inhomogeneity annihilation and fast dynamical regimes of ageing and medium range ordering processes, not affecting density, related to a

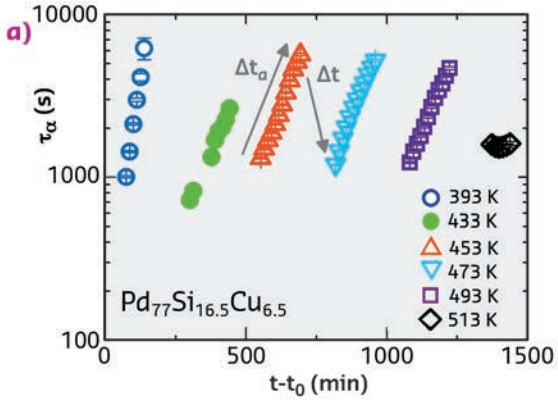

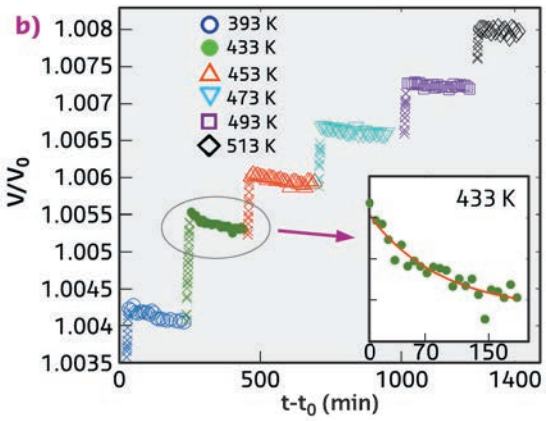

Fig. 104: a) Time and temperature evolution of the structural relaxation time measured with XPCS as a function of t-t_0, where t_0 is the time corresponding to the beginning of the heating protocol. b) Relative volume change, reported as a function of t-t_0. Each temperature ramp (x) is followed by an isotherm Inset: zoom of the curve at 433 K reported as a function of time from the beginning of the isotherm, together with the best fit to an exponential law.

more localised atomic motion. The evolution between these regimes is probably associated with a ductile-to-brittle transition.

To clarify the unique atomic motion in metallic glasses **[3]**, we have investigated the microscopic structural and dynamical changes occurring in a rapidly quenched $Pd_{77}Si_{16.5}Cu_{6.5}$ metallic glass (glass transition temperature T_g = 625 K), during successive annealing below T_g, using X-ray photon correlation spectroscopy (XPCS) at beamline **ID10**. **Figure 104a** shows structural relaxation times τ_α as a function of the time elapsed from the beginning of the heating protocol. This parameter represents the characteristic time for the dynamics at the probed length-scale. For T < 513 K, τ_α increases exponentially during the isotherm signalling a non-stationary dynamics, while it abruptly decreases during T changes due to the increasing thermal motion. The exponential increase corresponds to the fast ageing regime observed also in other hyper-quenched metallic glasses **[3]**, which can be described by the relation $\tau_\alpha(t_a,T) \sim \exp(t_a/\tau^*)$, with an almost constant growth rate parameter $\tau^* \sim 6000$ s. At T = 513 K, the ageing abruptly stops even if the system is well below T_g: the glass enters a stationary regime where τ_α remains constant at least on the probed experimental timescale.

Figure 104b presents the corresponding volume evolution as tracked by the position change of the first sharp diffraction peak (FSDP) measured by high-resolution high-energy X-ray diffraction (XRD) at beamline **ID15B**. During isotherms, the volume decreases slightly, most likely corresponding to the annihilation of residual density inhomogeneity. For increasing temperatures, the total isothermal densification decreases. Simultaneously to the onset of the stationary regime in dynamics, at T = 513 K, the volume reduction stops, corresponding to full structural defect annihilation. This suggests that structural defect annihilation is the process responsible for the fast ageing.

As shown in **Figure 105a**, a continuous narrowing of the FSDP takes place from the ageing itself, which continues even when there is no further densification. This narrowing can be taken as an indicator of an increasing medium range order, for r ≥ 6 Å **[4]**.

Both the volume and the FSDP width can be described by an exponential law with characteristic times τ_V and τ_Γ, respectively. While the volume and FSDP width have a different T dependence from the dynamical time for ageing τ^*, the agreement between τ^* and their average is striking (**Figure 105b**), suggesting that the fast dynamical ageing is due to both processes: structural defect annihilation and medium range ordering to the extent that they affect the density.

Once the structural defects are completely annihilated, the density is frozen. and thus XPCS does not see further ageing and the stationary regime is entered where dynamical measurements indicate that other stresses still exist, most likely from frustration in the repetition and ordering of atomic clusters.

These results provide a direct connection between dynamical and structural microscopic evolution

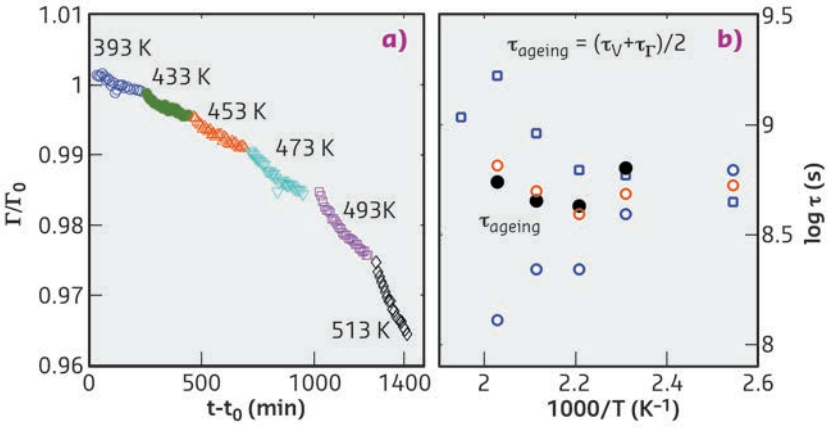

Fig. 105: a) Temporal evolution of the relative change of the width of the FSDP. b) Characteristic time for ageing as obtained from the volume relaxation (blue squares), the narrowing of the FSDP (blue circles) and from XPCS data (black dots). The average of τ_V and τ_Γ is also shown (red circles), called τ_{ageing}.

in metallic glasses which is fundamental for the development of a microscopic theory of ageing and ultimately designing new amorphous materials with improved stability.

PRINCIPAL PUBLICATION AND AUTHORS

Unveiling the structural arrangements responsible for the atomic dynamics in metallic glasses during physical aging, V.M. Giordano (a) and B. Ruta (b), *Nature Communications* **7**, 10344 (2016); doi: 10.1038/NCOMMS10344.
(a) Institute of Light and Matter, UMR5306 Université Lyon 1-CNRS, Université de Lyon, Villeurbanne, (France)
(b) ESRF

REFERENCES

[1] Y. Zhang *et al.*, *Nat. Mat.* **5**, 857 (2006).
[2] W.H. Wang, *Prog. Mater. Sci.* **57**, 487 (2012).
[3] B. Ruta *et al.*, *Phys. Rev. Lett.* **109**, 165701 (2012).
[4] D. Ma *et al.*, *Nat. Mater.* **8**, 30 (2009).

ELEMENT-SPECIFIC DEPTH PROFILES IN BIOMOLECULAR LAYERS

Molecular layers are major components of all biological systems and they are very important for biotechnological applications. The understanding of biological processes in molecular layers requires detailed structural insight. Standing-wave X-ray fluorescence (SWXF) is a label-free and element-specific technique for the structural investigations of molecular layers, at atom-scale resolution, perpendicular to the interface. It is therefore a powerful tool for the structural analysis of biological and biotechnologic surfaces.

In nature biomolecules are often organised as functional thin layers in interfacial geometries. The most prominent examples are biological membranes. But biomolecular layers also play important roles at biotechnological surfaces, for example, when they are the result of adsorption processes. For the understanding of many biological or biotechnologically relevant processes, a detailed insight into the structure of such layers is crucial.

X-ray and neutron scattering are particularly well suited for the investigation of such layers. In contrast to commonly used specular reflectometry, which reveals "global" matter density profiles perpendicular to a planar interface, standing-wave X-ray fluorescence (SWXF) allows the density profiles specifically of chemical elements of interest to be determined. SWXF is based on the standing wave created above a solid surface by the interference of the incident X-ray wave with the wave reflected from a multilayered solid substrate around the Bragg condition. During a scan of the incidence angle θ across the Bragg peak at θ_B, the maxima of the standing wave move along the surface normal (z, see **Figure 106**) and induce X-ray fluorescence with element-characteristic energies.

The angle-dependent fluorescence intensity $I_j(\theta)$ of a target element j is proportional to the overlap of its density profile perpendicular to the interface, $\rho_\varphi(z)$, and the angle-dependent standing wave $\Phi(\theta, z)$,

$$I_j(\theta) = A \int_{-\infty}^{\infty} \Phi(\theta,z)\rho_j(z)dz$$

The method thus allows elemental depth profiles to be reconstructed from the angle-dependent fluorescence **[1, 2]**. In fact, the centre of mass position of an elemental distribution can be determined with atom-scale resolution. SWXF studies have so far dealt with relatively heavy elements, typically metal ions, as artificial labels for the molecular layers under investigation **[2]**.

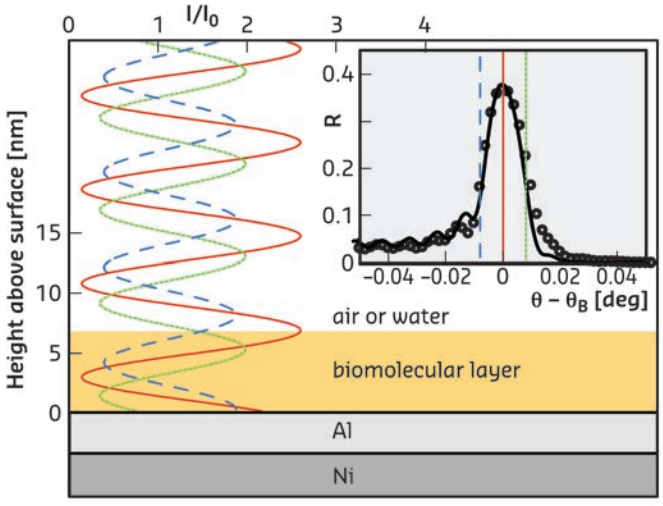

Fig. 106: X-ray standing wave above the solid surface for various incident angles θ around the Ni/Al multilayer Bragg angle θ_B. The characteristic fluorescence of the target is enhanced when the maxima of the standing wave overlap with the element distribution. (Inset) X-ray reflectivity (symbols) around θ_B and modelled reflectivity curve (solid line). Vertical lines indicate the incident angles corresponding to the standing waves in the main panel.

In recent experiments at beamline **ID03** and at SOLEIL/DIFFABS employing specially-designed Ni/Al multilayer substrates, we have demonstrated that the SWXF approach can be extended also to light, biologically-relevant chemical elements such as sulfur and phosphorus, which are found in the most important classes of biomolecules and therefore particularly interesting.

Figure 107 summarises experimental results obtained with sulfoglycolipid, phospholipid, and human serum albumin (HSA) monolayers on Al oxide surfaces. Phospholipids and sulfoglycolipids are abundant lipid classes in eukaryotic cell membranes that contain P and S atoms, respectively, in their headgroups (see **Figure 107a,b**). The protein human serum albumin (HSA) is the most abundant protein in the human blood serum and carries numerous S atoms in the cysteine and methionine amino acids distributed throughout its molecular structure. The graphs in **Figure 107a-d** show angle-dependent S and P fluorescence intensities (symbols) together with the simulated intensities (solid lines) corresponding to the best-matching elemental distributions. Distinct differences between the angle-dependence of the S and P fluorescence intensities from sulfoglycolipid (**Figure 107a**) and phospholipid (**Figure 107b**) monolayers, respectively, revealed an approximately 4 Å height difference of the sulfate and phosphate groups with respect to the solid surface. Dramatic differences are observed when comparing the shape of the fluorescence curves in (**Figure 107a,b**) with those of the S fluorescence intensities obtained with HSA for various conditions (**Figure 107c,d**). The differences in the angle dependence reflect that the S distribution of the adsorbed HSA monolayers is centred much higher above the surface, at approximately 17 Å in air and 37 Å under water.

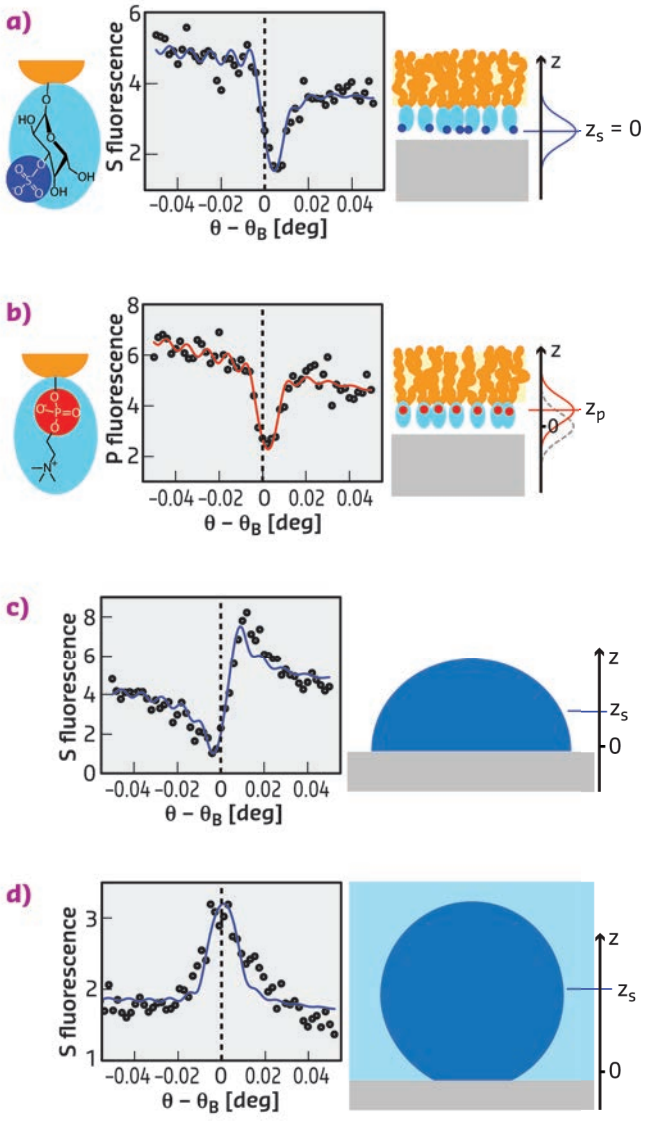

These results demonstrate that our label-free implementation of SWXF allows the investigation of complex biomolecular interfaces with great structural detail.

Fig. 107: Experimental results on sulfoglycolipid (a) and phospholipid (b) monolayers in air as well as on protein monolayers in air (c) and under water (d), all on Al oxide surfaces. The graphs show the angle-dependent P and S fluorescence intensities (symbols) together with the simulated intensities (solid lines) corresponding to the best-matching models. Vertical dashed lines indicate the Bragg condition. Cartoons on the right illustrate the architectures of the layers studied. The axis perpendicular to the sample surface is denoted *z*.

PRINCIPAL PUBLICATION AND AUTHORS

Atom-scale depth localization of biologically important chemical elements in molecular layers, E. Schneck (a,b), E. Scoppola (b,c), J. Drnec (d), C. Mocuta (e), R. Felici (d), D. Novikov (f), G. Fragneto (b) and J. Daillant (e), *PNAS* **113**, 9521-9526 (2016);
doi: 10.1073/pnas.1603898113.

(a) Max Planck Institute of Colloids and Interfaces, Potsdam (Germany)
(b) Institut Laue-Langevin, Grenoble (France)
(c) Institut de Chimie Séparative de Marcoule, Bagnols sur Cèze (France)
(d) ESRF
(e) Synchrotron SOLEIL, Gif-sur-Yvette Cedex (France)
(f) Deutsches Elektronen-Synchrotron DESY, Hamburg (Germany)

REFERENCES

[1] E. Schneck *et al.*, *PNAS* **107**, 9147 (2010).
[2] E. Schneck and B. Demé, *Curr. Opin. Colloid Interface Sci.* **20**, 244 (2015).

COLLECTIVE ACTION AT THE NANOSCALE: WITNESSING THE FORMATION OF A 2D SUPERLATTICE

Two-dimensional systems have recently emerged as very promising candidates for future electronic devices. An ordered 2D array of nanocrystals can be created by letting nanocrystals self-assemble on a liquid surface. This new structure shows excellent long range order at the nanocrystal and atomic level. Experiments at beamline ID10 revealed how nanocrystals order themselves and 'click together' to produce beautiful 2D superlattices.

PbSe nanocrystals self-assemble at the liquid/air interface **[1,2]**. We have studied this phenomenon using multiple techniques: small-angle X-ray scattering (SAXS) - to study the motion of the nanocrystals on the liquid surface - and wide-angle X-ray scattering (WAXS) - to study the orientation and self-assembly of the nanocrystals at the interface. We performed the experiments in grazing incidence mode (GI), which means that the X-ray beam impinges at a very tiny angle of only 0.3° with respect to the liquid/air interface. This made **ID10** our beamline of choice as it is specialised in grazing-incidence scattering experiments on liquid surfaces.

We followed the formation of nanocrystals on two different length scales: on the nanoscale for the movement of the nanocrystals on the liquid surface with GISAXS; and at the atomic length scale with GIWAXS, which probes both the orientation of the nanocrystals with respect to the liquid surface and the crystalline domain size. The results of the *in situ* X-ray scattering data, together with *ex situ* electron microscopy and diffraction, are shown in **Figure 108**.

By combining all the data and performing Monte Carlo simulations, a detailed picture of the self-assembly process was obtained as shown in **Figure 109**. The nanocrystals are initially dispersed in an apolar solvent which is placed onto a polar liquid substrate. The two solvents do not mix and the nanocrystals are not soluble in the bottom liquid. At stage 1 of the self-assembly process, while the apolar solvent of the nanocrystal solution is evaporating, the increasing concentration of nanocrystals forces them to slowly attach to the interface. At stage 2, most of the apolar solvent has evaporated, and the nanocrystals self-assemble into an energetically favoured dense hexagonal array of nanocrystals (similar to hard-spheres). At stage 3, the hexagonal monolayer starts to deform towards the final square lattice. At stage 4, the nanocrystals are in close proximity and can atomically fuse together by forming crystalline bridges between the nanocrystals.

Synchrotron radiation played a pivotal role in this study. While electron microscopy provided important insights into the structures formed at different stages of the process, it was essentially *ex situ*. The intermediate structures at stage 2 were only observed using synchrotron techniques as they do not survive upon the sample drying on a grid. Further insights into the mechanism were provided by computer simulations that indicate that there must be an attraction between the nanocrystal {100} facets, caused by either electrostatic or strong Van der Waals interactions.

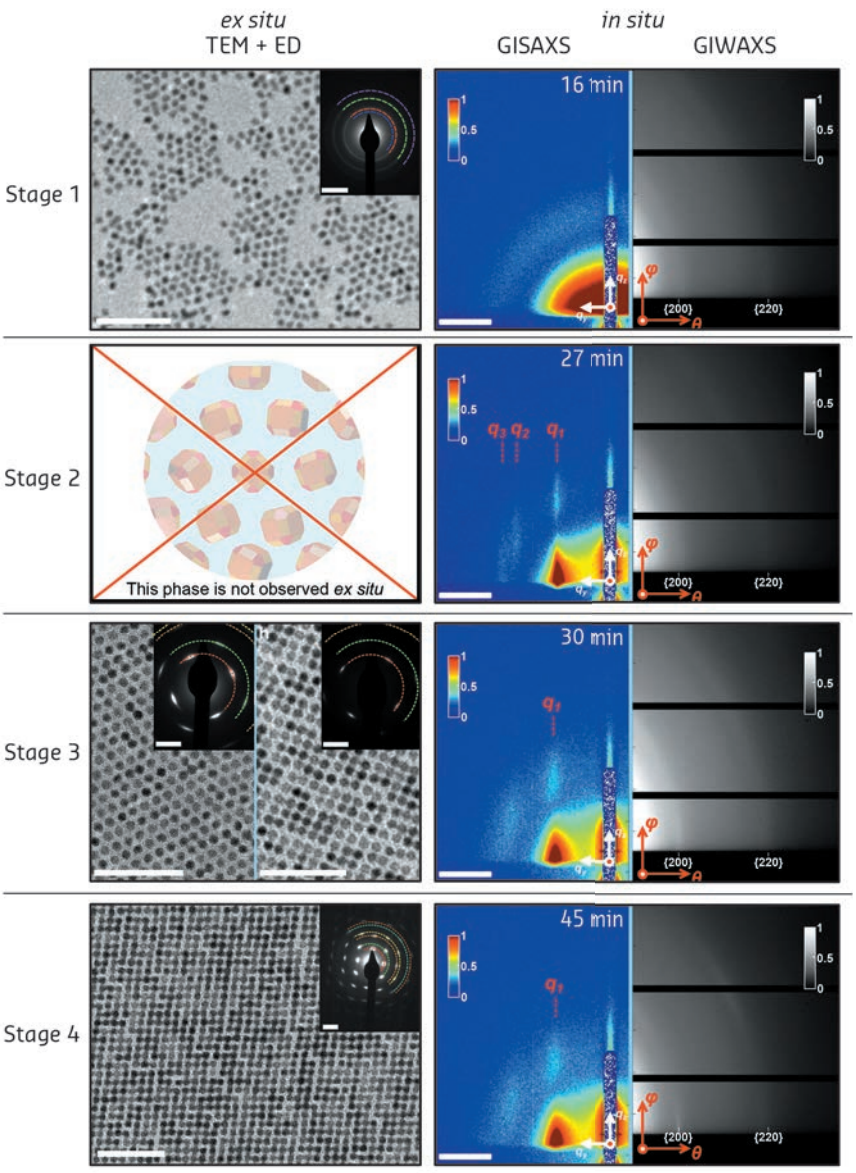

Fig. 108: The different stages during the self-assembly process as monitored by *ex situ* electron microscopy, electron diffraction and *in situ* GISAXS/GIWAXS.

We have succeeded for the first time in capturing this incredible sequence of phase transitions of nanocrystals during their self-assembly process on a liquid interface. The insights obtained may result in bottom-up routes towards a diversity of 2D electronic or photonic materials based on nanocrystals. The presented procedures will be developed further, such that the self-assembly of nanocrystal colloids can become a feasible alternative to top-down lithography based methods.

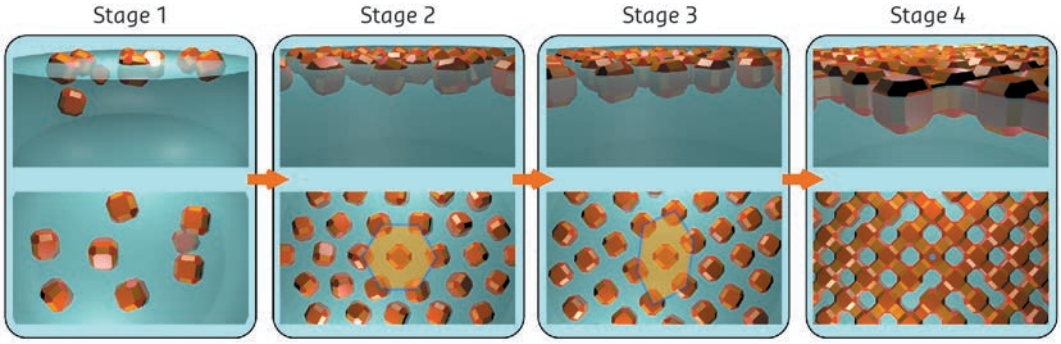

Fig. 109: Model for the self-assembly derived from a combination of *in situ* X-ray scattering, *ex situ* electron microscopy and Monte Carlo simulations.

PRINCIPAL PUBLICATION AND AUTHORS

In situ study of the formation mechanism of two-dimensional superlattices from PbSe nanocrystals, J.J. Geuchies (a,e), C. van Overbeek (a), W.H. Evers (b,c), B. Goris (d), A. De Backer (d), A.P. Gantapara (f), F.T. Rabouw (a), J. Hilhorst (e), J.L. Peters (a), O. Konovalov (e), A.V. Petukhov (g,h), M. Dijkstra (f), L.D.A. Siebbeles (b), S. Van Aert (d), S. Bals (d) and D. Vanmaekelbergh (a), *Nature Materials* **15**, 1248–1254 (2016); doi: 10.1038/nmat4746.

(a) Condensed Matter and Interfaces, Debye Institute for Nanomaterials Science, Utrecht University (The Netherlands)
(b) Optoelectronic Materials Section, Department of Chemical Engineering, Delft University of Technology (The Netherlands)
(c) Kavli Institute of Nanoscience, Delft University of Technology (The Netherlands)
(d) Electron Microscopy for Materials Science (EMAT), University of Antwerp (Belgium)
(e) ESRF
(f) Soft Condensed Matter, Debye Institute for Nanomaterials Science, Utrecht University (The Netherlands)
(g) Physical and Colloidal Chemistry, Debye Institute for Nanomaterials Science, Utrecht University (The Netherlands)
(h) Laboratory of Physical Chemistry, Department of Chemical Engineering and Chemistry, Eindhoven University of Technology (The Netherlands)

REFERENCES

[1] W.H. Evers *et al.*, *Nano Lett.* **13**, 2317–2323 (2013).
[2] M.P. Boneschanscher *et al.*, *Science* **344**, 1377-1380 (2014).

X-RAY COLOUR PROVIDES DIRECT 3D INFORMATION IN CRYSTALLOGRAPHIC TEXTURE MEASUREMENTS

Preferred crystal orientation, crystallographic texture, is a common phenomenon in complex materials. Conventionally, texture determination by X-ray diffraction involves many 2D diffraction images combined into 3D information by sample rotation. We have shown that the photon energies ("X-ray colours") in a white beam can be exploited to gain direct 3D crystallographic information in texture measurements. The method was used on carbon fibres and lobster cuticle.

For many decades, crystallographic texture has been measured by X-ray diffraction involving a monochromatic beam and area detectors delivering intensity information and hence "grey-scale" diffraction images. True 3D information about crystallite orientation could only be obtained by rotating the sample in the beam and by collecting diffraction images at different rotation angles. This puts severe limitations on the exploration of complex materials, since the local crystallographic texture may change dramatically from one point to the next, even on the micrometre scale.

A new class of pixelated X-ray area detectors now allows the discrimination of different photon energies in every pixel (pnCCD type detectors, SLcam) **[1]** and, together with a polychromatic X-ray beam, yields "X-ray colour images" **[2]**. In diffraction experiments, different photon energies can be used to collect information from different crystal plane orientations due to the sensitivity of the diffraction condition to both crystallite orientation and incident energy (known from white beam Laue diffraction). In contrast to conventional "grey scale" Laue patterns, the X-ray colour approach, energy

dispersive Laue diffraction, EDLD **[3]**, yields one-shot 3D orientation information even for complex and highly polycrystalline samples.

Within a research project supported by the Partnership for Soft Condensed Matter (PSCM), we used EDLD for crystallographic texture measurements. At **BM28,** we employed the full white beam from the bending magnet together with an energy dispersive X-ray camera and a setup accessing a wide range of scattering angles, *i.e.* a large angle portion of reciprocal space. The principle is shown in **Figure 110**.

The sample was raster scanned and the conventional 2D diffraction information was complemented by an energy spectrum recorded for each pixel. By using a straightforward reconstruction algorithm based on the Ewald sphere geometry, the photon energies were used to calculate the missing third dimension in space. In this way, a 3D representation of scattering data was achieved without *a priori* knowledge of the sample and without sample rotation.

We applied the new texture measurement method to map the orientation of graphite planes in carbon fibres and of calcite crystallites in lobster cuticle. The example of two crossed strands of carbon fibre is shown in **Figure 111**. The two orientations are immediately visible from the 3D reconstruction of the scattering image. In lobster tail cuticle, the method revealed a calcite crystal orientation roughly perpendicular to the cuticle plane. At the same time, it allowed determination of the Ca distribution, since the energy dispersive detector also records the X-ray fluorescence from the sample and thus yields chemical information as well.

In this way, 3D crystallographic and chemical information could be acquired in a single shot, without sample rotation and at a lateral spatial resolution only limited by the beam size. The method is therefore of particular value for fast 2D texture mapping of complex samples or for any setup or system that does not allow rotation. The approach combines the benefits of both traditional Laue diffraction and monochromatic diffraction, and can therefore be expected to become a powerful and elegant tool in future crystallography, applied chemistry and materials science.

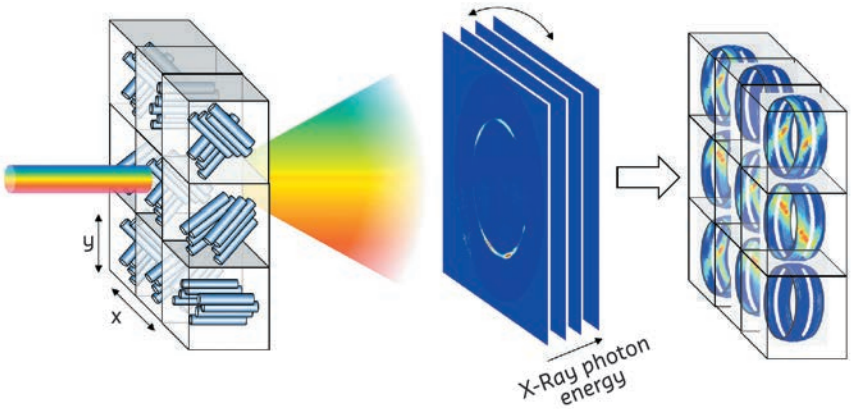

Fig. 110: EDLD texture measurement: a sample with locally different crystal orientations is raster scanned with a polychromatic beam. The energy dispersive X-ray camera delivers an energy spectrum for each pixel, which can be regrouped into a stack of diffraction images at different energies. The local 3D scattering pattern can be displayed directly for each beam position in the sample.

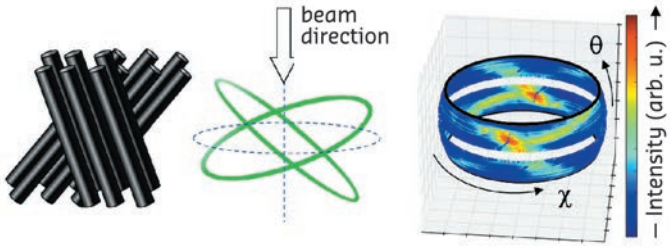

Fig. 111: Example of EDLD texture measurements on two crossed carbon fibre bundles (left). In reciprocal space, each carbon fibre yields a reflection ring from the (002) graphite planes perpendicular to the fibre axis (fibre texture). The crossed rings are observed directly in the 3D scattering patterns (right) and can be used to reconstruct the carbon fibre orientations.

PRINCIPAL PUBLICATION AND AUTHORS

Photon energy becomes the 3rd dimension in crystallographic texture analysis, T.A. Grünewald (a), H. Rennhofer (a), P. Tack (b), J. Garrevoet (c), D. Wermeille (d,e), P. Thompson (d,e), W. Bras (f), L. Vincze (b) and H.C. Lichtenegger (a). *Angewandte Chemie Int. Ed.* **55,** 12190–12194 (2016); doi: 10.1002/anie.201603784.

(a) Institute of Physics and Materials Science, Department of Materials Sciences and Process Engineering, University of Natural Resources and Life Sciences – BOKU, Vienna (Austria)
(b) Department of Analytical Chemistry, Ghent University (Belgium)
(c) Deutsches Electronen Synchrotron, Hamburg (Germany)
(d) XMaS -The UK CRG Beamline, ESRF, Grenoble (France)
(e) Department of Physics, University of Liverpool (UK)
(f) Netherlands Organization for Scientific Research (NWO), DUBBLE@ESRF, Grenoble (France)

REFERENCES

[1] O.Scharf *et al.*, *Analytical Chemistry* **83**, 2532-2538 (2011).
[2] P. Tack *et al.*, *Analytical Chemistry* **86**, 8791-8797 (2014).
[3] S. Send *et al.*, *J. Appl. Cryst* **42**, 1139-1146 (2009).

SYNTHESIS OF BIMETALLIC NANOPARTICLES WITH TAILORED SIZE AND COMPOSITION

A novel recipe based on atomic layer deposition has been established for the fully-tailored synthesis of supported Pt-In bimetallic nanoparticles. The combination of *in situ* X-ray diffraction and *in situ* grazing-incidence small-angle X-ray scattering measurements revealed the mechanism of bimetallic nanoparticle formation.

Bimetallic nanoparticles play a pivotal role in optical, magnetic and electronic applications, and are true workhorses during the catalytic transformation of chemicals. In particular, supported Pt nanoparticles alloyed with In, Ga or Sn are highly selective catalysts for the dehydrogenation of propane to propylene. It is well established that the size and composition of the nanoparticles strongly impact the catalytic properties and performance. Yet, conventional synthesis strategies lack proper control over the nanoparticle morphology and composition.

We report a new procedure for the tailored synthesis of bimetallic nanoparticles containing a non-noble metal next to a noble metal, here exemplified for nanoalloys containing In as non-noble and Pt as noble metal. The recipe is based on the use of atomic layer deposition (ALD), a vapour phase deposition method that is characterised by alternating exposure of the sample to chemical precursors **[1]**. ALD ensures that the amount of deposited material can be controlled at the monolayer level and enables conformal depositions on 3D substrates. **Figure 112a** schematically describes the steps involved in the fabrication process of the Pt-In bimetallic nanoparticles. Thin layers of In_2O_3 **[2]** and Pt are sequentially deposited by ALD, yielding a Pt/In_2O_3 bilayer structure. These bilayers are then subjected to a temperature programmed reduction (TPR) in hydrogen to induce the formation of Pt-In nanoalloys.

Using *in situ* X-ray diffraction (XRD) at UGent and *in situ* grazing-incidence small-angle X-ray scattering (GISAXS) at beamline **BM26** (Dubble CRG), the mechanism of bimetallic particle formation was studied in detail. **Figure 112b** shows the structural evolution of a Pt/In_2O_3 bilayer during TPR in hydrogen as measured with XRD. Initially, the pattern shows diffraction from In_2O_3 (222) and metallic Pt (111). The disappearance of the In_2O_3 (222) peak around 330°C is indicative of complete reduction of the In_2O_3 layer. The In_2O_3 reduction is accompanied by a shift of the Pt (111) diffraction towards lower 2θ angle, implying expansion of the Pt fcc lattice due to insertion of In into the Pt structure. The stabilisation of the shifted diffraction peak indicates the formation of an $InPt_3$ fcc alloy. The evolution of the nanoscale morphology of the sample during TPR was monitored with *in situ* GISAXS. The temporal evolution of the main scattering feature is visible in the 2D colour plot in **Figure 112c**. A stable scattering pattern is observed up to 300°C, followed by a gradual peak shift to lower q_y-values until 450°C. These results indicate that the insertion of In in the Pt fcc lattice, as monitored by XRD, is accompanied by the migration and redistribution of Pt atoms across the surface, as schematically illustrated in **Figure 112d**.

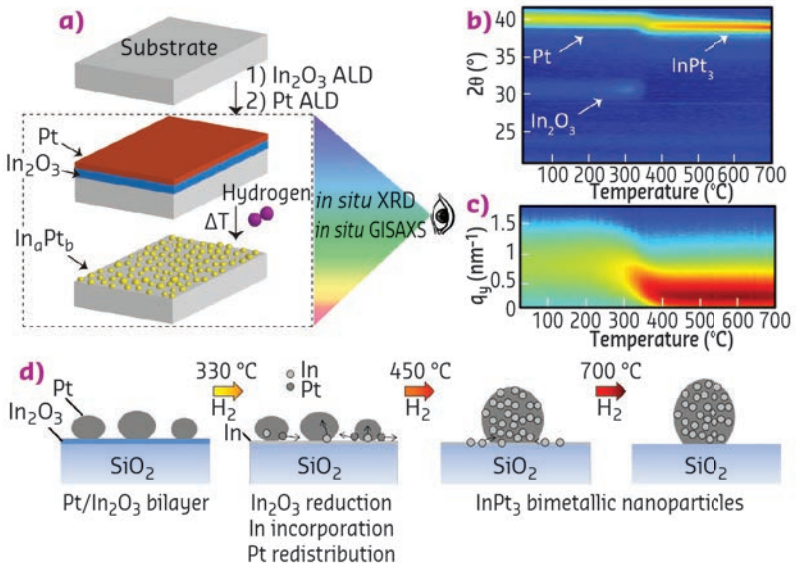

Fig. 112: a) ALD-based Pt-In bimetallic nanoparticle synthesis. b) *In situ* XRD patterns measured during TPR in hydrogen. c) *In situ* GISAXS line profiles measured during TPR in hydrogen. d) Bimetallic nanoparticle formation mechanism as interpreted from *in situ* XRD and GISAXS.

The composition of the formed bimetallic alloys can be tuned by controlling the ratio of the deposited thickness of Pt to the thickness of In_2O_3. **Figure 113a** presents the relation between the as-deposited Pt/(Pt+In) atomic ratio and the alloy phase(s) obtained after TPR. These phases were found to be independent of the total deposited thickness of the as-deposited bilayer. Four different phase-pure alloys are achievable, with wide Pt/(Pt+In) atomic ratio windows for $InPt_3$, In_9Pt_{13} and In_2Pt, and only a small window for $In_{48}Pt_{52}$. For Pt/(Pt+In) atomic ratios below 20%, metallic In is observed next to the most In-rich phase, In_7Pt_3. In addition, our method enables tuning of the particle size with high precision in a range from 1 to 30 nm by changing the total thickness of the ALD-grown Pt/In_2O_3 bilayer (**Figure 113b**). Tuning of the particle size while keeping the composition the same can thus be achieved by scaling the layer thicknesses of the Pt and In_2O_3 layers while keeping the Pt/(Pt+In) atomic ratio constant.

Finally, successful bimetallic nanoparticle synthesis was achieved on mesoporous silica, resulting in high surface area nanocatalysts which showed promising high activity for propane dehydrogenation.

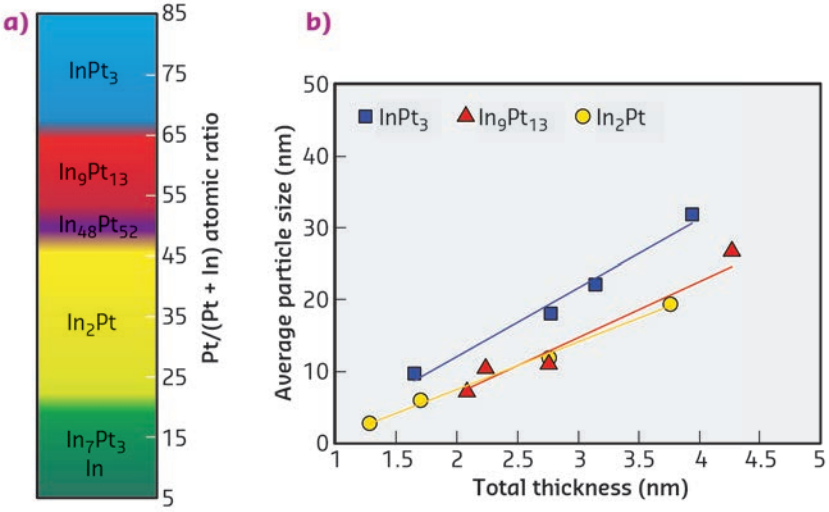

Fig. 113: a) Colour bar demonstrating composition tuning. b) Graph demonstrating size tuning.

PRINCIPAL PUBLICATION AND AUTHORS

Atomic layer deposition route to tailor nanoalloys of noble and non-noble metals, R.K. Ramachandran (a), J. Dendooven (a), M. Filez (b), V.V. Galvita (b), H. Poelman (b), E. Solano (a), M.M. Minjauw (a), K. Devloo-Casier (a), E. Fonda (c), D. Hermida-Merino (d), W. Bras (d), G.B. Marin (b) and C. Detavernier (a), *ACS Nano* **10**, 8770-8777 (2016); doi: 10.1021/acsnano.6b04464.
(a) Department of Solid State Sciences, COCOON, Ghent University, Ghent (Belgium)
(b) Laboratory for Chemical Technology, Ghent University, Zwijnaarde (Belgium)
(c) Synchrotron SOLEIL, SAMBA Beamline, Gif-sur-Yvette (France)
(d) Netherlands Organisation for Scientific Research, DUBBLE@ESRF, Grenoble (France)

REFERENCES

[1] C. Detavernier *et al.*, *Chem. Soc. Rev.* **40**, 5242–5253 (2011).
[2] R.K. Ramachandran *et al.*, *J. Phys. Chem. C* **119**, 11786-11791 (2015).

MEDICAL APPLICATION OF SYNCHROTRON RADIATION: TOWARDS A NEW NON-INVASIVE METHOD TO SUPPRESS EPILEPTIC SEIZURES

For about a third of patients with epilepsy, current medication is ineffective and, in some cases, surgical resection is the only possible solution. However, this invasive procedure is risky and can only be achieved if the lesion is accessible. Synchrotron microbeam irradiation could offer an interesting alternative for these drug-resistant patients.

At **ID17,** the biomedical beamline, we have developed a method using microbeams of a few tens of microns that allow the accurate irradiation of specific areas of the brain. Crossing these microbeams at the target region can deposit a sufficient radiation dose for the destruction of certain cells without opening the skull. Previous studies have shown the tolerance of biological tissues to this type of radiosurgery, *i.e.* the absence of lesions in the immediate vicinity of the microbeam and very few side effects, a significant advantage over current techniques that often present "collateral" damage. The development of the microbeam approach is possible due to

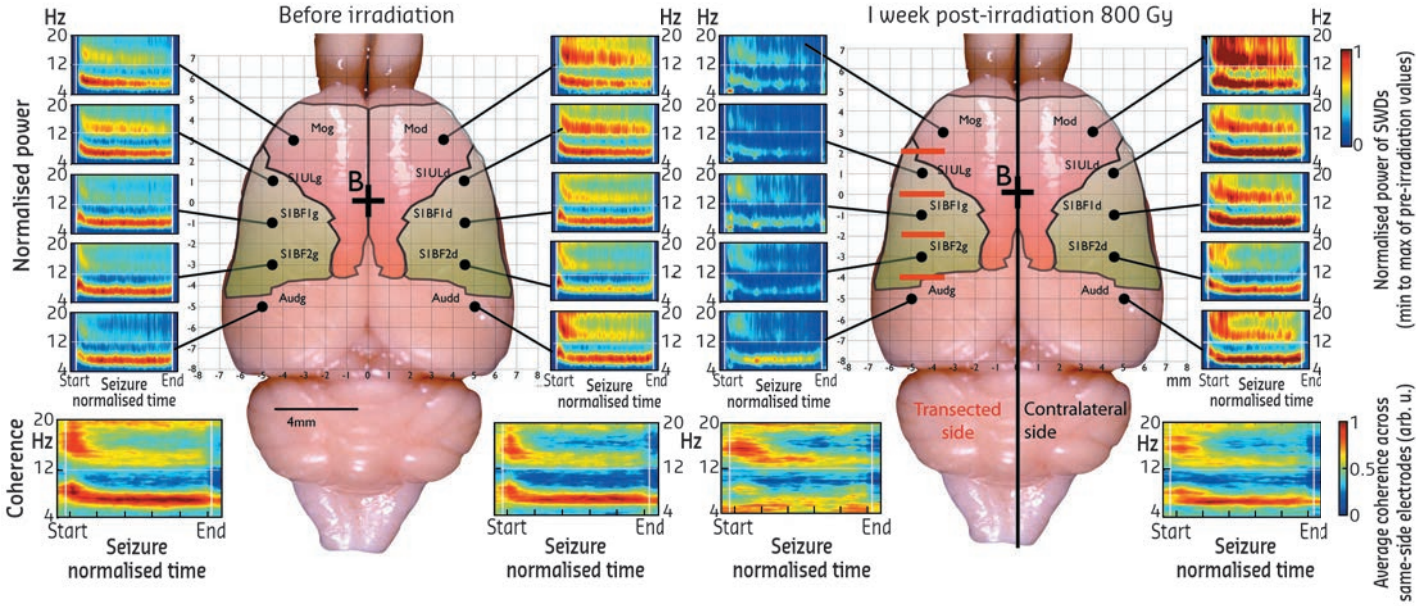

Fig. 114: Power of the electroencephalographic signal and consistency in the absence of epileptic seizures in rat GAERS before and after irradiation by synchrotron microbeam (red bars). The somatosensory cortex on the right is the non-irradiated control.

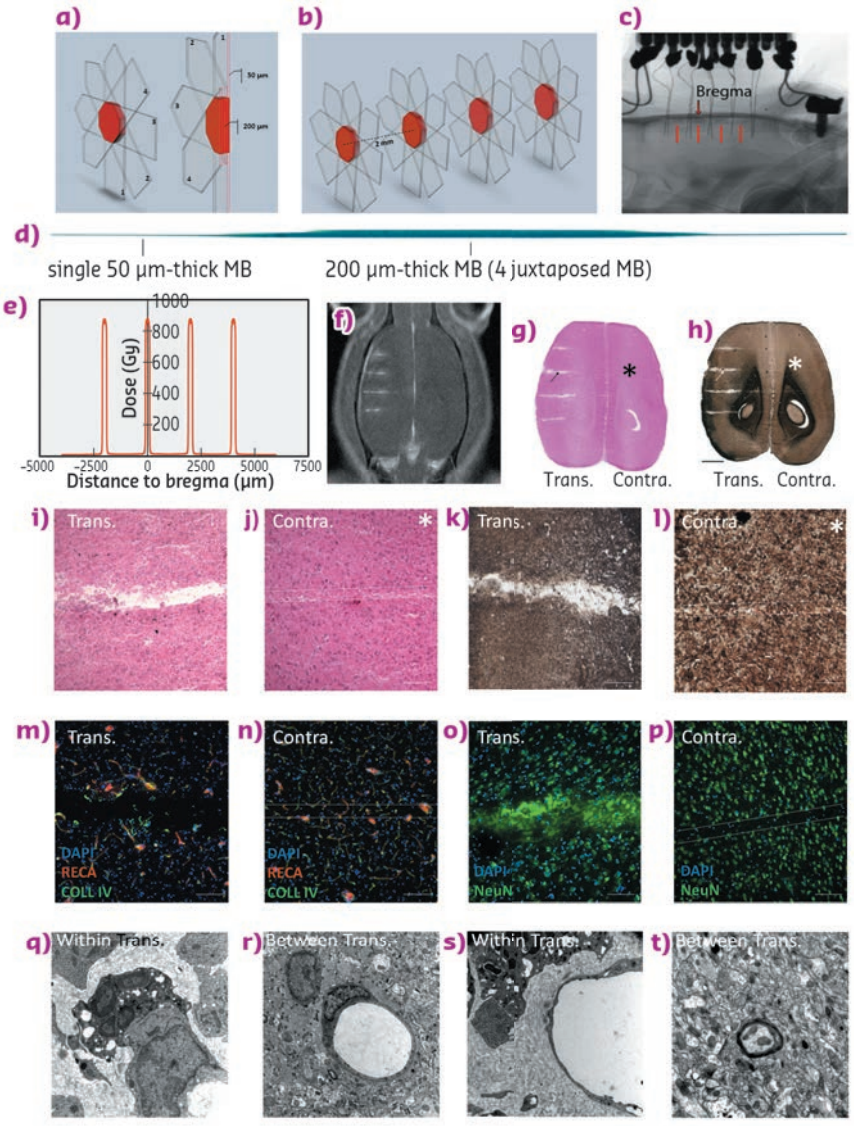

Fig. 115: Synchrotron X-ray transections. Irradiation parameters and tissular effects. a), b) 3D Microbeam interlacement; transparent arrows denote the trajectory of each microbeam. Numbers represent the sequence of their delivery. The interlaced volume (transection) is shown in red. c) X-ray image of a GAERS brain with two rows of 5 implanted electrodes. Transections are indicated by red bars. d) The scan of a Gafchromic™ film shows 4 microbeams, interlaced to create a 200 µm wide, octahedric irradiated transection. e) Radiation dose deposition profile for the 4 transections. Estimated peak dose in the transection 820 Gy, entrance dose of a single microbeam 800 Gy. f) Gadolinium contrasted T_1 MR image of a rat after 4 transections. g) to t) Horizontal brain sections 2 months post-irradiation, haematoxylin and eosin (g), myelin stain (h); scale: 2 mm. Microphotographs of cortical transections (i, k) show a tissue gap (i), and myelin loss (k), while the path of a single microbeam in the contralateral hemisphere shows only loss of cell nuclei (j and l); scale: 200 µm). Immunolabelling of brain vasculature (RECA and Type IV Collagen (m, n) and neurons (NeuN (o, p)) in transected (m, o) and contralateral (n, p) hemispheres (scale: 50 µm). Ultrastructural changes, as described in the text, within (q, s) and between transections (r, t). (TEM, magnification 12,000).

the exceptional physical properties of the X-rays produced by the ESRF.

We have demonstrated the possibility of using microbeams to treat some forms of epilepsy during preclinical research. After an initial proof of concept performed on rats **[1]**, we have shown that microbeam irradiation, applied at four different levels of the somatosensory cortex (which generates seizures in this model), has beneficial effects for more than nine weeks (**Figure 114**).

The non-invasive 200 micron wide transections reduce the neuronal connections in the target area, with a resulting reduction in the synchronising capability of neurons, which is monitored by local field potentials. Between radiation zones, magnetic resonance imaging and histological analyses showed that the tissue is not altered and behavioural tests have shown that animals retain normal locomotion and motor coordination. **Figure 115** shows the irradiation geometries, a lateral dose profile, MRI images together with histological sections using various staining techniques.

This new study confirms the interest of using synchrotron radiation to reach epileptic foci where conventional surgery is too risky. It constitutes a new therapeutic approach that needs to be confirmed in other models before considering clinical studies. The method can also be applied with very fine transections (50 microns) to reach precise brain regions and it can also find applications in the study of brain connectivity in neuroscience.

PRINCIPAL PUBLICATION AND AUTHORS

Synchrotron X-ray microtransections: a non invasive approach for epileptic seizures arising from eloquent cortical areas, B. Pouyatos (a,b,c), C. Nemoz (d), T. Chabrol (e), M. Potez (b), E. Bräuer (d), E. Renaud (f,g), K. Pernet-Gallay (a,b), F. Estève (e), O. David (a,b), P. Kahane (a,b,h), J.A. Laissue (i), A. Depaulis (a,b) and R. Serduc (e), *Scientific Reports* **6**, 27250 (2016); doi: 10.1038/srep27250.
(a) Inserm, U1216, Grenoble (France)
(b) Université Grenoble Alpes, Grenoble Institut des Neurosciences, GIN, Grenoble (France)
(c) Synapcell S.A.S, La Tronche (France)
(d) ESRF
(e) Grenoble Alpes EA RSRM, Grenoble (France)
(f) CNRS;CE2F PRIM UMS3537, Aix-Marseille Université (France)
(g) Aix Marseille Universite, Centre d'exploration Fonctionelle et de Formation (France)
(h) CHU Grenoble Alpes, Grenoble (France)
(i) University of Bern (Switzerland)

REFERENCES

[1] B. Pouyatos *et al., Neurobiology of Disease* **51**, 152–160 (2013).
[2] F. Studer *et al., Phys Med* **31**, 607–614 (2015).

OPTIMISED PHASE-CONTRAST IMAGING METHOD SLASHES RADIATION DOSE IN MAMMOGRAPHY

A new approach to X-ray phase contrast imaging developed at the ESRF enables unprecedented low doses in breast imaging and has the potential for being translated into clinical use.

Since the emergence of X-ray phase-contrast imaging (XPCI) more than two decades ago, breast imaging has been considered as one of the applications with the highest potential impact. Conventional attenuation-based X-ray imaging methods are limited in the soft tissue contrast they can achieve, and thus in the discrimination between healthy and cancerous tissues. Additionally, the radiation dose needs to be kept as low as possible due to the high radiosensitivity of the breast. As a consequence, mammography has shortcomings in both sensitivity and specificity, leading to undetected malignancies and unnecessary biopsies, respectively. XPCI provides highly-enhanced soft-tissue contrast. Besides, higher X-ray energies can be used since X-rays do not need to be absorbed in tissue to generate contrast, potentially enabling dose reduction strategies. If implemented in the clinics, dose reduction and image quality improvement would be extremely beneficial, as they would make mammography both a safer and a more accurate exam for breast cancer detection.

Impressive contrast enhancements have been demonstrated in breast imaging through XPCI **[1]**. However, researchers have struggled to obtain significant dose reductions with respect to conventional mammography, with most studies actually reporting doses exceeding clinical limits **[1]**. Here, we set out to demonstrate that

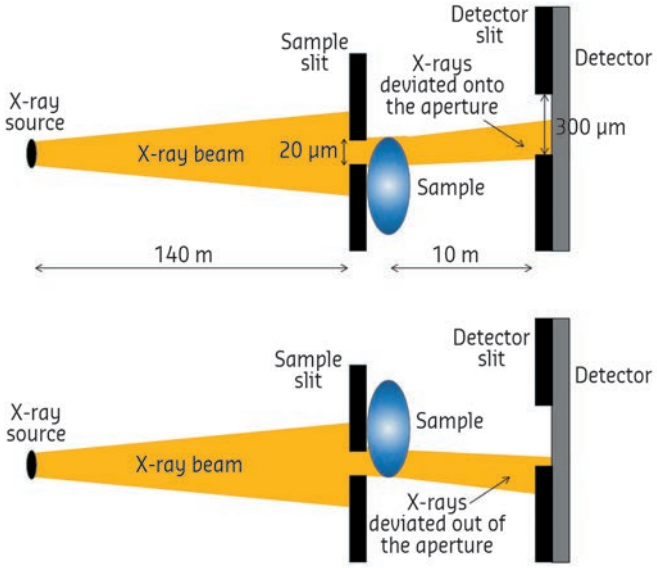

Fig. 116 : Schematic diagram of the EI XPCI setup (not to scale).

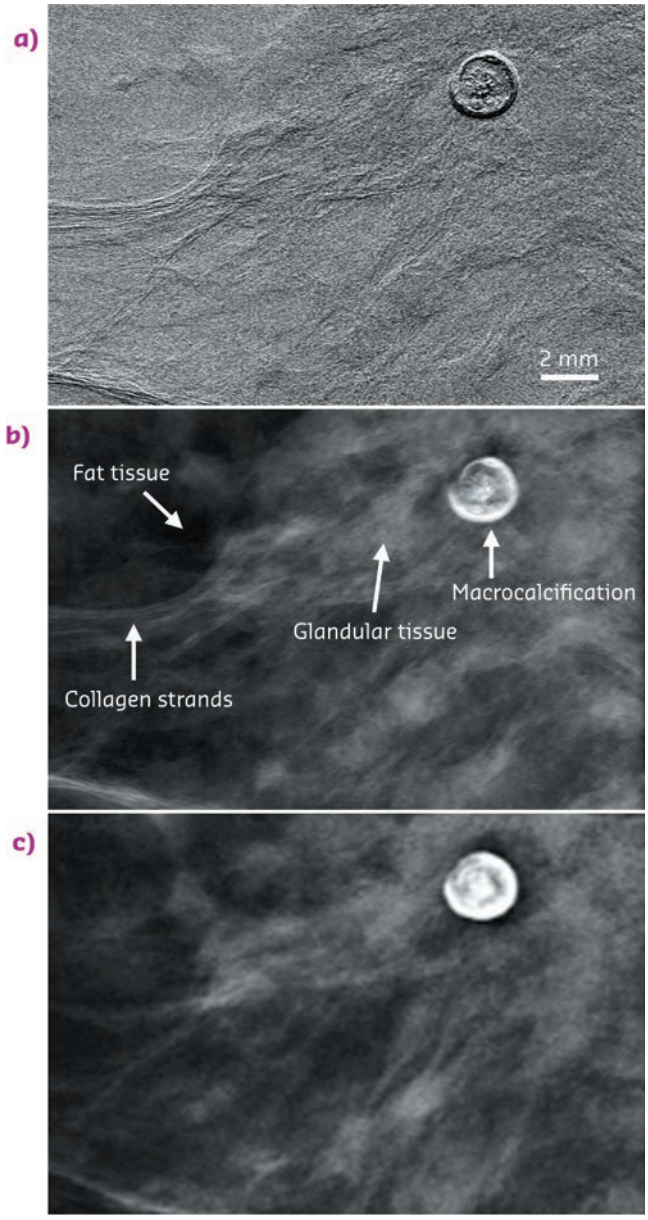

Fig. 117: Images of a 2 cm thick breast sample:
a) EI raw image,
b) retrieved phase image,
c) conventional mammogram.

an optimised approach to XPCI can lower the dose in mammography by at least one order of magnitude compared to clinical practice. To reach this aim, we exploited a combination of cutting-edge developments in novel detector technologies, XPCI and image processing.

Edge illumination (EI) XPCI was chosen due to its high phase sensitivity [2] and low-dose capabilities [3]. This technique is based on the use of two absorbing slits, placed before the sample and detector respectively, slightly misaligned with respect to each other (**Figure 116**). In this way, tiny refraction angles are converted into a measurable intensity modulation, as they change the fraction of photons reaching the detector [2]. So far, to retrieve absorption and phase maps of the sample, two EI images needed to be acquired at different slit misalignments and combined [2,3]. In this work, a new retrieval method based on the acquisition of a single image was used [4], which exploits the near homogeneous composition of the breast by assuming the sample absorption and phase to be proportional. Besides simplifying the acquisition procedure, the use of a single-image algorithm enables dose reduction and faster implementations of EI.

A high X-ray energy (60 keV) was chosen to reduce the radiation dose to the sample. At this energy, however, the efficiency of most detectors is limited. Therefore, the MAXIPIX detector, developed at the ESRF [5], was employed. Due to its photon-counting capabilities and its detection efficiency close to 100% at this energy, MAXIPIX is able to minimise image noise for a given X-ray fluence.

Images of excised breast samples of 2-4 cm thickness were acquired at beamline **ID17** (The Biomedical Beamline), with a mean glandular dose of only 0.12 mGy. In **Figure 117**, the raw EI image (**Figure 117a**) and the retrieved phase image (**Figure 117b**) are compared to the conventional mammogram acquired at a hospital (**Figure 117c**) (32 kVp, dose of 4.1 mGy). Despite the high X-ray energy and the extremely low radiation dose, all the breast structures are highlighted in the raw EI image by the refraction-induced signal present at their boundaries. The area contrast typical of conventional X-ray images (more easily interpretable to radiologists), in turn, is restored

in the retrieved phase map. This image depicts breast features with at least the same quality as in the conventional mammogram, although at a dose reduced by more than one order of magnitude.

The EI method has also been demonstrated to work efficiently in table-top setups exploiting conventional rotating anode sources **[3]**. The next step in our research will thus focus on the translation of these considerable dose reductions to a laboratory EI setup, as this would enable the method to be implemented in a clinical setting. Several steps are still needed, including the identification of suitable X-ray sources, beam filtration and optimum system geometry, and the design of larger masks able to cover the entire size of the breast.

PRINCIPAL PUBLICATION AND AUTHORS

A method for high-energy, low-dose mammography using edge illumination X-ray phase-contrast imaging, P.C. Diemoz (a), A. Bravin (b), A. Sztrókay-Gaul (c), M. Ruat (b), S. Grandl (c), D. Mayr (d), S. Auweter (c), A. Mittone (e), E. Brun (b,e), C. Ponchut (b), M.F. Reiser (c), P. Coan (c,e) and A. Olivo (a), *Phys. Med. Biol.* **61**, 8750-8761 (2016); doi: 10.1088/1361-6560/61/24/8750.
(a) Department of Medical Physics and Biomedical Engineering, University College London (UK)
(b) ESRF
(c) Institute for Clinical Radiology, Ludwig-Maximilians University, Munich (Germany)
(d) Institute for Pathology, Ludwig-Maximilians University, Munich (Germany)
(e) Department of Physics, Ludwig-Maximilians University, Garching (Germany)

REFERENCES

[1] P. Coan *et al.*, *J. Phys. D: Appl. Phys.* **46**, 494007 (2013).
[2] P.C. Diemoz, *et al.*, *Phys. Rev. Lett.* **110**, 138105 (2013).
[3] C.K. Hagen *et al.*, *Med. Phys.* **41**, 070701 (2014).
[4] P.C. Diemoz *et al.*, *J. Synchrotron Radiat.* **22**, 1072-7 (2015).
[5] C. Ponchut *et al.*, *J. Instrum.* **6**, C01069 (2011).

Matter at extremes

Within the Matter at Extremes (MEx) Group, 2016 has been a year full of new and exciting scientific results, a selection of which is reported in this chapter. At the same time, it was a year of review of the past and preparation for the future.

The three high pressure diffraction beamlines (**ID06LVP**, **ID09A/ID15B** and **ID27**) were reviewed together in May. This exercise highlighted the breadth of the science addressed at the three beamlines, with the promise that new science will emerge by further expanding the limits of pressure, temperature, time resolution and diversity of measurements. In addition to their positive appraisal of the technical and scientific accomplishments of the staff and users, the review panel provided important recommendations. It also emphasised the potential to significantly increase the impact of the ESRF in the field of high pressure science by developing a more coherent strategy between the three beamlines. With the advent of the EBS, and the possible realisation of new beamlines optimised for hard X-ray microscopy for materials research and high pressure science with nanobeams, high pressure diffraction-based research at ESRF could exploit three complementary beamlines: one for large-volume press activities (ID06), one with nanobeam capabilities (ID27), and one for single–crystal applications (ID15B).

For **ID18**, the nuclear resonance beamline, reviewed in 2015, two scenarios for an upgrade have been considered: an ultimate and a cost-effective scenario respectively, both making full use of the EBS. The former provides a nanobeam of 75 nm × 45 nm and an improved energy resolution bridging the currently existing gap between 0.01 and 0.5 meV. These numbers have attracted user communities from fields such as Earth, planetary, and environmental science, magnetism and superconductivity, and dynamics for first feasibility tests.

The preparation of conceptual design reports (CDRs) for new science–oriented platforms and new EBS beamlines was one of the major activities of the year, involving many of the senior scientists in the group, with the help of users, who kindly contributed to the CDRs as external experts, and with precious input from ESRF's engineering staff.

The CDR for the High Power Laser Facility (HPLF-Phase I), one of the pillars for the Medium Term Scientific Plan 2016-2020, was submitted in April and the project officially launched in the autumn. It foresees the installation of a 100-200 J, ns shaped pulsed laser at the X-ray absorption spectroscopy beamline **ID24** in 2018 before the long shutdown.

The MEx group presented three CDRs as candidate upgrade beamlines (UPBLs) for EBS: CDR5: Advanced high-flux nano-XRD beamline for science under extreme conditions; CDR6: Facility for dynamic compression studies; and CDR7: High brilliance EXAFS beamline.

CDR5 proposes the construction of a new high pressure X-ray diffraction beamline to take full advantage of the outstanding performance of the EBS, *i.e.* the significantly higher photon flux density and higher coherence, especially for photon energies above 30 keV, the energy range most relevant for diffraction and imaging at extreme conditions. The new instrument will have a profound impact in extreme conditions science and will put the ESRF at the front line in this field.

CDR6 proposes the construction of a new beamline for single-shot and fast time-resolved diffraction and imaging. This project (HPLF-Phase II) comprises a high-power laser facility exploiting different X-ray techniques (diffraction, imaging, spectroscopy) and will provide the European scientific community with the possibility to extend the P and T range reachable by static compression and address the dynamic behaviour of matter under high strain rates.

CDR7 proposes to convert one branch of the energy dispersive XAS beamline ID24 to a scanning EXAFS beamline. This will allow the 40-fold decrease in source size offered by EBS to be fully exploited. It will provide a 0.5 x 0.5 μm^2 (FWHM) spot for XAS/XES spectroscopy in a large energy range from 5-40 keV, expanding the capacity of the ESRF spectroscopy beamline portfolio towards studies of highly-dilute systems at extreme conditions and/or with time resolution.

In parallel to the preparation for the future source, the six beamlines of the group have continued to produce many exciting results, only a small fraction of which made it into this chapter. Here are a few that were left out.

Some very exciting work from **ID18** on the observation of collective strong coupling between X-rays and matter excitations **[1]** extends the range of methods for X-ray quantum optics and paves the way for the observation and exploitation of strong-coupling-related phenomena at X-ray energies.

The large volume press at **ID06LVP**, which this year offered a 30% increase in user beamtime, has been used to study the allotropy of silicon,

which is both rich and very promising for tackling immediate challenges in electronic and photovoltaic applications [2]. Also noteworthy is a deformation study on olivine [3] which provides a comprehensive overview of the potential of **ID06LVP** for studies of strain, yield strength, differential stress and viscosity in minerals.

Diffraction studies at **ID27** and ID09A (now **ID15B**) have tackled a wide variety of pressure-induced phenomena in solid state physics, from spin crossovers [4] to metal-insulator transitions in iridates [5], from suppression of ferromagnetism in Heusler alloys [6], to reduction of magnetic ordering and Jahn Teller distortion in 1D ferromagnets [7].

The X-ray absorption spectroscopy beamlines, **ID24** and **BM23**, have maintained high productivity in catalysis, for example, with studies on Pd–Pt/Al_2O_3 model catalysts [8] and Pt/CeO_2 for room-temperature CO oxidation [9]. In 2016, we also witnessed an increase in environmental applications, such as the study of uranium species in lake sediments [10], and in high pressure investigations. Among the latter is the work on pressure-induced amorphous-amorphous transitions in glasses [11].

Finally, the exploration of new optical systems at **ID06** works towards a better characterisation of hard X-ray spatial coherence [12]. In view of EBS and other similar upgrades of accelerator based sources, these will be particularly useful for the optimisation of electron beam parameters, including emittance.

In 2016, the MEx Group also took the time to strengthen links between different beamlines through regular group meetings, and for social activities. By the way, MEx went social in 2016. Please follow us on: twitter.com/MEx_ESRF.

S. PASCARELLI

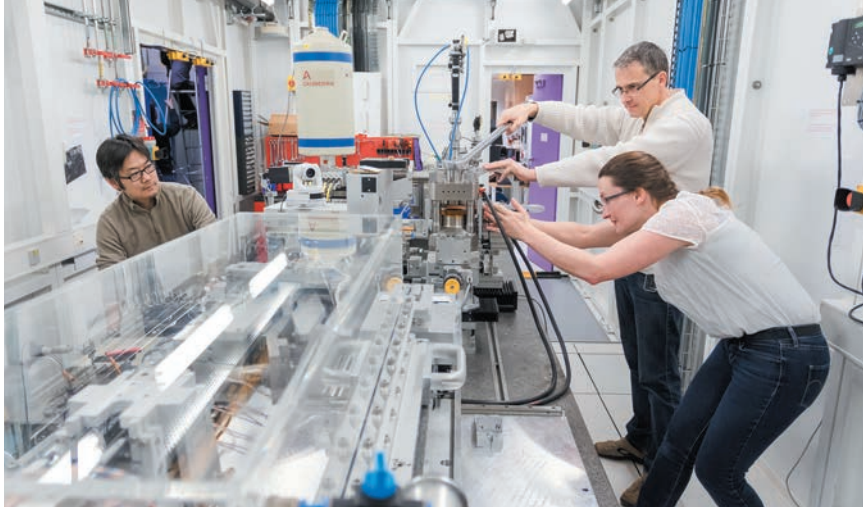

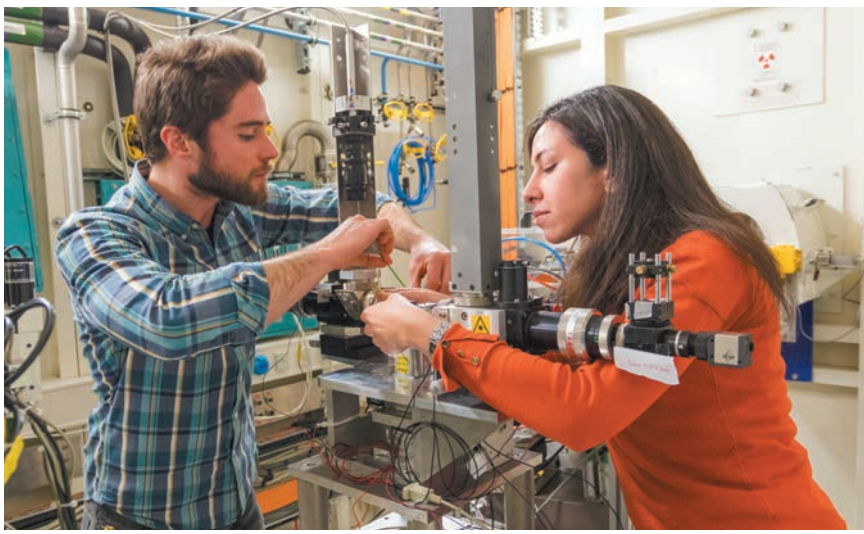

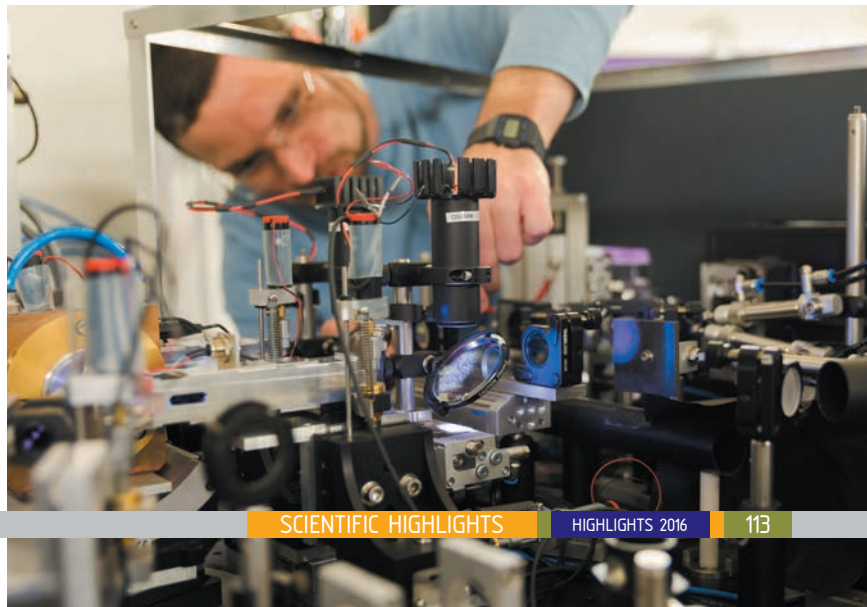

REFERENCES

[1] J. Haber *et al., Nature Photonics* **10**, 445–449 (2016).
[2] O.O. Kurakevych *et al., Inorg. Chem.* **55**, 8943 (2016).
[3] A. Proietti *et al., Physics of the Earth and Planetary Interiors* **259**, 34 (2016).
[4] V. Svitlyk *et al., Inorg. Chem.* **55**, 338 (2015).
[5] C. Donnerer *et al., Phys. Rev. B* **93**, 174118 (2016).
[6] C. Salazar Mejía *et al., Applied Physics Letters* **108**, 261903 (2016).
[7] K. Caslin *et al.*, Phys. Rev. B, **93**, 022301 (2016).
[8] N.M. Martin *et al., J. Phys. Chem. C* **120**, 28009 (2016).
[9] S. Gatla *et al., ACS Catal.* **6**, 6151 (2016).
[10] G. Morin *et al., Geochemical Perspectives Letters* **2,** 95 (2016).
[11] C. Yildirim *et al., Scientific Reports* **6**, 27317 (2016).
[12] M.M. Lyubomirskiy *et al., Optics Express* **24**, 13679 (2016).

XAS AND XES UNRAVEL Cu-SPECIATION IN ZEOLITE-BASED deNO$_x$ CATALYSTS IN *OPERANDO* CONDITIONS

To design improved zeolite-based deNO$_x$ catalysts, a complete understanding of both structural and electronic properties of the metal active sites at the atomic scale under lean conditions is required. We have combined *operando* XAS and XES to monitor the Cu-CHA catalyst during an NH$_3$-SCR reaction in the 150-400°C range, revealing a strong influence of operation temperature on Cu-speciation.

NH$_3$-assisted selective catalytic reduction (NH$_3$-SCR) catalysed by metal-exchanged zeolites is a promising way to remove hazardous NO$_x$ from diesel engine exhaust gases. Cu-exchanged chabazite (Cu-CHA) has been selected as one of the best candidates for commercial SCR applications, due to its enhanced catalytic activity and hydrothermal stability **[1,2]**. Despite several advances in recent years, the rationalisation of the structure-performance relationship in this outstanding catalyst is still an ongoing challenge.

We have combined X-ray absorption (XAS) and valence-to-core emission spectroscopy (vtc-XES) at beamlines **BM23** and **ID26** to shed light on the Cu active sites hosted by the CHA zeolite **[3-5]**. We employed an ESRF microtomo reactor cell connected to a gas rig to monitor the Cu-CHA catalyst at temperatures and gas compositions relevant for industrial applications (**Figure 118a**). This versatile experimental setup allowed us to gradually tackle the structural complexity of the investigated system. Initially, we probed *in situ* the catalyst dehydration process, revealing that redox-active Z−[Cu(II)OH$^-$] complexes (where Z denotes a charge balancing Al site, **Figure 118b**) represent the largely dominant coordination environment in the investigated catalyst **[3]**. Subsequently, *in situ* experiments allowed us to separately explore oxidation and reduction catalytic half-cycles, supporting a consistent scheme for the SCR reaction on isolated Cu sites in Cu-CHA **[4-6]**.

In our most recent study, we have exploited the unique sensitivity of the XAS/XES techniques to monitor the Cu-CHA catalyst 'in action' during *operando* NH$_3$-SCR experiments in the 150-400 °C range (**Figure 118c-e**).

We applied linear combination (LC) fit analysis of *operando* XANES employing a series of well-characterised Cu-references (**Figure 119**) and validated the results by complementary *operando* EXAFS and vtc-XES data to quantitatively estimate temperature-dependent Cu-speciation during SCR. *Operando* XAS/XES during SCR revealed a strong influence of reaction temperature on Cu-speciation. In agreement with the recent study by Paolucci *et al.* **[7]**, in the low-temperature range up to *ca.* 200°C, the catalyst hosts balanced populations of Cu(I)/Cu(II) sites, with a dominant presence of mobile NH$_3$-solvated Cu-species. A different scenario was revealed in the 250-400°C range: Cu is largely present as framework-coordinated Cu(II) species, with preferential O-ligation, accounting for ca. 70% to more than 90% of total Cu sites. Importantly, the transition between low- and high-temperature ranges for Cu-speciation matches the steep

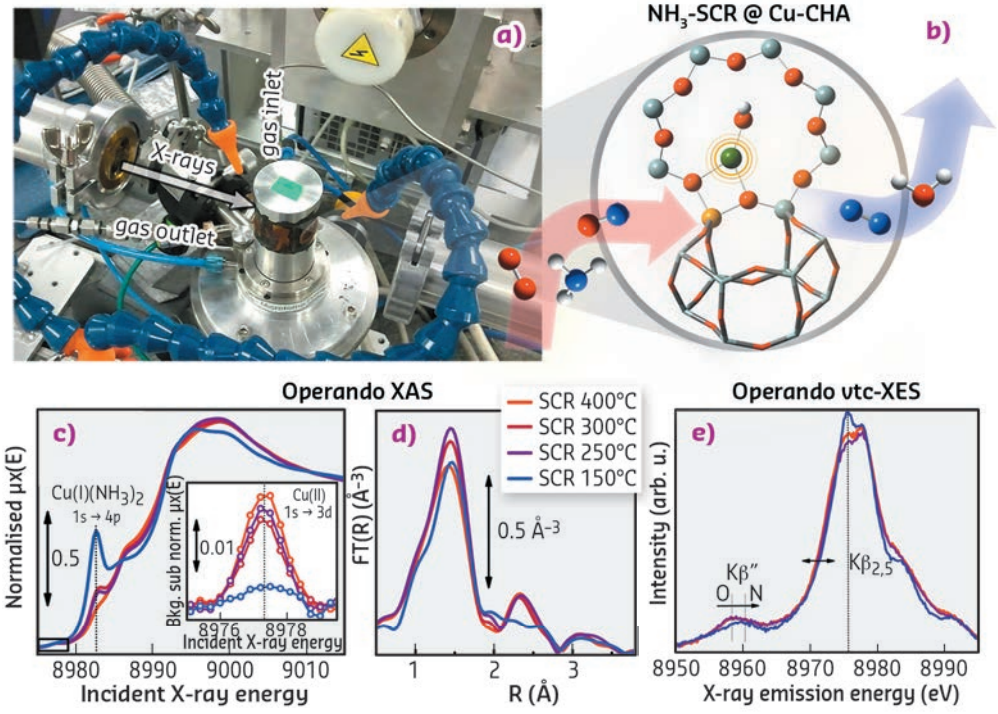

Fig. 118: a) Experimental setup for *operando* XAS/XES on the Cu-CHA catalyst during temperature-dependent NH$_3$-SCR at BM23. b) Schematic representation of the SCR reaction on isolated Cu-sites in Cu-CHA. (c-e) Temperature-dependent c) XANES, d) FT-EXAFS and e) vtc-XES spectra of Cu-CHA during NH$_3$-SCR in the 150-400°C range.

rise in the SCR conversion rate, qualitatively evaluated during *operando* XAS/XES experiments and measured by dedicated laboratory catalytic tests (**Figure 119a**, black squares).

These results highlight the strong influence of operation temperature and reactive environment on Cu-speciation in zeolite-based deNO$_x$ catalysts, demonstrating the potential of *operando* synchrotron-based spectroscopies in heterogeneous catalysis.

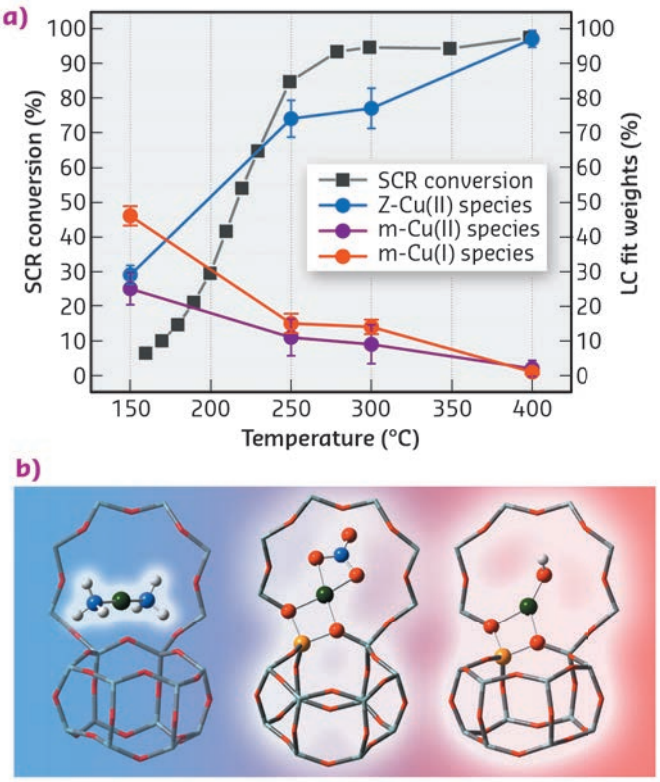

Fig. 119: a) Cu-speciation during temperature-dependent SCR on Cu-CHA from LC fit analysis of *operando* XANES spectra (circles, right axis) and NH_3-SCR conversion rate (squares, left axis). Reported Cu-species include framework-coordinated Cu(II), labelled as Z-Cu(II), and mobile Cu(II) and Cu(I) complexes, labeled as m-Cu(II) and m-Cu(I), respectively. b) Structural snapshots of the dominant Cu-species for each probed temperature: mobile $[Cu(I)(NH_3)_2]^+$ complexes in the low-temperature range and framework-coordinated Cu(II) moieties in the high-temperature range (colour code: Cu: green, O: red, N: blue, Al: yellow, Si: grey, H: white).

PRINCIPAL PUBLICATION AND AUTHORS

The Cu-CHA deNO$_x$ catalyst in action: temperature-dependent NH_3-assisted selective catalytic reduction monitored by *operando* XAS and XES, K.A. Lomachenko (a,b), E. Borfecchia (a), C. Negri (a), G. Berlier (a), C. Lamberti (a,b), P. Beato (c), H. Falsig (c) and S. Bordiga (a), *J. Am. Chem. Soc.* **138**, 12025-12028 (2016); doi: 10.1021/jacs.6b06809.
(a) Department of Chemistry, NIS Centre and INSTM Reference Center, University of Turin (Italy)
(b) IRC "Smart Materials, Southern Federal University, Rostov-on-Don (Russia)
(c) Haldor Topsøe A/S, Lyngby (Denmark)

REFERENCES

[1] U. Deka *et al.*, *ACS Catal.* **3**, 413-427 (2013). A.M. Beale *et al.*, *Chem. Soc. Rev.* **44**, 7371-7405 (2015).
[2] K.A. Lomachenko, *et al.*, *J. Phys.: Conf. Ser.*, **712**, Art. n. 012041 (2016).
[3] E. Borfecchia *et al.*, *Chem. Sci.* **6**, 548 (2015).
[4] F. Giordanino *et al.*, *J. Phys. Chem. Lett.* **5**, 1552-1559 (2014).
[5] T.V.W. Janssens *et al.*, *ACS Catal.* **5**, 2832-2845 (2015).
[6] C. Tyrsted *et al.*, *Catal. Sci. Technol.* **6**, 8314-8324 (2016).
[7] C. Paolucci *et al.*, *J. Am. Chem. Soc.* **138**, 6028-6048 (2016).

A REVERSIBLE Ru-Cs PARTICLE RECONSTRUCTION DEMONSTRATES THE ROLE OF Cs PROMOTION IN THE FISCHER-TROPSCH REACTION

Time-resolved X-ray absorption studies of the Ru-Cs system under *in situ* conditions reveal a reversible particle reconstruction upon syngas reactant switching. This work unravels Fischer-Tropsch gas-phase component interaction with the active metal Ru mediated by Cs promotion and determines the characteristics of the metal and the promoter.

The Fischer–Tropsch (FT) synthesis allows the transformation of syngas, a mixture of CO and H_2, into clean hydrocarbons that are convenient substitutes for compounds produced by oil refining. Ruthenium catalysts present some unique features in FT synthesis as they possess higher intrinsic activity than other metals and can work under higher partial pressures of water or other oxygenate-containing atmospheres. Such atmospheres are particularly important when using biomass produced syngas.

FT catalysts often contain chemical promoters such as alkali elements. An alkali metal increases both the activity and selectivity for high molecular weight hydrocarbons and also

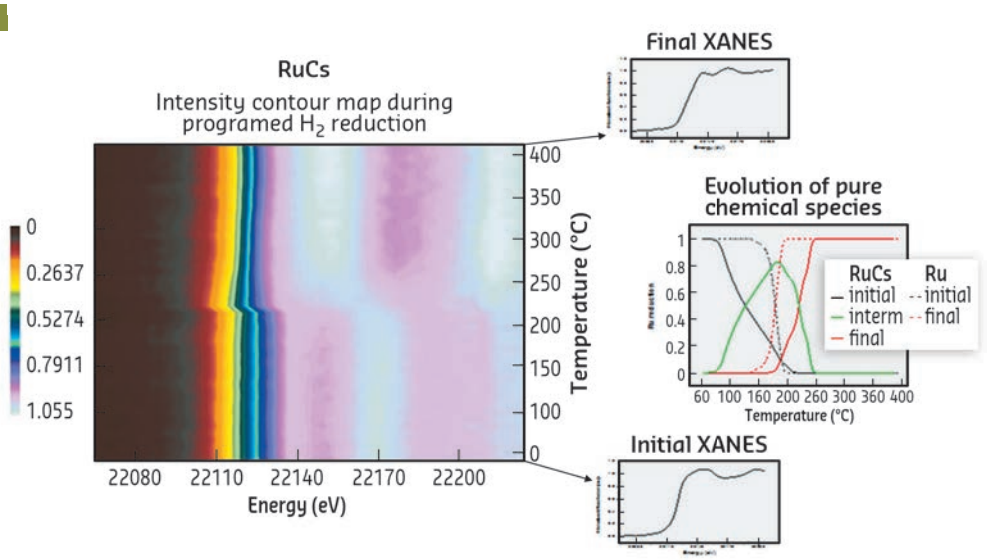

Fig. 120: Normalised absorbance intensity contour map during programmed H_2 reduction for 4%Ru-4%Cs/C. XANES spectra and concentration evolution of the pure chemical species present along H_2-TPR.

favours the formation of olefinic products [1]. This enhanced activity/selectivity is often explained in terms of the basicity of the alkali promoter, which is suggested to increase the CO dissociative adsorption rate, resulting in an increase in the surface coverage of dissociated CO species. This results in higher selectivities towards longer chain hydrocarbon and olefin products [1]. Some interpretations state that the alkali element is an electronic promoter which donates a part of its electron density to Ru even in its oxidised state. Also, another debate is ongoing about the alkali promoter location in the catalyst, which could be inside or at the surface of the metal nanoparticles, or segregated on the support surface with the promotion occurring at the contact point between metal and alkali nanoparticles [2].

In this work, high surface area graphite carbon was employed due to its surface inertness that could facilitate the reduction of the metal precursor to the zero valence state and favour the metal-promoter interaction over that of the metal-support [2]. Furthermore, this support presents good stability for metal particles due its low reactivity to gasification under reaction conditions and high external surface area without micropores which precludes mass transfer problems during the reaction.

Specially-designed time-resolved X-ray absorption spectroscopy experiments [3], performed at beamline **ID24** under temperature-programmed reduction (TPR) conditions and during FT reactant (H_2/CO) switching have allowed us to unravel Fischer-Tropsch gas-phase component interaction with the active metal Ru mediated by Cs promotion and to determine the electronic properties and local chemical environment of the metal and the promoter supported on graphite materials.

XANES analysis at both Ru K- and Cs L_1-edges was carried out during TPR conditions. This allowed us to learn that Ru reduction is a complex process occurring in two steps via an intermediate oxidation state and to show the concomitant Cs partial reduction (**Figure 120**). Time resolved EXAFS analysis at Ru K-edge proved the presence of Cs atoms as first neighbours of Ru. Fitting the data gave structural parameters which match with Ru-Cs nanoparticles where the Cs atoms surround the Ru cluster. Under H_2 atmosphere, a new feature around 3 Å (at close distance from the Ru-Ru first shell) was revealed and this can be attributed to Cs atoms in the vicinity of Ru entities. Moreover, the near absence of the second Ru-Ru coordination shell in H_2 suggests a particle morphology resembling a flat single-layer structure. However, when the H_2 atmosphere is switched to CO, the appearance and gradual increase of Ru neighbours in the second shell implies some restructuring of the nanoparticles to a 3D shape with low first and second shell coordination numbers. In addition, the Ru-Cs particle morphology changes reversibly during cycles of alternate H_2/CO exposure, staging the strong interaction of CO with the surface of the Ru-Cs nanoparticles supported on graphite (**Figure 121**). The latter has been measured directly by microcalorimetry of CO adsorption.

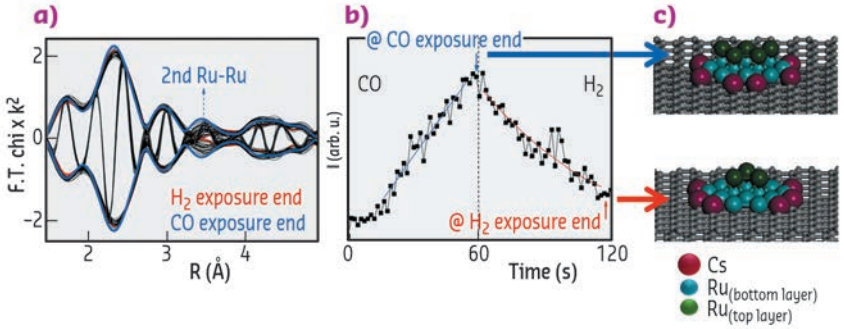

Fig. 121: a) Modulus and imaginary part Fourier transform of EXAFS spectra obtained during a H_2 to CO switch. b) 2nd Ru-Ru coordination shell time evolution during one CO-H_2 cycle for 4%Ru4%Cs/C catalyst. c) Calculated morphologies for the Ru nanoparticles after CO or H_2 exposure, respectively.

Therefore, this study provides evidence of the electronic interaction between Cs and Ru. The presence of the alkali leads to a stronger interaction with the CO molecule. This in turn results in an increase of the adsorbed CO coverage and likely hinders the hydrogen adsorption, resulting in higher olefin selectivity and more long-chain hydrocarbon production in the Fischer-Trospch reaction.

PRINCIPAL PUBLICATION AND AUTHORS

Time resolved XAS investigation of the local environment and evolution of oxidation states of a Fischer-Tropsch Ru-Cs/C catalyst, J.L. Eslava (a), A. Iglesias-Juez (a), G. Agostini (b), M. Fernández-García (a,c), A. Guerrero-Ruiz (c,d) and I. Rodríguez-Ramos (a,c), *ACS Catal.* **6**, 1437-1448 (2016); doi: 10.1021/acscatal.5b02489.
(a) Instituto de Catálisis y Petroleoquímica, CSIC, Madrid (Spain)
(b) ESRF
(c) Grupo de Diseño y Aplicación de Catalizadores Heterogéneos, Unidad Asociada UNED-CSIC (ICP) (Spain)
(d) Departamento de Química Inorgánica y Química Técnica, UNED, Madrid (Spain)

REFERENCES

[1] N. Lohitharn *et al.*, *J. Catal.* **260**, 7-16 (2008).
[2] F. R. García-García *et al.*, *Phys. Chem. Chem. Phys.* **13**, 12892-12899 (2011).
[3] A. Iglesias-Juez *et al.*, *J. Amer. Chem. Soc.* **133**, 4484-4489 (2011).

STABLE SUBNANOMETRIC PLATINUM CATALYST CHARACTERISED BY XAS

Single metal atoms and clusters have unique catalytic properties compared with conventional nanoparticulate catalysts. In this work, subnanometric Pt species (single atoms and clusters) were encapsulated within a three-dimensional zeolite MCM-22 during its synthesis from a two-dimensional precursor. X-ray absorption spectroscopy provided an insight into the local environment of the Pt species in the Pt@MCM-22 complex.

Single metal atoms and metal clusters have attracted much attention thanks to their efficacy as heterogeneous catalysts **[1]**. However, the generation of stable single atoms and clusters on a solid support is still challenging **[2]**. Here we describe a new strategy for the generation of single Pt atoms and Pt clusters with exceptionally high thermal stability, formed within purely siliceous MCM-22 during the transformation of a two-dimensional precursor of the zeolite into the three-dimensional structure. This platinum zeolite complex remains stable even on heating in air to 540°C.

As shown in **Figure 122**, the subnanometric Pt species are finely dispersed in the MCM-22 crystallites. The size of the Pt species and their location in the crystallites was determined with the help of aberration-corrected electron microscopy. The Pt atoms and clusters are located both in the surface "cups" of MCM-22 and within the zeolite framework. In particular, a large proportion of the subnanometric Pt species are located in the internal space of the structure.

A Pt@MCM-22 sample has been studied at beamline **BM23** using X-ray absorption spectroscopy (XAS) to examine the local environment of Pt and to estimate the coordination number of Pt species. The Fourier transform of extended X-ray absorption fine structure (EXAFS) spectra of Pt@MCM-22 and the Pt and PtO_2 reference are shown in **Figure 123a**. Considering the first shell, the Pt@MCM-22 spectrum is dominated by a peak centred around 2.65 Å with a smaller contribution at 2.08 Å (both distances are not phase corrected). Comparing with reference samples, the stronger contribution can be assigned to Pt-Pt bonds in Pt clusters. The weaker peak can be assigned to Pt-O bonds between Pt and the zeolite frameworks. The presence of Pt-O bonds in the Pt@MCM-22

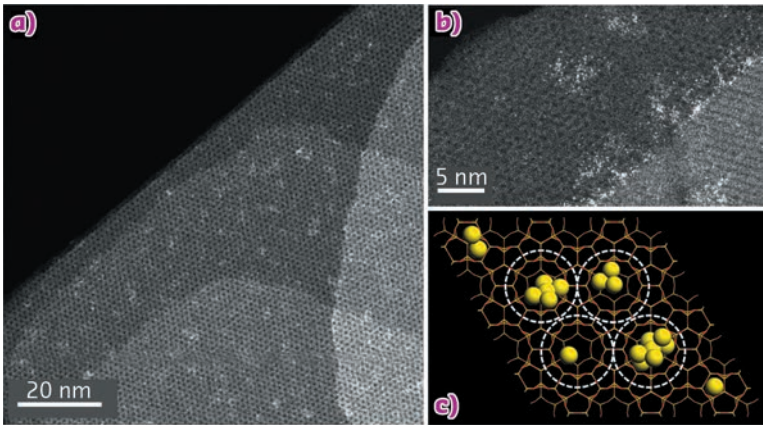

Fig. 122: Atomic structure of Pt@MCM-22 sample. a) and b), HAADF-STEM image of Pt@MCM-22. The bright dots correspond to subnanometric Pt species, including single atoms and clusters with a few atoms. c) Schematic illustration of Pt@MCM-22 in a 'top-down' view along the c axis. Pt clusters and individual Pt atoms are located in the surface cups, cavities and 12-MR supercages.

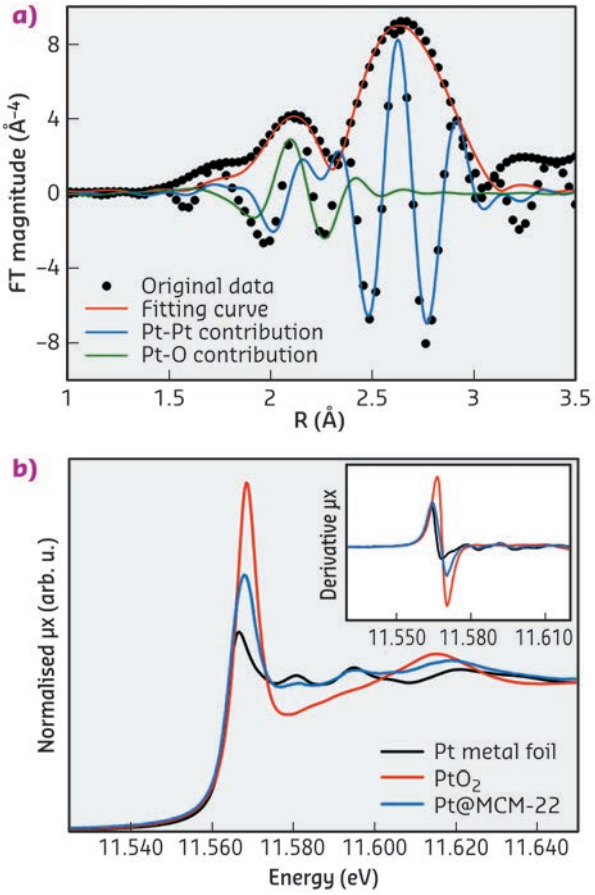

Fig. 123: Characterisation of Pt@MCM-22 with XAS. a) Fourier transform of k^3 -weighted EXAFS spectrum of the Pt@MCM-22 sample (not phase corrected). The fitting curves for Pt–O and Pt–Pt contribution are also presented. b) XANES spectrum of Pt@MCM-22, with the first-order derivative spectrum given in the inset.

sample has also been confirmed by the X-ray absorption near edge structure (XANES) spectrum of Pt@MCM-22. In **Figure 123b**, the curve shape for the Pt@MCM-22 sample looks like Pt(0) (first derivative and oscillations around 11580 and 11595 eV) but its white line intensity is higher, indicating the presence of Pt-O bonds. Based on the fitting results of the EXAFS spectrum, the coordination number of Pt in Pt@MCM-22 is ca. 4.7, which would correspond to Pt clusters of less than 0.7 nm (*i.e.* less than 13 atoms), assuming that Pt clusters show cubo-octahedral shape. The information obtained from electron microscopy and XAS support the hypothesis that the subnanometric Pt species are encapsulated by the zeolite structure.

These stable Pt species confined within internal framework cavities show size-selective catalysis for the hydrogenation of light olefins. Pt@MCM-22 shows higher activity in the hydrogenation of propylene rather than isobutene. Furthermore, high-temperature oxidation-reduction treatments result in the growth of encapsulated Pt species into small nanoparticles in the approximate size range of 1 to 2 nm. The stability and catalytic activity of the encapsulated Pt species is also reflected in the dehydrogenation of propane to propylene. Therefore, this new method provides a means to generate highly stable subnanometric metal catalysts in pure siliceous zeolites for high-temperature catalytic reactions.

PRINCIPAL PUBLICATION AND AUTHORS

Generation of subnanometric platinum with high stability during transformation of a 2D zeolite into 3D, L. Liu (a), U. Díaz (a), R. Arenal (b,c), G. Agostini (d), P. Concepción (a) and A. Corma (a,e), *Nature Materials* **16**, 132–138 (2017); doi: 10.1038/nmat4757.

(a) Instituto de Tecnología Química, Universitat Politècnica de València-Consejo Superior de Investigaciones Científicas (UPV-CSIC), Valencia (Spain)
(b) Laboratorio de Microscopias Avanzadas, Instituto de Nanociencia de Aragon, Universidad de Zaragoza (Spain)
(c) ARAID Foundation, Zaragoza (Spain)
(d) ESRF
(e) King Fahd University of Petroleum and Minerals, Dhahran (Saudi Arabia)

REFERENCES

[1] M. Boronat *et al., Acc. Chem. Res.* **47,** 834-844 (2014).
[2] A. Corma *et al., Nat. Chem.* **5,** 775-781 (2013).

HIGH PRESSURE SYNTHESIS OF 1D POLYMER/ZEOLITE NANOCOMPOSITES

High pressure (GPa) synthesis of polyacetylene and polycarbonyl has been performed in the 1D channels of a pure SiO_2 zeolite, thereby obtaining nanocomposites, which are good candidates as highly-directional semiconductors and high energy density materials, respectively.

Recently, simple carbon-based polymers have been synthesised at high pressures (GPa) in silicalite, a pure SiO_2, non catalytic zeolite with a 3D system of mutually interconnected microchannels **[1-3]**. Pressure and confinement of the reacting monomers at the angstrom scale are the driving forces of the synthesis. These protocols permitted otherwise unstable polymers to be stabilised and protected from the atmosphere, and to obtain an entirely

novel class of nanocomposites with modified physical properties. Unfortunately, channel interconnection in silicalite prevents ideal, isolated polymer chains from being obtained. In this work, we overcame these limitations by using a non-catalytic, all SiO_2 zeolite, ZSM-22 (TON), with a 1D channel system as the host material, which could permit the exploitation of the directional properties of the polymers. In this zeolite, we have synthesised polyacetylene (PA) and polycarbonyl (pCO), two archetypal, linear polymers, a 1D semiconductor and a high energy density polymer, respectively. These two nanocomposites were named PA/TON and pCO/TON.

For the synthesis, acetylene and carbon monoxide were cryogenically loaded into diamond anvil cells in the solid and the liquid phase, respectively, together with hydrophobic TON powder. IR absorption spectra of the reacting mixtures at pressures up to 10 GPa and of nanocomposites recovered under ambient conditions revealed chemical signatures of the embedded polymers such as the C-H stretching peak for C in planar, sp^2 hybridisation in PA/TON, and the C=O stretching peak in pCO/TON. Synchrotron powder X-ray diffraction (XRD) patterns of the recovered samples were measured at beamline ID09A (now **ID15B**) and then refined with the Rietveld method. Very high quality data and structural refinement of the SiO_2 framework and of embedded C atoms were obtained for PA/TON, as reported in **Figures 124a** and **125a**. The PA content is two chains per pore with 50% occupancy, which is consistent with the presence of a degree of disorder in the chain isomers and positions and corresponds to 100% pore filling. The PA chains have a planar zigzag conformation parallel to the *bc* plane (**Figure 125a**), and density functional theory (DFT) calculations indicate that the cis-PA conformer may dominate. A very good fit to the XRD patterns of pCO/TON was also obtained from the Rietveld refinement, **Figure 124b**. The refined occupations give a CO content of 2.4 molecules per unit cell corresponding to 30% pore filling in a statistical distribution. Incomplete pore filling is probably linked either to an incomplete polymerisation of CO and subsequent loss of remaining monomers after pressure release or to incomplete filling by the initial CO monomers. The structural model consists of alternating cis and transoid CO configurations lying in the *bc* planes, which are commensurate with the framework and consistent with the observed Fourier map, **Figure 125b**, as also shown by DFT calculations. In addition, DFT calculations of the electronic density-of-states of ordered pCO/TON and PA/TON show van Hove singularities within the band gap of the TON due to the 1-D nature of the polymer chains.

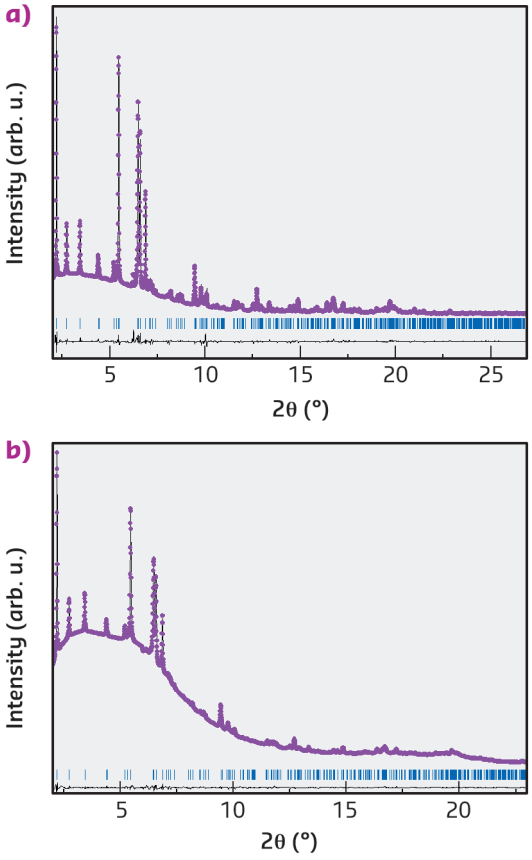

Fig. 124: Experimental (dots) and calculated (solid line) XRD profiles from the Rietveld refinement of PA/TON (a) and pCO/TON (b) recovered at ambient pressure. Wavelengths: 0.414132 Å for pCO/TON, and 0.415352 Å for PA/TON.

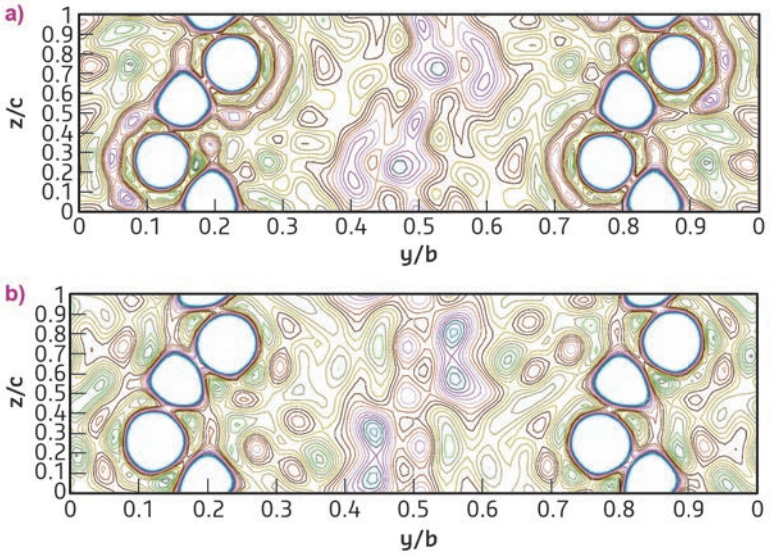

Fig. 125: Section of the electron density map at x/a = 0.5. The white circles represent the framework atoms, whereas the polymerised chains are visible at y/b = 0.4-0.6 for PA/TON (a) and pCO/TON (b).

Confined PA and pCO in the nanocomposites are chemically ordered, with some isomeric disorder in PA, in contrast to bulk PA and pCO. pCO/TON is a material with an energy storage capacity

higher than that of dynamite. The protecting TON allows this energy to be retained/stored in the presence of atmospheric moisture. In PA/TON, where TON also prevents PA from reacting with moisture, the 1D nature of the polymers may lead to the use of this class of materials as quantum devices for important applications such as quantum computation.

PRINCIPAL PUBLICATION AND AUTHORS

M. Santoro (a,b), D. Scelta (b,c), K. Dziubek (b,d), M. Ceppatelli (c,b), F.A. Gorelli (a,b), R. Bini (b,e), G. Garbarino (f), J.-M. Thibaud (g), F. Di Renzo (g), O. Cambon (g), P. Hermet (g), J. Rouquette (g), A. van der Lee (h) and J. Haines (g), *Chem. Mater.* **28**, 4065 (2016);
doi: 10.1021/acs.chemmater.6b01639.

(a) CNR-INO, Sesto Fiorentino (Italy)
(b) LENS, Sesto Fiorentino (Italy)
(c) CNR-ICCOM, Sesto Fiorentino (Italy)
(d) Faculty of Chemistry, Adam Mickiewicz University, Poznań (Poland)
(e) Chemistry Department, University of Florence, Sesto Fiorentino (Italy)
(f) ESRF
(g) ICGM-CNRS, and Université de Montpellier (France)
(h) IEMM-CNRS, and Université de Montpellier (France)

REFERENCES

[1] M. Santoro *et al.*, *Nat. Commun.* **4**, 1557 (2013).
[2] D. Scelta *at al.*, *Chem. Mater.* **26**, 2249 (2014).
[3] M. Santoro *et al.*, *Chem. Mater.*, **27**, 6486 (2015).

A NEW ROUTE TO PENTAVALENT POST-PEROVSKITE

The postperovskite form of $NaOsO_3$ can be synthesised from the known perovskite form at pressures in excess of 16 GPa. Also, this new postperovskite can be more advantageously grown from a lower pressure $KSbO_3$-type at less than 6 GPa. *In situ* X-ray diffraction using the ID06 large volume press was instrumental in these studies.

The 5*d* compounds have fascinating properties that can be adopted for spintronics and other advanced electronic technologies. In recent years, a variety of new compounds have been isolated in the Na-Os oxide system. These include the high-pressure production of pentavalent, hexavalent and heptavalent compounds, all of which we have observed in the course of this study. The pentavalent $NaOsO_3$ stoichiometry has been previously described as a $KSbO_3$-type and a perovskite **[1,2]**. These $KSbO_3$-type structures are, generally, a family of tunnel-containing compounds that exhibit a range of chemistries and a plethora of attractive physical properties; including ionic conduction, catalytic activity and oxygen sensing. The wider $KSbO_3$ family also support great flexibly in their chemistries. This, combined with the wide range of valences available in the Na-Os-O system, makes them an ideal system for exploring new synthetic protocols that can exploit changes in oxidation state and bulk chemistry to produce novel phases.

Such *in situ* synthetic work at high pressures and temperatures is rather complex and we have sought to overcome some of the technical difficulties by first pre-synthesising two samples offline, in Pt capsules, at 6 GPa. We have used two near-identical schemes that incorporate the same nominal mixtures of 1:1 Na_2O_2:OsO_2 with excess oxygen source, from sodium peroxide, to produce perovskite and $KSbO_3$-type-rich initial starting materials.

In a first run, using the large-volume press at beamline **ID06LVP**, a single phase sample of perovskite (pv) $NaOsO_3$, was pressurised up to 16.35 GPa and the temperature increased. At 1135 K, inspection of the changed diffraction profiles readily demonstrated the formation of $CaIrO_3$-type ppv-$NaOsO_3$. This was quite unexpected as many structural indicators are completely against pv-$NaOsO_3$ forming post-perovskite (ppv); for example, its lattice parameters at ambient conditions (*Pnma*; Z = 4, a = 5.3830(3), b = 7.5763(4), c = 5.3245(3) Å) are closer to pseudocubic, ϕ = 10.55°, than are normally considered sufficient to lead to the crystallisation of ppv at high P. The tolerance factor is also higher than t = 0.9 (at t = 0.924), as is the ratio of polyhedral volumes, V_A/V_B = 4.82, which are both well above normal cut-offs for pv to ppv transitions. Assuming a dP/dT slope of 10-17 MPa/K, and that the synthesis is representative of an equilibrium transformation, this would place the room temperature transition at less than 5 GPa.

Using the less dense and alternate $KSbO_3$-type rich sample, at 6.05 GPa, **Figure 126, A**, the secondary Na_2OsO_4 phase (due to Na_2O_2 excess) is consumed into the single-phase rhombohedrally distorted $KSbO_3$-like phase at 750 K, **Figure 126**, **B**. Immediately after this, a continuous transformation from *rR* to *c*-$NaOsO_3$ is observed (830 K), **Figure 126**, **C**. From these results, higher temperatures and lower pressures favour the crystallisation of the

Pn-3 type $KSbO_3$-form over the rhombohedral distortion. With further heating, following intermediate quench (**D**), we evidence two almost coincident events: (i), at 750 K, the sharp 's'-shaped kink in the *c*-$NaOsO_3$ peaks (**E**) that occur with the growth of rutile-type OsO_2 and, (ii) at 825 K, **F**, the growth of ppv-$NaOsO_3$. The rapid peak-shift to lower *d*-spacing of all cubic peaks and concomitant growth of OsO_2 is indicative of a reduction of lattice size, with presumably, loss of Os to its rutile-structured oxide. Ppv crystallises immediately after. At conversion, the lattice of ppv is a = 2.8192(17) Å, b = 10.4047(21), c = 7.3179(18) Å (V/Z = 53.66 Å^3/f.u.); with *c*-$NaOsO_3$ at a = 9.0709(7) Å (V/Z = 61.20 Å^3/f.u.) and their relative volume difference is ΔV = -12.3%. A recovered sample, quenched at point **G**, shows fine-grained texture for the ppv, while the minor $KSbO_3$-like phase is spotty and has reverted to a new rhombohedral distortion.

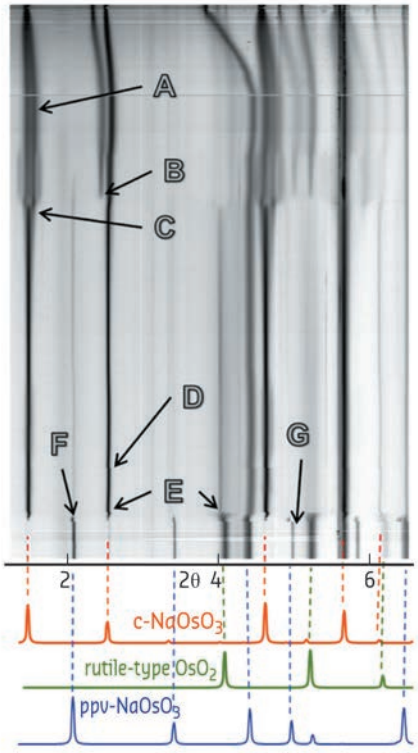

Fig. 126: A series of semi-continuous X-ray diffraction patterns collected upon pressurising and during two heating-cooling cycles. Shown is the lower angle part only. Of note: (A) Increased splitting of the (110/1-10) pair; (B) Loss of Na_2OsO_4; (C) *rR* to *c*-$NaOsO_3$ transformation; (D) Quench, end heating cycle 1 (E) 's'-shaped-kink, onset of OsO_2 and crystallisation of ppv (F). (G) Quench end of heating cycle 2, followed by reheat. Simulated diffraction patterns for *c*-$NaOsO_3$, OsO_2 and ppv-$NaOsO_3$ are shown as key.

From this alternative route, we observe that i) pv-$NaOsO_3$ can be advantageously formed from an assemblage that does not yet contain any pv, ii) ppv can be formed from phases other than pv (even in systems where pv occurs) and iii) the growth of pv as a precursor or indicator to ppv is counterproductive, requiring more than 10 GPa higher pressure to initiate the transformation. The difference in volumes of >10% ($KSbO_3$-type to ppv) compared to just 1-2% for pv-ppv at transformation no doubt influences this. From both $NaIrO_3$ and $NaOsO_3$, limits in both pseudocubic tilt and tolerance factor could be reassessed to include more pentavalent chemistries.

PRINCIPAL PUBLICATION AND AUTHORS

A new route to pentavalent post-perovskite, W.A. Crichton (a), K. Yusenko (b), S. Riva (b), F. Mazzali (b) and S. Margadonna (b), *Inorganic Chemistry* **55**, 5738-5740 (2016); doi: 10.1021/acs.inorgchem.6b00780.
(a) ESRF
(b) College of Engineering, Swansea University (U.K.)

REFERENCES

[1] A.W. Sleight *et al., J. Solid State Chem.* **183**, 402 (**2010**).
[2] Y. Shi *et al., Phys. Rev. B* **80**, 1661104 (**2009**).

PHOSPHORUS BECOMES FIVE-COORDINATED AT HIGH PRESSURE

The behaviour of the spin-Peierls compound titanium orthophosphate, $TiPO_4$, was investigated up to a pressure of 56 GPa using single-crystal X-ray diffraction. Four high-pressure phase transitions lead to the phase containing phosphorus coordinated by five oxygen atoms.

Phosphorus plays a key role in the chemistry of life and many technological applications. Unusually high coordination numbers of cations like phosphorus are often associated with interesting physical properties such as high density, ultra-high hardness or low compressibility, which are important for engineering applications. So far, examples of a phosphorus atom coordinated by five oxygen atoms are known for liquids and molecular compounds, but were never found in inorganic network compounds, which usually contain stable PO_4 groups.

In this study, we investigated the high-pressure behaviour of titanium orthophosphate ($TiPO_4$) by means of single-crystal X-ray diffraction at the beamlines ID09A of ESRF (now **ID15B**) and P02.2 (DESY, Petra III, Hamburg). $TiPO_4$ belongs

to the family of phosphates MPO_4 (M = Ti, Tl, V, In) that crystallise in the $CrVO_4$ structure type. $TiPO_4$ is a very peculiar member of the $CrVO_4$ structure family, because of its low-dimensional magnetic properties. On cooling, it undergoes normal–incommensurate–commensurate phase transitions towards a so-called spin-Peierls state. **[1]** The spin-Peierls transition is a magneto-elastic transition that occurs in quasi one-dimensional antiferromagnetic materials leading to the formation of spin singlets and dimerisation of the chains of antiferromagnetic atoms. Application of pressure to the spin-Peierls systems may lead to various magnetostructural transitions replacing the phase transitions predicted by classical crystal chemistry considerations. Indeed, we have found that the moderate compression of $TiPO_4$ leads to the formation of the incommensurate phase $TiPO_4$-II, which undergoes the lock-in transition towards commensurate $TiPO_4$-III above 7 GPa.

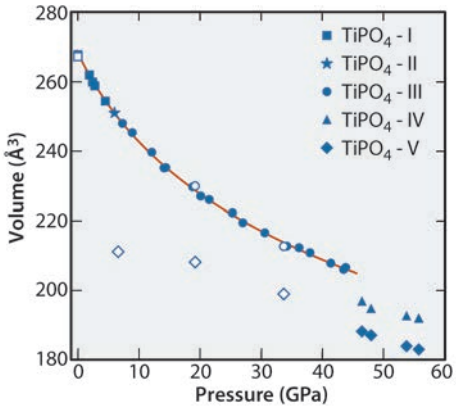

Fig. 127: Pressure dependence of the unit cell volume. For $TiPO_4$-II and for $TiPO_4$-III, the volumes given are the volumes of the average structures. Open symbols correspond to the decompression experiment. The solid curve represents the fit of the third-order Birch-Murnaghan equation of state to the experimental data.

Both $TiPO_4$-II and $TiPO_4$-III contain Ti-Ti singlet dimers inherent to the spin-Peierls state **[2,3]**. This result improves our understanding of the spin-Peierls transitions and reveals new possibilities to examine this transition without low temperatures.

Compression above 46 GPa leads to the transformation to the coexisting phases $TiPO_4$-IV and $TiPO_4$-V with the volume drops of 4.2 and 8.0% respectively (**Figures 127, 128**). The structure of $TiPO_4$-IV consists of TiO_7 trigonal prisms capped on a single rectangular face. They share their trigonal faces, thus forming infinite chains along one of the crystallographic directions while Ti atoms along the chains remain dimerised. The chains are interconnected by PO_4 groups via common edges and vertices.

The structure of $TiPO_4$-V is composed of PO_5 trigonal-bipyramids which form chains along the [1 0 1] direction through shared apical oxygen atoms. The chains are interconnected with each other by Ti atoms, linked to the equatorial oxygen atoms of the PO_5 groups, thus forming layers parallel to (1 0 -1), such that the Ti atoms are confined between these layers. Ti atoms have highly distorted snub disphenoid coordination.

The experimental demonstration that phosphorus could form PO_5 polyhedra suggests that similar compounds may appear as intermediate (metastable, short- lived, and hardly or not at all detectable) products of different chemical processes involving phosphorus and oxygen. Experimental evidence of phosphorous penta-coordinated by oxygen may open new routes in high-pressure phosphorous chemistry.

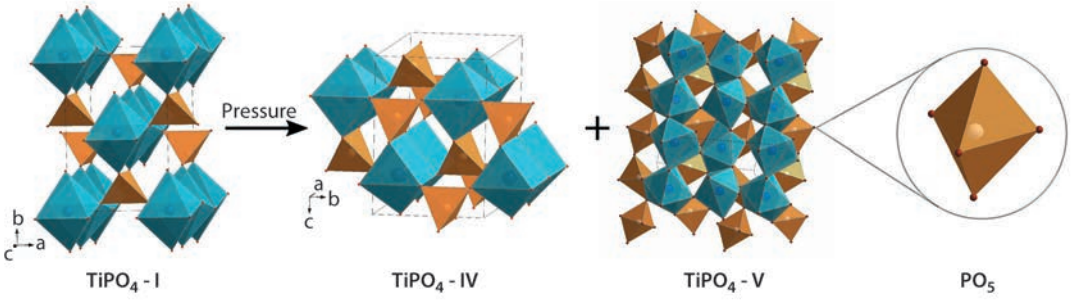

Fig. 128: Crystal structures of $TiPO_4$-I, $TiPO_4$-IV and $TiPO_4$-V. TiO_6, TiO_7 and TiO_8 polyhedra are blue, PO_4 and PO_5 polyhedra are orange.

PRINCIPAL PUBLICATION AND AUTHORS

High-pressure phase transformations in TiPO4: a route to pentacoordinated phosphorus, M. Bykov (a, b), E. Bykova (a), M. Hanfland (c), H.-P. Liermann (d), R.K. Kremer (e), R. Glaum (f), L. Dubrovinsky (a) and S. van Smaalen (b), *Angewandte Chemie Int. Ed.* **55**, 15053-15057 (2016); doi: 10.1002/anie.201608530.

(a) Bayerisches Geoinstitut, Universität Bayreuth (Germany)
(b) Laboratory of Crystallography, Universität Bayreuth (Germany)
(c) ESRF, Grenoble (France)
(d) Deutsches Elektronen-Synchrotron (DESY), Hamburg (Germany)
(e) Max Planck Institute for Solid State Research, Stuttgart, (Germany)
(f) Institute of Inorganic Chemistry, University of Bonn (Germany)

REFERENCES

[1] A.A. Buzdin *et al. Soviet Physics Uspekhi* **23**, 409 (1980).
[2] J.M. Law *et al. Phys. Rev. B* **83**, 180414(R) (2011).
[3] M. Bykov *et al. Phys. Rev. B* **88**, 184420 (2013).

NEW TYPE OF CHARGE-ORDERING TRANSITION IN THE NOVEL IRON OXIDE Fe_4O_5

Synthesis of new classes of compounds can lead to discoveries of novel physical phenomena as well as innovative applications. Fe_4O_5 is the first member of a very recently discovered family of iron oxides that can be synthesised only under high-pressure conditions. A multi-technique study of Fe_4O_5 reveals that it undergoes a unique charge-ordering transition below 150 K that involves competing dimeric and trimeric ordering within the chains of Fe ions. This electronic transition drives an intricate incommensurate distortion in its crystal structure.

At ambient pressure, only three iron oxide polymophs were known, FeO, Fe_3O_4, and Fe_2O_3. Recently, several new iron oxide polymorphs with hitherto unknown stoichiometries have been discovered under high pressure conditions **[1,2]**. Among them, Fe_4O_5 looks particularly exciting as it can be readily quenched at ambient pressure **[1]**. We have performed a series of low-temperature studies on a recently-discovered high-pressure polymorph of iron oxide, Fe_4O_5 **[1]** and discovered a new type of charge-ordering transition involving the formation of competing dimeric and trimeric ordering within the chains of Fe ions, as revealed by X-ray diffraction studies at beamline **BM01**, SNBL. These findings were supported in neutron diffraction experiments and in measurements of magnetic and transport properties. To date, such exotic transitions have never been observed, and, hence, it brings new perspectives on charge-ordered states and transitions.

At ambient conditions, Fe_4O_5 crystallises in a $CaFe_3O_5$-type structure featuring linear chains of octahedrally-coordinated iron ions and linear chains of FeO_6 trigonal prisms along the *a*-axis (**Figure 129a,c**). This compound contains equal amounts of Fe^{2+} and Fe^{3+} ions, and like another mixed-valent iron oxide, magnetite (Fe_3O_4), it is a good electrical conductor owing to a charge transfer between Fe^{2+} (charges) and Fe^{3+} (vacancies). Magnetite is known to undergo a charge-ordering phase transition below 125 K, which is accompanied by a jump in electrical resistivity **[3]**. This transition in magnetite had been discovered by Verwey in 1939 **[3]**, but only recently by means of single-crystal X-ray diffraction, the charge-ordering pattern in its low-temperature phase has finally been uncovered to involve 'three-site-distortions', called 'trimerons' **[4]**. Analysis of the bond valence sums in the lattice of Fe_4O_5 indicated the mixed valence states of iron at the octahedrally-coordinated sites (**Figure 129c**), and, hence, one could expect that Fe_4O_5 also undergoes some charge ordering at relatively low temperatures.

The high-quality single crystal X-ray diffraction patterns of Fe_4O_5 collected at beamline **BM01** demonstrated the appearance of superlattice

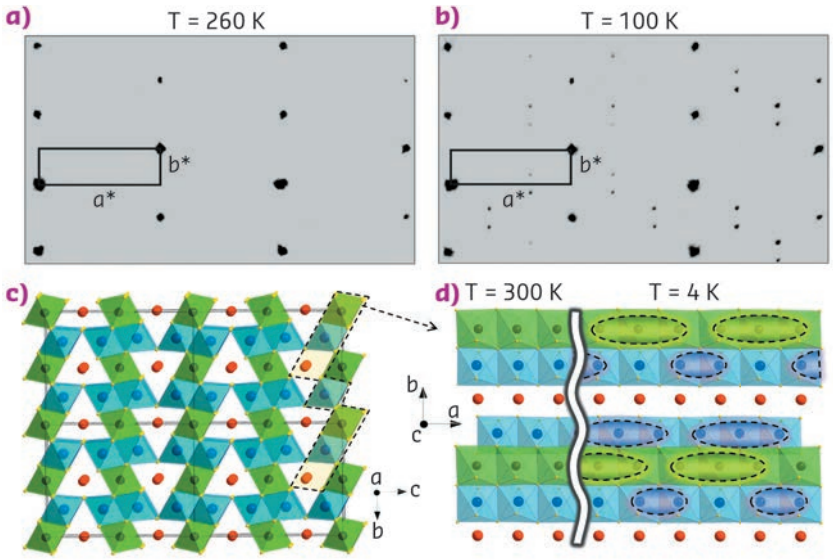

Fig. 129: (a, b) Examples of reciprocal lattices of X-ray diffraction intensities of Fe_4O_5 at 260 K and 100 K (c) Crystal structure projected down the *a*-axis at room temperature. d) Crystal structure of Fe_4O_5 projected along the *c*-axis at room and low temperatures.

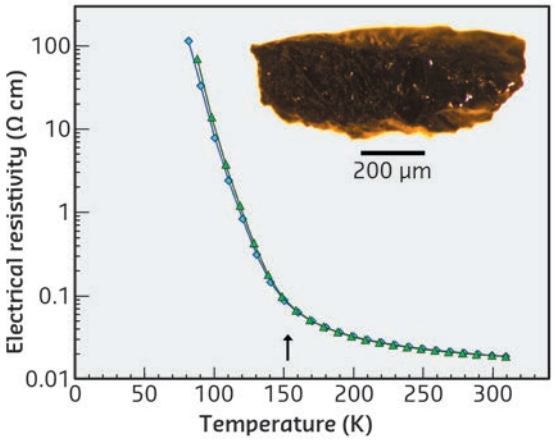

Fig. 130: Temperature dependencies of electrical resistivity of Fe_4O_5 in 0 and 12 T magnetic fields (blue and green curves, respectively). These curves exhibit a bend at 150 K (marked by the arrow), indicating a 'metal-insulator'-type transition. A photograph of the Fe_4O_5 sample is included.

reflections upon cooling below 150 K (**Figure 129a,b**). Analysis of these patterns revealed that the low-temperature structure is incommensurately modulated and contains the Fe dimers and trimers within the chains of the octahedrally-coordinated iron (**Figure 129d**). A constant Fe-Fe distance of 2.861 Å (at 4 K) in the trigonal chains of ferrous iron enabled the dramatic shortening of some interoctahedra distances (marked by elongated ellipsoids in **Figure 129d**) to be highlighted. Each chain of

the octahedral cations contains either dimers composed of Fe^{2+}–Fe^{3+} pairs with one shared electron, or trimers composed of one Fe^{2+} and two Fe^{3+} ions, similar to the trimerons in Fe_3O_4 **[4]** (**Figure 129d**). This unusual charge-ordering transition in Fe_4O_5 is concurrent with a significant increase in electrical resistivity (**Figure 130**), and therefore, it may be classified as a "metal-insulator"-type transition. The magnetic susceptibility measurements and neutron diffraction establish the formation of a collinear antiferromagnetic order above room temperature and a spin canting at 85 K that gives rise to spontaneous magnetisation.

PRINCIPAL PUBLICATION AND AUTHORS

Charge ordering transition in iron oxide Fe_4O_5 involving competing dimer and trimer formation, S.V. Ovsyannikov (a), M. Bykov (a,b), E. Bykova (a,b), D.P. Kozlenko (c), A.A. Tsirlin (d,e), A.E. Karkin (f), V.V. Shchennikov (f,g), S.E. Kichanov (c), H. Gou (a,h), A.M. Abakumov (i,j), R. Egoavil (i), J. Verbeeck (i), C. McCammon (a), V. Dyadkin (k), D. Chernyshov (k), S. van Smaalen (b) and L.S. Dubrovinsky (a), *Nature Chemistry* **8**, 501-508 (2016); doi:10.1038/nchem.2478.

(a) Bayerisches Geoinstitut, Universität Bayreuth (Germany)
(b) Laboratory of Crystallography, Universität Bayreuth (Germany)
(c) Frank Laboratory of Neutron Physics, JINR, Dubna (Russia)
(d) National Institute of Chemical Physics and Biophysics, Tallinn (Estonia)
(e) Institute of Physics, University of Augsburg (Germany)
(f) Institute of Metal Physics, Russian Academy of Sciences, Yekaterinburg (Russia)
(g) Institute for Solid State Chemistry, Russian Academy of Sciences, Yekaterinburg (Russia)
(h) Key Laboratory of Metastable Materials Science and Technology, Yanshan University, Qinhuangdao (China)
(i) Electron Microscopy for Materials Research (EMAT), University of Antwerp (Belgium)
(j) Department of Chemistry, Moscow State University (Russia)
(k) Swiss–Norwegian Beamlines at the ESRF, Grenoble (France)

REFERENCES

[1] B. Lavina, *et al. Proc Nat. Acad. Sci. US* **108**, 17281 (2011).
[2] E. Bykova, *et al.*, *Nature Commun.* **7**, 10661 (2016).
[3] E.J.W. Verwey, *Nature* **144**, 327 (1939).
[4] M.S. Senn *et al.*, *Nature* **481**, 173 (2012).

DISCOVERY OF NEW HIGH PRESSURE IRON OXIDES POINTS TO A LARGE OXYGEN SOURCE IN EARTH'S MANTLE

Studies of iron oxides under extreme conditions reveal a possible novel mechanism of oxygen recycling in the Earth's interior with potentially great impact on geochemical processes.

Materials exposed to extreme conditions such as high pressures and high temperatures (HPHT) can undergo chemical reactions that are totally different from those known at ambient conditions. Recent revolutionary developments in the field of high pressure crystallography have extended the achievable range of pressures useable for single crystal studies by an order of magnitude, beyond 150 GPa. Quantitative *in situ* characterisation of chemical changes in materials heated to thousands of degrees at pressures of dozens of GPa used to be a dream for high pressure scientists, but now we have demonstrated that this is indeed possible. We have acquired high quality single-crystal X-ray diffraction data from samples in the Fe-O system using laser heated diamond anvil cells at third generation synchrotrons, in particular at the ESRF at beamline ID09A (now **ID15B**), and combined these results with those from the unique energy-resolved synchrotron Mössbauer spectroscopy at beamline **ID18** that allowed a detailed characterisation of structural, chemical, and electronic processes under extreme conditions.

Our work is focused on the investigation of iron (III) oxide, Fe_2O_3, at pressures above 100 GPa and temperatures above 2500 K. Despite a strikingly simple chemical composition, this oxide undergoes a series of enigmatic structural and electronic transitions at elevated pressures and temperatures. We observed two transformational paths in Fe_2O_3 depending on the type of external stimuli applied. During room-temperature compression, Fe_2O_3 undergoes two phase transitions (to ζ-Fe_2O_3 at 54 GPa and θ-Fe_2O_3 at 67 GPa) accompanied by an iron spin crossover and a related abrupt change of the unit cell volume. The highest-pressure phase θ-Fe_2O_3, having Fe^{3+} in only a low spin state, can be observed to at least 100 GPa and is metastable.

Moderate heating with a laser provokes its transformation to a η-Fe_2O_3 phase with a post-perovskite structure, which is stable down to at least 50 GPa; heating results in transformations of this phase first into ζ-Fe_2O_3 and then ι-Fe_2O_3. **Figure 131** show these numerous phases and phase transformations, accompanied by changes in the electronic structure of Fe_2O_3.

The most intriguing observation was that Fe_2O_3 is chemically unstable at high pressures and temperatures: if heated at pressures above ~60 GPa, Fe_2O_3 with the post-perovskite structure (η-Fe_2O_3) releases oxygen and forms a novel Fe_5O_7 compound. Inspired by this observation, we performed experiments on Fe_3O_4 and found that this iron oxide also decomposes to form the previously unknown $Fe_{25}O_{32}$ upon heating at pressures above ~70 GPa. Thus, it is firmly established that the chemistry of the Fe-O system at even moderate pressures is remarkably different from that which is known at ambient pressure.

The results of this work have important implications not only for fundamental high-pressure chemistry, but also for the understanding of the global rock development processes. Hematite (α-Fe_2O_3) and magnetite (Fe_3O_4) are major components of the so-called banded iron formations (BIFs) and ironstones, huge sedimentary rock formations occurring on all continents (and the main source of iron for our civilisation). BIFs may reach up to several hundred metres in thickness and hundreds of kilometres in length. Deposited in the world's oceans about two billion years ago, BIFs as part of the ocean floor are recycled into the Earth's interior by subduction to depths extending possibly to the core-mantle boundary region. According to the present study, hematite and magnetite would undergo numerous phase transformations upon subduction of BIFs into the lower mantle (**Figure 132**). At pressures above ~60 GPa, iron oxides (particularly η-Fe_2O_3) start to decompose, producing oxygen. Based on estimates of the amount of BIFs subducted into the Earth's mantle, the amount of oxygen produced by the formation of Fe_5O_7 alone can be as high as 8 to 10 times the mass of oxygen in the modern atmosphere. An oxygen-rich fluid could either locally oxidise surrounding materials or pass to the transition zone, or even to the upper mantle, thus shifting Fe^{2+}/Fe^{3+} equilibria in silicate minerals and greatly raising the oxygen fugacity in this region. In any case, our study suggests the presence of an oxygen-rich fluid in the deep Earth's interior that can significantly affect geochemical processes by changing oxidation states and mobilising trace elements.

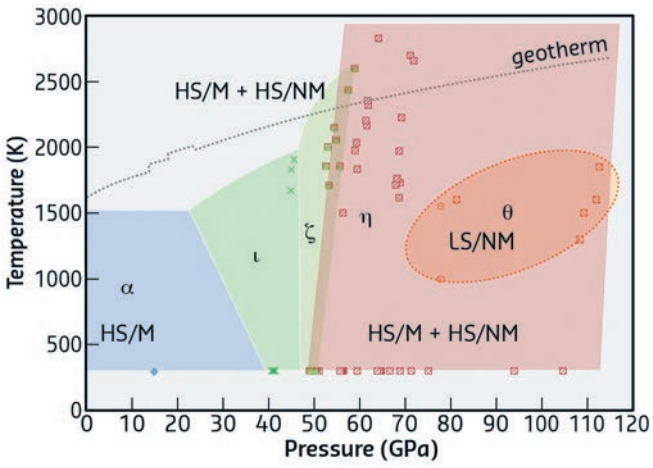

Fig. 131: Transformational phase diagram of Fe_2O_3. Legend: diamond - hematite (α-Fe_2O_3), triangles - distorted perovskite (ζ-Fe_2O_3), circles - *Aba2* (θ-Fe_2O_3, probably metastable), squares - *Cmcm* post-perovskite (η-Fe_2O_3), crosses - Rh_2O_3-II type phase (ι-Fe_2O_3). Letters designate the electronic and magnetic state of iron atoms: HS – high-spin, LS – low spin, M – magnetic ordering, NM – absence of magnetic ordering.

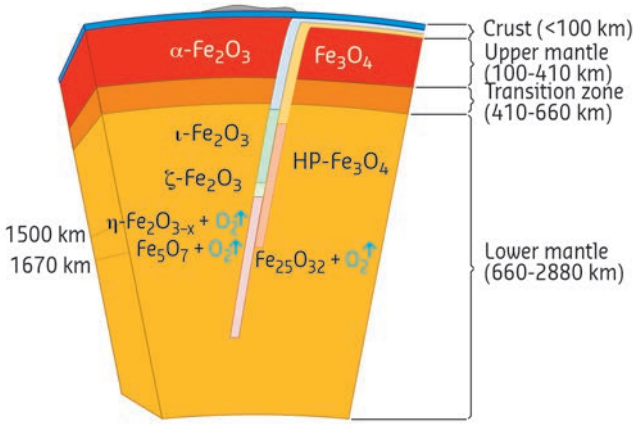

Fig. 132: Possible consequence of phase transitions of Fe_2O_3 and Fe_3O_4 in a BIF subducted to the lower mantle.

PRINCIPAL PUBLICATION AND AUTHORS

Structural complexity of simple Fe_2O_3 oxide at high pressures and temperatures, E. Bykova (a,b), L. Dubrovinsky (a), N. Dubrovinskaia (b), M. Bykov (b), C. McCammon (a), S.V. Ovsyannikov (a), H.-P. Liermann (c), I. Kupenko (a,d), A.I. Chumakov (d), R. Rüffer (d), M. Hanfland (d) and V. Prakapenka (e), *Nature Communications* **7**, 10661 (2016); doi: 10.1038/NCOMMS10661.

(a) Bavarian Research Institute of Experimental Geochemistry and Geophysics, Universität Bayreuth (Germany)
(b) Laboratory of Crystallography, Universität Bayreuth (Germany)
(c) Photon Sciences, Deutsches Elektronen-Synchrotron, Hamburg (Germany)
(d) ESRF
(e) Center for Advanced Radiation Sources, University of Chicago, Argonne (USA)

REVEALING THE MOLECULAR STRUCTURE OF KEROGEN IN GAS SHALE

Fracking is a controversial recovery method to extract oil or gas from shale rock. Little is known about the microscopic structure of kerogen, the organic matter which hosts hydrocarbons in gas shales. Using a hybrid strategy, combining molecular simulation and experiment, we have developed molecular models of kerogen which capture the complexity of such geological structures. These atom-scale structures, which have been derived and validated against experimentally-determined properties, can be used to unravel the behaviour of this complex organic matter.

Oil and natural gas are produced from the decomposition of organic matter, known as kerogen, in shale rocks. In these structures, the kerogen is embedded within a mineral mixture (**Figure 133**) resulting in permeabilities a million times lower than in conventional hydrocarbon reservoirs. Owing to such ultra-low permeability combined with fast, unexplained productivity decline, the hydrocarbons are recovered through a controversial extraction technique known as hydraulic fracturing, or fracking. To develop new techniques that would be both effective and lower in environmental impact, one needs a better understanding of the shale structure in general and the kerogen structure in particular.

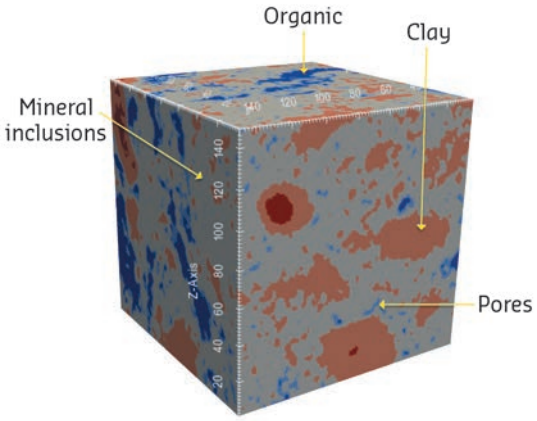

Fig. 133: X-ray microscopy image of an untreated sample of gas shale, showing inclusions of clay, organic matter and other minerals. Copyright: M. Hubler (MIT) and J. Gelb (Carl Zeiss X-ray Microscopy).

We have studied four different kerogen samples of different geological origins and degrees of maturation. Their atomic structure, texture, density and mechanical properties were characterised thanks to beamlines **ID11** and **ID27**. At ID11, we measured the pair distribution functions that were later used in our atomistic reconstruction procedure. At ID27, the sample was placed in a diamond anvil cell with varying pressures of up to 5.1 GPa in order to measure its bulk modulus. We have also used inelastic neutron scattering and neutron diffraction at Oak Ridge National Laboratory in the USA in order to have a complete set of structural and vibrational information about our samples.

Using a hybrid method that combines experimental structural constraints and Monte Carlo minimisation (the so-called Hybrid Reverse Monte Carlo method), we developed molecular models of kerogen with different maturities based on their chemical composition, texture and density (**Figure 134**). These atomistic models were then validated by comparing them to experimentally accessible kerogen properties, such as bulk moduli, vibrational densities of states, pore size distributions, etc. Once the models are validated, they can be used to study properties of kerogen that are otherwise difficult to access experimentally. For example, we showed that kerogen's maturation, which

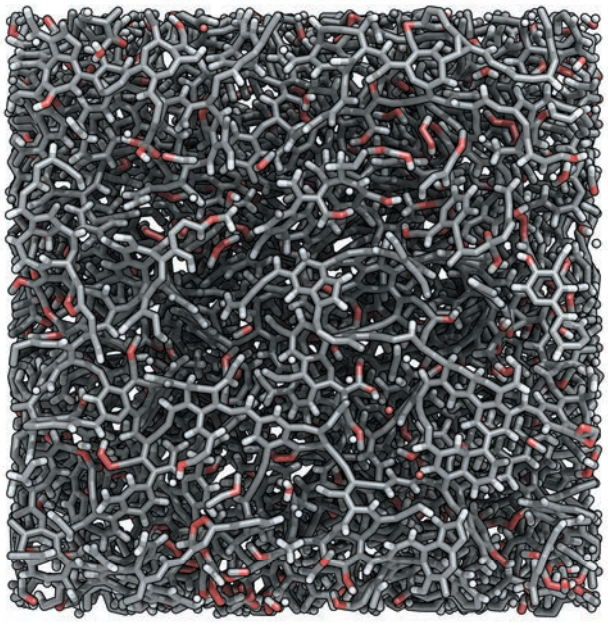

Fig. 134: Molecular model of a sample of the Marcellus kerogen studied (the organic phase constitutes the source of hydrocarbons in shale gas). Carbon, hydrogen and oxygen atoms are shown in grey, white and red respectively. The size of the image is 5 × 5 nm. Four samples with different maturities, that is, with different extents of thermal alteration in the subsurface, were considered. Copyright: C. Bousige (CNRS).

manifests itself as an increase in the sp^2/sp^3 hybridisation ratio, entails a crossover from plastic to brittle rupture mechanisms.

In brief, these molecular models are a fundamental building block that allows the adsorption, mechanical, and transport properties to be unravelled for this complex organic matter known as kerogen. These results can be used in up-scaling strategies such as lattice methods in order to bridge the gap in a "bottom-up" fashion between the atomic and the engineering scales.

PRINCIPAL PUBLICATION AND AUTHORS

Realistic molecular model of kerogen's nanostructure, C. Bousige (a,b), C. Matei Ghimbeu (c), C. Vix-Guterl (c), A.E. Pomerantz (d), A. Suleimenova (d), G. Vaughan (e), G. Garbarino (e), M. Feygenson (f), C. Wildgruber (f), F.-J. Ulm (a,b), R.J.-M. Pellenq (a,b,g) and B. Coasne (a), *Nature Materials* **15**, 576–582 (2016); doi: 10.1038/nmat4541.
(a) Department of Civil and Environmental Engineering, Massachusetts Institute of Technology, Cambridge (USA)
(b) <MSE>², UMI 3466 CNRS-MIT, Cambridge (USA)
(c) Institut de Science des Matériaux de Mulhouse (IS2M), UMR 7360 CNRS – UHA, Mulhouse (France)
(d) Schlumberger-Doll Research, Cambridge (USA)
(e) ESRF
(f) Oak Ridge National Laboratory (USA)
(g) CINaM, CNRS/Aix Marseille Université, Marseille (France)

STABILITY OF XENON OXIDES Xe_2O_5 AND Xe_3O_2 UNDER PRESSURE

Although the most inert atomic group of the periodic table, noble gases can become reactive under extreme conditions. Diamond-anvil-cell experiments and *ab initio* modelling have been used to investigate a possible direct reaction between xenon and oxygen at high pressure. Two oxides with unusual stoichiometries, Xe_2O_5 and Xe_3O_2, have been synthesised at pressures above 78 GPa, pressures that exist in the Earth's interior.

In geochemistry, models of the evolution of the deep Earth and atmosphere have relied on the chemical inertness of the noble gases. These models were built using measurements of the noble gas content in the Earth's atmosphere. However, the xenon content of the Earth's atmosphere is anomalously low in comparison with that of stony meteorites. One theory to explain this "missing xenon paradox" is that xenon could be stored in the deep Earth. A better understanding of the chemistry of xenon under pressures relevant to the Earth's interior (up to 3.6 million atmospheres at the centre) is needed to investigate this theory. As the binding of the valence electrons to the ionic core of a noble gas atom decreases with increasing atomic number, the heaviest noble gases (Kr, Xe) could be encouraged to form bonds using extreme conditions.

We therefore looked for possible chemical reactions under high pressure between xenon and oxygen, the most abundant element in the Earth's mantle. Mixtures of xenon and oxygen gases were loaded into diamond anvil cells, compressed to the million-atmosphere range and heated with an infrared laser to induce reactions. We observed a reaction above 78 GPa (0.78 million atmospheres), and the products have been characterised with microfocused X-ray diffraction and X-ray absorption at the xenon K-edge at beamlines **ID27** and **BM23**.

Figure 135 shows data collected on one of these products: X-ray absorption spectroscopy demonstrated the existence of an Xe-O bond, while X-ray diffraction allowed its crystal space

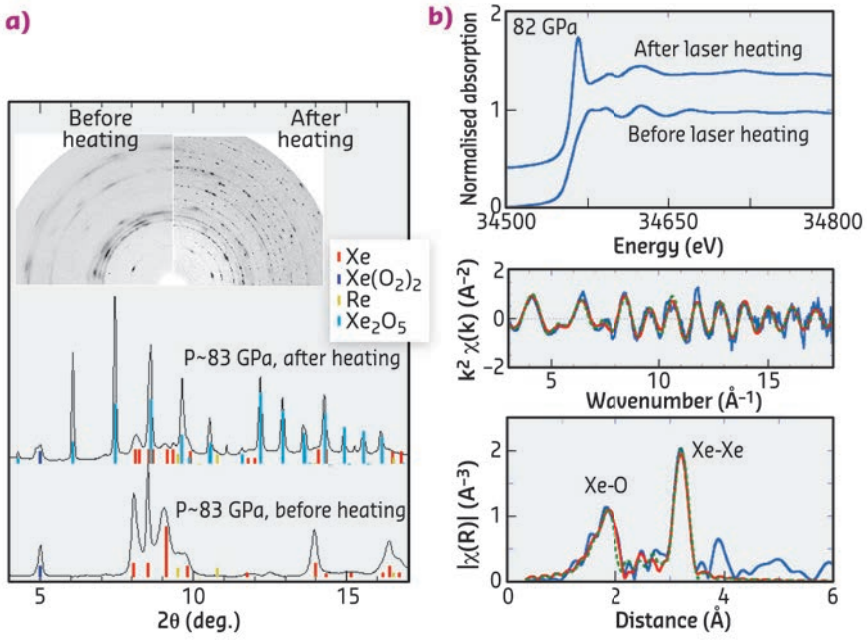

Fig. 135: X-ray diffraction and absorption patterns of ~35% Xe–65% O_2 mixtures at around 82 GPa, before and after laser-heating. a) Monochromatic X-ray diffraction: the insets show the two-dimensional patterns before circular integration. Prior to laser-heating, the phases were Xe and partially amorphised $Xe(O_2)_2$. After laser-heating, the pattern consists of mostly Xe_2O_5 (light blue ticks). b) X-ray absorption at the Xe K-edge. The EXAFS function $\chi(k)$ and its Fourier transform $\chi(R)$ have been calculated, which enabled the determination of Xe-O and Xe-Xe distances in Xe_2O_5.

group and lattice parameters to be determined. Experimental data were interpreted with the help of *ab initio* material modelling, which also predicted new compounds that would be stable under high pressure.

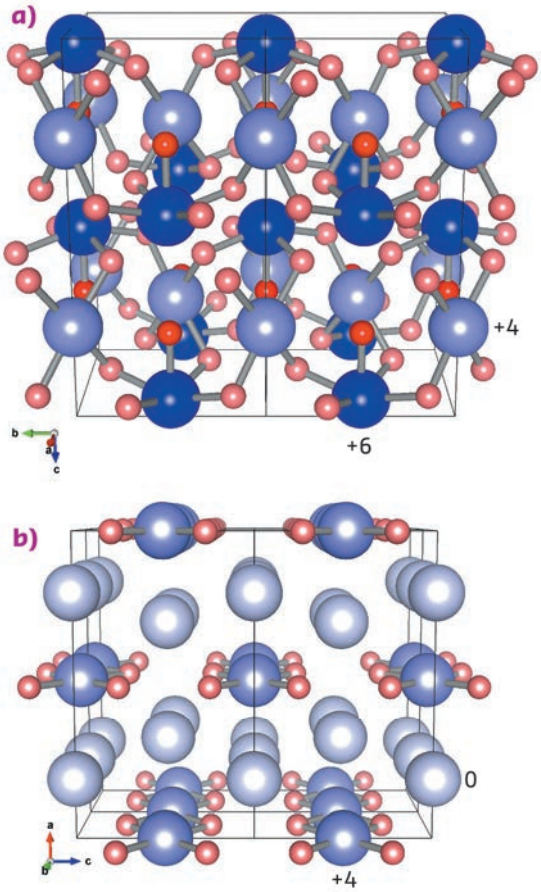

Fig. 136: Structures of the stable xenon oxides at 82 GPa. a) Xe_2O_5 and b) Xe_3O_2. Xenon atoms are shown in blue and oxygen atoms in red. The oxygen atoms have an oxidation state of –2, and the darker shade of red indicates an oxygen atom that bonds with only one xenon atom. The oxidation states of the xenon atoms are indicated by different shades of blue.

From different starting mixtures, two oxides, Xe_2O_5 and Xe_3O_2, have been synthesised and their structures, which were predicted to have the lowest enthalpies by *ab initio* modelling, are represented in **Figure 136**. Xenon atoms adopt mixed oxidation states of 0 and +4 in Xe_3O_2 and +4 and +6 in Xe_2O_5. Both oxides form extended networks incorporating oxygen-sharing XeO_4 squares, while Xe_2O_5 additionally incorporates oxygen-sharing XeO_5 pyramids.

The reactivity of xenon and oxygen is predicted to further increase with pressure, yielding new oxides such as XeO_2 and XeO_3. It is interesting to note that xenon atoms adopt mixed valence states in the oxides stable at the lowest pressure, *i.e.* compounds with unusual stoichiometries. This may be a general trend for compounds formed under high compression. Xenon is also predicted to react with other elements that are abundant in the earth, such as iron and nickel **[1]**; this remains to be confirmed experimentally. Although the laboratory syntheses of Xe_2O_5 and Xe_3O_2 don't directly solve the missing Xe problem — the element's scarcity makes it unlikely to form its own separate phase in the mantle — they demonstrate that this element is even more reactive under pressure than previously predicted.

PRINCIPAL PUBLICATION AND AUTHORS

Synthesis and stability of xenon oxides Xe_2O_5 and Xe_3O_2 under pressure, A. Dewaele (a), N. Worth (b), C.J. Pickard (c,d,e), R.J. Needs (b), S. Pascarelli (f), O. Mathon (f), M. Mezouar (f) and T. Irifune (g,h), *Nature Chem.* **8**, 784–790 (2016); doi: 10.1038/nchem.2528.

(a) CEA, Direction des applications militaires, Arpajon (France)
(b) Cavendish Laboratory, University of Cambridge (UK)
(c) Department of Physics and Astronomy, University College London (UK)
(d) Department of Materials Science & Metallurgy, University of Cambridge (UK)
(e) Advanced Institute for Materials Research, Tohoku University, Sendai (Japan)
(f) ESRF
(g) Ehime University, Matsuyama (Japan)
(h) Earth-Life Science Institute, Tokyo Institute of Technology (Japan)

REFERENCES

[1] L. Zhu *et al.*, *Nature Chem.* **6**, 644 (2014)

PROBING IRON DYNAMICALLY COMPRESSED TO 500 GPa AND 17000 K

We present data from a proof-of-principle experiment demonstrating that single pulse XAS synchrotron measurements enable the determination of structural and electronic properties of warm dense matter with accuracy close to that obtained for materials at ambient conditions. We show the first EXAFS data of Fe compressed to 500 GPa and heated to 17000 K. Our data indicate a persistent local order in the dense Fe fluid and stimulate further work to improve the electronic treatment of warm dense matter within the density functional theory.

Dynamic compression in the ns range obtained by direct laser ablation allows matter to be brought to very extreme states of pressure and temperature, well beyond the limit of static compression, to mimic the conditions of the interior of Earth and other planets. These are exotic states, like the warm dense matter (WDM) state, where conventional approximations used

in condensed matter or plasma physics break down.

We present here a first feasibility test performed at the ESRF to investigate the local and electronic structure of warm and dense iron by coupling a 35 J portable laser to the energy dispersive X-ray absorption beamline **ID24**. In the direct laser ablation technique **[1]**, a plasma is formed when the laser hits the target surface; a shock wave is created by the expansion and relaxation of the plasma and it propagates though the target causing it to reach very hot and dense states.

The sketch of the experimental configuration is presented in **Figure 137a**. The dispersive geometry of beamline ID24 allows the simultaneous collection of the whole XAS spectrum. Data were acquired using a single X-ray pulse of 100 ps duration, focused to 5 × 7 μm² at the sample position. Laser pulses of energy < 35 J and duration ~ 10 ns impinged on the target with an angle of 30° and focal spot of 300 μm. The target was made of a thin (3.5 μm) deposit of pure Fe sandwiched between two diamond windows, which act to confine the shocked state over a time interval much longer than the 100 ps X-ray pulse.

The evolution of the K-edge EXAFS spectra at different pressures is shown in **Figure 137b**; the transition from cubic (bcc) to shock induced hexagonal (hcp) structure is clearly observed in the modifications of the spectra. The data quality allows EXAFS quantitative analysis to be performed, providing an estimate of the thermodynamic conditions (volume and temperature) directly from the data, which is a remarkable advantage of this technique.

To reach more extreme conditions, the laser was focused to 90 μm. A new set of data was acquired (**Figure 138**, left panel): the compression and heating trend are revealed from the shift to higher energy and the broadening of the EXAFS oscillations respectively. As pressure increases, the bump in the edge starts to flatten, indicating the onset of melting. Remarkably, weak EXAFS oscillations remain as liquid Fe is further compressed and heated (500 GPa and 17000 K), indicating a persisting local order in the warm dense state.

Changes in the features of the absorption edge reflect the coupling between local order and the electronic state, which is an important issue for WDM modelling. The theoretical calculation for the absorption spectrum of liquid iron shown here (**Figure 138**, right panel) **[2]** is capable of grasping the main changes in the data (indicated with arrows). However, an important discrepancy is found in the energy shift of the absorption

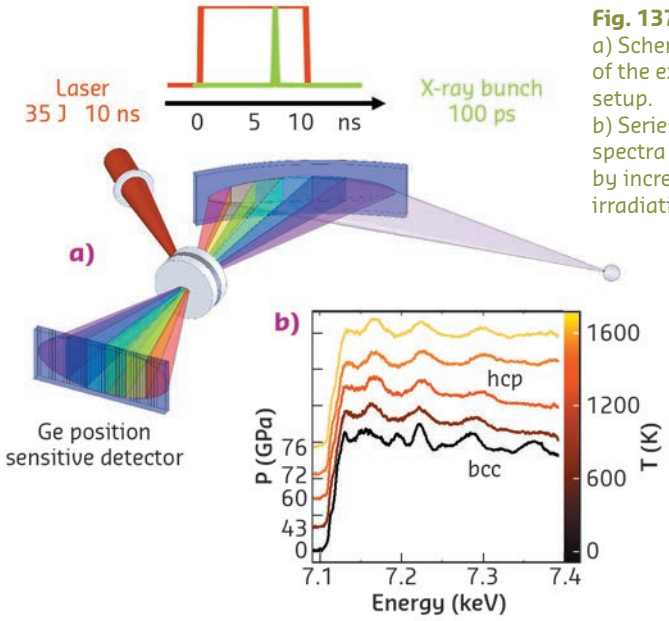

Fig. 137: a) Schematic view of the experimental setup. b) Series of EXAFS spectra obtained by increasing the irradiation intensity.

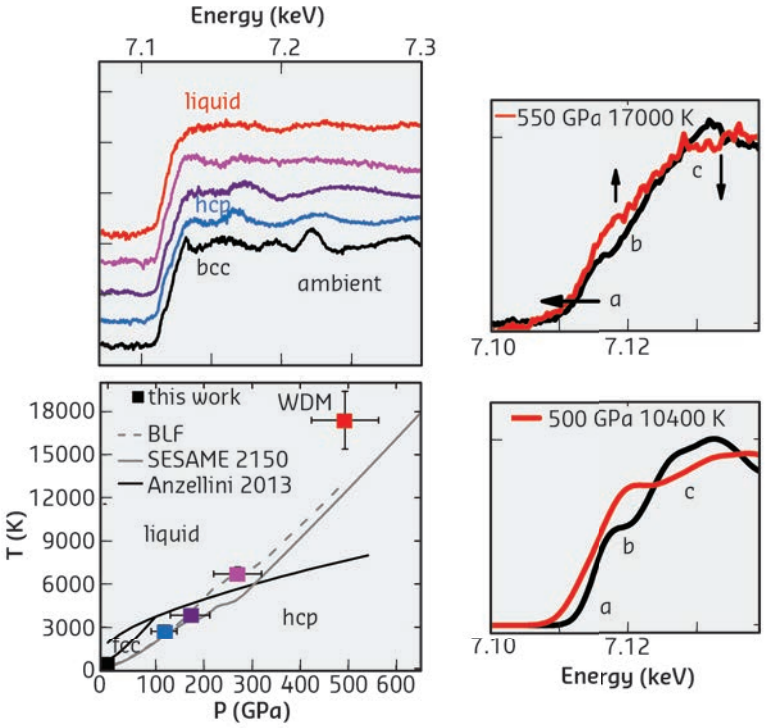

Fig. 138: Left top: a series of EXAFS spectra obtained in the highly-focused configuration of the laser. The P T conditions are indicated with the corresponding colours in the phase diagram (left bottom). Right: comparison between experimental and theoretical spectra of the K-edge of Fe.

onset (7.112 keV, feature *a*): the theoretical shift is ~ −2 eV, whereas the experimental shift is ~ −0.5 eV. This shift reflects the modification of the core energy level and of the electron density and, in the warm dense regime, it is particularly sensitive to changes in electronic shielding due to ionisation, and to continuum lowering depression. The XANES data therefore provide important constraints on the electronic treatment of WDM within the density functional theory (DFT) framework.

This approach could be extended to higher pressures and temperatures by using a more powerful (100–200 J) laser that would remain compatible with the beamline configuration.

PRINCIPAL PUBLICATION AND AUTHORS

Probing local and electronic structure in warm dense matter: single pulse synchrotron X-ray absorption spectroscopy on shocked Fe, R. Torchio (a,b), F. Occelli (a), O. Mathon (b), A. Sollier (a), E. Lescoute (a), L. Videau (a), T. Vinci (c), A. Benuzzi-Mounaix (c), J. Headspith (d), W. Helsby (d), S. Bland (e), D. Eakins (e), D. Chapman (e) , S. Pascarelli (b) and P. Loubeyre (a), *Scientific Reports* **6**, 26402 (2016); doi: 10.1038/srep26402.
(a) Commissariat à l'Énergie Atomique, Bruyères-le-Châtel (France)
(b) ESRF
(c) LULI, Ecole Polytechnique, CNRS, CEA, UPMC, Palaiseau (France)
(d) Science and Technology Facilities Council, Daresbury Laboratory, Sci-Tech Daresbury, Warrington (UK)
(e) Institute of Shock Physics, South Kensington Campus, London (UK)

REFERENCES

[1] S.N. Luo *et al.*, *Rev. Sci. Instrum.* **83**, 073903 (2012).
[2] M. Harmand *et al.*, *Rev B*. **92,** 024108 (2015).

MOTT GAP AND MAGNETIC INTERACTIONS IN NiO AT ULTRA-HIGH PRESSURE

Combined experimental and theoretical studies of NiO revealed the stability of its antiferromagnetic state up to 280 GPa and indicate the absence of a Mott transition to this pressure.

Many novel materials at the frontier of solid state physics are strongly correlated systems. They include high-Tc superconductors, Mott insulators, spintronic materials, ferroelectrics, and heavy fermion materials. In such materials, correlations between the more localised 3d or 4f electrons play a key role in determining the properties of the system.

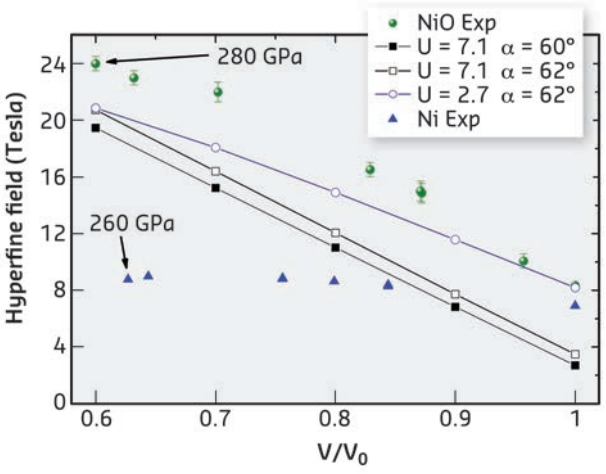

Fig. 139: Pressure dependence of the magnetic hyperfine field in NiO obtained by experiment and *ab initio* calculations (LSDA+U) within various approximations: filled olive circles - NiO by NFS, filled black squares by LSDA+U for U = 7.1 eV and α_R = 60°, black squares by LSDA+U for U = 7.1 eV and α = 62°; blue circles by LSDA+U for U = 2.7 eV and α = 62°. Filled blue triangles represent the dependence of the magnetic hyperfine field in Ni by NFS from **[5]**, given here for comparison. The lines are guides for the eye.

NiO is considered one of the most important compounds for the field of strongly correlated materials for two reasons. Firstly, it was treated as a prototype by Mott to explain the nature of the insulating state that came to bear his name. Secondly, it is chemically a compound with a rather simple crystal structure and d8 electron configuration (*i.e.* lacking high-spin - low-spin transitions, Jahn-Teller effects, etc.) making it well suited to the experimental validation of theoretical models. Additionally, the absence of a spin-state degree in NiO is an advantage of the material as a system for investigations of insulator-to-metal transition (IMT) due to Mott or charge transfer gap closure compared to MnO, FeO or CoO. Futhermore, nothing other than a decrease of interatomic distances will affect the balance between charge transfer and Mott-Hubbard gap. Thus NiO is the only case where we may definitely observe the pure Mott type IMT and therefore determine its exact mechanism and effects on magnetic ordering and magnetic moment. The pressure of the IMT has been studied theoretically, with results ranging between 230 GPa **[1]** and 3.7 TPa **[2]**. Due to the many difficulties to conduct experiments at such ultra-high pressure, which drastically limit the number of available methods for measurements, the amount of experimental work on the actual IMT in NiO is scarce. However, the long-sought IMT in NiO was recently reported to be found at 240 GPa by resistivity measurements **[3]**. In all known cases, an IMT in a Mott insulator has been associated with the loss of magnetic order, and this is expected to apply to NiO as well **[1]**.

Therefore, magnetic investigations are essential to understand the IMT in Mott insulators, as the disappearance of magnetic ordering is the only clear indication of the Mott type IMT.

We measured nuclear forward scattering (NFS) that was successfully applied to the Mössbauer transition of ^{61}Ni **[4,5]** at beamline **ID18**, to perform an investigation of the magnetic properties of NiO at room temperature up to 280 GPa (**Figure 139**). We found that the antiferromagnetic order is preserved in the system up to at least 280 GPa, the highest pressure at which magnetism has been observed so far in any material. We complemented our magnetic ordering investigation by X-ray diffraction at beamline **ID09A** (now **ID15B**) and APS beamline 13IDD to 220 GPa and extended X-ray absorption fine structure (EXAFS) at beamline **ID24** for structural investigations to 280 GPa. This is, to the best of our knowledge, the highest pressure at which an EXAFS spectrum has ever been collected. Neither technique indicates any change attributed to structural and/or electronic phase transitions up to the highest pressure achieved. These experimental observations are well reproduced by our *ab initio* calculations, which also yield a Mott insulator gap in the entire pressure range of this study. Our results thus indicate the absence of a Mott transition in NiO up to approximately 300 GPa. Thus additional experimental and theoretical investigations are necessary for this topic that everyone believed to be closed.

PRINCIPAL PUBLICATION AND AUTHORS

Magnetic interactions in NiO at ultrahigh pressure, V. Potapkin (a), L. Dubrovinsky (b), I. Sergueev (c), M. Ekholm (d), I. Kantor (e), D. Bessas (e), E. Bykova (b), V. Prakapenka (f), R.P. Hermann (a,g), R. Rüffer (e), V. Cerantola (b), H.J.M. Jönsson (h), W. Olovsson (h), S. Mankovsky (i), H. Ebert (i) and I.A. Abrikosov (d,j,k), *Physical Review B* **93**, 201110(R) (2016); doi: 10.1103/PhysRevB.93.201110.
(a) Jülich Centre for Neutron Science (JCNS) and Peter Grünberg Institut (PGI), JARA-FIT, Forschungszentrum Jülich GmbH, Jülich (Germany)
(b) Bayerisches Geoinstitut, Universität Bayreuth (Germany)
(c) Deutsches Elektronen-Synchrotron, Hamburg (Germany)
(d) Swedish e-Science Research Centre (SeRC), Department of Physics, Chemistry and Biology (IFM), Linköping University (Sweden)
(e) ESRF
(f) CARS, University of Chicago (USA)
(g) Materials Science and Technology Division, Oak Ridge National Laboratory (USA)
(h) Department of Physics, Chemistry and Biology (IFM), Linköping University (Sweden)
(i) Department of Chemistry, Ludwig-Maximilians-Universität München (Germany)
(j) Materials Modeling and Development Laboratory, National University of Science and Technology 'MISIS', Moscow (Russia)
(k) LACOMAS Laboratory, Tomsk State University (Russia)

REFERENCES

[1] R.E. Cohen, *Science* **275**, 654 (1997).
[2] X.-B. Feng and N.M. Harrison, *Phys. Rev. B* **69**, 035114 (2004).
[3] A.G. Gavriliuk *et al.*, *Phys. Rev. Lett.* **109**, 086402 (2012).
[4] I. Sergueev *et al.*, *Phys. Rev. Lett.* **99**, 097601 (2007).
[5] I. Sergueev *et al.*, *Phys. Rev. Lett.* **111**, 157601 (2013).

OBSERVATION OF SUPERCONDUCTIVITY IN H_2S BY NUCLEAR RESONANT SCATTERING

Synchrotron Mössbauer spectroscopy at the ESRF was used to prove the superconducting nature of a material created inside a high pressure cell. The shielding of the magnetic field by superconducting hydrogen sulfide at 150 GPa was monitored using ^{119}Sn as a sensor.

Recent resistivity and magnetic susceptibility measurements indicated that a superconducting transition occurs in H_2S compressed to 150-190 GPa with a high onset temperature of 203 K **[1]**. For an unambiguous identification of the superconducting state, a direct observation of the Meissner effect in an external magnetic field is desirable. However, the small size of the sample, contained within a diamond-anvil high-pressure cell (DAC), is the main problem for the study of the superconducting properties of samples at such high pressures.

We have developed a new method to follow the shielding of the magnetic flux by a superconducting sample at high pressure by employing nuclear resonance scattering (NRS) at beamline **ID18** **[2]**. A thin foil of tin enriched with the ^{119}Sn isotope to 95% is immersed in the superconductor sample and is used as the sensor of the external magnetic field. The sensor monitors the magnetic field via the magnetic interaction at the ^{119}Sn nucleus using NRS which ensures that we acquire data only from the ^{119}Sn sensor.

We used this method to determine the superconducting properties of hydrogen sulfide at 150 GPa. The experimental setup is shown in **Figure 140** for an external magnetic field applied perpendicular to the sample. When H_2S is not in the superconducting state, or the state has been partially destroyed, the magnetic field penetrates into the sample volume and the ^{119}Sn nuclear ground level spin $I_g = 1/2$ and exited level with spin $I_{ex} = 3/2$ are split by the magnetic field producing quantum beats in the time spectra (**Figure 140a**). In contrast, while H_2S is in the superconducting state, the magnetic field does not penetrate to the tin foil, the ^{119}Sn nuclear levels are not split, and the corresponding time spectra show an exponential decay (**Figure 140b**).

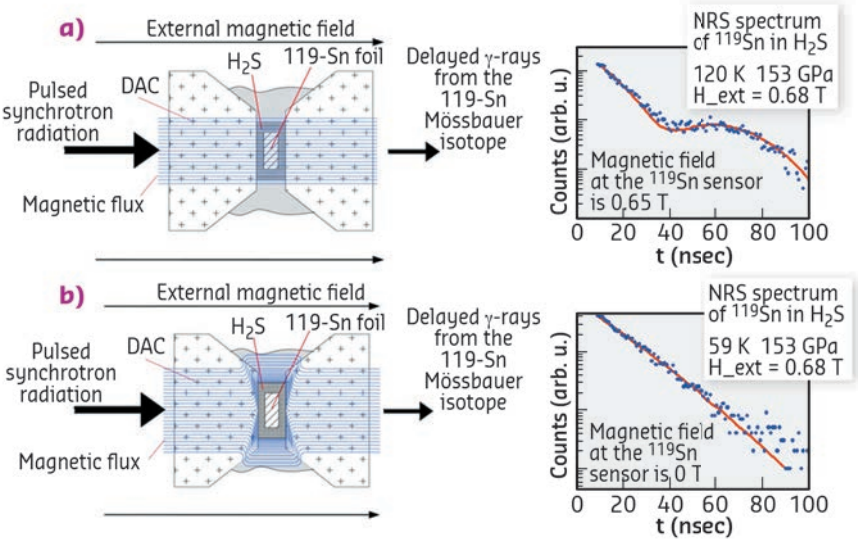

Fig. 140: Layout of the experiment. The tin foil, surrounded by compressed hydrogen sulfide, is located in a diamond anvil cell at a pressure of about 153 GPa. Pulsed synchrotron radiation excites the nuclei of the tin Mössbauer isotope ^{119}Sn. The detection system measures the time evolution of radiation emitted by the tin nuclei in the forward direction.

To verify that superconductivity occurs in the H_2S sample and not in the sensor ^{119}Sn foil, the measurements were conducted simultaneously with two DACs. One contained the H_2S sample and the ^{119}Sn sensor foil, and the other contained the reference ^{119}Sn foil loaded with hydrogen (H_2) as a pressure transmitting medium. The sample was cooled in zero magnetic field down to the lowest temperature of 5 K and a magnetic field of about 0.7 T was applied. The NRS spectra were then recorded at each temperature point while the temperature was increased.

Figures 141a and **b** show the results obtained with the external magnetic field of 0.68 T applied along the X-ray beam, *i.e.*, perpendicular to the sample plane. In the range of 4.7-59 K, the NRS spectra show an exponential decay,

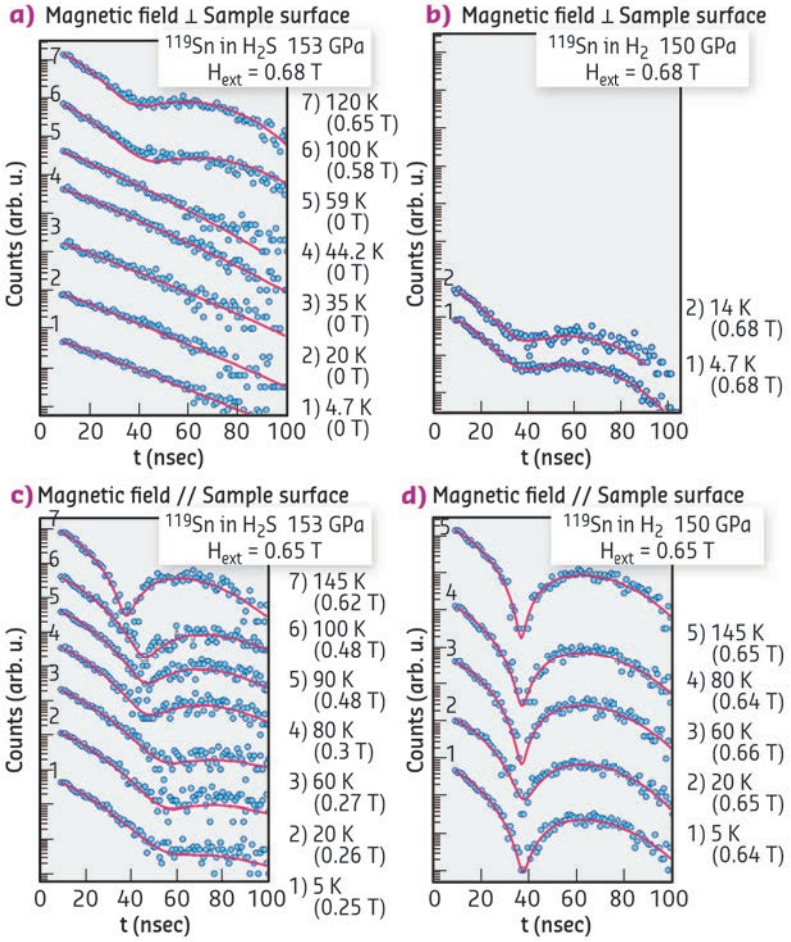

Fig. 141: Time NRS spectra from ^{119}Sn in H_2S at 153 GPa (left panels) and in H_2 at 150 GPa (right panels) in an external magnetic field in the horizontal (upper panels) and vertical (bottom panels) field geometry. Symbols (blue) are the experimental data and solid lines (red) are the fits by the MOTIF software. Temperatures of the samples and the values of magnetic fields at the ^{119}Sn nuclear site were obtained from the fits and are shown in parentheses next to the corresponding NRS spectra.

which demonstrates that the magnetic field is completely expelled from the sensor by the superconducting H_2S. At 100 K, quantum beats appear indicating that the external magnetic field starts penetrating into the sensor foil and it then increases gradually above 100 K. However, even for the data point at 120 K, the magnetic field at the sensor still does not reach the value of the external magnetic field (**Figure 141a**). This demonstrates that partial screening still remains up to at least 120 K. A similar trend was observed when an external magnetic field of 0.65 T was applied vertically, *i.e.*, parallel to the sample plane (**Figure 141c** and **d**).

These results demonstrate that the superconducting H_2S sample effectively shields the sensor from strong magnetic fields of about 0.7 T up to temperatures of 90-100 K. The proposed method should allow the range of pressure for the study of superconductivity to be expanded up to 300 GPa.

PRINCIPAL PUBLICATION AND AUTHORS

Observation of superconductivity in H_2S from nuclear resonant scattering, I. Troyan (a,b), A. Gavriliuk (b,c), R. Rüffer (d), A. Chumakov (d,e), A. Mironovich (c), I. Lyubutin (b), D. Perekalin (f), A.P. Drozdov (a) and M.I. Eremets (a), *Science* **351**, 1303-1306 (2016);
doi: 10.1126/science.aac8176.

(a) Max-Planck-Institut für Chemie, Mainz (Germany)
(b) Shubnikov Institute of Crystallography of Russian Academy of Sciences, Moscow (Russia)
(c) Institute for Nuclear Research, Troitsk (Russia)
(d) ESRF
(e) National Research Center "Kurchatov Institute", Moscow (Russia)
(f) A.N. Nesmeyanov Institute of Organoelement Compounds of Russian Academy of Sciences, Moscow (Russia)

REFERENCES

[1] A.P. Drozdov *et al.*, *Nature* **525**, 73–76 (2015).
[2] R. Rüffer and A.I. Chumakov, *Hyperfine interact*. **97-98**, 589 (1996).

ACKNOWLEDGEMENT

This work was done with support of The Russian Ministry of Education and Science.

Industrial research

Another year has gone by with industrial research becoming increasingly important at the ESRF. We have reached our goals in terms of commercial revenue (5% increase from 2015). Our clients continue to come to us for high quality data and solutions to their scientific challenges with new opportunities opening thanks to the Upgrade beamlines. The Structure of Materials and Structural Biology beamlines now both lead as the most sought-after areas of research of our commercial clients (**Figure 142**).

We have strengthened relations with companies with the aim of fostering longer term collaborations through different channels. Examples include the workshop on Synchrotron Applications in Pharma Innovation and Research, organised by AstraZeneca in autumn 2016 with ESRF and MAX IV (Sweden). Both the ESRF and MAX IV had the opportunity to highlight their complementary capabilities in pharmaceutical research. At AstraZeneca we heard first-hand what the research and innovation (R&I) challenges are for the coming years in pharma and biotech companies. Other examples of collaboration are a post-doctoral researcher position funded by OCAS, a research centre in Belgium that develops alloys and coatings, which was catalysed by a non-conventional imaging workshop for industry held at the ESRF, and the visit of a thesis student working for Jaguar-Land Rover over the summer to investigate automotive safety foams.

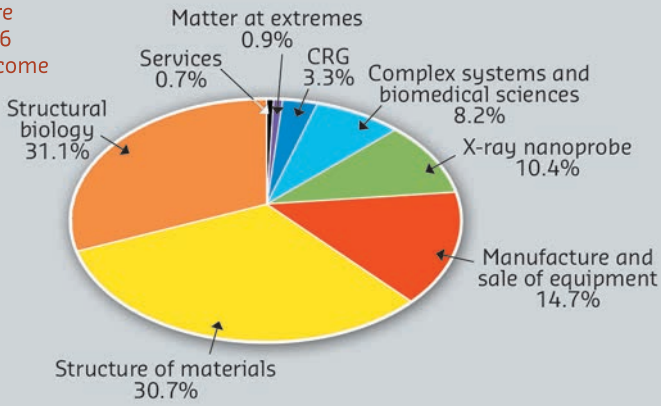

Fig. 142: Where the ESRF's 2016 commercial income was realised.

Fig. 143: The event "Re-Industrialisation of the EU", organised as part of the Slovakian EU Presidency, offered an opportunity to discuss how research and innovation can be pushed forward in Europe. The ESRF, as one of 9 partners in the "RI Village", jointly organised a session and a booth to highlight the role of research infrastructures in European innovation. The booth attracted a delegation of the European Commission.

Our networking is not exclusive to the Business Development Office (BDO) staff; the scientific and engineering staff at the ESRF are heavily involved in spreading the word and communicating to industry the opportunities that we offer. Their contribution to the industry programme is invaluable and we encourage more staff to keep industry in mind when they go to conferences or seminars. This intrinsic closeness with the beamline staff has led to a move of the Business Development Office from the Directorate to the Experiments Division at the start of 2017.

Growing sales

The ESRF has a rich vein of instrumentation design and know-how which is being increasingly developed as a commercial resource. Particular areas are where the know-how of the ESRF has translated into the creation of specialised production laboratories, where skilled professionals create material for modern synchrotron sources. Crystal analysers, newcomers in the sales portfolio at the ESRF, are now the "bestsellers" of the ESRF. They are followed closely by very high performance scintillators, which have been sold to many synchrotrons around the world.

Marketing and communication

In 2016, we carried out a survey amongst our clients with the aim of improving our communication towards them. A vast majority requested an industrial newsletter to be sent by e-mail, so, from early 2017, we are planning to start a monthly e-newsletter. We are already present on LinkedIn with an industrial showcase page (*www.linkedin.com/company/esrf-for-industry)*.

ESRF will also be present at a wide range of events during 2017, often in collaboration with other synchrotrons and research infrastructures (**Figure 143**). For this we are leveraging partnerships in H2020 and national projects: Nano-Science Foundries and Nano-Analysis (NFFA) and IRT Nanoelec.

Exciting times are ahead. The industrial activity is in good health and the future is looking bright, with new projects and new strategies to attract potential clients. So watch this space!

E. MITCHELL

HOW DO CRACKS APPEAR DURING SOLIDIFICATION WHILE WELDING STEEL?

Scientists from the University of Leicester (UK) and the company Tata Steel followed solidification cracking *in situ* at beamline ID19 during welding of steel.

Welding is the most effective way to join metals permanently; over 50% of global domestic and engineering products are estimated to contain welded joints. In welding, work-pieces are mixed with filler materials and melted, to form a pool of metal that upon solidification becomes a strong, permanent joint. Cracking may occur during solidification of the melt pool, and solidification cracking is an important issue in welding, casting and solidification-related additive manufacturing processes. A sustained deficiency in understanding the fundamental mechanism for damage has driven experimental efforts towards the observation of the phenomenon *in situ*. At beamline ID19, the team installed a novel strain-based deformation stage. The beamline has a small source size while the divergence and the length of 145 m allows macroscopically-large beam diameters at the position of the experimental hutch. Furthermore, the length of ID19 reduces the effective source size contribution to the images and therefore allows the coherence properties of the beam to be exploited by means of inline X-ray phase contrast.

Researchers observed the solidification cracking during welding of steel *in situ* using high-speed, high-energy radiography. Synchrotron X-ray micro-tomography was used to visualise and analyse the 3D crack network (**Figure 144**). Isolated micro-cavities are situated away from the bulk crack, in the region where damage initiation is observed during *in situ* radiography. Quantitative analysis of these isolated cavities reveals a size range between 10-27 µm with highly spherical morphologies. In some cases, the micro-cavities coalesce to form isolated micro-cracks, indicating that coalescence is the dominant mechanism for growth in the early stages of damage development.

Damage initiation is dependent upon strain rate. Higher strain rates induce cracking at a relatively higher volume fraction of liquid. The true strain required to initiate the damage in this thermodynamic state is higher than for low strain rate due to the increased presence of liquid in the semi-solid skeleton. The extra liquid maintains permeability within the semi-solid skeleton, allowing liquid metal to remain mobile and heal any deformation-induced cavity openings. As a result, the strain required for damage initiation increases.

The scientists also found that cracks grow by linking micro-porosities in the meshing zone in the solidifying weld pool.

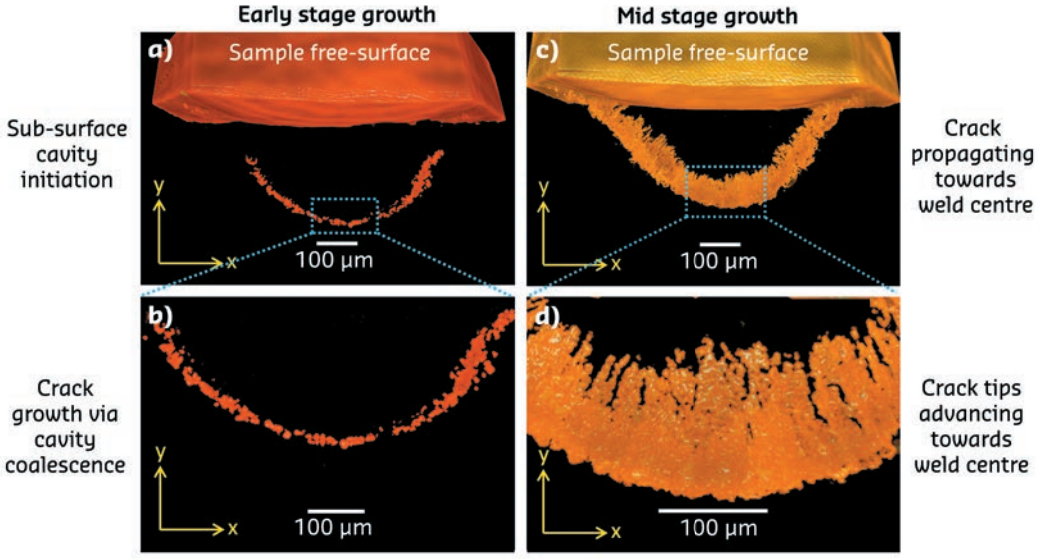

Fig. 144: Transverse cross-sectional tomography images showing the solidification crack growth path: a,b) early stage growth; c,d) mid stage growth.

PRINCIPAL PUBLICATION AND AUTHORS

Initiation and growth kinetics of solidification cracking during welding of steel, L. Aucott (a), D. Huang (b), H.B. Dong (a), S.W. Wen (a,c), J.A. Marsden (c), A. Rack (d) and A.C.F. Cocks (b), *Sci. Rep.* **7**, 40255 (2017); doi: 10.1038/srep40255.
(a) University of Leicester (UK)
(b) Oxford University (UK)
(c) Tata Steel, Research & Development, Rotherham (UK)
(d) ESRF

MODELLING ROCKS FOR THE OIL AND GAS INDUSTRY

iRock Technology Co., Ltd. Is a rock-core analysis company at the service of the oil and natural gas industry. Conventional CT scans are not enough to scan rocks, so scientists at iRock come to the ESRF beamlines to create 3D digital rock models.

Digital rock analysis is a pore-scale imaging and numerical modelling technology to extract nanometre to centimetre scale geological and petrophysical information, as well as multi-phase fluid-flow data based on pore-scale displacement processes from digitised rock samples.

A prerequisite for calculating representative rock properties are high-quality 3D multi-scale images of a rock sample that capture the representative elementary volume (centimetre-millimetre) and at the same time resolve the finest structures, such as the smallest pores (micrometre-nanometre scale). Computed tomography is currently the best-suited technique to acquire 3D images of rock samples over several decades of length scales.

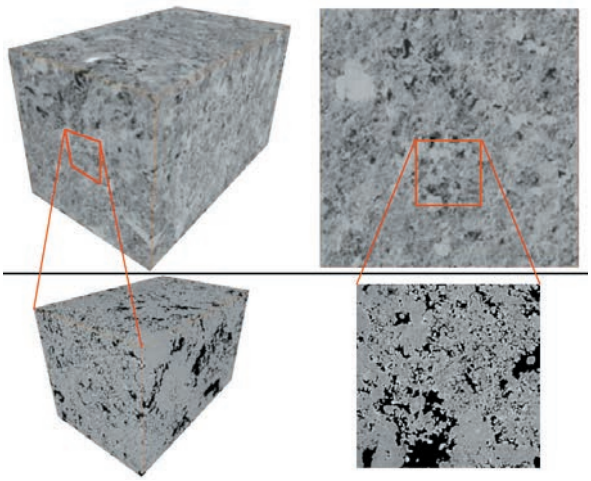

Fig. 145: Comparison of a carbonate rock imaged with conventional micro-CT (upper panel; 2mm side length, 1 micrometre voxel size) and synchrotron CT (lower panel; 0.5 mm side length, 280 nm voxel size). To the left are the 3D volumes, to the right are 2D slices. Black colour is pore space, light grey indicates solid grains and intermediate grey shades are unresolved voxels (partial volume effect).

However, CT imaging with benchtop micro-CT machines below 1-micron voxel size are of lower quality and are extremely time consuming (>1 day/sample); imaging below 0.5 microns/voxel is not possible in a reasonable time and with acceptable quality.

The crux is that more than 60% of the reservoirs worldwide consist of rocks with very small pore systems, which require imaging at voxel sizes (far) below 1 micrometre with ideal scanning resolutions between 100 and 300 nanometres/voxel.

IRock scientists came to beamline ID19 to scan rock samples with varying sample diameters at resolutions ranging from micro- to nano-scale. They obtained quick and high-quality imaging at flexible voxel sizes and a range of sample sizes, which is not achievable with laboratory CT machines. The acquired images provide a profound base to build representative 3D digital rock models and extract rock properties at a high confidence level (**Figure 145**).

In addition to the image quality, the higher sample throughput compared to laboratory devices helps iRock to plan and conduct projects for the oil and gas industry in a shorter time.

AMPK: A MULTIPROTEIN DRUG TARGET UNRAVELLED

The quest for drug development against several diseases has led CRELUX/WuXi AppTec, a company providing drug discovery solutions for global pharma, to analyse an AMPK (AMP-activated protein kinase) at the structural biology beamlines.

AMPK (AMP-activated protein kinase) is a Ser/Thr kinase composed of two regulatory subunits and a catalytic subunit that together as a complex regulates the levels of energy in the cells. This complex is evolutionarily conserved and ubiquitously expressed. There are a total of 12 possible isoforms, which are distributed in the human body in a tissue-specific manner. For example, one isoform is highly expressed in skeletal muscles and a different isoform is more

specific to heart, brain or liver. All in all, AMPK senses the energy levels of the cells (in the form of the so-called ATP) and allows upstream signals to activate it, in response to external nutritional stress. AMPK substrates are involved in lipid metabolism, autophagy, mitochondrial biogenesis, and in the maintenance of glucose homeostasis. Therefore, this complex is a highly promising therapeutic drug target against diabetes, obesity, Wolff-Parkinson-White Syndrome, cancer, and ageing.

There are, however, several challenges in the generation of soluble and stable complexes, and this is one of the many reasons why few X-ray structures are available, especially at resolutions suitable to drive drug discovery efforts. Firstly, it is very complicated to be able to make crystals of the complex with the activated compound bound to it. Another obstacle is the extreme sensitivity of the tiny crystals to radiation damage.

Scientists from CRELUX/ WuXi AppTec, a company that is a worldwide expert in premium drug discovery solutions for global pharma, biotech and research organisations, sent crystallised AMPK samples to beamline ID30-A. Because of the complexity of the project, they needed a powerful beamline, a state-of-the-art detector and a skilled scientist in-house to carry out the experiment. They managed to solve the structure of the complex at a resolution of 2.9 angstroms (**Figure 146**), which was enough for CRELUX/ WuXi AppTec to see the detailed chemical environment of the compound in the complex binding site. This corresponds to one of the highest resolution structures published so far for any AMPK isoform.

The work at the ESRF will help CRELUX to support their clients in the discovery and development of novel and more specific drugs that can influence AMPK activity in the cell and, as a result, adjust the energy balance in disease affected organs. Debora Konz Makino, Lab Head at CRELUX/ WuXi AppTec, explains: "Our long-standing collaboration with the ESRF has greatly contributed to the success of most of our clients' projects in the early stages of drug discovery. The ESRF provides not only cutting edge infrastructure, but also excellent scientific support for X-ray data collection of biological macromolecules. We at CRELUX highly appreciate the ESRF's prompt and open communication."

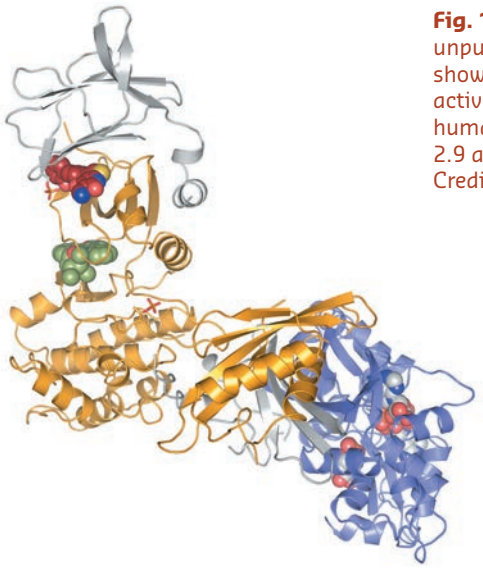

Fig. 146: The unpublished structure shows an allosteric activator bound to a human AMPK isoform at 2.9 angstrom resolution. Credits: CRELUX.

LICENSING

Licensing products owned by the ESRF is one of the activities of the Business Development Office. In 2016, the BDO licensed two sets of equipment, both of them to IRELEC, a French company.

The first one was a micro-furnace for experiments on beamlines at synchrotron sources. This furnace enables scientists to conduct *in situ* experiments at up to temperatures of 1300 K. Being compact and lightweight, it is easy to install on many beamlines for experiments such as tomography, X-ray scattering (reflection, transmission) or diffraction in fluorescence mode. Already widely used at the ESRF, the furnace allows complex setups, such as those with gas flow, and it is easily adaptable to any existing beamline design.

The other licensed equipment is an 8-axis attenuator system. Raphaël Richaud, business development manager of IRELEC, explains the interest for this device: "It is a good way for IRELEC to enrich its offer for synchrotrons and we liked its design: compact and easy adaptable to any existing beamline and UHV compliant. It has already proven efficient and reliable, so we were confident in its technical quality".

On the longstanding collaboration between the ESRF and IRELEC, he added that "the ESRF is a source of an enormous amount of engineering expertise and designs and it has been very important for the development of our business". Focused on precision and reliability, IRELEC provides research and development facilities with custom positioning systems and smart robotic cells.

Enabling technologies

The 2016 highlight contributions provide a representative slice through the diverse R&D activities, and testify to the balance between accelerator and experimental station based developments. The articles on the longitudinal gradient dipole magnets and the RF fingers are only two out of many examples where novel designs and cutting-edge engineering were applied to meet the stringent requirements of the new EBS machine. The third contribution underlines the importance of starting software-related activities as early as possible to ensure that the EBS storage ring can be reliably controlled and tuned from day one of operation. The fourth article is dedicated to a new facility, the Crystal Analyser Laboratory, which has been operational for more than a year, and has produced so far about 200 crystal analysers for experimental stations at the ESRF and other research centres. The cryogenically-cooled Laue-Laue monochromator, installed on ID15 and ID31, has been selected as an example of state-of-the-art beamline instrumentation. Serial crystallography, initially developed at free-electron laser facilities, has found its place now as well at storage-ring based X-ray sources, and the article by U. Zander *et al.* presents a genetic algorithm to analyse serial crystallographic data. The last two contributions relate to ancillary characterisation tools and advanced sample environments. The study on direct atomic force microscopy imaging of liquid interfaces opens a new way to investigate liquid-liquid interfaces which can be applied to any kind of molecule or object capable of assembling at liquid interfaces with high coverage once the system is at equilibrium. The new compact and versatile ESRF helium flow cryostat offers efficient cooling down to 3 Kelvin, operation in any orientation, and a quick sample change.

In addition to the results presented in the Highlights articles, 2016 has witnessed many other important accomplishments and activities in various technological areas:

The development of silx (http://www.silx.org/), the Sclentific Library for eXperimentalists, is in full swing, and version 0.3.0 has been released. The project provides a collection of Python packages to support the development of data assessment, reduction and analysis applications at synchrotron radiation facilities.

The systematic recording of metadata is under test at ID01, ID11, ID31, and the MX beamlines. The implementation of archiving metadata and raw data is progressing at a rate of about ten beamlines per year, as part of the plans to have the ESRF data policy fully operational by 2020.

Within the detector development programme, first strategic collaborations have been established with the Paul Scherrer Institute and Tomsk State University. Other joint R&D activities such as the development of ultra-fast data acquisition schemes and X-ray wavefront characterisation via X-ray speckle tracking (H2020 project EUCALL) and characterisation of diamond single crystals (H2020 project Green Diamond) are other important elements of our R&D programme.

The ESRF continues to federate and coordinate joint developments with other research facilities such as the IcePAP, TANGO, LImA, ISPyB, mxCuBE and PaNDaaS collaborations. The TANGO collaboration has welcomed four new members in the last few months and will have a total of twelve partners in 2017, thus providing sufficient critical mass to initiate software developments of common interest to all partners.

Significant progress has been made in testing cloud software for in-house and external IT provisioning. The acquired know-how will help in possible scenarios to outsource peak processing demands which cannot be covered by on-site investments. Developments will continue within the CERN led H2020 HNSciCloud project, a Pre-Commercial-Procurement (PCP) initiative engaging IT industry and major European Research Infrastructures.

The instrumentation beamline, **BM05**, continued to be a strategic tool for instrumentation development such as the characterisation of detectors, scintillators, and X-ray optical components. The diffractometer for the new IRT NanoElec station for X-ray diffraction, reflectivity, and topography, is now fully commissioned, and its operation started in spring 2016. This station opens up new and very promising perspectives that aim to provide new services for proprietary research, especially for customers from the semiconductor industry.

The past twelve months have allowed tremendous progress to be made in the design and procurement of the EBS storage ring components. The EBS project will remain the main focus of the technical staff in the year to come to ensure that all contracts progress

according to schedule, that the remaining contracts are placed in a timely manner and all preparatory on site work is executed on time, within budget and fit for purpose, such that the 18-month construction shutdown can start as planned at the end of 2018. An important milestone for this will be the availability of the ESRF01 and ESRF02 buildings, in October and June 2017 respectively, to allow the assembly process for the 128 girders to be started.

M. KRISCH
and **R. DIMPER**

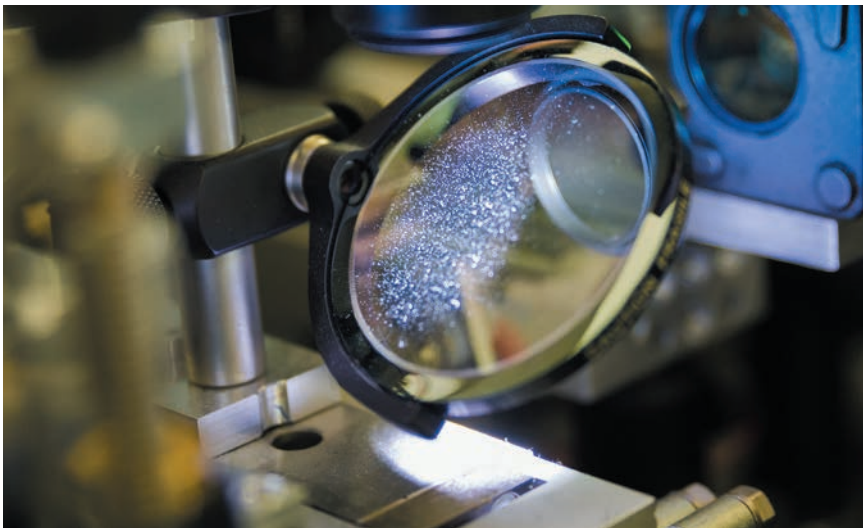

LONGITUDINAL GRADIENT DIPOLE MAGNETS FOR THE ESRF-EBS STORAGE RING

The new magnet lattice of the ESRF-EBS will need an ensemble of 128 dipoles with longitudinal gradient. Due to the specificity of their magnetic field, these dipoles will be built with high performance permanent magnets. Their assembly and magnetic characterisation will take place at the ESRF.

The electron beam of the ESRF-EBS storage ring will have a horizontal emittance 30 times smaller than the existing storage ring. This major step forward requires new magnet designs. Besides the development of high gradient quadrupoles and sextupoles, the design of the bending magnets needed to evolve considerably from the conventional dipole structure due to the specific geometrical distribution required for the magnetic field. Consequently, the new lattice will comprise new types of combined-function bending magnets: 96 combined dipole-quadrupole bending magnets and 128 dipoles with longitudinal field gradient. The dipoles will be based on high performance permanent magnets. They will be assembled and magnetically characterised/tuned at the ESRF.

The magnet field of the dipole magnets varies along the electron beam path, from 0.65 T to 0.17 T over a distance of 1.784 m. The concept of a continuous field variation was found impractical due to the resulting magnetic complexity and also for economic reasons. The best approach was to segment a dipole into several almost independent modules with different fields. In practice, each dipole is segmented into 5 modules of about 0.35 m each. From initial studies in 2012-2013, permanent magnets appeared to be the best solution for such magnetic structures because of their compactness, adaptation to segmentation and ease of installation (no need for electrical power). In addition, the ESRF has long-standing experience with permanent magnets through the development of insertion-devices. We predict that the use of permanent magnets in accelerators will grow significantly in the near future due to the demand for high performance and compact magnets **[1]**.

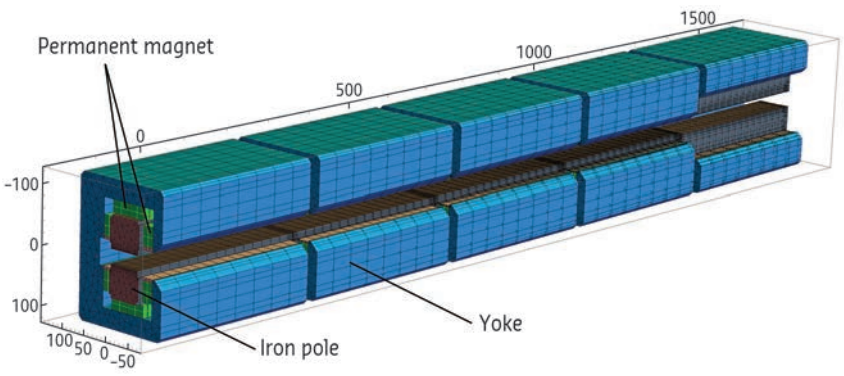

Fig. 147: 3D magnetic model of a dipole magnet.

Figure 147 shows the 3D magnetic design of a dipole with 5 modules with a pole to pole separation of 4 mm. Magnet blocks of type Sm_2C0_{17} are sandwiched between an iron pole and a low carbon steel C-shape yoke. The successive modules have a different number of magnet blocks to achieve a step-like field variation along the structure. The high field module (0.65 T) on the left is entirely filled with 36 magnet blocks while the low field module (0.17 T) on the right has only 8 magnet blocks. The low field module has a modified yoke to allow the integration of dedicated vacuum components. In total about 100 magnet blocks are needed for one complete dipole. For all 128 dipoles, it will be necessary to build 12800 magnet blocks, corresponding to 6 tons of Sm_2C0_{17}. This material was found the most suitable in order to achieve a low dependence upon temperature and an excellent long-term stability against radiation-induced demagnetisation. The temperature stability of the magnets is further improved with the use of flux shunts made of a special iron-nickel alloy with a Curie temperature of 60°C.

The engineering design of the dipoles required substantial efforts in many aspects of the project. This included the procurement and control of the high quality iron needed to reach the field quality, the selection and follow up of subcontractors for the precise machining of the iron blocks and the delivery of assembled empty modules (without permanent magnet blocks). Special assembly benches have been developed to mount the permanent magnet blocks in the modules. **Figure 148** shows the assembly of the 5 modules of a dipole. The modules are mounted on a base plate along a curved path corresponding to the electron beam trajectory in the magnet; the angular defection induced by a dipole is about 30 mrad. An important task was to control the magnetic forces between the modules during their assembly. Several important technological developments were needed to prepare and set up the construction of the dipole series.

The assembly and magnetic characterisation of the 128 dipoles will be carried out over a period

of one year. All the modules (640 units) will be carefully measured with an accurate magnetic measurement system developed specifically for the ESRF-EBS magnets. The magnetic field of each module will need to be accurately tuned to the design value using thin iron flux shunts. The construction of two complete dipoles was started in mid-November. The first magnetic measurements show very good agreement with simulations and we are optimistic for the remaining steps in the development of these magnets.

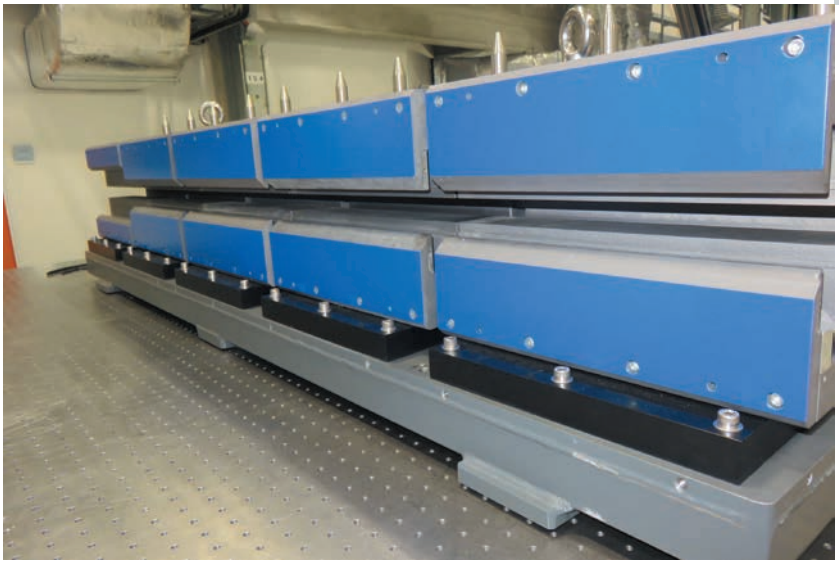

Fig. 148: Dipole modules assembled on a base plate.

AUTHORS

C. Benabderrahmane, J.Chavanne, G. Le Bec, L. Eybert, C.Penel, D. Gibson and F. Villar.
ESRF

REFERENCES

[1] J. Chavanne and G.Le Bec, *IPAC* **14**, Dresden Germany (2014).

RF FINGERS FOR THE ESRF-EBS STORAGE RING

The ESRF-EBS storage ring features new vacuum chamber profiles with reduced aperture. Radio frequency (RF) fingers are a key component to ensure good vacuum conditions and reach the best possible machine performance. A more compact, more robust and more reliable design has been produced for the new storage ring.

To absorb chamber-to-chamber misalignment and thermal expansion, for instance during bake-out, bellows are used to inter-connect a large number of chambers along the ring circumference. These bellows, however, are seen as resonant cavities by the beam hence breaking the geometrical continuity of the beam pipe and leading to degraded vacuum and stability. The continuity is restored by electrically shielding the bellows from the beam using so-called RF fingers which consist of conductors matching the vacuum chamber profile and connecting the beam pipes on either side of the bellows. The RF fingers are meant to absorb mechanical movements while providing the best possible electrical and geometrical continuity: designing such a device is therefore far from trivial since many aspects have to be carefully optimised.

The new omega-shaped chamber profile is incompatible with the present RF finger design if geometrical continuity is to be enforced. Therefore, a dedicated in-house design based on new concepts was devised for the ESRF-EBS ring. **Figure 149** shows the final design, which is the result of several iterations to optimise its beam coupling impedance and mechanical properties.

The first step was to ensure that the cavity formed by the bellows was properly shielded from the beam. This was achieved by adding four blades (two top and two bottom) on either side of the initial design, thus extending the horizontal dimensions of the RF fingers as seen in **Figure 150.** If the bellows are invisible to the beam then the beam coupling impedance is given

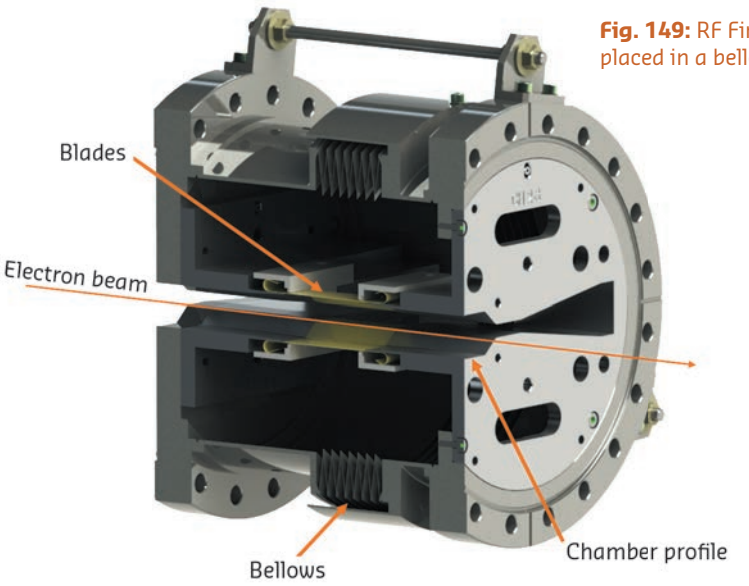

Fig. 149: RF Finger placed in a bellows.

only by the geometrical discontinuities of the inner volume. In this case, it is the steps and taper angle at the entrance and exit of the RF fingers, which can be seen in **Figure 150.** The step height was fixed at 0.3 mm for mechanical criteria and the only parameter left for optimisation was the taper angle, a good compromise was found with a reduction of the taper angle from 5° to 2° leading to a reduction of the beam coupling impedance by a factor 4. This result was found satisfactory as the resulting full contribution of the RF fingers to the total impedance of the machine became significantly smaller than the contribution of beam pipes themselves.

The shielding blades (the RF fingers) are made with copper-beryllium (*CuBe2)* and the flange parts with an aluminum alloy. Copper-beryllium is a high resistance, highly conductive alloy, ideal for the RF finger's function, whereas an aluminium alloy is easier to machine to achieve the desired complex shape of the flange part.

A thorough structural mechanical finite element analysis (FEA) was performed to validate the new RF finger design with respect to mechanical stress and the necessary electrical contact. At the same time, the FEA served to study the design optimisation possibilities considering the specific component requirements. A parameter study of three key geometrical dimensions was carried out to gain knowledge about their influence on the performance and mechanical safety. One of the parameters that varied in the course of this analysis was the blade thickness of the fingers.

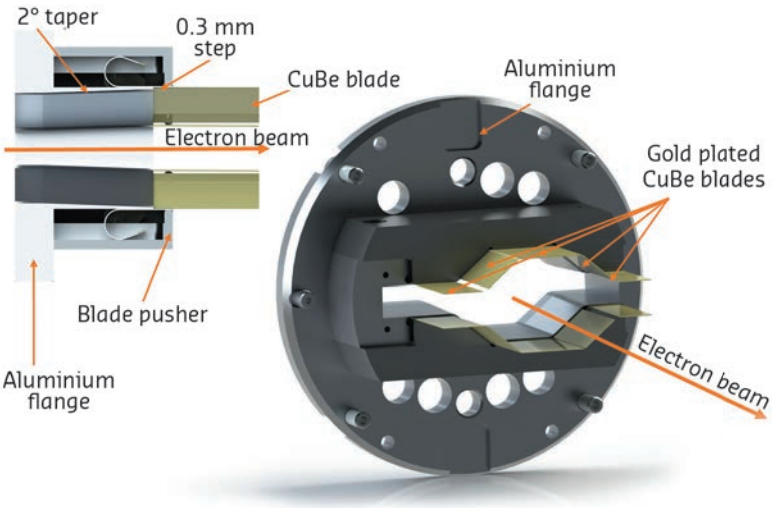

Fig. 150: RF Finger cut view.

In the structural analysis, the new component concept generally showed good compliance for the defined requirements as the electric contact quality is very high. The latter mainly depends on the contact force which is comparably high for all parameter variations and of at least 1.5 N per blade. This contact should be sufficient as the image current on the surrounding walls is most likely a surface current. In all load cases and movements, the blades are in good contact at the relevant contact position.

The required flexibility can be safely guaranteed. We considered different blade thicknesses. While thinner blades tend to be more flexible, their contact force drops but the safety margin of occurring mechanical stress is higher. The use of thinner blades that lead to a lower contact force could be a solution to reduce friction-caused wear while maintaining a very good electric contact. The safety factor between mechanical stress and the elastic limit is at least 1.2 for the analysed parameter variations during a relative flange movement of 2 mm between both flanges; this was considered as sufficiently flexible. Small plastic deformations in the flange part turned out to be tolerable and the component's functionality can also be maintained.

The new design, patented, will be used on all chamber profiles, high, low and straight section profiles. For the RF performance, a test in the current machine is foreseen in March 2017.

AUTHORS

T. Brochard, P. Brumund, L. Goirand, J. Pasquaud and S. White.
ESRF

SIMULATING THE CONTROL SYSTEM OF THE EBS

A simulator has been built to aid in the programming and testing of the future EBS accelerator complex and to perform beam dynamics studies. Already this system is proving useful for the visualisation of feedback from various components of the system.

The control system is an essential component of a particle accelerator complex such as the ESRF-EBS. A new control system has to be ready and working from day one even though most of the equipment will only be assembled and installed during the long shutdown in 2019. To facilitate the construction of the control system, a virtual ESRF-EBS has to be built before it is physically

available. This is the purpose of the ESRF-EBS simulator, which will aid our development of graphical user interface (GUI) applications required to control the ESRF-EBS. It will also help us to prepare all components of the interface for day 1 to manage the large number of devices (power supplies, beam position monitors, etc.) of the EBS. Simulating the ESRF-EBS will help us to decide on device hierarchies and to develop the interfaces that permit the machine physicists to control the equipment.

The simulator is split into two parts: the physics simulation, and the Tango devices (Tango is an open source controls toolkit that originated from the ESRF). The physics simulation is done by the Accelerator Toolbox, which is an open source Matlab layer originating from SLAC and now developed by the ESRF. Its role is the computation of the beam propagation around the ring including the computation of its main parameters including the beam positions, tunes and chromaticities. Within Accelerator Toolbox, it is possible to change the values of a huge number of parameters. Within the control system simulator, only the parameters corresponding to modifiable physical values in the real machine (like power supply current) are handled and made available via a set of Tango devices. The Tango devices have a user interface as close as possible to the real hardware interface. However, instead of sending their requests to any kind of hardware, they change the corresponding parameters in the Accelerator Toolbox definition of the EBS ring.

The simulator could be seen as an infinite loop with three actions which are: first updating the definition of the EBS ring in the Matlab Accelerator Toolbox according to the Tango device servers controlling the machine equipment, then computing the new ring optics, and finally distributing the new beam properties to Tango devices simulating beam diagnostics equipment. A dedicated Tango control system has been set up to handle this simulator. Today, around 2300 devices have been declared. Following the requirements of the accelerator physicists, the simulator has enabled the definition of a new way to control the numerous EBS power supplies. Even if control by current will obviously still be possible, a control by "strength" has been added.

In terms of beam dynamics studies, the simulator is extremely useful for studying the beam behaviour in various conditions and also for preparing and testing the software tools necessary for the commissioning of the new ring. Though the response time of the simulator

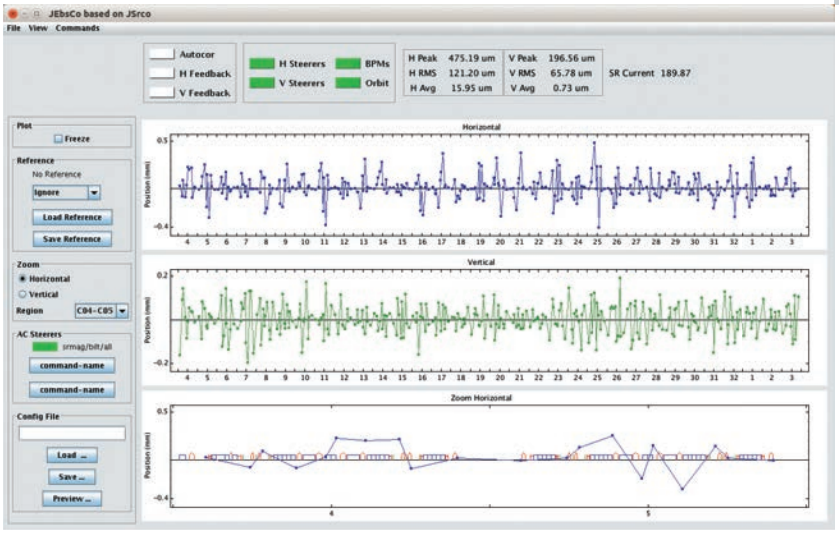

Fig. 151: Prototype graphical application for the EBS beam orbit.

is much longer than the response of a real machine, it is short enough to be transparent for human perception or for most automated tuning sequences. Work has now started on tools like beam steering along the first turn in the ring, orbit response matrix measurements, optics correction for the modulation of beta-functions or horizontal/vertical coupling, sextupole tuning, etc. The tools developed from now on will run without any modification on the real control system when it is available. Until then, the accelerator model will be improved with any newly available information (for example, magnet calibration), and the interface to the device servers may be updated when needed. In the longer term, the simulator can be kept running in parallel with the real machine, since if the measurable beam parameters are validated with measured values, it can give access to many other parameters which cannot be measured.

As an example, the simulator enabled us to develop the software loop controlling the slow orbit correction, using 320 beam position monitors and 288 steering magnets. It is already running today, three years before its production debut. Thanks to the simulator, it was even possible to develop a prototype of the graphical application which will be used in the control room to display the EBS beam orbit and to control the slow orbit correction loop (see **Figure 151**).

To conclude, even if the simulator is not yet complete (for instance, all vacuum related equipment is still missing), it has already proven to be a very fruitful tool in enabling us to work on the different aspects of the EBS control system before the first magnet is connected to any power supply.

AUTHORS

E. Taurel and L. Farvacque.
ESRF

CRYSTAL ANALYSER LABORATORY

The increasing application of hard X-ray emission spectroscopy techniques has led to a significant increase in demand for the critical optical components that permit high resolution energy discrimination of the X-ray emission signal from the sample. The ESRF has invested in a new laboratory dedicated to the development and production of these optics.

Bent analysers are optical devices for X-rays consisting of a thin single-crystal wafer bonded onto a shaped (often spherically concave) glass surface. The adhesion is normally performed with epoxy glue or by anodic bonding and the wafers are principally made from Si or Ge. Through a combination of Bragg diffraction and focusing, these analyser crystals permit a very precise measurement of X-ray energies for spectroscopic applications such as X-ray Raman spectroscopy (XRS), resonant inelastic X-ray scattering (RIXS), inelastic X-ray scattering (IXS) and emission spectroscopy (ES). There are currently six beamlines at the ESRF using spectroscopic techniques requiring the use of such crystal analysers and others are in the design phase. Most of them operate spectrometers requiring multiple analyser crystals to ensure a maximum collection solid angle. The biggest, at the ID20 beamline, has 72 spherical Si(nn0) analysers installed with curvature radius of 1 m **[1]**.

Fig. 152: View of the CAL "clean room" with main processing tools. 1) Laminar flow hoods; 2) 3-axis-robot with glue dispenser; 3) Micro-interferometer; 4) Semi-automatic anodic bonding machine; 5) Grinding machine; 6) Spin coater; 7) wafer dicing saw; 8) wafer mounting machine.

The ESRF has been manufacturing spherical analyser crystals for many years **[2]**. In response to the increasing internal demand for analyser crystals for multi-analyser spectrometers, the ESRF recently built a dedicated facility for the fabrication of spherical (cylindrical) analyser crystals. The Crystal Analyser Laboratory (CAL) has been in operation since February 2015 and covers an area of roughly 120 m^2 including a "clean room" of 60 m^2 where the main processing tools are installed (**Figure 152**). The laboratory is equipped with a combination of commercial instruments (wafer grinder, wafer dicing saw) as well as in-house designed fabrication and characterisation systems (for anodic bonding, glue dispersion and inspection). In addition, the laboratory is able to draw upon the expertise and instruments of other laboratories at the ESRF, notably the Crystal Polishing and Optical Metrology laboratories. Moreover the proximity to the beamlines allows rapid performance testing of new processing technologies prior to routine production.

The CAL manufactures essentially three types of analyser crystals, with the different types satisfying the various experimental conditions required by our scientists in terms of energy resolution, intensity and collected solid angle. The typical diameter of the spherical glass substrate is 100 mm and the curvature radius varies from 0.5 m to 7 m. Most of the analyser crystals use Si wafers but there is an increasing demand for Ge and other single-crystal materials (*e.g.* quartz, lithium niobate).

The three most common types of analyser crystals which are produced are shown in **Figure 153**:

***a)* Bent analyser:** Thin wafer (~200 µm) bonded to a spherical concave glass substrate by anodic bonding. Such analysers are used for applications requiring moderate energy resolution (0.4 to 1 eV).

b) Bent-diced analyser: Consists of a bent analyser with cuts providing stress relief. This improves both the energy resolution (< 0.3 eV) and the performance uniformity over the surface of the crystal.
c) Diced analyser: Thousands of Si crystal cubes glued onto a spherical concave glass substrate. All the cubes are well aligned and behave as a perfect flat crystal (stress-free). The typical cube size is ~ 0.9 mm x 0.9 mm x 2.7 mm. This analyser is used for spectroscopic studies requiring very high energy resolutions (of the order of meV).

Since the beginning of operation, the laboratory has produced around 200 analysers of the different types for both ESRF beamlines and other laboratories worldwide. Future activity will reinforce the analyser development and concentrate upon developing techniques to extend the range of materials that can be produced (germanium, quartz, lithium niobate) as well as investigating alternative analyser geometries (van Hamos, Johansson).

Through its capacity to produce high quality analyser crystals efficiently, the new CAL laboratory is a key element towards ensuring the continuing high performance of emission spectroscopy beamlines at the ESRF. The laboratory also provides the essential infrastructure necessary for the long-term development of diverse analyser crystal geometries and systems. Further investment into production capacity is planned in the coming months.

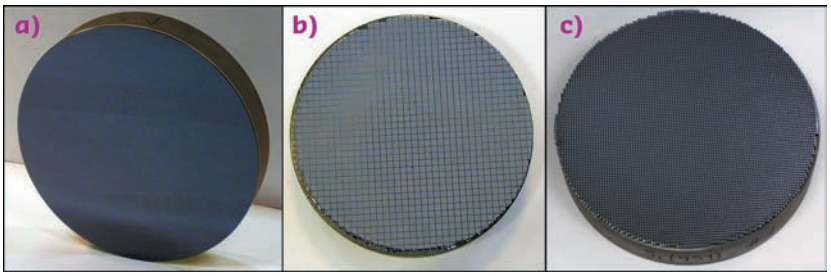

Fig. 153: Spherical analyser crystals of 100 mm diameter produced at CAL: a) elastically bent; b) elastically bent-diced (dicing raster 2.0 mm); c) diced with cubes size ~ 0.9 x 0.9 x 2.7 mm^3.

AUTHORS

R. Verbeni, C. Lapras, C. Cohen, M. Kocsis and R. Barrett.
ESRF

REFERENCES

[1] S. Huotari *et al.*, *Journal of Synchrotron Radiation, accepted* (2016).
[2] R. Verbeni *et al.*, *J. Phys. Chem. Solids* **66**, 2299-2305 (2005).

LIQUID NITROGEN COOLED BENT CRYSTAL LAUE-LAUE MONOCHROMATOR

The ID31 Laue-Laue monochromator covers the energy range from 50 to 150 KeV. Its main feature is an adjustable energy-band which is proportional to the inverse of the bending radius of the Si(111) crystals. The key technical element is the cryocooled crystal bender based on a new design.

At high photon energies, silicon crystals become transparent to X-rays allowing monochromators to work in transmission geometry (Laue) instead of reflection geometry (Bragg). Furthermore, the extinction length increases in proportion to energy and any distortion of the crystal makes it diffract kinematically rather than dynamically **[1]**. This can be used to increase the flux when the highest resolution is not needed.

Bending of the crystal introduces an easily controllable distortion whilst the brightness of the source can be conserved. However, the thermal distortion due to the large thermal load introduces a thermal bump reducing the source properties. Therefore, the crystal should be cooled down to 125 K where the thermal expansion coefficient of silicon approaches zero and the heat conductivity increases.

Cooling and control of the geometrical shape of the bent crystal are complicated. Technical problems arise mostly from vibrations in the cooling circuit. Furthermore, at high X-ray energies, the angular widths of the reflections decrease, which further restricts the technical specifications. With all this in mind, the most desirable quality in the design of the Laue-Laue monochromator for ID31 was stiffness. In particular, the design of the bender has to allow stiff mounting of the silicon crystal even when the crystal is flat.

The ID31 Laue-Laue monochromator, located at 105.2 m from the source, covers the energy range from 50 to 150 KeV, characterised by an adjustable energy-band which is proportional to the inverse of the bending radius of the crystal. The Laue-Laue monochromator consists of two

bent Si(111) crystals in non-dispersive geometry with an asymmetric cut of –36°. The crystals can be rotated so that other reflections in the (110) or (001) plane can be used, *e.g.* the Si(311) reflection with an asymmetric cut of –6.5°. The crystals are 5 mm thick. The beam offset can vary between 7 and 25 mm. To allow the full energy range with 20 mm offset, the second crystal has a translation along the incident beam from 250 to 750 mm relative to the other crystal. A 3D inside view of the monochromator tank is shown in **Figure 154**: each crystal tower has a sideways translation, coarse rotation, cross tilt and fine rotation stages; the tower of the second crystal (left in **Figure 154**) has, in addition, a 500 mm long translation stage along the incident beam. The beam stop before the second crystal is water cooled whereas both crystals are liquid nitrogen cooled. The support of each bender is thermalised with resistive heaters.

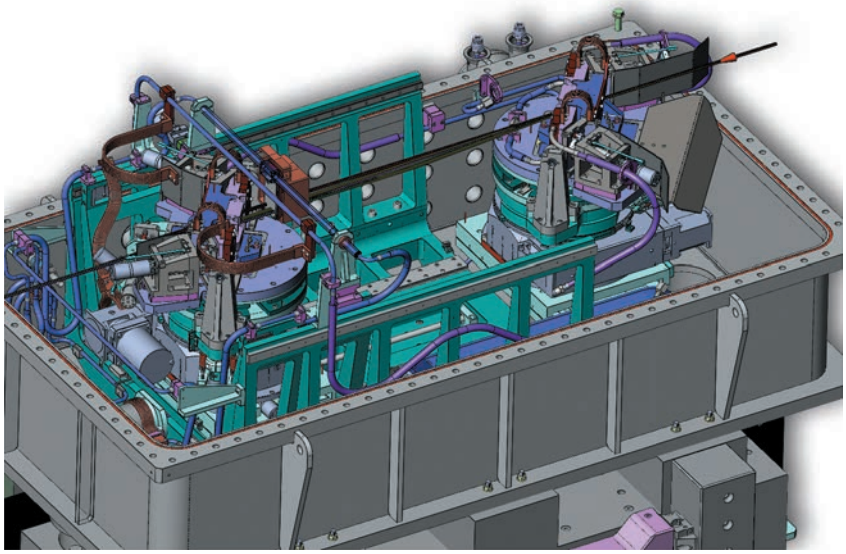

Fig. 154: 3D inside view of the monochromator.

The key technical element is the cryocooled crystal bender **[2]** based on a new concept shown in **Figure 155**: the crystal is stiffly mounted at the points A and B on the cryocooled Invar bender. The bending is achieved with two piezo-jacks which are controlled in close-loop with the capacitive sensors, with a resolution of 20 nm. The positions of the flexures are chosen so that the crystal is cylindrically bent. The rigid part of the bender is strongly attached to the support. This concept of the bender allows stiff mounting of the silicon crystal even when the crystal is flat and therefore it is less sensitive to the vibrations caused by the liquid nitrogen cooling.

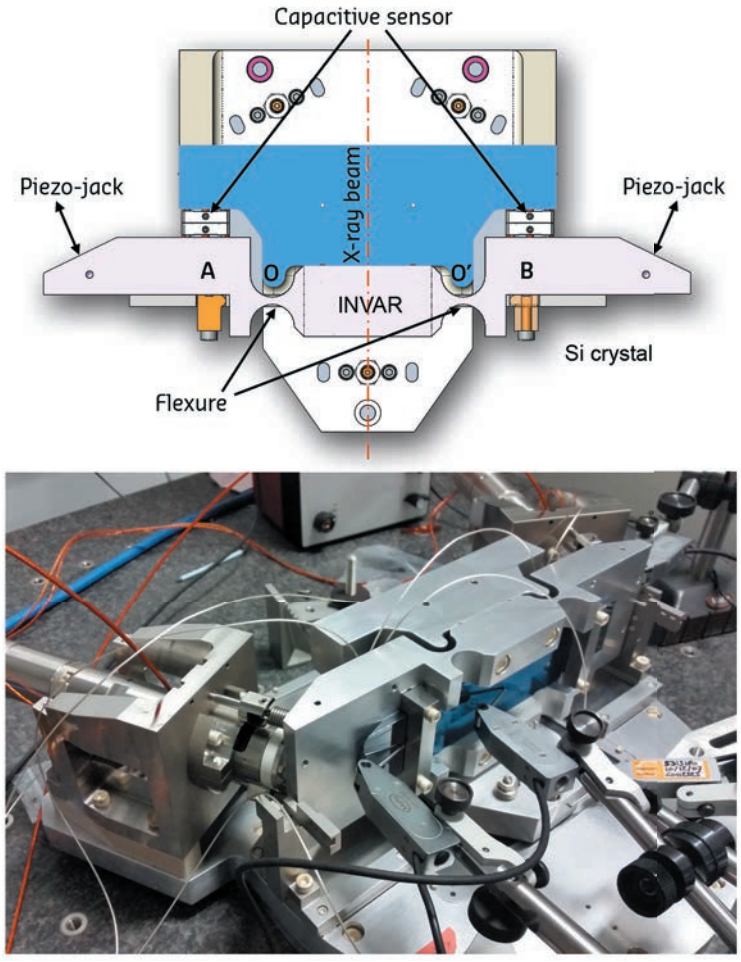

Fig. 155: Top: Schematic diagram of the crystal bender. Bottom: The prototype of the bender.

Copper cooling parts are strongly attached on both sides of the bender and are in direct contact with the end parts of the crystal as well to ensure excellent thermal contact between the cooling parts, bender and the silicon crystal. Moreover, the absorbed power can be tuned with the up-stream attenuators so that the heat load on the first crystal is optimum. The crystals and bending mechanism are high vacuum compatible. An extensive study of thermal and mechanical distortion of the crystal benders was performed using finite-element analysis.

Both crystals are cooled down to liquid nitrogen temperatures, and their bending mechanism allows both concave and convex bending with a minimum absolute bending radius of about 20 m. This ensures a maximum flexibility in the positioning of the virtual source created by the upstream compound refractive lens system and a flexible choice of the energy band pass.

The Laue-Laue monochromator is now installed at ID31 and the first X-ray commissioning measurements are very promising. The stability in energy is better than 0.5 eV over long periods of time including refills. Note that the Darwin width, *i.e.* energy band pass of a flat crystal, at 70 keV is 10 eV. The maximum band pass of 500 eV at 70 keV was achieved when the crystals were bent down to 20 m bending radius. No broadening of the focus size due to the vibrations has been observed.

AUTHORS

M. Mattenet, K. Amraoui, P. Got, A. Homs, B. Lantelme, G. Malandrino, B. Picut , L. Rousset, H.P Van Der Kleij, A. Vivo, H. Witsch and V. Honkimäki.
ESRF

REFERENCES

[1] P. Suortti and C. Schulze, *J. Synchrotron Rad.* **2**, 6-12 (1995).
[2] M.Magnin-Mattenet *et al.*, MEDSI 2016 Proceedings (JACoW), accepted September 2016.

MERGING OF SYNCHROTRON SERIAL CRYSTALLOGRAPHIC DATA BY A GENETIC ALGORITHM

A new method has been developed for the analysis of serial crystallographic data using a genetic algorithm.

In the early days of macromolecular crystallography (MX), it was not uncommon to collect data from multiple crystals and merge them in order to obtain single, high quality datasets. It was quickly discovered, however, that non-isomorphism between crystals could be a severe limitation to this technique. In the ensuing years, advances in detectors, diffractometers, synchrotron beamlines and cryo-cooling, have made the collection of datasets from single crystals the standard for MX. Pioneering work at the ESRF at the **ID13** beamline introduced a new twist: collecting multiple sub-datasets from a single crystal **[1]**. Multi-crystal and multi-position data collection strategies are referred to as serial crystallography (SX) and have seen an enormous upswing in interest, largely spurred by successes at the LCLS and SACLA free electron lasers **[2,3]**. Recently, some FEL sample delivery and data analysis methods have been adapted and extended for use at synchrotron sources at both cryogenic and ambient temperatures **[4,5]**. One particularly exciting adaptation of SX is a cryogenic method that takes advantage of the ability to collect small oscillation ranges from multiple crystals **[6]**. However, the problem of dealing with non-isomorphism has again entered the limelight. The degree of non-isomorphism is dependent on many factors, including the inherent differences between the crystals as well as changes induced by crystal handling (dehydration, for example). To address this challenge, hierarchical cluster analysis (HCA) has been the method of choice to date. Specifically, HCA is used to construct a "family tree" of a population of datasets, which can then be used as a guide to select which "branches" can be merged. This method uses metrics of similarity between datasets, most notably correlation coefficients between intensities, similarity of unit cell parameters and relative correlation of intensities in anomalous pairs **[7–9]**. With the exception of the latter, these values are a proxy for the presumed data quality of the merged data, which is a severe limitation of this methodology. We have therefore chosen to use merged data quality, in particular data metrics such as R values $CC^{1/2}$ and <I/sig(I)>, as a guide for selecting merging groups. If the number of sub-datasets is very small, all possible combinations of subsets can be evaluated. However, for a set of *n* sub–datasets, the number of possible combinations is 2^n-1, thus an exhaustive search quickly becomes computationally unfeasible even with relatively few sub-datasets. To address this problem, we have therefore used global optimisation as a means of identifying sets of sub-datasets that can be merged with good statistics. Genetic algorithms (GAs) are a well known global optimisation method. In this work we show that

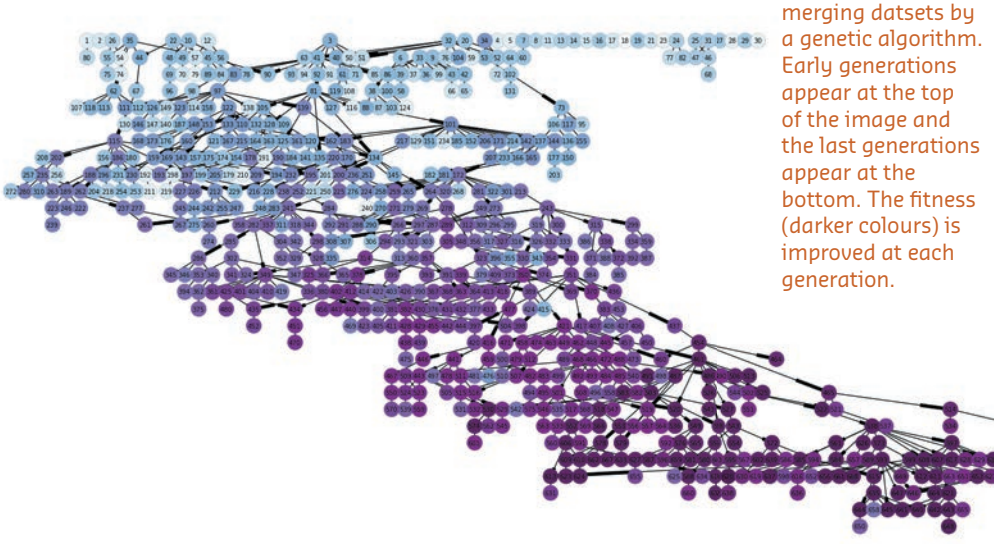

Fig. 156: Graphical representation of the optimisation of merging datsets by a genetic algorithm. Early generations appear at the top of the image and the last generations appear at the bottom. The fitness (darker colours) is improved at each generation.

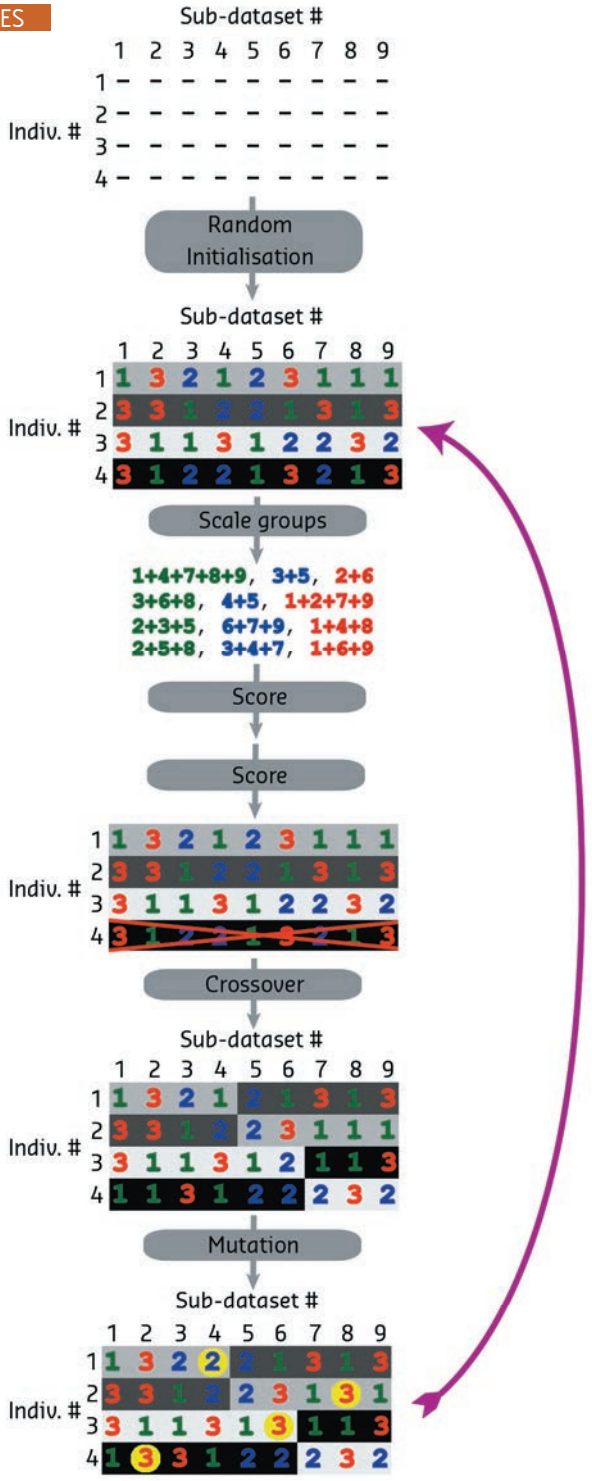

a GA (**Figures 156**, **157**) can be used to select which sub-datasets can be merged into a high quality dataset. We show that for data from well-known test systems such as thermolysin, insulin and glucose isomerase, improvements to data quality can be made, as assessed by both merging statistics and paired refinements. We furthermore show that similar improvements can be seen even for a difficult low symmetry test case with very poor diffraction limits.

Fig. 157: Schematic diagram of the genetic algorithm steps. After random initialisation, scaling is performed in XSCALE for each group in an individual. The merging statistics are then converted into fitness scores. In this case, individual 4 is removed from the population because of lower fitness and replaced with a new randomised individual. Mutation and crossover genetic modifiers are then applied, followed by cycling back to the scoring step. The background colour indicates the source of the chromosome.

PRINCIPAL PUBLICATION AND AUTHORS

Merging of synchrotron serial crystallographic data by a genetic algorithm, U. Zander (a), M. Cianci (b), N. Foos (a), C.S. Silva (c), L. Mazzei (d), C. Zubieta (c), A. de Maria (a) and M.H. Nanao (a,e), *Acta Cryst.* **D72**, 1026–1035 (2016); doi: 10.1107/S2059798316012079.
(a) ESRF
(b) European Molecular Biology Laboratory, Hamburg Outstation, c/o DESY, Hamburg (Germany)
(c) Laboratoire de Physiologie Cellulaire & Végétale, Univ. Grenoble Alpes, CNRS, CEA, INRA, BIG, Grenoble (France)
(d) Laboratory of Bioinorganic Chemistry, Department of Pharmacy and Biotechnology, University of Bologna (Italy)
(e) EMBL Grenoble (France)

REFERENCES

[1] A. Perrakis *et al.*, *Acta Cryst.* ***D55***, 1765–70 (1999).
[2] S. Boutet *et al.*, *Science* **337**, 362–4 (2012).
[3] H.N. Chapman, *Synchrotron Radiat News* **28**, 20–4 (2015).
[4] C. Gati *et al.*, *IUCrJ.* **1**, 87–94 (2014).
[5] F. Stellato *et al.*, *IUCrJ.* **1**, 204–12 (2014).
[6] U. Zander *et al.*, *Acta Cryst.* **D71**, 2328–43 (2015).
[7] R. Giordano *et al.*, *Acta Cryst.* **D68**, 649–58 (2012).
[8] Q. Liu *et al.*, *Science* **336**, 1033–7 (2012).
[9] J. Foadi *et al.*, *Acta Cryst.* **D69**, 1617–32 (2014).

DIRECT ATOMIC FORCE MICROSCOPY IMAGING AT LIQUID INTERFACES

In this study we show that atomic force microscopy (AFM) can be used to image films at liquid/liquid interfaces providing local and quantitative structural information.

The assembly of nanoscopic objects and molecules at liquid interfaces is currently attracting extensive research interest as it can be employed to prepare functional monolayers and membranes for relevant technological applications **[1]**. The precise control of the assembly process requires a thorough structural characterisation which, so far, has mainly been

carried out by reciprocal space techniques, namely X-ray and neutron scattering and reflectivity [2]. While these methods provide invaluable high-resolution and statistically significant data, the information obtained is averaged over macroscopic areas, preventing detailed characterisation of individual nanoscale defects and direct observation and manipulation of localised nanostructures. This characterisation can be performed only by microscopies but, in the case of liquid interfaces, it has so far been limited to molecules with specific functionalities.

In this study, we show that atomic force microscopy (AFM) can be applied to image films at liquid/liquid interfaces providing local and quantitative structural information by taking into account certain experimental precautions. AFM has been used for decades to characterise solid and molecular films supported on solid substrates with nanometric resolution and without the need for any specific treatment. We have proven AFM's applicability also to liquid-liquid interfaces by imaging cetyltrimethylammonium bromide (CTAB)-decorated silica nanoparticle monolayers at the water/heptane interface and comparing the results with independent grazing-incidence small-angle X-ray scattering (GISAXS) measurements performed at beamline ID10. Indeed, by varying the CTAB concentration, it is possible to tune the spacing between adjacent interfacially adsorbed nanoparticles with nanoscale precision. In **Figure 158** the topographical images of silica nanoparticle monolayers in the presence of 0.01 mM (a) and 0.05 mM (b) CTAB are reported. These images were acquired with a Cypher AFM (Asylum Research, Oxford Instruments) that is now available at the AFM platform of the Partnership for Soft Condensed Matter (PSCM). The average centre-to-centre distance between adjacent nanoparticles was determined to be 28.7 ± 2.7 and 24.6 ± 2.5 nm respectively by counting the number of nanoparticles in each image and with the assumption of hexagonal packing. These values are consistent with those determined from the GISAXS measurements reported in **Figure 158c-d**, 28.4 ± 0.6 and 24.7 ± 0.3 nm respectively.

In addition to topographical data, AFM can also measure force-distance curves providing information about the interaction force between the AFM probe and the liquid interface. Two typical force-distance curves are reported in **Figure 159**. Once the contact between the AFM probe and the interface is established, that is at distance 0, the probe starts indenting the interface over several hundreds of nanometres (distance < 0). Interestingly, the liquid interface without nanoparticles (blue curve) is stiffer. As the deformation of the interface is resisted

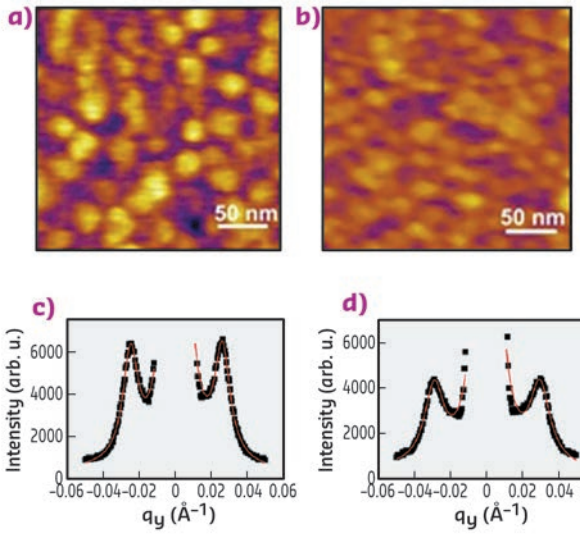

Fig. 158: AFM topographical images of nanoparticle monolayers with CTAB 0.01 mM (a) and 0.05 mM (b), GISAXS 1D profile of the nanoparticle monolayers with CTAB 0.01 mM (c) and 0.05 mM (d).

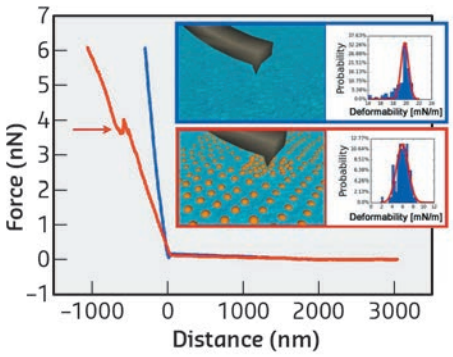

Fig. 159: Typical force-distance curves of the water/heptane interface in the absence (blue) and in the presence (red) of a silica nanoparticle monolayer. The insets show the distribution of the linear slope (deformability) obtained from several independent curves.

by its interfacial tension, the lowering of the slope in the presence of surfactant-nanoparticle complexes can be interpreted in terms of a reduction of the interfacial tension. Thus, with suitable modelling, force distance curves at the liquid interfaces can be employed to locally measure the interface tension with nanoscale resolution, providing a significant improvement with respect to current macroscale tensiometry. Finally, the force curve in the presence of nanoparticles shows a jump, highlighted by the arrow. This represents the maximum force an interfacial nanoparticle can withstand before being displaced by the nanoscale apex of the AFM tip. Such force information could potentially be used to quantify local in–plane interfacial interactions between individual nanoparticles.

In conclusion, this study opens the way to a new investigation approach for liquid-liquid interfaces. AFM imaging can be applied to any kind of molecule or object capable of assembling at liquid interfaces with high coverage once the system is at equilibrium. The results obtained are not limited to structure, as local information on interfacial tension and interfacial forces can be obtained. These findings will help to control and optimise the structure of monolayers and films at liquid interfaces and to characterise more

complex systems, such as biological membranes, where the identification of domains with different assembly and properties is necessary for the full comprehension of several biophysical processes.

PRINCIPAL PUBLICATION AND AUTHORS

L. Costa (a,c), G. Li Destri (a), N.H. Thomson (b), O. Konovalov (a) and D. Pontoni (a), *Nano Letters* **16,** 5463-5468 (2016);
doi: 10.1021/acs.nanolett.6b01877.
(a) ESRF
(b) School of Physics and Astronomy, University of Leeds (UK)
(c) Present address: Centre de Biochimie Structurale, Montpellier (France)

REFERENCES

[1] L. Hu *et al.*, *Chem. Soc. Rev.* **41**, 1350-1362 (2012).
[2] L. Cristofolini, *Curr. Opin. Colloid Interface Sci.* **19**, 228-241 (2014).

DYNAFLOW CRYOSTAT

A new compact and versatile flow cryostat was developed for more efficient cooling of samples to very low temperatures. The cryostat can operate in any orientation, has large-angle optical access and quick sample change. The cryostat is in use at beamlines in three different synchrotrons.

Low temperature measurements at synchrotron radiation beamlines provide important data for materials science and physics on structural, magnetic and electronic material properties. Over the last few decades, a wide range of X-ray techniques has been developed for low temperature research. During this time, the continuously increasing brilliance of synchrotron radiation sources and the associated absorption of larger numbers of high-energy photons in the sample has rendered the cooling of samples to very low temperatures more difficult. By positioning the sample in exchange gas, sample cooling can be enhanced with respect to cryostats with the sample in vacuum in mechanical contact with the cold source. In the dynamic flow cryostat (DynaFlow) presented here, the sample is positioned in direct contact with a cooling flow of helium. The DynaFlow cryostat is of modular construction, is compact and offers a large-angle optical access. It operates from 325 kelvin down to below 3 kelvin; at minimum temperature the helium consumption is slightly above 2 litres per hour. Three cryostats have been built for beamlines ESRF ID20, ALBA BL04-MSPD and BL22-CLÆSS and for Diamond Light Source I-11.

The DynaFlow cryostat has a peculiar mixed construction in metal and plastic. Most of the outer envelope is constructed in stainless steel for high strength; the cryogenic interior construction is made of copper for the best thermal conductivity for the heat exchangers combined with Torlon®4203 polyamide-imide for high strength thermally isolating parts of low thermal expansion. The different elements of the interior construction (**Figure 160a** and **b**) form a central tube inside of which the sample holder is placed and through which the cooling helium flows. The inner and outer vacuum chambers are designed to suit the optical angles of the experiment. Cooling from room temperature to base temperature takes about 90 minutes (**Figure 160c**); warmup of the cryostat can be faster. To change the sample holder, the helium circulation pump is stopped and the helium circuit is brought up to ambient pressure. Replacement of the sample holder is then straightforward. After restarting the pump, a certain time is necessary to cool down the sample holder.

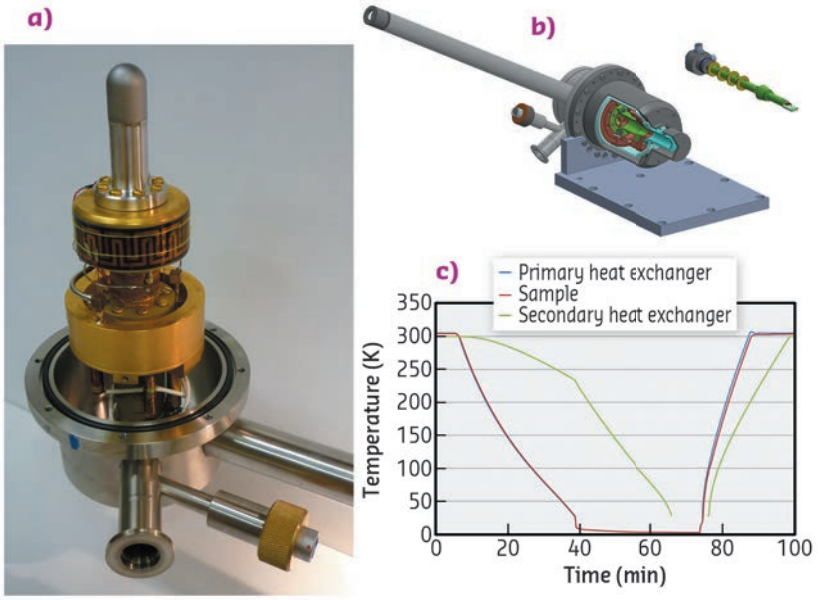

Fig. 160: DynaFlow overview. a) interior of the cryostat with copper heat exchangers and beryllium inner vacuum chamber; b) cut view of the cryostat with outer vacuum chamber mounted and sample holder; c) graph of the cryostat warmup and cooldown.

Two examples of experiments involving the DynaFlow cryostat follow. The first from **ID20** reports the RIXS study of the magnetic excitations in $CaIrO_3$, an antiferromagnetic insulator with post-Perovskite structure. In these experiments, it was necessary to lower the temperature below the Néel temperature of 110 K of $CaIrO_3$ to observe magnetic excitations. The temperature dependence of the RIXS spectra for a momentum transfer of Q = (1,2,9) in **Figure 161a** shows the elastic line at zero energy loss to be much lower at low temperature; the peak at 0.04 eV and the broad distribution up to 0.3 eV are associated with the magnetic excitations. The almost temperature-independent broad distribution between 0.4 and 0.8 eV is associated with spin-orbital transitions. The influence of temperature is clearly visible in the RIXS response and can be directly linked to a change in physical properties of the system under study.

The second example from ALBA BL04-MSPD reports the case of powder diffraction on $Mn_{0.75}Co_{0.25}WO_4$. Although the number of photons absorbed in the sample during a powder diffraction experiment is usually quite low, the thermalisation of the sample in a spinning glass capillary is not very good and the sample temperature may still rise significantly. It was thus questioned what could be the lowest attainable temperatures. The probed system is known to undergo successive magnetic transitions below 40 K. Data were collected in narrow temperature steps from 30 K down to 5 K. Selected unit cell parameters refined from the collected patterns are shown in **Figure 161b** and **c** together with magnetic susceptibility measurements which highlight the onset of magnetic transitions at 7 and 21 K. The reliability of data collection down to 5 K is evidenced by the match between the magnetic transition temperatures and structural parameter anomalies.

The DynaFlow cryostat is in routine operation at three different synchrotron research centres. The instrument has proven reliable and easily adaptable to different X-ray configurations in the tender to hard X-ray range. Its compact nature, the different accessible working geometries, the efficient and reliable sample cooling and fast sample changing are at the origin of its competitiveness with respect to existing cryostats in the market.

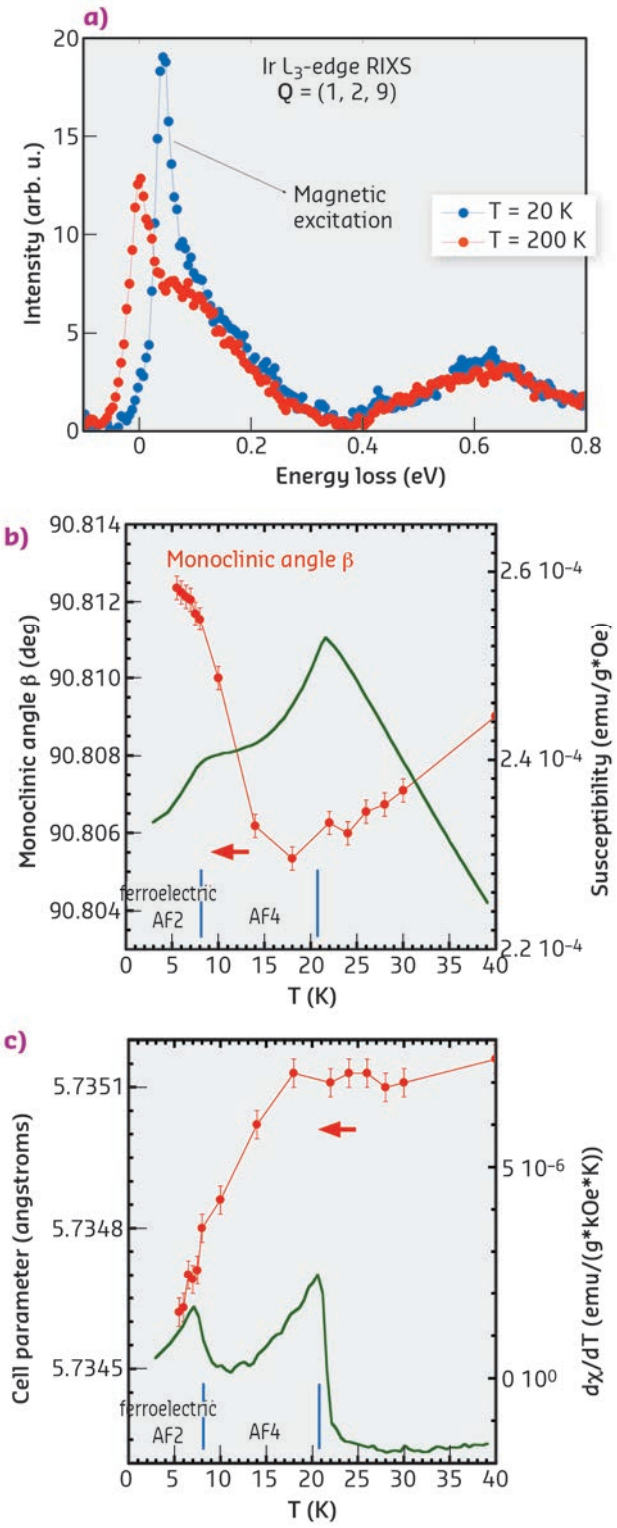

Fig. 161: a) Temperature dependence of the RIXS spectra of $CaIrO_3$. b) and c) Temperature dependence of the susceptibility and lattice parameters of $Mn_{0.75}Co_{0.25}WO_4$.

PRINCIPAL PUBLICATION AND AUTHORS

A compact and versatile dynamic flow cryostat for photon science, P.J.E.M. van der Linden (a), M. Moretti Sala (a), C. Henriquet (a), M. Rossi (a), K. Ohgushi (b), F. Fauth (c), L. Simonelli (c), C. Marini (c), E. Fraga (c), C. Murray (d), J. Potter (d) and M. Krisch (a), *Rev. Sci. Instrum.* **87**, 115103 (2016); doi: 10.1063/1.4966270.
(a) ESRF
(b) Department of Physics, Graduate School of Science, Tohoku University, Sendai (Japan)
(c) ALBA Synchrotron Light Source, Cerdanyola del Vallès, Barcelona (Spain)
(d) Diamond Light Source Ltd., Harwell Science and Innovation Campus, Didcot (U.K.)

Accelerator and Source

The Accelerator and Source Division (ASD) is in charge of the production of synchrotron light from the ESRF's 6 GeV storage ring. Much of the division's development work in 2016 has been focused on the ESRF-EBS, and major progress has been made in design and procurement, with the first components already arriving on site, as already detailed in the 'Status of the EBS' section of this report. Despite the challenges faced by the increased workload of the project, the division has also continued to ensure excellent machine availability and reliability throughout 2016, including running preventative maintenance campaigns to replace ageing equipment, developing new diagnostics devices, installing new in-vacuum undulators and maintaining the high quality power supplies.

As a result of these efforts, the operation statistics for 2016 are very positive. A total of 5485 hours of beam was delivered out of 5537 scheduled hours, representing an excellent availability of 99.06% and coming very close to the ESRF's all-time record (99.11%). The mean time between failures (MTBF) was high, at an average of 93.8 hours. More information on the main parameters of the storage ring can be found at the end of this chapter in Appendix 1.

In April 2016, for the first time, refill in top-up mode was delivered to users, providing better beam stability, low vertical emittance in all filling modes and a nearly constant beam current. The implementation followed several years of upgrades and modifications to the machine, including, in 2016, a new timing sequence, the development of cleaning in the booster and the start of commissioning of the new ramped injection power supply for the booster. Feedback from the beamlines was extremely positive and top-up is set to be improved even further in 2017 when the new booster power supply is put into operation.

The ESRF also hosted the ninth Continuous Wave and High Average RF Power (CWRF) Workshop in June 2016. The workshop provided an opportunity for designers and users of high-power CWRF systems to share experience, ideas and developments for such systems.

This year's achievements would not have been possible without the dedication of the ASD staff and the continuous support of the other ESRF divisions. May this continue in 2017 as we face the challenges of entering the assembly phase of the ESRF-EBS while simultaneously ensuring optimal operating conditions for our users.

P. RAIMONDI

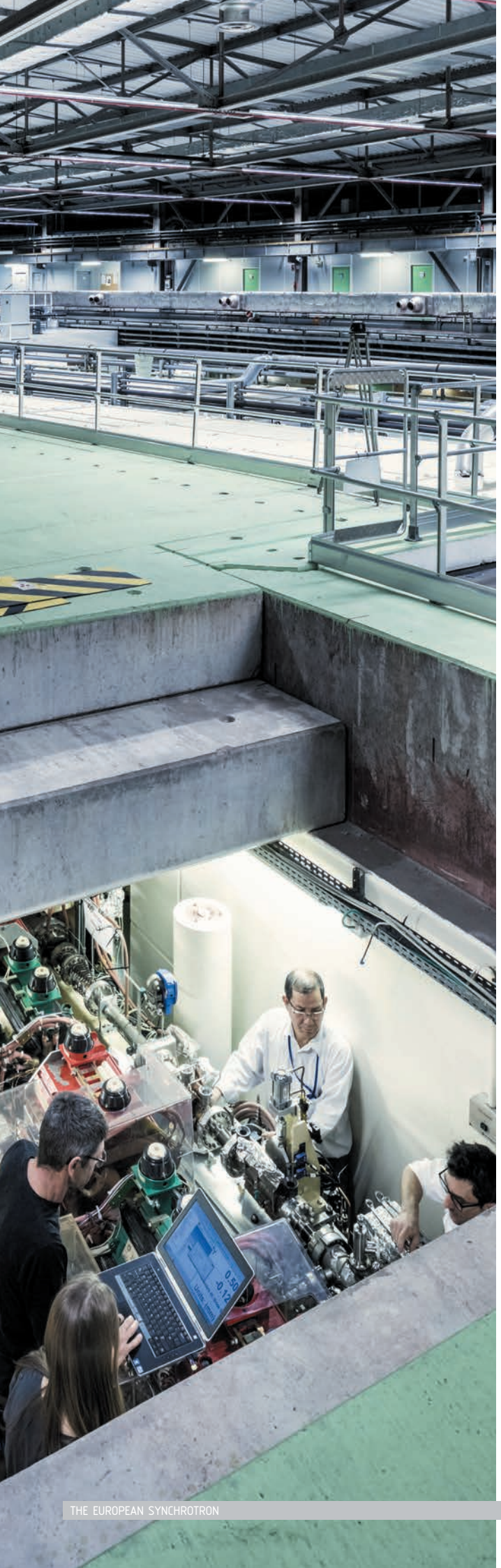


ID 10

SUMMARY OF ACCELERATOR OPERATION

With 5485 hours of beam delivered out of 5537 scheduled hours, the overall availability reached 99.06% compared to 98.53% in 2015. This high level of availability (as a reminder, the all-time record was 99.11% in 2014) reveals the success of a global preventive maintenance programme leading to the absence of very long failures in 2016.

Moreover, this year, we must emphasise the excellent reliability of the injectors. Indeed, every year, the number of refills in user mode is close to 560. This year, due to the several weeks delivered in top-up mode, the number of refills reached more than 4100. This is as many refills as are generally carried out in seven years! Except for a very low percentage (~ 3%) of skipped refills for minor reasons, the linac and the booster demonstrated their robustness thanks to an effective overhaul of the system and improvement of their components.

Over the year, only four trips lasted more than three hours: two of them attributed to the vacuum (one PLC power supply failure lasting 3.5 hours and one fugitive interlock due to a damaged cable lasting 3 hours) and two attributed to the radio frequency system (one tuner problem lasting 3.5 hours and a PLC power supply failure of 3.25 hours). Meriting a special mention is the second run, in which availability reached 99.75%, while 1508 refills in total took place for the first USM operation with top-up mode. The mean time between failures in 2016 reached 94 hours, exactly the same figure as in 2015.

Once again, the second run was the standout of the year since only five failures occurred during the 1287 hours of USM, giving an exceptional MTBF of 257 hours over the run. It was also during this run that the longest period without a failure took place (see **Figure 162** below) with 575 hours of delivery in two different modes only interrupted by the scheduled machine development time (MDT).

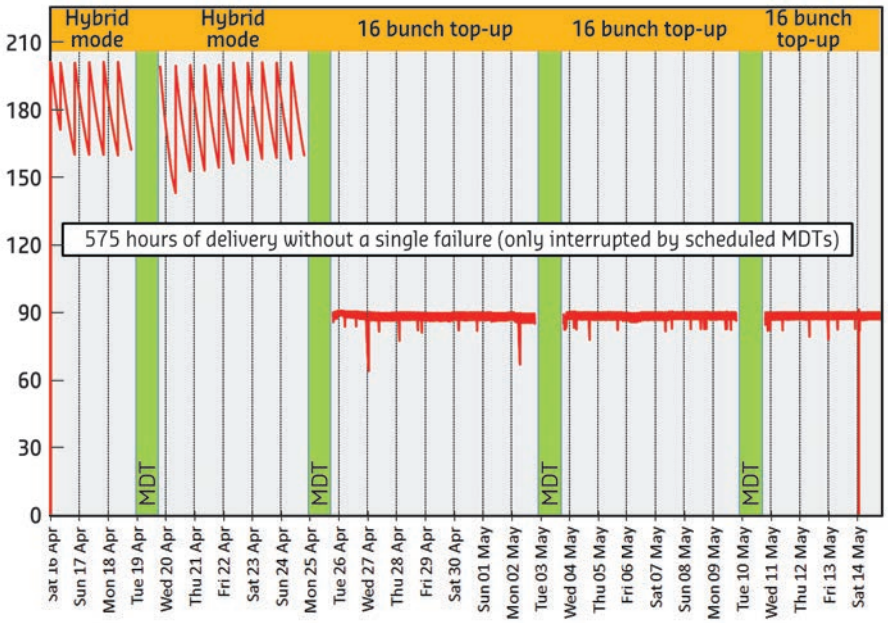

With respect to the repetitive failures, a dramatic improvement was seen in the detection of false RF arcs. From 14 arc detections in 2015 (false or real), only six were detected in 2016. The reduction was due to the successful diagnosis of the sources of the problem and corresponding corrective action. In addition, a new type of RF detector was tested for a year on an

Fig. 162: Uninterrupted beam delivery for 24 days (575 hours) in hybrid and 16-bunch modes during the run 2016-02. This illustrates the high availability in top-up mode and near constant beam current.

RUN NUMBER	2016-01	2016-02	2016-03	2016-04	2016-05	TOTAL 2016
Scheduled beam time (h)	860	1287	1241	907	1242	**5537**
Beam available including refill time (h)	849	1283.80	1229.90	896.98	1225.40	**5485.08**
Availability	**98.72%**	**99.75%**	**99.11%**	**98.90%**	**98.66%**	**99.06%**
Dead time for failures	1.3%	0.2%	0.9%	1.1%	1.3%	**0.94%**
Number of failures	11	5	14	12	17	**59**
Mean time between failures (h)	78.2	257.4	88.6	75.6	73.1	**93.8**
Mean duration of a failure (h)	1	0.6	0.8	0.8	1	**0.88**

Table 1: Overview of storage ring operation in 2016.

RF station. Following the successful results, 20 of the detectors (50% of the total stock) were replaced during the 2016-2017 winter shutdown, so that even fewer false arc detections should be achievable in 2017, the new detectors being based on a sophisticated system of coincidence before triggering.

A summary of storage ring operation for the year is presented in **Table 1**.

FILLING PATTERNS

In 2016, the distribution of the modes (**Figure 163**) was very similar to 2015. A fundamental improvement was the delivery of seven weeks in 16-bunch and two weeks in 4*10 mA (or sometimes 8 mA), both in top-up mode. This allowed a permanent delivery with a very low vertical emittance in the 7 pm.rad range and even less on some occasions. During the runs 2016-02 and 04, the cleaning of impurities was done in the storage ring, inducing a short but visible disturbance (vertical emittance blow-up) during the cleaning.

The final touch occurred during the last run when the beam was successfully cleaned in the booster before being sent to the storage ring. This removed the last visible perturbation seen by the users during the previous runs, to their great satisfaction. More details can be found in the dedicated paragraph.

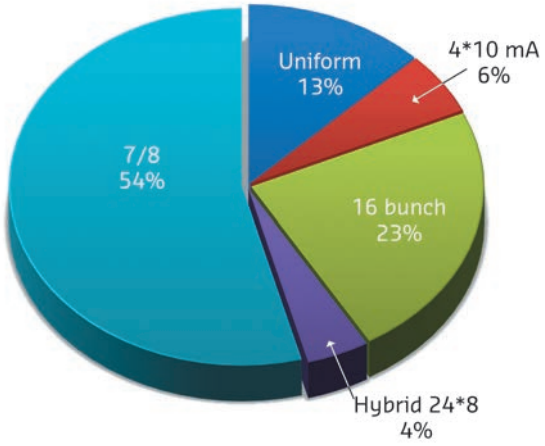

Fig. 163: Distribution of the various filling modes in 2016.

PROGRESS OF THE TOP-UP PROJECT

After over four years of preparatory work including major upgrades to the injector and the development of new diagnostics tools to limit disturbance to the beam, injection in top-up mode was officially launched to users in April 2016.

The new mode sees the accelerators refilled with electrons every 20 minutes rather than every four to 12 hours. This results in a much higher integrated current over a 24-hour period, meaning more photons for the users and better beam stability due to smaller current variations. It also means a low vertical emittance in all filling modes. Previously, the vertical emittance would be artificially increased in some modes in order to increase the lifetime, but the nearly constant beam current provided by top-up mode means that the emittance – and the resulting brilliance and resolution for users – no longer has to be

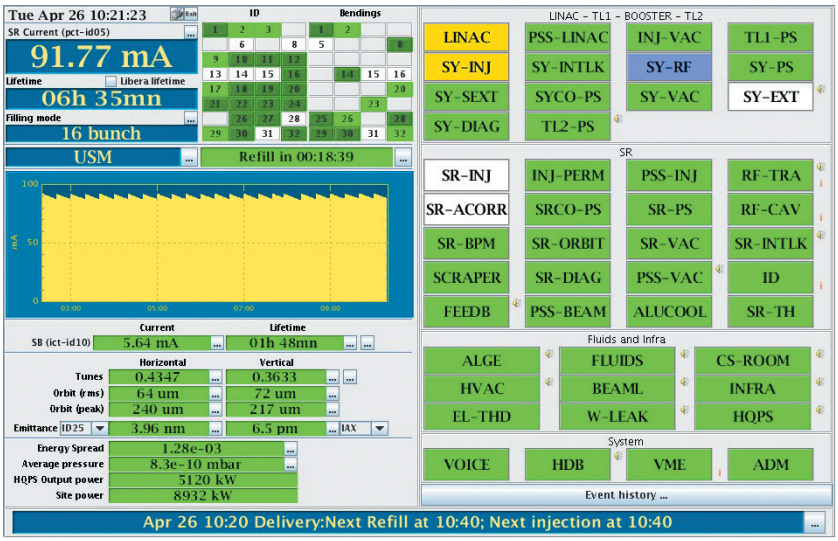

Fig. 164: The control room synopsis display on the first day of top-up operation in April 2016, showing the 20-minute injection periods and a low vertical emittance of 6.5 pm rad.

sacrificed. The first reactions from beamlines were positive, with many benefitting from an almost constant X-ray power on the optics.

A top-up trial period (**Figure 164**), with three weeks in 16-bunch mode and one week in 4*10mA mode, was run until the shutdown in May, followed by five weeks in 16-bunch and 4*8 mA throughout the rest of the year. Top-up should be further improved in 2017 once the new ramped injection power supply system (RIPS) for the booster is commissioned. Its implementation will enable cleaning to be carried out more reliably in the booster, which will further reduce disturbance to the beam during and after injection.

LAUNCH OF CLEANING IN THE BOOSTER

In parallel with top-up injection, work to implement cleaning in the booster, instead of in the storage ring, was completed at the end of 2016. Most of the filling patterns in the storage ring necessarily include some empty buckets free of electrons. However, sometimes undesired electrons can be introduced into these buckets at an early stage of the injection process. After injection, the electron beam undergoes a 'cleaning' process, which consists of removing these parasitic electrons.

When performed in the storage ring, the cleaning process takes approximately 40 seconds and induces a slight disturbance of the stored beam. To avoid this disturbance during top-up operation another cleaning system has been installed in the booster, where it is possible to clean the beam in just a few milliseconds and with no disturbance to the users. It is more challenging to perform cleaning in the booster than in the storage ring because the fluctuation of the booster characteristics from cycle to cycle has to be taken into account in real time.

Before using this cleaning system in operation, all the booster parameters that could affect the quality of the cleaning were identified and tested to make sure they could be reliably controlled over the duration of a top-up operation week. In December 2016, this new system was used for the first time in operation with 16-bunch filling mode. The purity of the beam in the storage ring was constantly checked in collaboration with beamline ID18, the most sensitive beamline to beam purity, and proved to be almost perfect.

NEW BOOSTER POWER SUPPLIES

A new 4 Hz ramped injection power supply (RIPS) was developed for the booster and delivered to the ESRF in April 2016 (**Figure 165**). The hardware underwent site acceptance and tests with the RF and pre-injector throughout the summer, while work in the autumn focused on software debugging and current regulation. Commissioning of the equipment is nearly finalised and first operation in user mode is planned for early 2017.

Fig. 165: The H-bridge of the new RIPS for the booster.

START OF TEN-YEAR MAINTENANCE OF HQPS

A programme of heavy maintenance was launched in autumn 2016 for the rotating machines of the high quality power supply (HQPS). This operation will be transparent for the users, and will be spread over two years. It entails a complete refurbishment of the 20 kV vital switches during the long shutdown of 2019 to enable them to be disconnected reliably from the public mains during protection sequences.

DEVELOPMENT OF A NEW BEAM LOSS MONITORING SYSTEM

The monitoring of the 6 GeV electron losses around the ESRF storage ring is presently done by a hybrid system consisting of ionisation chambers and scintillators. It allows a rough localisation of the losses, but has numerous limitations, including size, weight, time-resolution, sensitivity, versatility, and cost. A new system was developed in 2016 consisting of a detector head and the electronics for signal acquisition and control. The monitoring system is compact, based on a scintillator coupled to a small photo-multiplier module. Its volume and weight is only a fraction of the old version, allowing for easy installation.

The monitoring system controls four independent detector heads and acquires data with sampling rates up to 125 MHz and has flexible signal processing. Measurements performed on different configurations of detector head prototypes have led to an optimised design that allows a wide range of applications to be covered such as measurement of fast and strong losses as well as detection of very small variations of weak losses during the slow current decay.

After satisfactory results were obtained from prototypes installed in the injection zone and in close vicinity to in-vacuum undulators, the project of installing 128 regular units (*i.e.* four per cell at identical positions) plus a set (up to 30) of additional units at zones and locations of special interest is now underway (early 2017). All these units will be retained for ESRF-EBS operation.

ID STRAIGHT SECTIONS

Following the installation of a canting scheme on ID15 in 2015, the straight section was completed in 2016 with two in-vacuum undulators (an IVU22 on branch A and an IVU20 on branch B), angularly separated by 4 mrad. A short wiggler with a period of 76 mm and a peak field of 1.85 T was also completed for ID15. A new helical undulator was finalised during the year and will be installed on ID12 in January 2017.

The high-performance cryogenic permanent magnet undulator, initially foreseen to be installed in the middle of the ID31 straight section at the end of 2015, was finally put into place during summer 2016. The undulator has a magnetic period of 14.4 mm and a peak field of 1 T at the minimum operating gap of 5 mm. The performance of this undulator is among the best ever reached in the world and, in particular, exceeds by far that of superconducting undulators of similar characteristics.

APPENDIX 1: BEAM PARAMETERS OF THE STORAGE RING

Table 2 presents a summary of the characteristics of the storage ring electron beam.

Table 3 gives the main optic functions, electron beam sizes and divergences at various source points. For insertion device source points, the beta functions, dispersion, sizes and divergences are calculated in the middle of the straight section. For bending magnets, two representative source points have been selected for each type of magnet (even or odd cell number), corresponding to magnetic fields of 0.4 T and 0.85 T. These points differ by the observation angles, of respectively 3 and 9 mrad from the entrance of the magnet.

Electron beam profiles are Gaussian and the size and divergence are presented in terms of rms values. The associated full width at half maximum sizes and divergences are 2.35 times higher. Horizontal electron beam sizes and divergences are given for the multibunch filling modes and apply to almost all filling patterns, except when the current per bunch is larger than 4.5 mA, for which a slightly larger size and divergence are attained because of the increased energy spread of the electron beam.

Vertical electron beam sizes and divergences are given for a vertical emittance of 4 pm, which is now the standard for 2 x 1/3 and 7/8+1 filling modes. The vertical sizes and divergences are about 1.4 times larger in uniform filling mode (due to ion effects, which are partially corrected by the use of a vertical bunch-by-bunch feedback). To increase the lifetime of the stored beam, the vertical beam sizes and divergences are deliberately increased by about a factor of 4 in the 16-bunch, 4-bunch and hybrid filling patterns.

The lifetime, bunch length and energy spread mainly depend on the filling pattern. These are given in **Table 4** for a few representative patterns. Note that in 16-bunch and 4-bunch filling patterns, the energy spread and bunch length decay with the current (the value indicated in the table corresponds to the maximum current). The bunch lengths are given for the usual radiofrequency accelerating voltage of 9 MV (8 MV for 16-bunch and 4-bunch).

Energy	[GeV]	6.04
Maximum current	[mA]	200
Horizontal emittance	[nm]	4
Vertical emittance	[pm]	4
Revolution frequency	[kHz]	355
Number of bunches		1 to 992
Time between bunches	[ns]	2.82 to 2816

Table 2: Principal characteristics of the electron beam.

		Even ID (ID2, ID6...)	Odd ID (ID1, ID3...)	Even BM (ID2, ID6...) 3 mrad	Even BM (ID2, ID6...) 9 mrad	Odd BM (ID1, ID3...) 3 mrad	Odd BM (ID1, ID3...) 9 mrad
Magnetic field	[T]	Variable	Variable	0.4	0.85	0.4	0.85
Horiz. Beta function	[m]	37.6	0.35	1.33	1.06	2.12	1.61
Horiz. Dispersion	[m]	0.134	0.031	0.062	0.051	0.089	0.075
Horiz. rms e- beam size	[µm]	413	50	99	85	132	113
Horiz. rms e- divergence	[µrad]	10	107	116	114	104	99
Vert. Beta function	[m]	2.95	2.97	41.7	42	32.1	32.2
Vert. rms e- beam size	[µm]	3.4	3.4	12.9	13	11.3	11.4
Vert. rms e- divergence	[µrad]	1.17	1.16	0.50	0.50	0.36	0.36

Table 3: Beta functions, dispersion, rms beam size and divergence at the various source points.

Filling pattern		Uniform	7/8 + 1	Hybrid	16-bunch	4-bunch
Number of bunches		992	870+1	24x8+1	16	4
Maximum current	[mA]	200	200	200	90	40
Lifetime	[h]	50	45	30	16	9
Rms energy spread	[%]	0.11	0.11	0.11	0.12	0.16
Rms bunch length	[ps]	20	20	25	48	55

Table 4: Current, lifetime, bunch length and energy spread for a selection of filling modes.

Facts and Figures

MEMBERS AND ASSOCIATE COUNTRIES

(AS OF JANUARY 2017)

Member countries:

27.5%	France
24%	Germany
13.2%	Italy
10.5%	United Kingdom
6%	Russia
5.8%	Benesync (Belgium, The Netherlands)
5%	Nordsync (Denmark, Finland, Norway, Sweden)
4%	Spain
4%	Switzerland

Associate countries:

1.5%	Israel
1.3%	Austria
1%	Poland
1%	Portugal
1.05%	Centralsync (Czech Republic, Hungary, Slovakia)
0.3%	South Africa

THE BEAMLINES

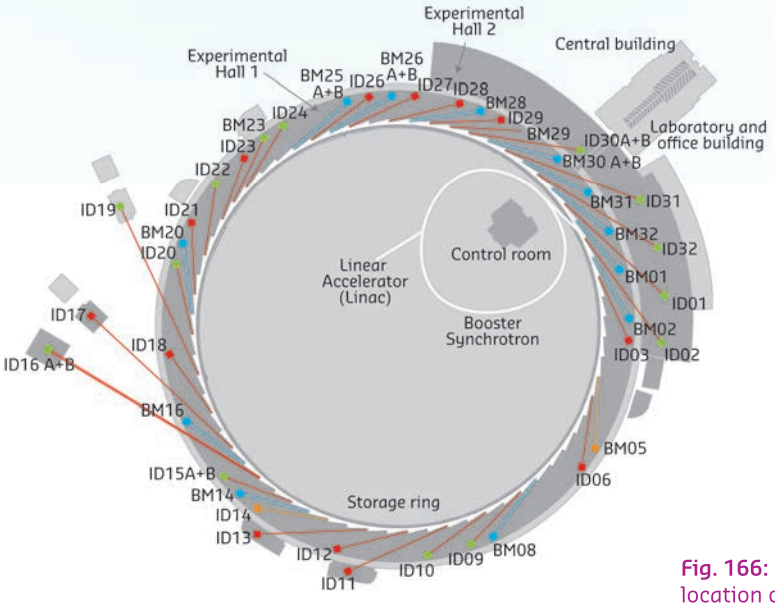

Details of the public ESRF beamlines as well as those operated by Collaborating Research Groups (CRG) are given in **Tables 5** and **6**. **Figure 166** shows the location of the beamlines in the experimental halls.

Fig. 166: Experimental hall showing location of the beamlines (public and CRG beamlines).

SOURCE POSITION	NUMBER OF INDEPENDENT END-STATIONS	BEAMLINE NAME	STATUS	
ID01	1	Microdiffraction imaging	Operational	since 12/14
ID02	1	Time-resolved ultra-small-angle X-ray scattering	Operational	since 07/14
ID03	1	Surface diffraction	Operational	since 09/94
ID06	0.3	Large volume press	Operational	since 10/13
ID09	1	Time-resolved structural dynamics	Operational	since 09/94
ID10	1	Soft interfaces and coherent scattering	Operational	since 06/12
ID11	1	Materials science	Operational	since 09/94
ID12	1	Polarisation-dependent X-ray spectroscopy	Operational	since 01/95
ID13	1	Microfocus	Operational	since 09/94
ID15A	0.7	Materials chemistry and engineering	Operational	since 11/16
ID15B	0.5	High-pressure diffraction	Operational	since 11/16
ID16A	1	Nano-imaging	Operational	since 05/14
ID16B	1	Nano-analysis	Operational	since 04/14
ID17	1	Medical	Operational	since 05/97
ID18	1	Nuclear scattering	Operational	since 01/96
ID19	1	Microtomography	Operational	since 06/96
ID20	1	Inelastic X-ray scattering	Operational	since 06/13
ID21	1	X-ray microscopy / IR spectroscopy	Operational	since 12/97
ID22	1	High resolution powder diffraction	Operational	since 05/14
ID23	2	Macromolecular crystallography MAD	Operational	since 06/04
		Macromolecular crystallography microfocus	Operational	since 09/05
ID24	1	Dispersive EXAFS	Operational	since 02/96
ID26	1	X-ray absorption and emission	Operational	since 11/97
ID27	1	High pressure	Operational	since 02/05
ID28	1	X-ray scattering II	Operational	since 12/98
ID29	1	Multiwavelength anomalous diffraction	Operational	since 01/00
ID30A	2	Macromolecular crystallography	Operational	since 07/14
ID30B	1	Macromolecular crystallography	Operational	since 04/15
ID31	1	Interfaces and materials processing	Operational	since 11/15
ID32	1	Soft X-ray spectroscopy	Operational	since 11/14
BM14	1	Macromolecular crystallography (MAD)	Operational	since 01/10
BM23	1	X-ray absorption spectroscopy	Operational	since 03/11
BM29	1	Bio SAXS	Operational	since 06/12

Table 5: List of the ESRF public beamlines.

SOURCE POSITION	NUMBER OF INDEPENDENT END-STATIONS	BEAMLINE NAME	FIELD OF RESEARCH	STATUS
BM01	1	Swiss-Norwegian BL	X-ray absorption and diffraction	Operational since 01/95
BM02	1	D2AM (French)	Materials science	Operational since 09/94
BM08	1	LISA (Italian)	X-ray absorption and diffraction	Operational since 09/94
BM20	1	ROBL (German)	Radiochemistry	Operational since 09/98
BM25	2	SPLINE (Spanish)	X-ray absorption and diffraction	Operational since 04/05
BM26	2	DUBBLE (Dutch/Belgian)	Small-angle scattering	Operational since 12/98
			EXAFS	Operational since 06/01
BM28	1	XMAS (British)	Magnetic scattering	Operational since 04/98
BM30	2	FIP (French)	Protein crystallography	Operational since 02/99
		FAME (French)	EXAFS	Operational since 08/02
BM31	1	SNBL II (Swiss-Norwegian)	X-ray absorption and diffraction	Operational since 09/16
BM32	1	IF (French)	Interfaces	Operational since 09/94
Operational in 2017:				
BM14	1	Assigned to DUBBLE (Dutch/Belgian)	EXAFS	Operational from 09/17
BM16	1	FAME-UHD (French)	XES from ultra high diluted samples	Operational from 02/17

Table 6: List of the Collaborating Research Group beamlines.

USER OPERATION

User operation at the ESRF during 2016 has been at an all-time high, breaking several long-standing records in both interest from the user community and provision of beamtime by the ESRF to satisfy the needs of the growing community. In terms of the beamline portfolio, ID15, the final refurbished beamline, took its first users in early November, while BM14, the structural biology bending-magnet beamline, closed definitively at the end of October; this port and its infrastructure will now be used by the Dutch-Belgian consortium DUBBLE to operate a new CRG beamline to replace BM26A.

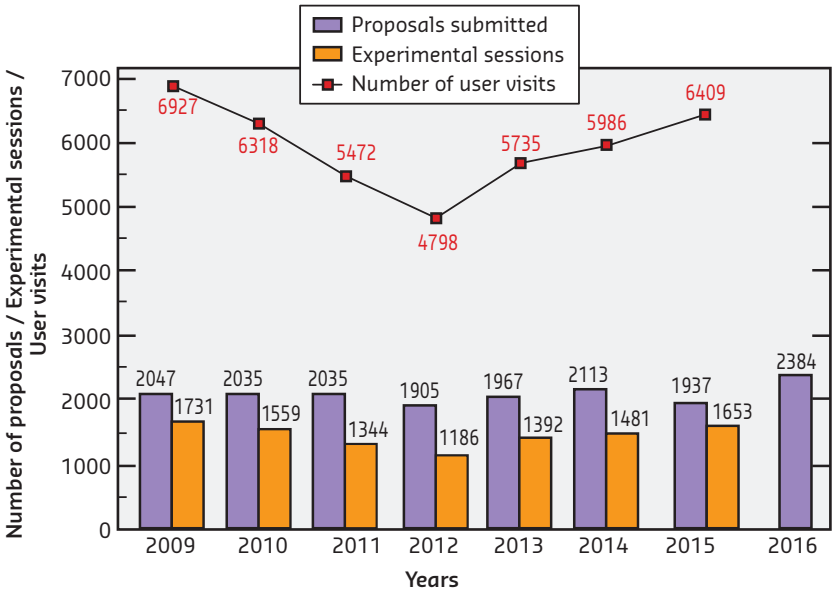

Fig. 167: Numbers of applications for beamtime, experimental sessions and user visits, 2009 to 2016. N.B. Final numbers of experimental sessions and user visits for 2016 were not available at the time of going to press.

Scientific field	Total shifts requested	Total shifts allocated
Chemistry	5 456	1 869
Earth Sciences	2 432	924
Environment	904	287
Hard Condensed Matter Science	9 823	3 464
Cultural Heritage	397	153
Life Sciences	1 664	683
Applied Materials Science	6 170	2 187
Medicine	1 256	561
Engineering	282	69
Methods & Instrumentation	534	249
Structural Biology	2 666	2 825
Soft Condensed Matter	2 425	891
Totals	**34 009**	**14 162**

Table 7: Shifts of beamtime requested and allocated for user experiments, year 2016.

The X-ray diffraction and XAFS SNBL CRG beamline BM01B was moved to its new port on BM31, opening to users in September. BM01 remains the SNBL single crystal and powder X-ray diffraction beamline (originally BM01A). The microfocus structural biology beamline, ID23-2, closed for an optics hutch upgrade in October and will reopen in May 2017, and finally BM16, the new CRG beamline FAME-UHD (French absorption spectroscopy beamline for material and environmental science - ultra-high dilution), was constructed and will take its first users early in 2017. **Figure 167** shows the number of applications for beamtime received since ESRF Upgrade Phase I began in 2009. The number of requests for beamtime in 2016 has broken all records with a 15% increase demonstrating clearly the very strong interest from the user community to use the upgraded facilities now available.

Proposals for experiments are selected and beamtime allocations are made through peer review. As in previous years, beamtime for 2016 was allocated based on recommendations made by review committees of specialists, for the most part from European countries, Israel and South Africa. These beamline-based committees review all proposals received for a particular beamline. This gives the committees an overview of all the projects proposed for a single beamline and allows them greater flexibility to optimise the selection of proposals that will be awarded beamtime on each beamline. Proposals for experiments in 2016 were reviewed by 11 review committees grouping the following beamlines of similar techniques or activities:

- C01 (ID01, ID03, BM25B, BM32)
- C02 (ID11, ID15A, ID22, ID31)
- C03 (ID12, ID32)
- C04 (BM08, BM16, BM20, BM23, BM25A, BM26A, BM30B, BM31)
- C05 (BM01, ID06-LVP, ID15B, ID18, ID27, ID28)
- C06 (ID17, ID19)
- C07 (ID16A, ID16B, ID21)
- C08 (ID02, ID13, BM26B)
- C09 (BM02, ID09, ID10, BM28)
- C10 (Structural biology beamlines)
- C11 (ID20, ID24, ID26)

The scientific areas of the ESRF research activities reviewed by these eleven committees are shown in **Table 7**.

The review committees met twice during the year, around six weeks after the deadlines for submission of proposals (10 September

2015 and 1 March 2016). They reviewed 2384 applications for beamtime in 2016 and selected 962 (40.4%) in total, the second highest ESRF allocation ever. The change of the September deadline date from 1st to 10th September has given proposers more time after the summer and conference season to prepare their beamtime proposals, and successive records for proposal submission for the Autumn deadline have been broken in both 2015 (1135) and 2016 (1154).

Requests for beamtime in 2016, which is scheduled in shifts of 8 hours, totalled 34 009 shifts, smashing all previous records by 10%. Of these, 14 162 shifts (41.6%) were allocated. The distribution of shifts requested and allocated by scientific area for 2016 is shown in **Table 7**, while the number of shifts requested, allocated and delivered per year since 2009 is shown in **Figure 168**.

The breakdown of shifts delivered for experiments by scientific area in the first half of 2016 is shown in **Figure 169**. This same period saw 3484 visits by scientists to the ESRF under the user programme, to carry out 920 experiments; both figures are again records for the first 6-month operation period. Overall, the number of users in each experimental team averaged 3.8 persons and the average duration of an experimental session was just over 8 shifts (less than 3 shifts for MX experiments and 12.8 shifts for non-MX experiments). Faster and more efficient experiments are ensuring that more proposals can be accepted, maintaining an acceptance rate of over 40% despite the 15% increase in the number of proposals received. For this same reason, more experiments and users can be supported; the annual number of experimental sessions and user visits since 2009 is shown in **Figure 167**. Based on beamtime delivered so far in 2016, the number of experiment sessions for the full year is expected to be around 1850, with user visits expected to surpass 6900, while the total beamtime delivered for users is expected to top 16000 shifts for only the second time ever. These beamtime usage figures are again at record levels, indicating clearly the successful outcome of the first phase of the Upgrade Programme.

One of the principle measurable output parameters of the ESRF is the number and quality of publications accepted in peer-reviewed journals. The number of publications rose continuously for many years, eventually reaching a plateau of over 1800 publications per year up until 2014, as shown in **Figure 170**. The publication figures in 2015 and 2016 show the expected drop in output resulting from the 5-month general shutdown of the ESRF back in 2011-2012 and the various beamline closures over the duration of Upgrade Phase I. This drop is however only very small, less than 100 publications per year, maintaining the ESRF output at a level well over 1700 publications

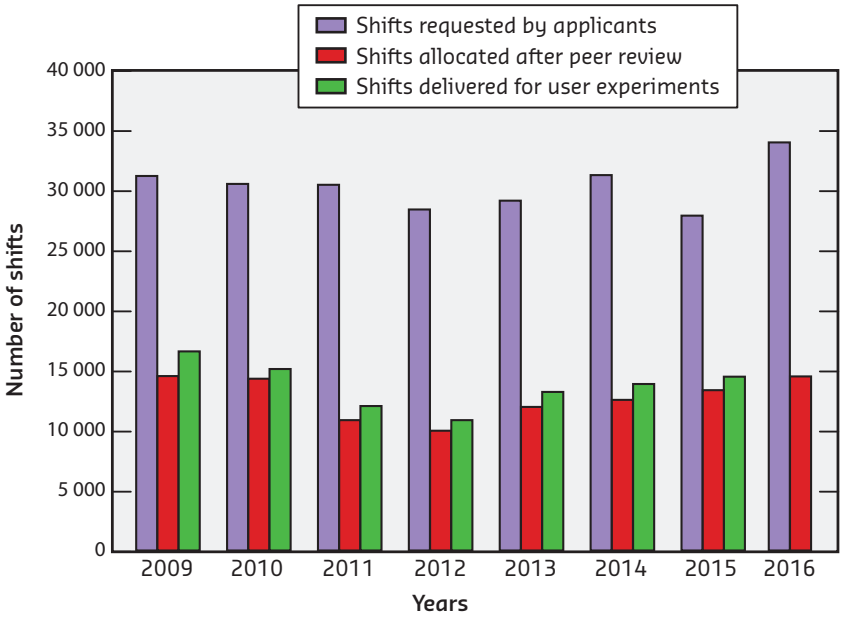

Fig. 168: Amount of beamtime requested, allocated and delivered, 2009 to 2016. N.B. The final number for beamtime delivered for 2016 was not available at the time of going to press.

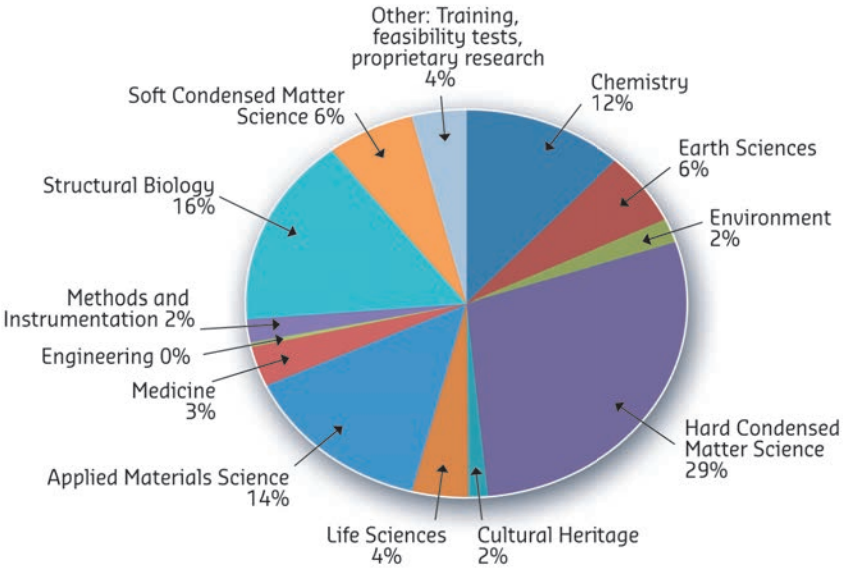

Fig. 169: Shifts delivered for experiments, March to July 2016, by scientific area, total 7895.

for 2016 once all publications will have been accounted for. Since the ESRF began user operation back in 1994, a total of 28 671 publications have been accepted in peer-reviewed journals. Of these, around 300 every year are published in high impact factor journals and no drop has been observed here. These are excellent figures, showing that the ESRF research output is maintained at a worldwide high.

User responses to questionnaires show once again that the ESRF continues to maintain its excellent reputation concerning the assistance and service given by scientists and support staff at the beamlines, and travel and administrative arrangements, in addition to the quality both of the beam and of the experimental stations. On site offline facilities, such as preparation laboratories and collaborative platforms offering complementary techniques and support, provide a vital contribution to the quality of user support but also to the quality of the science and results that can be achieved. Major scientific advances can be made through the collection of complete and complementary data and information on the most important scientific questions. These aspects remain key to the continuing success story of the ESRF.

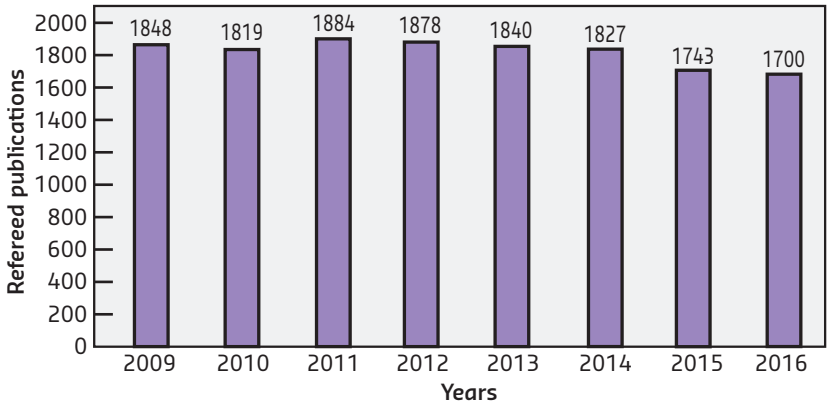

Fig. 170: Numbers of publications appearing in refereed journals reporting on data collected either partially or totally at the ESRF, 2009 to 2016.

ADMINISTRATION AND FINANCE

Expenditure and income 2015

Expenditure		kEuro
Accelerator and Source		
Personnel		6 945.9
Recurrent		2 050.4
Operating costs	*1 908.7*	
Other recurrent costs	*141.7*	
Capital		6 585.9
Accelerator and Source developments	*6 585.9*	
Beamlines, experiments and in-house research		
Personnel		19 102.6
Recurrent		5 285.3
Operating costs	*1 487.3*	
Other Recurrent costs	*3 798.0*	
Capital		11 113.0
Beamline developments	*11 113.0*	
Beamline refurbishment		
Technical and administrative supports		
Personnel		30 355.2
Recurrent		13 650.4
Capital		4 553.1
Industrial and commercial activity		
Personnel		435.4
Recurrent		221.6
Unexpended committed funds		
Funds carried forward to 2016		6 131.0
Total		**106 429.8**

Income	kEuro
2015 Members' contributions	84 990.6
Funds carried forward from 2014	998.7
Other income	
Scientific Associates	6 157.7
Sale of beamtime	1 883.4
Scientific collaboration and Special projects	5 964.5
Russian Fed. contribution to construction	10 000.0
Pre-financing / Balance	– 9 696.1
Funds carried forward to 2016	6 131.0
Total	**106 429.8**

Revised expenditure and income budget for 2016

Expenditure		kEuro
Accelerator and Source		
Personnel		7 257
Recurrent		1 959
Operating costs	*1 824*	
Other recurrent costs	*135*	
Capital		21 403
Accelerator and Source developments	*21 403*	
Beamlines, experiments and in-house research		
Personnel		19 665
Recurrent		5 391
Operating costs	*1 424*	
Other Recurrent costs	*3 967*	
Capital		9 187
Beamline developments	*9 187*	
Technical and administrative supports		
Personnel		30 504
Recurrent		14 548
Capital		5 623
Industrial and commercial activity		
Personnel		481
Recurrent		201
Total		**116 219**

Income	kEuro
2016 Members' contributions	92 442
Funds carried forward from 2015	6 131
Other income	
Scientific Associates	5 829
Income from industrial co.activity	2 042
Scientific collaboration and Special projects	3 667
Balance ESRF-EBS	6 108
Total	**116 219**

Expenditure 2015 by nature of expenditure

	kEuro
PERSONNEL	
ESRF staff	54 668.5
External temporary staff	6.9
Other personnel costs	2 163.6
RECURRENT	
Consumables	7 958.3
Services	10 759.5
Other recurrent costs	2 490.1
CAPITAL	
Buildings, infrastructure	1 040.6
Lab. and Workshops	1 875.1
Accelator and Source incl. ID's and FEs	6 585.9
Beamlines, Experiments	11 113.0
Computing Infrastructure	1 613.6
Other Capital costs	23.7
Unexpended committed funds	
Funds carried forward to 2016	6 131.0
Total	**106 429.8**

Revised budget for 2016 by nature of expenditure

	kEuro
PERSONNEL	
ESRF staff	55 463
External temporary staff	20
Other personnel costs	2 424
RECURRENT	
Consumables	8 755
Services	10 906
Other recurrent costs	2 438
CAPITAL	
Buildings, infrastructure	1 635
Lab. and Workshops	2 296
Accelator and Source incl. ID's and FEs	21 403
Beamlines, Experiments	9 187
Computing Infrastructure	1 592
Other Capital costs	100
Total	**116 219**

The budget for 2016 includes additional contributions from Members and Scientific Associates of 10 828 kEUR dedicated to the ESRF-EBS Project. The ESRF-EBS expenditure budget amounts to a total of 20 807 kEUR including 3 871 kEUR of ESRF operating budget.

2016 manpower *(posts filled on 31/12/2016)*

	Scientists, Engineers, Senior Administrators	Technicians and Administrative Staff	PhD Students	Total
Staff on regular positions				
Accelerator and Source*	40	46		86
Beamlines, instruments and experiments*	247	90	25	362
General technical services	32	54		86
Directorate, administration and central services	43	56		99
Sub-total	*362*	*246*	*25*	*633*
Other positions				
Short term contracts	17	10		27
Staff under "contrats de professionnalisation"		34		34
Total	**379**	**290**	**25**	**694**
Scientific collaborators and consultants	*8*			*8*

** Including scientific staff on time limited contracts.*

ORGANISATION CHART OF THE ESRF

(AS OF JANUARY 2017)

Administrative and Finance Committee
Chairperson: J. Scratcher

Council
Chairperson: B. Girard
up to 3 delegates per Contracting Party

Science Advisory Committee
Chairperson: D. McMorrow

Machine Advisory Committee
Chairperson: R. Walker

Director General
F. Sette

DG's Services:
- Head of DG's Office/Secretary of Council: I. Echeverria
- Communication Group
- Internal Auditor
- Safety Group

ACCELERATOR AND SOURCE
Director: P. Raimondi

- Beam dynamics and applications
- Power supplies
- Insertion devices
- Front-ends
- Radio frequency and linac
- Diagnostics
- Operation
- Secretariat

ADMINISTRATION
Director: L-J. Sánchez Ortiz

- Personnel
- Finance
- Purchasing

- Joint ILL/ESRF Medical service
- Joint ILL/ESRF

EXPERIMENTS

Director: J. Susini

Beamline groups:
- Complex systems and biomedical sciences
- Structural biology
- X-ray nanoprobe

Director: H. Reichert

Beamline groups:
- Electronic structure, magnetism and dynamics
- Matter at extremes
- Structure of materials

Scientific infrastructure
- Theory group
- User office
- CRG liaison office
- Business Development Office
- Library
- Secretariat

Beam Time Allocation Panels
- **C01** (ID01, ID03, BM25B, BM32) Chairperson: E. Lundgren
- **C02** (ID11, ID15A, ID22, ID31) Chairperson: O. Thomas
- **C03** (ID12, ID32) Chairperson: A. Severing
- **C04** (BM08, BM16, BM20, BM23, BM25A, BM26A, BM30B, BM31) Chairperson: F. Boscherini
- **C05** (ID06-LVP, ID15B, ID18, ID27, ID28, BM01) Chairperson: V. Giordano
- **C06** (ID17, ID19) Chairperson: B. Mueller
- **C07** (ID16A, ID16B, ID21) Chairperson: O. Addison
- **C08** (ID02, ID13, BM26B) Chairperson: H. Lichtenegger
- **C09** (ID09, ID10, BM02, BM28) Chairperson: M. Goldmann
- **C10** (Structural Biology Beamlines) Chairperson: G. Sulzenbacher
- **C11** (ID20, ID24, ID26) Chairperson: M. Feiters

INSTRUMENTATION SERVICES AND DEVELOPMENT DIVISION
Head: M. Krisch

- Advanced analysis and modeling
- Detector and electronics
- Software
- X-ray optics
- Mechanical engineering

TECHNICAL INFRASTRUCTURE DIVISION
Head: R. Dimper

- Management information systems and web
- Systems and communication
- Buildings and infrastructure
- EX2/CPER project team
- Survey and alignment
- Vacuum

We gratefully acknowledge the help of:

C. Argoud, T. Baudoin, A. Bosak, J.F. Bouteille, B. Boulanger, N. Brookes, J. Chavanne, D. Chenevier, K. Colvin, K. Clugnet, E. Dancer, R. Dimper, I. Echeverría, L. Farvacque, S. Gerlier, P. Glatzel, L. Graham, L. Hardy, V. Honkimaki, J. Jacob, E. Jean-Baptiste, A. Joly, M. Krisch, G. Leonard, S. Lombardo, M. Moretti-Sala, C. Mueller-Dieckmann, J. McCarthy, S. Pascarelli, P. Raimondi, H. Reichert, J.L. Revol, S. Rio, B. Roche. A. Rogalev, K. Scheidt, T. Schülli, F. Sette, J. Susini, M. Wulff and all the users and staff who have contributed to this edition of the Highlights.

Cover
Cover design by S. Lombardo
featuring images by S. Candé.

Photo credits:
C. Argoud, I. Ginzburg, A. Joly, P. Jayet, @StefCandé.

Editor
G. Admans
Layout
Pixel Project
Printing
Imprimerie du Pont de Claix

Communication Group
ESRF
CS40220
38043 Grenoble Cedex 9 • France
Tel. +33 (0)4 76 88 20 56
Fax. +33 (0)4 76 88 25 42
http://www.esrf.eu